TECHNISCHE UNIVERSITÄT MÜNCHEN

Lehrstuhl für Werkzeugmaschinen und Fertigungstechnik

am Institut für Werkzeugmaschinen und Betriebswissenschaften (*iwb*)

Laser Structuring of Graphite Anodes for Functionally Enhanced Lithium-Ion Batteries

Jan Bernd Habedank

Vollständiger Abdruck der von der Fakultät für Maschinenwesen der Technischen Universität München zur Erlangung des akademischen Grades eines

Doktor-Ingenieurs (Dr.-Ing.)

genehmigten Dissertation.

Vorsitzende: Prof. Dr. Petra Mela

Prüfer der Dissertation:

1. Prof. Dr.-Ing. Michael F. Zäh
2. Prof. Dr.-Ing. Arno Kwade

Die Dissertation wurde am 19.11.2020 bei der Technischen Universität München eingereicht und durch die Fakultät für Maschinenwesen am 20.03.2021 angenommen.

Preface

This dissertation was elaborated during my work as a research associate and as a member of the management board of the Institute for Machine Tools and Industrial Management (*iwb*) at the Technical University of Munich.

First of all, I would like to thank Prof. Dr.-Ing. Michael F. Zaeh, full professor of the *Chair of Machine Tools and Manufacturing Technology*, for giving me the opportunity to pursue a doctorate. Together with Prof. Dr.-Ing. Gunther Reinhart, you run a fascinating, diverse institute and you know how to provide young researchers with both scientific freedom and methodical expertise.

I would also like to thank Prof. Dr.-Ing. Arno Kwade for assuming the position of the co-advisor and Prof. Dr. Petra Mela for chairing the doctoral examination.

Many thanks to the colleagues at the *iwb*, particularly the groups for *Joining and Cutting Technology* and *Battery Production* as well as the Institute's management board. The valuable discussions with you have been an enrichment to my work. And the many, many activities outside the Institute's daily routine have provided the necessary balance. Some of you have become good friends, and I hope that our paths in life will continue to cross regularly.

Furthermore, I would like to thank all of the co-authors of my publications. Particular credit goes to Ludwig Kraft, Daniel Schwab, Prof. Dr. Andreas Jossen, Prof. Dr. Heinz P. Huber, and Dr. Ralph Gilles, with all of whom I have discussed the results and developed numerous ideas.

A big *thank you* goes to my godmother Brigitta Engelhard, my brother Clemens Habedank, and my colleagues and good friends Florian Günter, Johannes Kriegler, and Dr. Patrick Schmitz for their critical comments and corrections in this document.

Finally, I would like to thank all those who have not made a direct contribution to this work, but without whom I would never have come so far: my parents, Dr. Stephanie and Dr. Martin Habedank, and my wife Lea. Thank you for the continued support, the confidence, and the backing you have given me!

Munich, April 2021 *Jan Bernd Habedank*

Table of Contents

Table of Contents

List of Abbreviations

Acronym	Description
2D	Two-dimensional
3D	Three-dimensional
AR	Aspect ratio
BPP	Beam parameter product
CC	Constant current
CCCV	Constant current, constant voltage
cf.	Compare (lat.: confer)
CMC	Carboxymethyl cellulose
CV	Constant voltage
cw	Continuous wave
DC	Dimethyl carbonate
DEC	Diethyl carbonate
DOD	Depth of discharge
EC	Ethylene carbonate
EIS	Electrochemical impedance spectroscopy
EMC	Ethyl methyl carbonate
FDM	Fused deposition modeling
FEM	Finite Element Method

Acronym	Description
HAZ	Heat affected zone
ICALEO	International Congress on Lasers and Electro Optics
i.e.	That is (to say) (lat.: id est)
iwb	Institute for Machine Tools and Industrial Management at TUM
L	Loading (area-specific capacity of an electrode)
LCO	Lithium cobalt oxide
LDW	Laser direct write
LFP	Lithium iron phosphate
MEMS	Micro-electro-mechanical systems
NCA	Lithium nickel cobalt aluminum oxide
NMC	Lithium nickel manganese cobalt oxide
NMP	*N*-Methyl-2-pyrrolidone
OCV	Open circuit voltage
P	Publication
p2D	Pseudo-two-dimensional
PVDF	Polyvinylidene diflouride
SBR	Styrene-butadiene rubber
SEI	Solid electrolyte interphase
SEM	Scanning electron microscope
SO	Sub-objective
SOC	State of charge
TUM	Technical University of Munich

List of Symbols

Variable	Unit[1]	Description
a	$m^2 \cdot s^{-1}$	Thermal diffusivity
α	-	Bruggeman exponent
α_a	-	Anodic charge transfer coefficient
α_c	-	Cathodic charge transfer coefficient
α_{opt}	m^{-1}	Optical attenuation coefficient
C	h^{-1}	C-rate
c_l	$mol \cdot m^{-3}$	Liquid phase concentration
$c_{l,ref}$	$mol \cdot m^{-3}$	Reference liquid phase concentration
c_s	$mol \cdot m^{-3}$	Solid phase concentration
$c_{s,max}$	$mol \cdot m^{-3}$	Maximum solid phase concentration
D_0	$m^2 \cdot s^{-1}$	Electrolyte diffusion coefficient
$D_{l,eff}$	$m^2 \cdot s^{-1}$	Effective electrolyte diffusion coefficient
D_h	m	Bore hole depth
d	m	Direct ion transport path length
d_f	m	Focus diameter
d_L	m	Laser spot diameter on the workpiece
d_{path}	m	Ion transport path length

[1] The units are specified in their respective standard form without prefixes.

Variable	Unit[1]	Description
d_s	m	Bore hole diameter
d_{th}	m	Thermal diffusion depth
δ	m	Optical penetration depth
E_0	V	Equilibrium potential
$E_{a,0}$	V	Anode equilibrium potential
$E_{c,0}$	V	Cathode equilibrium potential
E_P	J	Laser pulse energy
ε	-	Porosity
η	V	Overpotential
η_a	V	Activation overpotential
η_{abs}	-	Optical absorbance
η_d	V	Diffusion overpotential
F	$As \cdot mol^{-1}$	Faraday constant
$f_{\pm}$	-	Mean molar activity coefficient
f_f	m	Focal length
f_{rep}	s^{-1}	Laser pulse repetition rate
I	A	Electrical current
I_L	$W \cdot cm^{-2}$	Laser beam intensity
i	$A \cdot m^{-2}$	Current density
i_0	$A \cdot m^{-2}$	Exchange current density at equilibrium
i_l	$A \cdot m^{-2}$	Liquid phase current density
k_a	$m \cdot s^{-1}$	Anodic rate constant
k_c	$m \cdot s^{-1}$	Cathodic rate constant
l_{sp}	m	Distance between laser pulses on the workpiece

Variable	Unit[1]	Description
λ	m	Wavelength
M^2	-	Beam quality factor
N_M	-	MacMullin number
$P_{L,abs}$	W	Absorbed laser power
P_L	W	Laser power
Φ_s	V	Solid phase potential
Φ_l	V	Liquid phase potential
Q	Ah	Capacity
Q_0	Ah	Nominal capacity
R	$J \cdot mol^{-1} \cdot K^{-1}$	General gas constant
T	K	Temperature
t	s	Time
t_+	-	Transference number
t_i	s	Laser interaction duration
t_p	s	Laser pulse duration
Θ_f	°	Aperture angle
τ	-	Tortuosity
U	V	Voltage
U_0	V	Equilibrium voltage
V_e	m^3	Electrode volume
V_p	m^3	Pore volume
v_L	$m \cdot s^{-1}$	Velocity of the laser focus on the workpiece
z_R	m	Rayleigh length

1 Introduction

1.1 Lithium-ion batteries: The workhorses of the 21st century

"The Nobel Prize in Chemistry 2019 rewards the development of the lithium-ion battery. This lightweight, rechargeable and powerful battery is now used in everything from mobile phones to laptops and electric vehicles. It can also store significant amounts of energy from solar and wind power, making possible a fossil fuel-free society." (THE ROYAL SWEDISH ACADEMY OF SCIENCES 2019)

With these words, the scientists John B. Goodenough, M. Stanley Whittingham, and Akira Yoshino were awarded the Nobel Prize for Chemistry by THE ROYAL SWEDISH ACADEMY OF SCIENCES (2019) for the development of rechargeable lithium-ion batteries. Since their first commercialization and market dissemination by SONY (1991), lithium-ion batteries have established their position in the consumer electronics market with virtually no alternative. But also for the decentralized storage of electrical energy from renewable sources and electrically powered vehicles, lithium-ion batteries have emerged as the dominant technology. Driven by political incentives and increasingly strict greenhouse gas emission regulations, the global automotive lithium-ion battery market is predicted to grow from 17.4 billion US dollars in 2019 to 95.3 billion US dollars in 2030 (ROOTS ANALYSIS 2019).

The market success of the lithium-ion technology can be attributed to the high achievable specific energy with reference to the battery mass and volume as well as the superior power delivery compared to other types of batteries (ANDRE ET AL. 2015). Furthermore, lithium-ion batteries excel by their long service life due to the almost entirely reversible reactions during charging and discharging (BLOMGREN 2017).

1.2 Challenges, objectives, and approach

Among the core components of a lithium-ion battery are the electrodes, also referred to as *anode* and *cathode*. In most of today's battery designs, the electrodes are porous layers of materials that enable the quasi-reversible storage and release of lithium ions via an ion-conducting liquid electrolyte. The ion transport routes in the electrolyte through the porous electrodes are complex and tortuous hindering the passing of the charge carriers. As indicated in Figure 1 a), this issue is particularly pronounced at the anode due to the flake-like shape of the commonly used natural graphite particles (JARA ET AL. 2019). These graphite flakes tend to align in parallel to the current collector during electrode production impeding efficient ion transport during battery operation. At high current loads, this unfavorable electrode micro-morphology may deteriorate the power delivery during discharge and restrict the applicable current when charging (JOSSEN & WEYDANZ 2019, pp. 24 f.). A limitation of the charging current implicates long charging times of the battery-powered devices, which, in turn, may lead to low customer acceptance.

Improving the transport of the charge carriers in lithium-ion batteries has been the objective of numerous research projects and development activities. A rather novel approach pursued in the context of this thesis is the modification of the porous anode by means of laser radiation (Figure 1 b)).

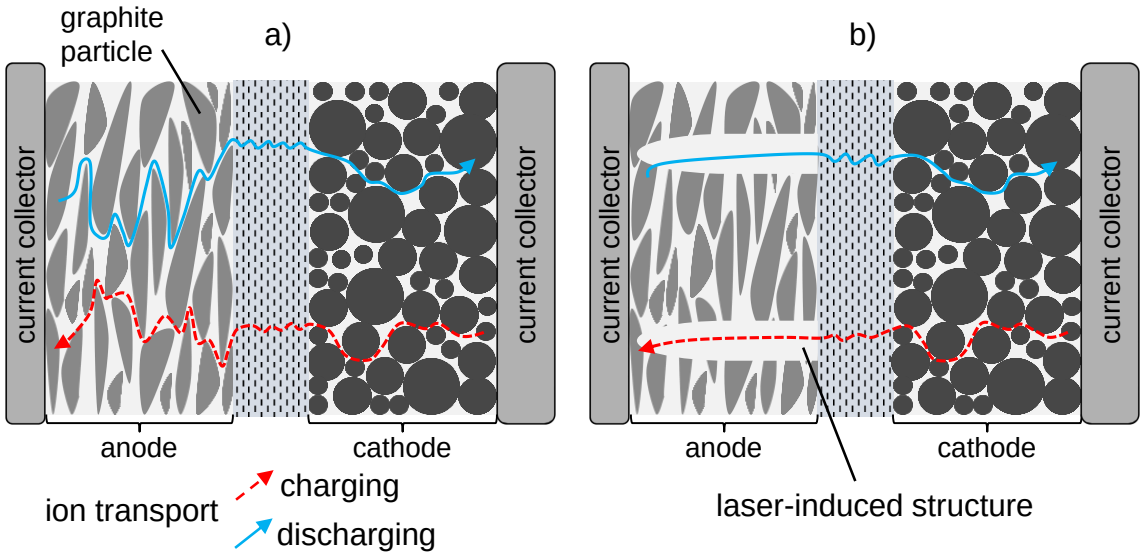

Figure 1: Schematic illustration of the lithium-ion transport routes during charging and discharging; a) conventional battery with complex and tortuous ion transport routes in the anode, b) battery with laser-structured anodes and shorter ion transport routes

Hereby, the objective is to alter the pore structure by precisely removing anode material so that the ion flow is favored by less complex and shorter transport routes. This laser-based pore morphology modification process will be referred to as *laser structuring* within the context of this work. The overall aim of this thesis is to demonstrate the potential of the laser structuring process in order to enhance aspects of battery performance[2]. This explorative research approach is substantiated by efforts to generate a more profound understanding of the charge carrier transport in lithium-ion batteries with laser-structured anodes.

To accomplish the abovementioned goals, fundamental evidence must first be provided that laser structuring is an appropriate process for obtaining the desired electrode morphology modifications. On the basis of this feasibility demonstration, lithium-ion batteries with laser-structured anodes are assessed with regard to their electrochemical properties in general and their charging and discharging characteristics in particular. The results are compared to the properties of conventional lithium-ion batteries containing untreated anodes. In order to create a more thorough understanding of the impact of the laser-induced anode structures, a physical-chemical model is developed that quantitatively represents the characteristics of the batteries under study. This model serves as the basis for the numerical simulation of the charge and mass transport inside the battery. It also provides the capability to predict the influence of laser-structured anodes on the battery performance in order to enable an application-specific electrode and battery design. Furthermore, the laser structuring process is assessed with regard to its technical viability in the context of mass production of battery cells. This includes the identification of technical challenges for enhancing the overall performance, particularly the processing speed, and the characterization of interactions with other process steps in battery production.

1.3 Structure of the thesis

This thesis is divided into six chapters. Following the introduction in chapter 1, chapter 2 provides selected fundamentals regarding the operating principles of lithium-ion batteries as well as laser materials processing. In chapter 3, the state of the art is presented. Here, the focus lies on published work on the laser-based

[2] Lithium-ion battery performance measures include, but are not limited to, the specific energy, the energy density, the power, the applicable charge current (particularly at low temperatures), the safety characteristics, and the cost (ANDRE ET AL. 2015).

modification of lithium-ion battery electrodes. Alternative processes for structuring and approaches for the modeling of lithium-ion batteries with structured electrodes are also included. Chapter 4 outlines the research approach of this thesis including the definition of scientific objectives as well as the refinement of the pursued methodology. Chapter 5 represents the publication-based part of this dissertation and briefly summarizes the core research findings of the author. The publications comprise process investigations on laser structuring of the anodes, experimental analyses on resulting cell properties, work on electrochemical modeling and simulation as well as considerations on the interactions of laser structuring with subsequent processes in cell production. Chapter 5 ends with a discussion of the results, a classification of the findings with reference to the state of the art, and a reflection on the scientific objectives defined in chapter 4. Finally, the thesis concludes in chapter 6 with a summary and an outlook on prospective research activities.

2 Fundamentals

2.1 Chapter overview

In this chapter, the relevant background on lithium-ion batteries is provided in section 2.2, while fundamentals in laser materials processing are presented in section 2.3.

Based on remarks on the scientific terminology in sub-section 2.2.1, sub-section 2.2.2 is dedicated to the structure and operating principle of lithium-ion batteries. Sub-section 2.2.3 provides electrochemical fundamentals, while in sub-section 2.2.4 more detailed explanations regarding cell-internal resistances are offered. A thorough understanding of these resistances is essential for the comprehension of the effects of laser structuring on the electrochemical cell performance. Sub-section 2.2.5 is dedicated to the rather specific phenomenon of lithium-plating, which can occur during fast charging of lithium-ion batteries. The characteristics of the ion transport properties in porous electrodes are addressed in sub-section 2.2.6. On this basis, sub-section 2.2.7 summarizes scientific studies on electrode design providing an overview of the interactions between individual electrode characteristics. Furthermore, in sub-section 2.2.8, the battery production process is depicted to enable a classification of the laser structuring of graphite anodes in the technical context of battery fabrication.

Building on general remarks regarding laser materials processing in sub-section 2.3.1, sub-section 2.3.2 provides the fundamentals of the spatial laser beam propagation. In sub-section 2.3.3, the difference between pulsed and continuous wave laser radiation is explained. Sub-section 2.3.4 addresses the interaction between laser radiation and matter. Since the precise removal of active material from the anode is essentially a drilling process, explanations on laser drilling and ablation are provided in sub-section 2.3.5. Sub-section 2.3.6 discusses the fundamentals of laser beam guidance by means of scanner optics, which are typically employed for the processing of large surface areas. A summary of chapter 2 is provided in section 2.4.

2.2 Lithium-ion batteries

2.2.1 General remarks

The terms *cell* and *battery* are used ambiguously in the contemporary technical and general language. Both terms designate galvanic systems that store chemical energy and convert it into electrical energy. By definition, a cell is the smallest functional galvanic element, while a battery is historio-linguistically referred to as the interconnection of several cells. Since the cells or batteries primarily used today are rechargeable systems, strictly speaking, they should be referred to as *secondary batteries* or *lithium-ion accumulators* (JOSSEN & WEYDANZ 2019, p. 7). Following customary usage, the terms *battery* and *cell* are used synonymously in this thesis, whereas the term *accumulator* is not applied. Unless explicitly stated otherwise, the terms *cell* and *battery* always refer to lithium-ion batteries within the context of this thesis.

2.2.2 Structure and operating principle

In lithium-ion batteries, chemical energy is reversibly converted into electrical energy in redox reactions. The main components of the battery are the porous electrodes, the electrically insulating porous separator, and the ion conducting electrolyte liquid (LEUTHNER 2018, p. 14). The electrodes consist of electrochemically active materials (usually in form of particles), which are able to reversibly store lithium ions and release them at a given point in time. This process of inserting an atom or a molecule into a host structure is referred to as *intercalation*, whereas the reverse process is denoted as *de-intercalation*. The active material particles are held together by a binder to form a cohesive layer and are applied onto metallic current collector foils (cathode: aluminum, anode: copper). Electrically conductive additives are commonly admixed to the other electrode materials in cell production (cf. sub-section 2.2.8) in order to improve the electrical conductivity (VUORILEHTO 2018, p. 23). When charging the battery, the lithium ions de-intercalate from the active material of the cathode overcoming the phase boundary to the electrolyte liquid and move to the anode, where they intercalate into the active material of the anode. At the same time, an electrical current (one electron per lithium ion) flows through the external circuit. When discharging, these processes are reversed, see Figure 2. According to the electrochemical definition (cathode: reduction; anode: oxidation), the assignment of the terms *cathode* and *anode* to the positive and negative electrode is only correct in the case of discharge, since the reduction and oxidation reactions are reversed during

charging. In general usage, however, a component-related classification of the terms has been established (VUORILEHTO 2018, p. 22), which is also used in this thesis.

For the anode and cathode, numerous combinations of active materials have proven successful depending on the application scenario of the battery. As stated in the introduction, the application-specific choice of the active materials depends on various considerations, such as diverse electrochemical characteristics, the material costs, the service life, and safety factors, which are often material inherent (ANDRE ET AL. 2015).

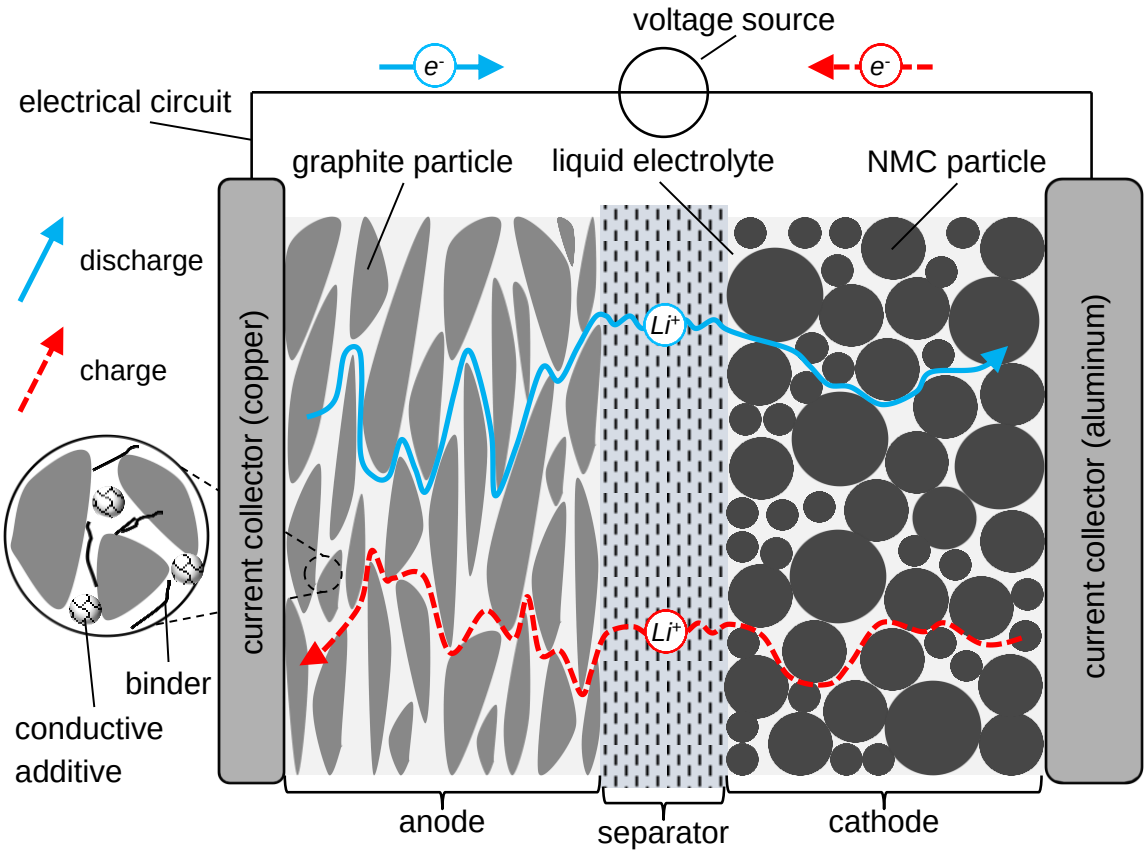

Figure 2: Structure and operating principle of an NMC-graphite lithium-ion battery; exemplary lithium-ion transport routes are indicated for both the charging and the discharging process; in the case of discharge, an electrical consumer replaces the voltage source; adapted from VUORILEHTO (2018)

Today, lithium nickel manganese cobalt oxide ($LiNi_yMn_zCO_{1-y-z}O_2$, NMC, cf. Figure 2) and lithium nickel cobalt aluminum oxide ($LiNi_yCo_zAl_{1-y-z}O_2$, NCA) are mostly used for the cathode of battery electric vehicles and hybrid electric vehicles (BLOMGREN 2017, p. 5022). The stoichiometric ratio of nickel, manganese, and

cobalt varies depending on the desired cell characteristics and the ongoing innovation in material development. For this thesis, a commercially well-established type of NMC, $LiNi_{1/3}Mn_{1/3}CO_{1/3}O_2$, was employed. To simplify the following chemical reaction equations, the term *lithium metal oxide* ($LiMO_2$) will also be used.

At the anode, mainly carbon compounds such as graphite (C) are used as active materials (WURM ET AL. 2018, p. 44). Compared to metallic lithium, which potentially enables the highest energy densities, graphite provides a longer cyclic life and superior safety properties (JOSSEN & WEYDANZ 2019, pp. 121 ff.).

The reactions at the anode and the cathode are shown in equations (2 - 1) and (2 - 2), respectively:

anode: $$Li_xC_6 \underset{charge}{\overset{discharge}{\rightleftarrows}} C_6 + xLi^+ + xe^- \quad (2 - 1)$$

cathode: $$Li_{1-x}MO_2 + xLi^+ + xe^- \underset{charge}{\overset{discharge}{\rightleftarrows}} LiMO_2 \quad (2 - 2)$$

where e^- is an electron and x is the stoichiometric factor of lithium in the reaction (KURZWEIL & DIETLMEIER 2015, p. 158).

The liquid electrolyte enables the exchange of lithium ions between anode and cathode during charging and discharging due to its ionic conductivity (YOSHIO ET AL. 2009, p. 75). It fills the pores of the electrodes and the separator and thus ensures complete wetting of the active material surface. The electrolyte usually consists of organic solvents, conductive salts and additives. Mixtures of carbonates such as ethylene carbonate (EC), dimethyl carbonate (DC), diethyl carbonate (DEC), or ethyl methyl carbonate (EMC) are commonly used as solvents (HARTNIG & SCHMIDT 2018, pp. 60 ff.). These can dissolve lithium salts, have a sufficiently low viscosity to penetrate into the pores of the electrodes, and exhibit electrochemical stability against the electrode materials in a wide voltage range (GULBINSKA 2014, p. 22). Today, lithium hexafluorophosphate ($LiPF_6$) is almost exclusively used as the conductive salt (HARTNIG & SCHMIDT 2018, p. 62). Soluble additives are employed in many commercial electrolytes to improve the cell properties. For detailed information on electrolyte additives, the reader is kindly referred to the work of YOSHIO ET AL. (2009).

2.2.3 Fundamentals and definitions

In this sub-section, essential concepts for understanding the lithium-ion transport within lithium-ion batteries are illustrated. A detailed derivation of the equations is omitted here and reference is made to fundamental literature on physical chemistry by ATKINS & PAULA (2010) or electrochemistry by NEWMAN & THOMAS-ALYEA (2012).

The equilibrium voltage U_0 of a cell comprising two electrodes of electrochemically active materials is determined by thermodynamics (JOSSEN & WEYDANZ 2019, pp. 13 f.). It corresponds to the difference of the two electrode equilibrium potentials ΔE_0:

$$U_0 = \Delta E_0 = E_{c,0} - E_{a,0} \qquad (2 - 3)$$

where $E_{c,0}$ and $E_{a,0}$ are the cathode and anode potentials at equilibrium, respectively. The amount of electrical charge that can theoretically be stored by the cell Q_0 is defined by the atomic structure of the active materials and their quantity employed within the cell (DANIEL & BESENHARD 2011). Q_0 is commonly referred to as the *nominal capacity* of a cell. The amount of electrical charge that is provided under specific operating conditions Q, commonly denoted as the *capacity* of a cell, depends on various parameters such as the applied current I, the cell temperature T, the ionic transport properties within the active materials and the electrolyte, the electrical conductivity of the current collectors and the kinetic properties at the interface between the active materials and the electrolyte (LEUTHNER 2018, p. 16), cf. sub-section 2.2.4.

For the description of the condition of a cell, the terms *state of charge* (SOC) and *depth of discharge* (DOD) have become established (KURZWEIL & DIETLMEIER 2015, p. 225):

$$SOC = \frac{Q}{Q_0} \qquad DOD = 1 - SOC \qquad (2 - 4)$$

An SOC of *one* corresponds to a fully charged cell, i.e. a high lithiation of the anode, while an SOC of *zero* corresponds to a fully discharged cell, i.e. a high lithiation of the cathode. Figure 3 schematically shows the equilibrium potential curves (versus the potential of the lithium reference electrode) of a cathode $E_{c,0}$, an anode $E_{a,0}$, and the resulting equilibrium cell voltage U_0 as a function of the SOC. The operating voltage window is formed by the interval between the upper and the lower cut-off voltage and describes the voltage range within which the battery cell is used. For the

active material combination of NMC and graphite considered in this thesis, the operating voltage window typically lies between approx. 2.7 V and 4.2 V.

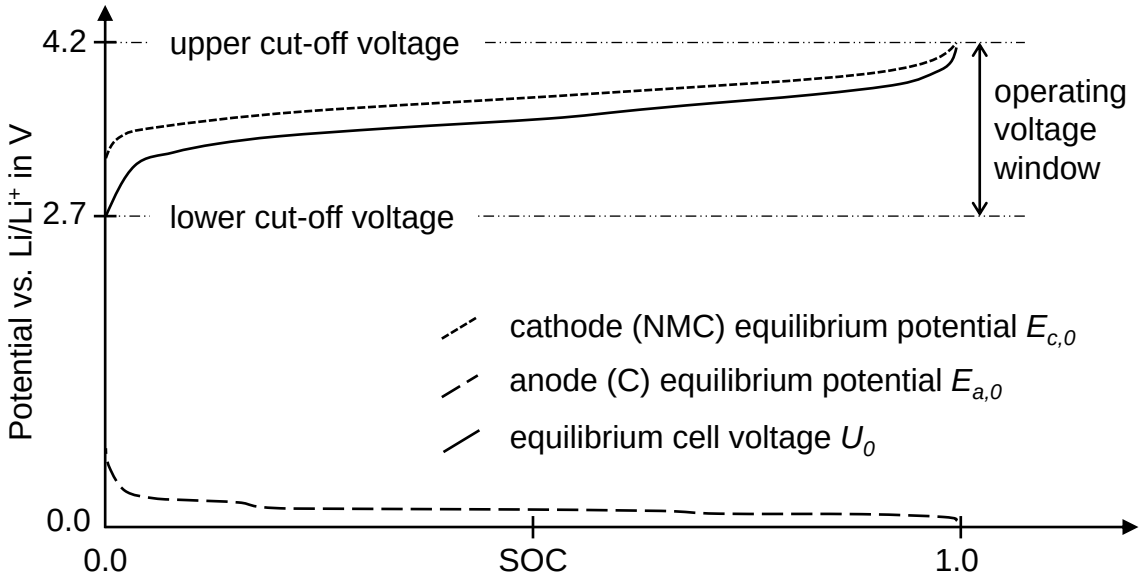

Figure 3: Schematic representation of the equilibrium potential curves vs. Li/Li⁺ of the cathode $E_{c,0}$ and the anode $E_{a,0}$ as well as the equilibrium cell voltage U_0 as a function of the SOC; the operating voltage window formed by the upper and the lower cut-off voltage is indicated; based on GRAF (2013) and WURM ET AL. (2018)

A frequently used measure of the current flow in a battery is the *C-rate*. It relates the electric current I to the nominal capacity Q_0:

$$C\text{-}rate = \frac{I}{Q_0} \tag{2 - 5}$$

and is applicable for both the charging and the discharging procedure (HUGGINS 2009, p. 22). By referencing the electric current to the nominal capacity, batteries of different sizes can be compared more effectively. Since the usable capacity of lithium-ion batteries decrease with increasing discharge current due to a higher internal resistance (cf. sub-sections 2.2.4, 2.2.6, and 2.2.7), it is important to specify the C-rate at which a capacity is determined. In this context, the term *C-rate capability* is frequently used. A high C-rate capability of a battery indicates that the usable capacity decreases less at high discharge currents (and the battery is therefore suitable for providing high electrical power) compared to a battery with a low C-rate capability.

2.2.4 Limitations due to overpotentials

The abovementioned electrode potentials are based on the assumption that no electric or ionic current is flowing in the cell. In this context the term *open circuit voltage* (OCV) is regularly used. The OCV indicates the potential difference measured at the electrodes if no current flows. However, every charge and mass transport is subject to resistances, which cause a deviation of the cell voltage U during operation from the equilibrium cell voltage U_0. Such current- and temperature-dependent voltage deviations are referred to as *overpotentials* η (NYMAN ET AL. 2010). Higher currents generally lead to greater overpotentials, while higher temperatures result in their reduction. When charging, the overpotentials increase the cell voltage and lead to a premature attainment of the upper cut-off voltage, i.e. before an SOC of 1.0 is reached. In order to enable further charging of the cell the charging current must be reduced. If no reduction of the charging current occurs and the upper cut-off voltage is exceeded, strong aging and increased safety risks are to be expected (cf. sub-section 2.2.5). In applications such as mobile devices or electric vehicles, these current limitations are expressed by restricting the fast charging function to a confined SOC range, which usually does not exceed an SOC of 0.7 or 0.8 (ZHANG 2020). In the case of discharge, the overpotentials cause the cell voltage to decrease, resulting in the lower cut-off voltage being reached before a DOD of 1.0 has been attained. Thus, at high discharge C-rates, only a fraction of the nominal capacity Q_0 of a cell can be used due to the occurring overpotentials.

The overpotentials in lithium-ion cells have different physical origins and can be subdivided into *ohmic*, *activation* and *diffusion* components (JOSSEN & WEYDANZ 2019, p. 19). They are discussed in the forthcoming paragraphs.

Ohmic overpotentials

The ohmic overpotentials η_Ω are due to the ohmic resistances of all the media involved in the transport of the charge carriers, such as the electrolyte and the electrodes, but also the current collector foils and the external current feeds within the electric circuit (cf. Figure 2). The electrolyte usually plays a dominant role due to its inferior ionic conductivity compared to the electrical conductivity of the solid state conductors (JOSSEN & WEYDANZ 2019, p. 19). The solid electrolyte interphase (SEI), a passivating layer consisting of decomposed organic and inorganic compounds formed on the anode particles during the first charge cycles of a cell, also significantly contributes to the ohmic overpotentials. For more information about the SEI, the reader is kindly referred to the work of BALBUENA & WANG (2004).

Activation overpotentials

During the charge transfer at the interface between the solid active material and the liquid electrolyte, a transition between electric and ionic conduction occurs. For this process, activation overpotentials η_a must be applied. The relationship between the current density i and the required activation overpotentials is shown in the Butler-Volmer equation, which aims at establishing a current balance for the electrode interfaces (ERDEY-GRÚZ & VOLMER 1930):

$$i = i_0 \cdot \left[\exp\left(\frac{\alpha_a \cdot F}{R \cdot T} \cdot \eta_a\right) - \exp\left(-\frac{\alpha_c \cdot F}{R \cdot T} \cdot \eta_a\right)\right] \quad (2 - 6)$$

where i_0 is the exchange current density at equilibrium, R the general gas constant, α_a and α_c the anodic and cathodic charge transfer coefficients (typically assumed to be 0.5 for battery applications) (NEWMAN & THOMAS-ALYEA 2012), F the Faraday constant, and T the temperature. The exchange current density at equilibrium:

$$i_0 = F \cdot k_c^{\alpha_a} \cdot k_a^{\alpha_c} \cdot (c_{s,max} - c_s)^{\alpha_a} \cdot c_s^{\alpha_c} \cdot \left(\frac{c_l}{c_{l,ref}}\right)^{\alpha_a} \quad (2 - 7)$$

depends on the anodic and cathodic rate constants k_a and k_c, the solid phase lithium concentration c_s, the maximum solid phase concentration $c_{s,max}$, the liquid phase lithium concentration c_l, and the liquid phase reference concentration $c_{l,ref}$. The exchange current density i_0 can thus be understood as an indication of the pace of the electrochemical reaction (JOSSEN & WEYDANZ 2019, p. 21).

Diffusion overpotentials

When discharging a lithium-ion battery, lithium ions are de-intercalated from the active material at the anode, thus increasing the lithium-ion concentration in the liquid electrolyte in the anode pores (JOSSEN & WEYDANZ 2019, p. 24). Simultaneously, lithium ions are consumed from the liquid electrolyte at the cathode, thus lowering the lithium-ion concentration there. As a result, a concentration gradient is formed, which can be only partially compensated by the ion influx from the anode through the separator. At a low discharge current, this compensation occurs sufficiently quickly so that the concentration gradient remains low. At a high discharge current, however, the resulting concentration gradient can no longer be entirely compensated. The result is a strong depletion of lithium ions in the electrolyte within the pores of the cathode, while the lithium-ion concentration strongly increases in the electrolyte within the pores of the anode. In order to sustain the reaction, i.e. the discharge

process, diffusion overpotentials η_d must be applied (DANIEL & BESENHARD 2011, p. 20).

When charging the cell, the concentration gradients are formed in reverse. The lithium ions de-intercalate from the cathode active material resulting in an increased concentration in the cathode pores, which are filled with electrolyte. At the anode, lithium ions from the electrolyte intercalate into the graphite. In order to maintain a high charging current, diffusion overpotentials η_d must therefore also be applied. These emerging concentration gradients are illustrated in Figure 4 for both the charging and the discharging process.

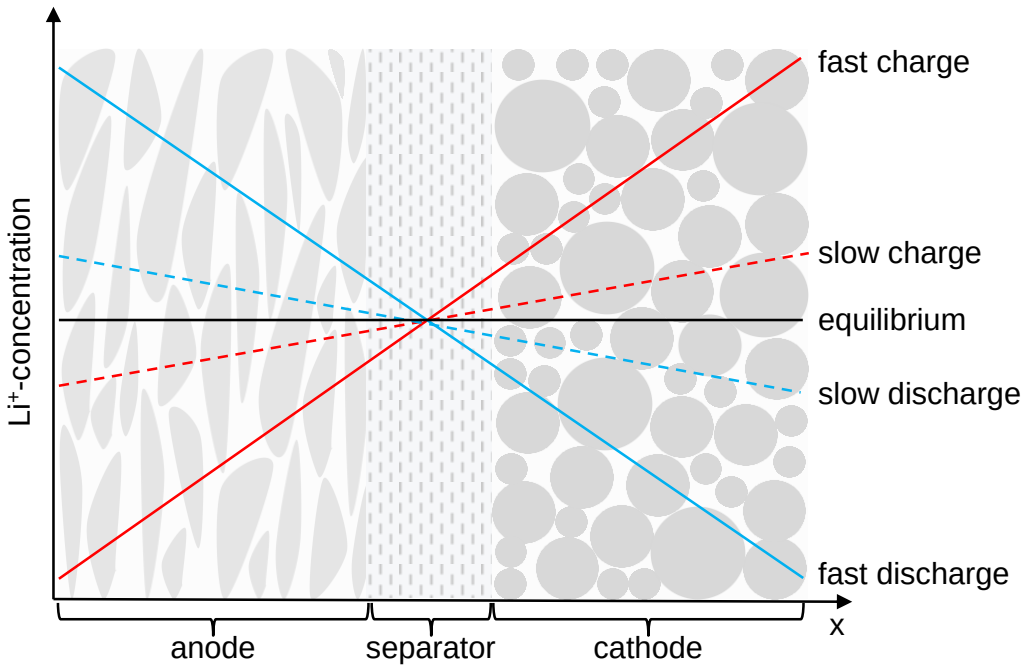

Figure 4: Lithium-ion concentration gradients in the electrolyte for charging and discharging compared to the equilibrium concentration; the displayed linear courses of the concentration gradients are for illustration purposes only and the real courses are likely to deviate from that in a real system; adapted from LANDESFEIND (2018, p. 5)

The abovementioned phenomena were modelled by DOYLE ET AL. (1993) for a binary electrolyte (one solvent and one salt), resulting in the following balancing equations, which are described in the scope of the *Newman Model* (NEWMAN & THOMAS-ALYEA 2012). The mass balance (neglecting convection in the electrolyte within the microporous media) is one-dimensionally described by:

$$\varepsilon \frac{\partial c_l}{\partial t} = \frac{\partial}{\partial x}\left(D_{l,eff}\ \frac{\partial c_l}{\partial x} + \frac{i_l(1-t_+)}{F}\right) \qquad (2\text{ - }8)$$

where ε is the volume fraction of the electrolyte of the porous medium (also referred to as porosity, cf. eq. 2 - 11, sub-section 2.2.6), τ the tortuosity of the porous structure (cf. eq. 2 - 12, sub-section 2.2.6), $D_{l,eff}$ the effective electrolyte diffusion coefficient (cf. eq. 2 - 14), i_l the current density in the electrolyte, and t_+ the transference number. The electrochemical potential in the electrolyte Φ_l is described as follows:

$$\frac{\partial \Phi_l}{\partial x} = -\frac{i_l}{\kappa_{eff}} + \frac{2RT}{F}\left(1 + \frac{\partial \ln f_{\pm}}{\partial \ln c_l}\right)(1-t_+)\frac{\partial \ln c_l}{\partial x} \qquad (2\text{ - }9)$$

where κ_{eff} is the effective ionic conductivity, and $f_{\pm}$ the mean molar activity coefficient (LANDESFEIND 2018, DOYLE ET AL. 1993). For a derivation of the equations, the underlying theory of concentrated solutions, and the respective solid phase equations, the reader is kindly referred to specific scientific literature, e.g. NEWMAN & THOMAS-ALYEA (2012).

The overpotentials are particularly critical during fast charging since this process can lead to a deposition of metallic lithium on the anode. This phenomenon is discussed in the following sub-section.

2.2.5 Lithium-plating

During fast charging, the emerging concentration gradients cause an inhomogeneous lithiation of the anode (HARRIS & LU 2013). The higher lithium-ion concentration in the electrolyte at the anode-separator interface results in a higher degree of lithiation of the graphite particles in that area (LIU ET AL. 2010). In contrast, lithium ions are quickly depleted in regions of the anode near the current collector causing the graphite particles located in this area to suffer a low degree of lithiation. A high degree of lithiation, i.e. a high SOC of the battery, cf. Figure 3, and the application of overpotentials promote the deposition of metallic lithium on the anode, which is referred to as *lithium-plating* (LIU ET AL. 2016). Lithium-plating occurs when the ionic current in the electrolyte surpasses the intercalation current or the solid state diffusion in the graphite. Thus, at high charging rates, the intercalation reaction (cf. eq. 2 - 1) and the lithium-plating reaction coexist (LEGRAND ET AL. 2014). For details on the lithium deposition process, the reader is kindly referred to the work of LI ET AL. (2014).

A frequently used indication for the occurrence of lithium-plating is the local potential difference between the local solid phase potential Φ_s and the local liquid phase potential Φ_l at the anode-separator interface:

$$\Phi_s - \Phi_l \leq 0 \qquad (2 - 10)$$

The lithium-plating reaction is problematic for various reasons. Firstly, the lithium deposition is not entirely reversible resulting in lithium residues on the anode and reducing the amount of lithium available to the intercalation reaction. In practice, this is expressed by a loss of available cell capacity Q (BURNS ET AL. 2015, p. 959). Furthermore, the lithium tends to be deposited in dendritic form. The dendrite growth is critical for cell safety, as the lithium dendrites can pierce the separator, which operates as the electrical insulation layer between the electrodes. An internal short circuit and a thermal runaway of the cell are among the possible consequences of that (VUORILEHTO 2018, p. 25). Lithium-plating occurs particularly at low temperatures, as all charge and mass transport processes in the cell operate more slowly (ZINTH ET AL. 2014).

To detect lithium-plating is challenging during cell operation. In laboratory cells, the introduction of an additional lithium metal reference electrode is common. This allows for the momentary electrochemical states of the electrodes to be recorded directly and independently (WALDMANN ET AL. 2015). For commercial applications, this appears not economically feasible. The same applies for advanced detection methods like neutron diffraction which were utilized by LÜDERS ET AL. (2017) and ZINTH ET AL. (2017). Several promising in situ detection methods have been assessed to date focusing on the identification of a characteristic voltage plateau that forms during a voltage relaxation period if lithium-plating occurred during the preceding charging process (UHLMANN ET AL. 2015, PETZL & DANZER 2014). To prevent premature cell aging and reduce safety risks, lithium-ion batteries and the electronic battery management systems (BMS) are usually designed very conservatively. This includes limiting the operating voltage to an uncritical range regarding lithium-plating and oversizing the anode, both in terms of electrode area (ensuring complete coverage of the cathode by the anode) and area capacity (avoiding complete lithiation of the anode).

2.2.6 Characteristics of porous electrodes

In the context of concentration gradients and diffusion overpotentials, the microstructure of the electrode must be discussed in detail. In most of today's lithium-

ion batteries, both the anode and the cathode are characterized by their porous structure. If the electrodes were pure solid state layers of the active materials, the cell would exhibit an extremely poor power density, as the solid state ionic conductivity is low compared to the ionic conductivity of the electrolyte. Thus, the porous structure aims at enhancing the power density at the expense of a decreased energy density. Furthermore, porous electrodes can be produced by cost-effective aqueous coating processes (cf. sub-section 2.2.8). The porosity ε is defined as the volume fraction of the electrolyte-filled pores in relation to the total volume of the electrode:

$$\varepsilon = \frac{V_p}{V_e} \tag{2 - 11}$$

where V_p is the pore volume and V_e is the entire electrode volume, including the volume of the active materials, the binders, the conductive additives, and the pores. A smaller porosity leads to a reduction of the effective cross-sectional area for ion transport, since only the pore volume can be used as diffusion paths (JOSSEN & WEYDANZ 2019, p. 25). Therefore, the lithium ions are subject to complex transport routes from the site of de-intercalation to the site of intercalation. A measure of the complexity of the electrode structure is the tortuosity τ. In the context of lithium-ion batteries, this dimensionless quantity describes the influence of the structure of a porous electrode on its effective ionic transport properties (NEWMAN & THOMAS-ALYEA 2012):

$$\tau = \frac{d_{path}}{d} \tag{2 - 12}$$

Geometrically interpreted, it relates the actual length of the lithium-ion transport path in the porous electrode d_{path} to the direct path length d, which would be available without the porous medium. A high tortuosity of the electrode hinders the transport of lithium-ions. The porosity and the tortuosity are related via the generalized Bruggeman relation (BRUGGEMAN 1935):

$$\tau = \varepsilon^{-\alpha} \tag{2 - 13}$$

where α is the Bruggeman exponent which depends on the size distribution and shape of the employed particles and is approx. 1.5 for spherical particles of uniform size. Recent investigations have shown that this purely geometric approximation of the measure tortuosity is insufficient (LANDESFEIND ET AL. 2016). Rather, other factors, such as the binder content of the electrode, must also be taken into account, since the

binder can lead to a clogging of the pores. This may restrict the lithium-ion transport paths. Experimentally determined tortuosities consequently tend to be higher than those predicted by the Bruggeman relation (LANDESFEIND ET AL. 2018).

The porosity and the tortuosity influence the effective lithium diffusion coefficient in the electrolyte $D_{l,eff}$ through the electrode pores:

$$D_{eff} = \frac{\varepsilon}{\tau} \cdot D_0 \qquad (2 - 14)$$

where D_0 is the electrolyte diffusion coefficient. Alternatively, the MacMullin number:

$$N_M = \frac{\tau}{\varepsilon} \qquad (2 - 15)$$

is regularly applied to describe the impact of the porous electrode structure on the ion transport (MACMULLIN & MUCCINI 1956). These considerations regarding the ion transport in porous electrodes have various implications on the electrode design and are briefly discussed in the following sub-section.

2.2.7 Aspects of electrode design

As stated in sub-section 2.2.6, for most applications today, porous electrodes offer the desired balance between energy and power density. The electrode design parameters, i.e. the porosity, the tortuosity, and also the *electrode loading*, which designates the capacity per electrode area, fundamentally define the characteristics of the lithium-ion cell. Thus, selected aspects of porous electrode design are presented below.

Influence of the electrode loading

Assuming a given ratio of a certain active material, binders and conductive additives, the energy density of an electrode can be enhanced either by increasing the thickness of the electrode or by reducing its porosity. The improvement in energy density by increasing the electrode thickness is due to the relative decrease in the mass share of the metallic current collector foil, which does not contribute to the electrode's energy content.

ZHENG ET AL. (2012A) comprehensively examined the effects of the electrode thickness on the electrochemical performance of lithium-ion batteries using NMC

and lithium iron phosphate (*$LiFePO_4$*, LFP) cathodes of different loadings. They discovered that increasing the cathode thickness, and thus the loading, has a restricting effect on the C-rate capability of the electrodes. The main cause of this effect was attributed to the ionic transport properties which deteriorated with increasing electrode thickness. Furthermore, it was observed that the aging of the cells with thicker electrodes was accelerated. This was attributed on the one hand to the higher lithium concentration gradients and on the other hand to a mechanical failure (e.g. crack formation within the coating or delamination of the coating from the current collector) of the electrodes with higher loading.

A similar trend was identified by SINGH ET AL. (2015) who compared NMC-graphite cells with cathode thicknesses of 70 µm and 320 µm. The increased electrode thickness led to a by 19 % enhanced energy density on the cell level due to the reduced share of inactive components (e.g. current collectors). However, the thicker electrodes suffered a significantly inferior high-current capability from a discharge C-rate of C/2 onwards due to kinetic losses.

GALLAGHER ET AL. (2015) performed an application-specific optimization of the areal capacities of the electrodes by studying the limiting mechanisms occurring at high currents. Especially for electrodes with high loading, the ionic transport in the electrolyte was identified as critical, as inadequate transport properties led to high overpotentials. The authors concluded that realistic charge and discharge profiles from the application must be considered for the design of the electrodes.

SON ET AL. (2013) explored the influence of the anode and cathode loading ratio. For this purpose, cathodes of the same capacity with differently oversized anodes were examined in test cells. The authors showed that highly oversized anodes led to both a decrease in the Coulomb efficiency during operation and accelerated cell aging due to enhanced SEI formation.

Influence of the electrode porosity

The porosity is an important factor in the design of electrodes. It is set in the calendering process during electrode production (described in sub-section 2.2.8 of this thesis). The influence of the porosity on the ionic transport within graphite anodes was examined by MANEV ET AL. (1995) in a comparative study. The electrodes yielding the highest capacity and showing the least aging had a porosity of approx. 30 %. NOVÁK ET AL. (1997) used pore-forming additives to create defined porosities in graphite anodes and confirmed the results of MANEV ET AL. (1995).

SHIM & STRIEBEL (2003) and STRIEBEL ET AL. (2004) investigated the influence of compression on natural graphite anodes in relation to various parameters relevant to the operation of lithium-ion cells. They found that highly porous as well as strongly compressed electrodes both resulted in accelerated cyclic aging of lithium-ion cells. However, a moderate compression of the electrodes was found to be advantageous.

ZHENG ET AL. (2012B) studied the influence of the porosity of NMC cathodes on their mechanical and electrochemical properties. They discovered an enhanced electrical conductivity of the porous electrode with an increasing compression, while the ionic conductivity decreased. In addition to a generally lower wetting of the active material particles with electrolyte at low porosity, a blocking of the ionic transport paths in the void volume of the electrode by the binder was discovered. In addition, a mechanical embrittlement of the electrodes at a low porosity was observed. A porosity range between 30 % and 40 % was identified as a reasonable compromise between energy density and high current capability. Supporting results also indicating such a trade-off were later found by ANTARTIS ET AL. (2015).

HASELRIEDER ET AL. (2013) found that, in contrast to NMC cathodes, the electrical conductivity of graphite anodes cannot be significantly enhanced by increasing compaction. They attributed this to the generally high electrical conductivity of the graphite layer, which could not be significantly enhanced by further inter-particular contact due to compression.

SHENG ET AL. (2014) examined the influence of the porosity on the wettability of the electrodes with the electrolyte liquid. The wettability decreased with declining porosity indicating a poorer electrolyte penetration and, thus, a restriction of the ionic transport through the electrode. Related studies were carried out by KITADA ET AL. (2016). They found that, within highly compressed NMC cathodes with a porosity of 18 %, areas with limited access to the electrolyte are formed which are severely limiting the C-rate capability.

Influence of the electrode tortuosity

A high electrode tortuosity impedes effective ion transport (cf. sub-section 2.2.6). In contrast to the porosity, which can be calculated by recording the mass and the thickness of the electrode, the tortuosity cannot be quantified using basic measurement techniques. However, as precise knowledge of the tortuosity is essential for understanding and modeling the intra-cellular process, many research activities focus on the determination of tortuosity values for porous electrodes.

THORAT ET AL. (2009) developed measuring techniques to determine the tortuosity of electrodes and separators. They found that the measured tortuosity and the corresponding MacMullin Number **(**cf. eq. 2 - 15**)** did not quantitatively match the prediction from the Bruggeman relation **(**cf. eq. 2 - 13**)** but yielded significantly higher values. This observation was confirmed by the subsequent work of DUBESHTER ET AL. (2014) and LANDESFEIND ET AL. (2016). As an explanation, an overestimation of the free pore volume in the Bruggeman relation was provided, due to the fact that, in physical electrodes, some pores are not accessible to ion transport. LANDESFEIND ET AL. (2018) were later able to show that, among other factors, the binder which accumulates in the electrode pores can be responsible for the underestimation of the MacMullin numbers by the Bruggeman relation.

EBNER ET AL. (2014) found out that the electrode tortuosity is usually not equal in all spatial directions but that a pronounced anisotropy is formed, particularly for aspherical active material particles, such as graphite flakes (cf. Figure 1). These flakes tend to align parallel to the current collector foil during electrode production. This results in a significantly higher through-plane than in-plane tortuosity for this type of electrode. Based on these findings, EBNER & WOOD (2014) developed an open-source software tool, the so-called *BruggemanEstimator*, which can be used to calculate the tortuosity of electrodes. As the input, a microscopic image of the electrode surface and a cross-section of the electrode is required, which can be recorded with the help of a scanning electron microscope (SEM).

Based on the findings on the tortuosity anisotropy of graphite anodes, BILLAUD ET AL. (2016) developed a method for magnetically aligning the graphite particles perpendicularly to the current collector during electrode production. The magnetic alignment was enabled by the addition of superparamagnetic nanoparticles to the electrode. The authors demonstrated that a through-plane tortuosity reduction can be achieved by the magnetic process resulting in a higher C-rate capability. While the reference electrodes had a tortuosity of $\tau = 14$, the modified electrodes showed a tortuosity of $\tau = 3.8$, which equals a reduction by a factor of almost four. The technology is currently being further developed by the Swiss company BATTRION under the name *Aligned Graphite® Technology* (BATTRION 2020). Related approaches were pursued by DANG ET AL. (2020) and BITSCH ET AL. (2016), attempting to produce low-tortuous electrodes using adapted drying or slurry manufacturing processes (cf. sub-section 2.2.8).

The large number of studies on the systematic improvement of the electrode structure clearly underlines the immense potential associated with this field of research. For

evaluating the feasibility of the proposed technologies for large-scale production, a thorough understanding of the production process for lithium-ion batteries is indispensable. Consequently, the following sub-section provides a brief overview of the process chain for the manufacturing of lithium-ion batteries.

2.2.8 Production process

In order to assess the laser-assisted modification of anodes in a production engineering context, a basic understanding of the manufacturing processes of lithium-ion cells is required. The production of lithium-ion cells encompasses numerous interdependencies between the individual processes and between the process parameters and the quality characteristics of the end product (GÜNTHER ET AL. 2016, KWADE ET AL. 2018). Fundamentally, the production of lithium-ion batteries can be subdivided into the three stages *electrode production*, *cell assembly*, and *cell conditioning* (KWADE ET AL. 2018), each of which comprise several individual production steps and processes.

The individual procedures in cell assembly differ depending on the cell housing type. For industrially relevant large-format cells, a distinction can be made between three different housing types: *cylindrical cells*, *pouch cells*, and *prismatic hard-case cells* (WOEHRLE 2018, p. 105). Each cell housing type has inherent advantages and disadvantages, and in the field of electromobility all cell types have been used to date (SCHRÖDER ET AL. 2017). Figure 5 shows the production process for pouch cells as it is implemented at the research institute of the author of this dissertation (Institute for Machine Tools and Industrial Management, *iwb*, of the Technical University of Munich, TUM) (REINHART ET AL. 2013).

Electrode production

The electrode production begins with the preparation of the active material pastes, also referred to as *slurries*. To produce these slurries, the active materials, which are initially in powder form, are mixed with binders, conductive additives, and a solvent. The resulting viscous slurries are applied to both sides of the metallic current collector foils in a coating process. At the cathode, aluminum is used as the current collector foil material, while copper is used at the anode (cf. sub-section 2.2.2). The foil thicknesses are usually between 6 and 15 µm for the copper foil compared to 15 and 25 µm for the aluminum foil (PETTINGER ET AL. 2018, p. 214).

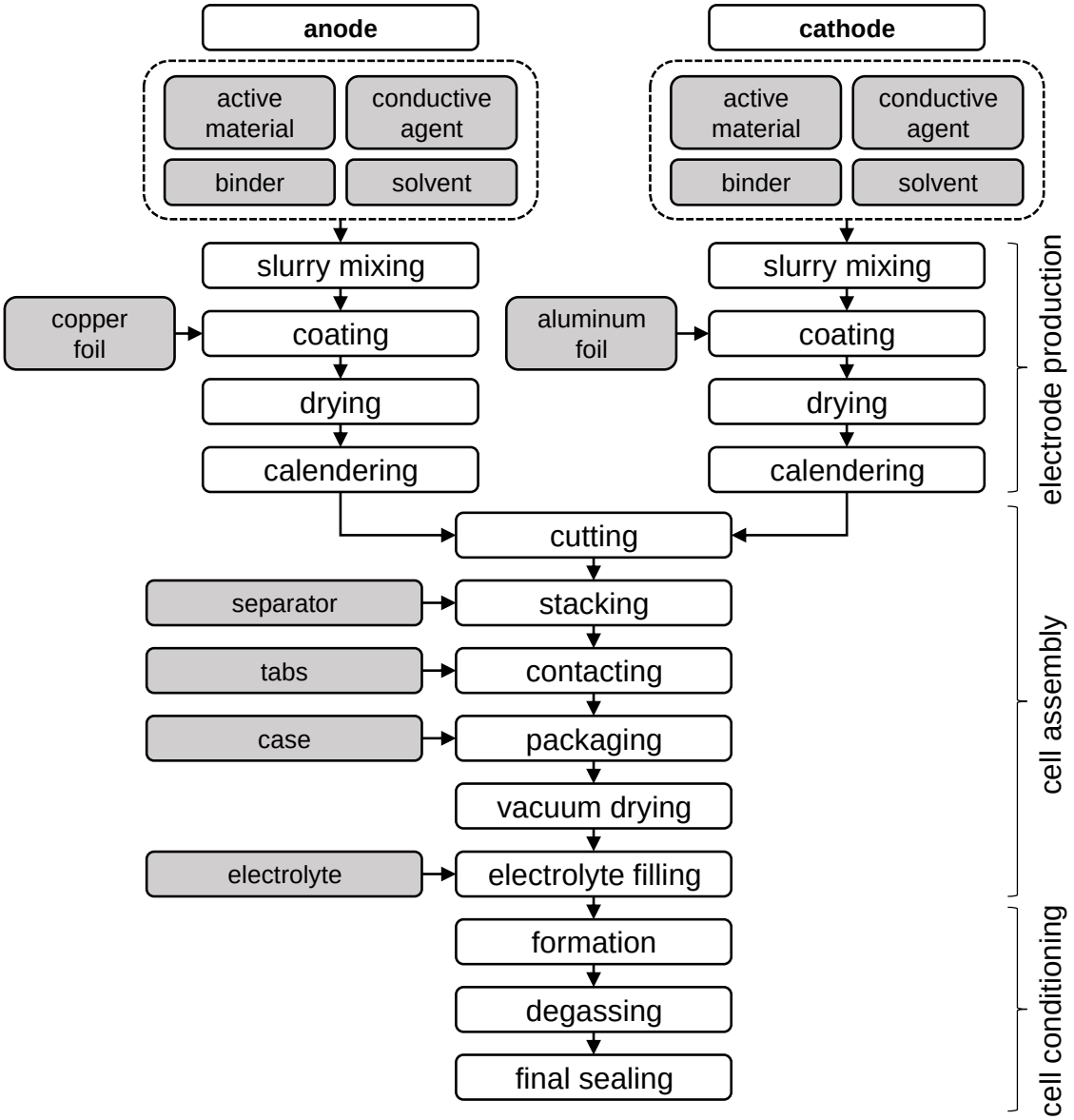

Figure 5: Production processes of lithium-ion pouch cells at the Institute for Machine Tools and Industrial Management (iwb) at the Technical University of Munich (TUM); adapted from REINHART ET AL. *(2013)*

The commonly employed binder polyvinylidene diflouride (PVDF) is not soluble in water, which is why *N*-Methyl-2-pyrrolidone (NMP) is needed as the solvent for the production of cathode slurries. Water-soluble binders are increasingly employed on the anode side. For water-based systems, mixtures of carboxymethylcellulose (CMC) and styrene-butadiene rubber (SBR) are applied. During the subsequent drying process, the solvents evaporate and leave the porous electrode structure behind (VUORILEHTO 2018, p. 23). It is important that the coatings are applied homogeneously in order to prevent local deviations in the electrode loading (cf. subsection 2.2.7). This leads to enormous challenges in production and quality control,

as the area throughput during coating is very high. According to PETTINGER ET AL. (2018), even in a rather small battery factory with a production capacity of two million 20-Ah cells per year, 26 000 km of anode and cathode foil are processed annually. This equals the production of around 14 000 m² of virtually immaculate electrode surface per day.

Subsequently, a rolling process is carried out, known as *calendering*, in which the electrode porosity is intentionally reduced. Thus, a higher energy density is achieved on the one hand, and, on the other hand, the interparticular contact is increased aiming at an improved electrical conductivity of the coating (PETTINGER ET AL. 2018, p. 215). The coating, drying, and calendering are continuous roll-to-roll processes. The end products of the electrode production are anode and cathode coils.

Cell assembly

The production processes of cell assembly (cf. Figure 5) differ depending on whether cylindrical cells (e.g. 18650 or 21700 cells), prismatic hard-case cells, or pouch cells are manufactured. Here, only the production processes for pouch cells will be discussed (TRASK ET AL. 2014), since these were assembled within the experimental framework of this thesis. The manufacture of laboratory coin cells, which were also employed, will not be described in detail. In general, the coin cell assembly performed in this thesis followed the guidelines published by MARKS ET AL. (2011), while the details can be retrieved from the experimental parts of the publications of this dissertation according to section 5.2.

Starting from the electrode coils, the cathode and anode sheets are first cut to shape in a separation process which can be performed by mechanical punching as well as laser cutting (KRONTHALER ET AL. 2012). This is followed by the assembly of the cell stack consisting of an alternating arrangement of cathodes and anode sheets separated by separator layers (TRASK ET AL. 2014). The uncoated foil overhangs are joined with the cell tabs which are thin aluminum (cathode) and nickel-plated copper (anode) sheets. These tabs conduct the electrical current out of the cell and form the external cell poles. The pre-assembled cell stacks are then packaged into a metal-polymer foil (pouch foil) from which only the tabs protrude. An opening is provided at one side of the packaging enabling the electrolyte injection. After the filling of the electrolyte, the cell housing is temporarily sealed (process step not displayed in Figure 5). Before the cell can be further processed, the electrolyte liquid must have wetted the entire cell stack. This is the only way to ensure ionic conductivity and thus the functionality of the cell (cf. Figure 2). Especially for large-format cells with a high number of

electrode and separator layers, this *wetting process* can take a very long time (several hours to days) (WEYDANZ ET AL. 2018, WOOD ET AL. 2015) and requires long intermediate storage, often at elevated temperatures (KNOCHE & REINHART 2015). The non-permeable current collector foils additionally impede the propagation of the liquid. Furthermore, the wetting progress is rather difficult to quantify (GÜNTER ET AL. 2018). In industrial production, the application of various pressure cycles has been established, which are intended to accelerate the wetting process (PETTINGER ET AL. 2018, p. 218).

Cell conditioning

In the formation process, the cells are charged and discharged several times with a low current under controlled conditions, so that a prediction can be made about the cell capacity and other quality-related parameters. During the formation, the SEI (a passivation layer on the anode consisting of organic as well as inorganic components, cf. sub-section 2.2.4) develops. The forming of this layer has a significant influence on the cell properties. Hence, numerous studies on the effects of electrolyte additives that are intended to support a controlled SEI formation have been carried out (JOSSEN & WEYDANZ 2019, pp. 148 f.). During formation, gas evolution may occur inside the cell, which is why a degassing procedure is performed before the cell is permanently sealed.

Following the cell production, the individual cells are then assembled into modules or battery packs. Details of the subsequent process steps and the applied components can be found in the technical literature, e.g. KORTHAUER (2018).

2.3 Laser materials processing

2.3.1 General remarks

The term *laser* is an acronym for *light amplification by stimulated emission of radiation* and describes the physical process of amplifying radiation by stimulated emission. This section provides the fundamentals of materials processing using laser radiation that are essential for this thesis. The focus lies on the use of pulsed laser radiation for the ablation of materials with the aim of introducing structures into a workpiece, which is the anode coating within the framework of this thesis. For a comprehensive description of further aspects of laser materials processing, please refer to the scientific literature, such as HÜGEL & GRAF (2009) or POPRAWE (2005).

2.3.2 Characteristics of laser radiation

In order to use laser radiation for materials processing, it is essential to focus the laser beam by means of an optical lens. The minimum beam diameter d_f, also referred to as the focus diameter, and the highest radiation intensity are achieved in a distance from the lens center called the focal length f_f. The Rayleigh length z_R is the distance along the optical axis measured from the focus point at which the cross-sectional area of the laser beam is doubled. These characteristics of laser beam caustics are illustrated in Figure 6.

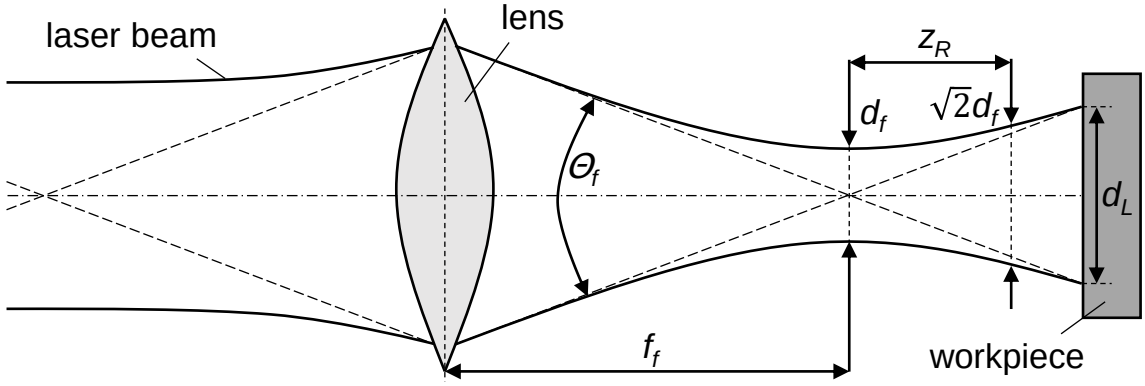

Figure 6: Laser beam caustics with characteristic parameters; adapted from HÜGEL & GRAF (2009, p. 34)

The aperture angle Θ_f can be determined using the Rayleigh length z_R and the focus diameter d_f:

$$\Theta_f = \frac{d_f}{z_R} \tag{2 - 16}$$

To evaluate the possibility to focus a laser beam, the beam parameter product *BPP* and the beam quality factor M^2 have been established:

$$BPP = \frac{d_f \cdot \Theta_f}{4} = M^2 \cdot \frac{\lambda}{\pi} \tag{2 - 17}$$

where λ is the wavelength of the laser radiation. A high laser beam intensity I_L is achieved by a high laser power P_L and a small cross-sectional area of the laser beam in the focal plane:

$$I_L = \frac{4 \cdot P_L}{\pi \cdot d_L^2} \qquad (2 - 18)$$

where d_L is the diameter of the laser spot on the workpiece assuming a homogeneous intensity distribution (cf. Figure 6).

2.3.3 Laser operating modes and process parameters

Lasers are often classified according to their operating mode. A distinction is made between continuous wave (cw) laser operation and pulsed laser operation. The operating mode has a significant influence on the introduction of the laser energy into the workpiece.

Continuous wave laser operation

In continuous wave laser operation, the laser resonator[3] is continuously stimulated, resulting in a permanent emission of the radiation. In materials processing, these cw systems operate with an output of up to several kilowatts and are mostly used for welding and cutting applications (HÜGEL & GRAF 2009, p. 57).

Pulsed laser operation

The emission of laser radiation can also be discontinuous in pulse mode. Within a laser pulse, the power is usually considerably higher than in continuous operation. The high laser power, in combination with the short irradiation time, can induce process phenomena that are not achievable in cw operation (cf. sub-section 2.3.4). The pulse durations of commercially available laser sources vary from a several hundred milliseconds down to a few femtoseconds. Depending on the desired pulse duration, the laser pulses are generated by means of different technical systems, which are described in detail in the scientific literature, e.g. by HÜGEL & GRAF (2009), EICHLER & EICHLER (2015) and POPRAWE (2005).

To further characterize the process of pulsed laser machining, knowledge of additional variables is required. In this respect, one important parameter is the pulse energy E_P, which represents the amount of energy contained in one single pulse. This parameter can be determined from the average laser power P_L and the repetition rate f_{rep}, which is the number of emitted pulses per second:

[3] A resonator is an arrangement of mirrors surrounding a laser-active medium. By reflecting the light back into the laser-active medium, the stimulated emission is reinforced before the laser beam is coupled out of the resonator (HÜGEL & GRAF 2009, pp. 55 f.).

$$E_P = \frac{P_L}{f_{rep}} \quad (2 - 19)$$

If the laser beam is moved over the workpiece surface at a certain velocity v_L in pulsed operation, an offset l_{sp} between two incoming laser pulses results:

$$l_{sp} = \frac{v_L}{f_{rep}} \quad (2 - 20)$$

In case of a distance l_{sp} between the circular exposure areas smaller than their diameter on the workpiece d_L, the points overlap and form a continuous, line-like machining area. Particularly with very short pulses, the influence of the translational speed v_L on the shape of the laser spot on the workpiece surface is negligible. For example, at a pulse duration of 1 ps, even a very high deflection velocity of v_L = 500 m/s only causes focus point distortions of 0.5 nm, which is four orders of magnitude below the typical focus diameter of a laser beam in micro materials processing.

2.3.4 Interaction between laser beam and workpiece

When a laser beam reaches a workpiece, a part of the radiation energy is absorbed, another part is reflected and, in the case of materials that are transparent for the corresponding wavelength, a third part is transmitted. For materials processing, the absorbed laser power $P_{L,abs}$ is particularly important, since this share contributes to the modifications to the workpiece. The magnitude of $P_{L,abs}$ depends on the laser power P_L, the intensity I_L, and the degree of absorption η_{abs}, which in turn depends on a number of influencing variables, such as the wavelength λ, the irradiated material, its temperature and its surface properties (HÜGEL & GRAF 2009, p. 116):

$$P_{abs} = P_L \cdot \eta_{abs} \quad (2 - 21)$$

Influence of the intensity

In materials processing with laser radiation, four characteristic process regimes can be formed depending on the intensity of the incident laser beam. In Figure 7, the process regimes for the coupling of laser radiation into a metal workpiece are displayed. Depending on the irradiated workpiece material, not all of these process regimes are applicable, e.g. if no molten phase of a material exists. The intensity values specified here are to be interpreted as an approximation and may vary

depending on the applied material and its surface condition. Particular interaction phenomena in materials processing with very short laser pulses will be discussed in more detail in the further course of this sub-section.

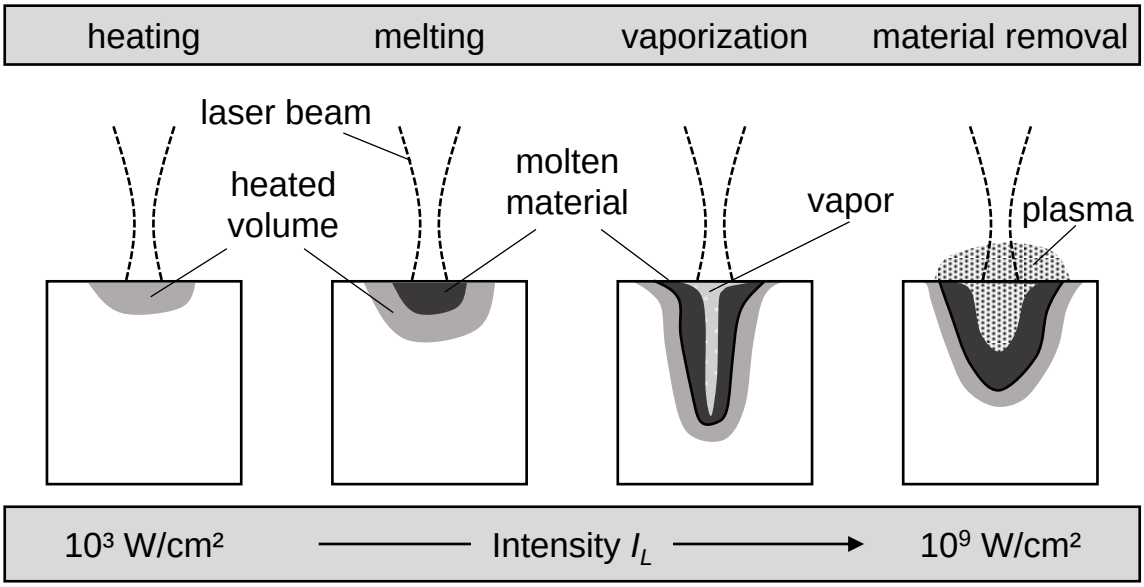

Figure 7: Process regimes for the coupling of laser radiation into a metal workpiece at increasing intensity with a) heating, b) melting, c) vaporization, and d) plasma formation and material removal; adapted from HÜGEL & GRAF (2009, p. 2)

At a low intensity of the laser beam, the workpiece temperature in the processing zone remains below the melting temperature of the material so that the material is merely heated. If the intensity is increased, the melting temperature of the material is surpassed so that a melt pool is formed. This process regime is used, for example, in heat conduction welding of metals. A further increase in intensity leads to a partial evaporation of the material and the formation of a vapor capillary which is often referred to as a *keyhole*. This phenomenon is exploited, for example, in deep penetration welding of metals. At even higher intensities of the incident laser radiation, the proportion of the vaporized material increases further compared to that of the molten material. In addition, due to the evaporation of the material, a high pressure is built up in the interaction zone, which causes vapor, plasma, and melt to be expelled from the process zone. Thus, a large share of the material is removed and only a small amount of melt remains. This process regime is used for laser drilling and laser ablation (cf. sub-section 2.3.5) (HÜGEL & GRAF 2009, pp. 2 f.).

Influence of the interaction duration

Besides the intensity, the duration of the interaction t_i substantially determines the occurring process regime. For pulsed laser radiation, t_i is equal to the pulse duration t_p. The pulse duration has a decisive influence on the interaction between the laser beam and the workpiece. Fundamentally, a distinction can be made between short and ultrashort pulses, whereby the distinction between these two categories is subject to a certain ambiguity in the literature. According to MEIJER ET AL. (2002), laser pulses can be considered as ultrashort when the thermal diffusion depth:

$$d_{th} = \sqrt{4 \cdot a \cdot t} \qquad (2 - 22)$$

during the pulse duration is equal to or lower than the optical penetration depth δ. Here, a is the thermal diffusivity of the material and t is the time. The optical penetration depth δ is defined by

$$\delta = \frac{2}{\alpha_{opt}} \qquad (2 - 23)$$

where α_{opt} is the optical attenuation coefficient of the material. According to the Lambert-Beer law, the intensity of a laser beam I, incident in the z-direction, is reduced from its initial intensity I_0 by

$$I(z) = I_0 \cdot e^{-\alpha_{opt} z} \qquad (2 - 24)$$

given a homogeneous attenuation coefficient of the material. For most materials, these definitions result in a threshold duration of a few picoseconds, below which laser pulses can be classified as ultrashort. For further details on the light absorption phenomena on an atomic level, the reader is kindly referred to specialized literature, e.g. LIU ET AL. (1997) or MEIJER ET AL. (2002).

Figure 8 illustrates the differences of the ablation processes for short and ultrashort laser pulses. For short pulses (Figure 8, left), the ablation is based on the vaporization and sublimation of material and thus on photo-thermal effects. The heating rate of the material depends on its absorption rate and the energy loss from the processing area through thermal conduction (LIU ET AL. 1997). The heat affected zone (HAZ) extends well beyond the ablated area and thus forms a boundary between the redeposited melt and microstructurally unaffected areas (MISHRA & YADAVA 2015). At higher intensities, vapor bubbles form, the material begins to boil, and a plasma cloud is created. For these micro- or nanosecond pulses, precise material removal is difficult

due to the fluid dynamics of the liquid and gaseous phases in the processing zone (CHICHKOV ET AL. 1996, p. 111).

When ultrashort laser pulses are applied to a workpiece, explosive boiling occurs with rapid formation and expansion of vapor bubbles. The absorption mechanism is based on the excitation of an electron by several photons which is referred to as *multiphoton ionization* (MISHRA & YADAVA 2015). The material absorbs the pulse energy very quickly while maintaining a constant density. Imbalances in the form of extreme pressures and temperatures build up and accelerate the ionized material rapidly along shock wave fronts (see Figure 8, right). A directed particle cloud then forms above the area of influence of the laser, which, at high laser intensities, turns into a plasma cloud (LEITZ ET AL. 2011). There is almost no heat transport to the surrounding matter (CHICHKOV ET AL. 1996).

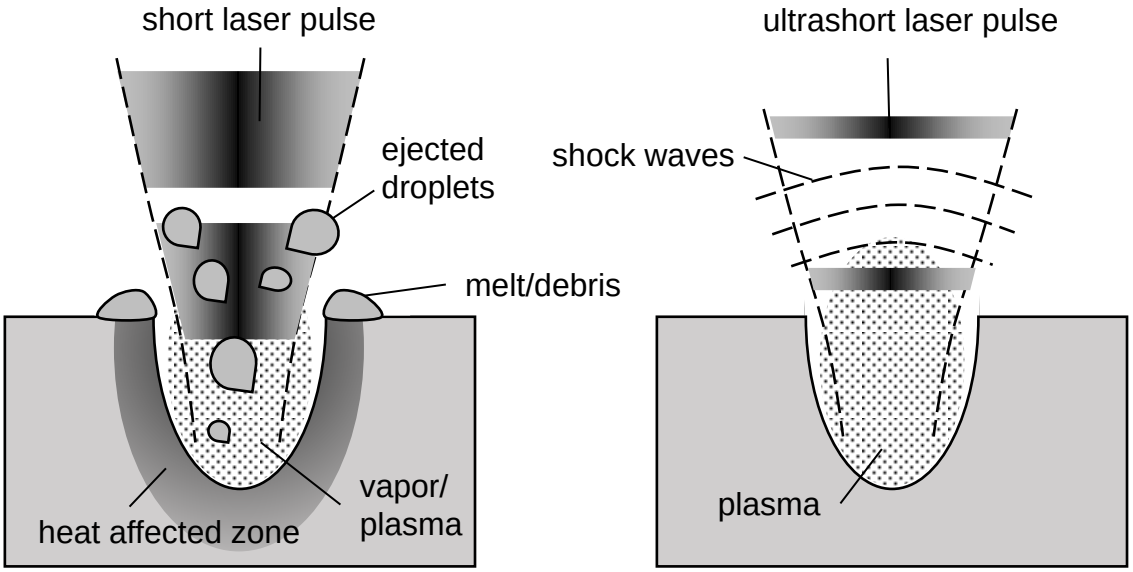

Figure 8: Ablation by short (left) and ultrashort (right) laser pulses; adapted from DESBIENS & MASSON (2007, p. 55) and LEITZ ET AL. (2011, p. 231)

Especially for low intensities, this leads to a high machining precision with a low heat impact to the surrounding material, qualifying ultrashort laser pulses for micromachining. In order to remove as much material as possible per laser pulse and thus achieve a high process efficiency, the interactions between material-specific parameters and the characteristics of the laser radiation must be taken into account (NEUENSCHWANDER ET AL. 2014).

2.3.5 Laser drilling and ablation

According to DIN 8580, both *drilling* and *ablation* are processes that leave defined geometric structures on the workpiece by removing material from its surface. Based on classical definitions, *drilling* designates the production of circular, cylindrical, or conical structures in which the ratio of depth to diameter of the structure is of the order of one or higher. The term *ablation* refers to the creation of structures that feature arbitrary two-dimensional shapes on a workpiece surface, where the depth is generally by far less than the largest lateral dimension (HÜGEL & GRAF 2009, p. 329).

From a production perspective, drilling with laser radiation is appropriate whenever conventional drilling methods reach their limits. These limits can be due to a challenging machinability of the employed material, or they can be of an economic or a geometric nature. For instance, the minimum drill diameters achievable with mechanical tools are significantly coarser than those achievable with highly focused laser radiation (HÜGEL & GRAF 2009, p. 352). In contrast to single-pulse drilling, where the final drill structure is generated by a single pulse, in percussion drilling laser pulses are applied repeatedly onto the same spot (PATWA ET AL. 2013). This allows for higher structure depths and aspect ratios (AR), which denote the ratio of the depth of a structure to its lateral dimensions. In the case of a bore hole, the AR is the ratio of the bore hole depth D_h to the bore hole diameter d_s at the surface:

$$AR = \frac{D_h}{d_s} \tag{2 - 25}$$

Laser drilling and ablation have been established as the preferred technologies for micro materials processing and are used in a wide range of applications, such as micro-optics, micro-electronics, microbiology and micro-chemistry (MISHRA & YADAVA 2015, p. 90, DU ET AL. 2012, DEMIR ET AL. 2013). A comprehensive review on pulsed laser drilling was provided by GAUTAM & PANDEY (2018). Lasers with pulse durations in the order of femto- to microseconds and wavelengths from the deep ultraviolet to the mid-infrared range are industrially used. Due to its inherent geometric flexibility and the achievable processing speed (JAEGGI ET AL. 2013), one laser system may substitute a multitude of mechanical tools (DUBEY & YADAVA 2008).

2.3.6 Beam guidance and shaping

In order to place and dynamically move the focus of the laser beam on the workpiece, optical focusing and beam guidance elements are required. A distinction is made between two fundamentally different technical systems, *fixed optics* and *scanner optics*. In fixed optics, the laser beam is shaped by optical elements, e.g. lenses, in such a way that the laser beam is focused at a defined processing distance outside of the fixed optics. The beam is deflected by moving the entire optical system (or the workpiece) with external handling devices, e.g. linear axes or robots. In contrast, scanner optics additionally contain elements for beam deflection, with which the laser beam can be positioned in a defined working field. As depicted in Figure 9, this function is usually realized via rotating mirrors, which, due to their orthogonal arrangement, allow a highly dynamic two-dimensional deflection of the laser beam.

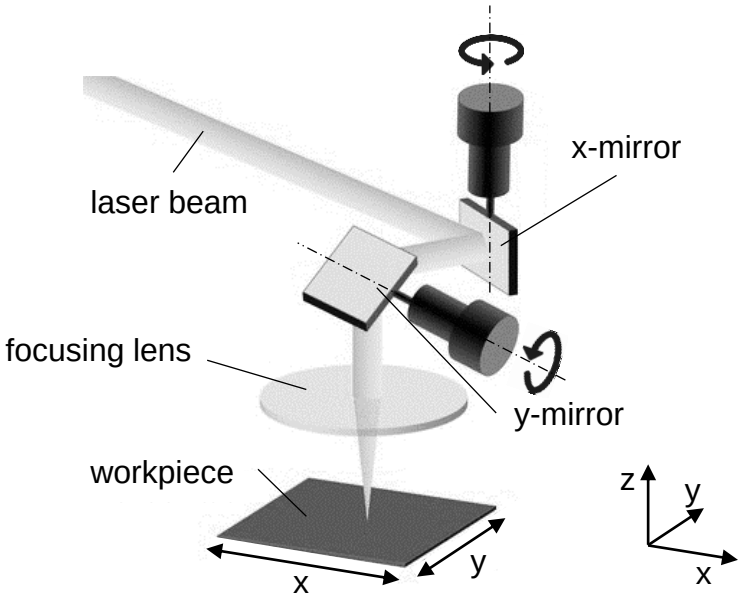

Figure 9: Internal structure and operating principle of scanning optics; adapted from HÜGEL & GRAF (2009, p. 95)

Focusing can be achieved either by lenses arranged in the beam path before or after the mirrors. The latter are referred to as *f-theta lenses* (HÜGEL & GRAF 2009, p. 96). They ensure that the focal point is always located in the working plane perpendicular to the optical axis of the lens during scanning. Due to the highly dynamic beam deflection, scanner optics are used for ablation, cutting, structuring, welding, and laser beam melting in additive manufacturing. Even though the forces required for beam deflection are small due to the low mirror masses and inertias, limitations arise at high deflection speeds or accelerations (JAEGGI ET AL. 2012). For applications with

the highest demands concerning the velocity of the laser beam on the workpiece surface, polygon scanners are also used, in which a continuously rotating multi-facet wheel provides the feed rate, whereas the fine positioning continues to be carried out via galvanometer mirrors (DE LOOR 2013). These polygon scanners enable beam deflection speeds of several hundreds of meters per second and continue to gain importance in the industrial processing of large surface areas (VAN DER STRAETEN ET AL. 2018).

2.4 Concluding remarks

In the preceding sections, the fundamentals of lithium-ion batteries (section 2.2) as well as laser materials processing (section 2.3) were presented. On the basis of an overview regarding the design and the operating principles of lithium-ion batteries, electrochemical fundamentals were outlined. A special focus lay on the understanding of the cell-internal ion transport. The occurrence of lithium concentration gradients throughout the electrode pore structure was discussed and related to the electrode morphology. The conclusion was drawn that electrode morphology modifications may have the potential to enhance the ion transport within the cell and thereby improve the fast charging and discharging characteristics. Section 2.2 was concluded with an overview on the production processes of lithium-ion batteries.

Section 2.3 then provided the background information on laser materials processing. Here, the emphasis was set on the pulsed mode of laser operation and the use of laser pulses for the generation of defined structures in workpieces. Finally, a short overview of technical systems for beam guidance and shaping was given.

The two research fields considered in sections 2.2 and 2.3 form the foundation on which the state of the art for laser structuring of electrodes for lithium-ion batteries, which is explained in chapter 3, is based. Thus, in the further course of this work, an overview of previous research on the generation of structured electrodes is presented. Available experimental and numerical investigations on the influence of electrode structures on the cell properties will also be discussed.

3 State of the Art

3.1 Chapter overview

As described in sub-section 2.2.7, numerous research activities have been dedicated to intentionally altering the pore morphology of the electrodes of lithium-ion batteries in order to enhance their performance. In many of these studies, the ion transport in the electrolyte was identified as the limiting factor for the performance of lithium-ion batteries. The approach to enhance the ion transport through the porous electrode, which is pursued in this dissertation, is the introduction of additional cavities into the anode. These aim at simplifying and shortening the ion transport paths and thus reducing the mean tortuosity (cf. Figure 1). Focused laser radiation is one possible tool to create these cavities in a subtractive process by the precise removal of a small volume fraction of the anode coating (SAUTER 2012).

Chapter 3 offers an overview on the state of the art concerning the morphology modification of lithium-ion battery electrodes. Section 3.2 specifically focuses on laser structuring of electrodes, while in section 3.3 alternative processes for the pore morphology modification are discussed. In section 3.4, numerical approaches for the modeling of structured electrodes are provided, whereas in section 3.5, the state of the art is summarized and the need for action is derived. Throughout chapter 3, both cathode and anode modifications are discussed, although the scope of this dissertation is confined to the processing of anodes.

3.2 Laser structuring of electrodes

General remarks

In addition to the subsequently discussed findings on the modification of porous electrodes by laser radiation, numerous publications on the laser-based processing of *thin-film electrodes* exist (KIM ET AL. 2014). These types of electrodes are typically applied in low-energy batteries and small-scale applications such as micro-electro-mechanical systems (MEMS). The dimensions of these batteries are usually between 1 and 10 mm^3, including all housing components (ROBERTS ET AL. 2011). In contrast to the production of porous thick-film electrodes by slurry coating (cf. sub-section 2.2.8), the application of the thin electrode films is performed by chemical or physical vapor deposition of the active materials. The resulting film thicknesses usually do not exceed a few micrometers (ROBERTS ET AL. 2011). An overview regarding advances in the field of laser-based thin-film electrode processing is given by PFLEGING (2018) and reference is made to several publications from his research group, e.g. KOHLER (2014), KOHLER ET AL. (2013), and PRÖLL ET AL. (2013). The physical effects occurring in the laser treatment of the thin-film electrodes differ significantly from those in batteries comprising porous thick-film electrodes. For example, KOHLER ET AL. (2013) observed the formation of conical, self-organized surface structures on the sub-micrometer scale when irradiating lithium cobalt oxide ($LiCoO_2$, LCO) thin-film electrodes. Such effects are not examined in this thesis. For this reason, a discussion of the publications regarding thin-film batteries is not included below. Likewise, related processes, such as laser cutting of electrodes, which was assessed e.g. by SCHMIEDER (2016), KRONTHALER ET AL. (2012), LUETKE ET AL. (2011), and LEE ET AL. (2013), will not be discussed in detail in this thesis.

Various patterns for the laser structuring of thick film electrodes have been introduced in the literature described in the forthcoming paragraphs. In principle, a distinction can be made between grid (Figure 10 a)), line (Figure 10 b)), and hole structures (Figure 10 c)), whereby the grid structures consist of intersecting lines. The spacing between the lines or holes as well as other structure parameters (e.g. diameter, depth, conicity etc.) were varying depending on the production process. The electrode recipes and laser process parameters are described in detail in the respective publications, which is why they are not included exhaustively in the following explanations.

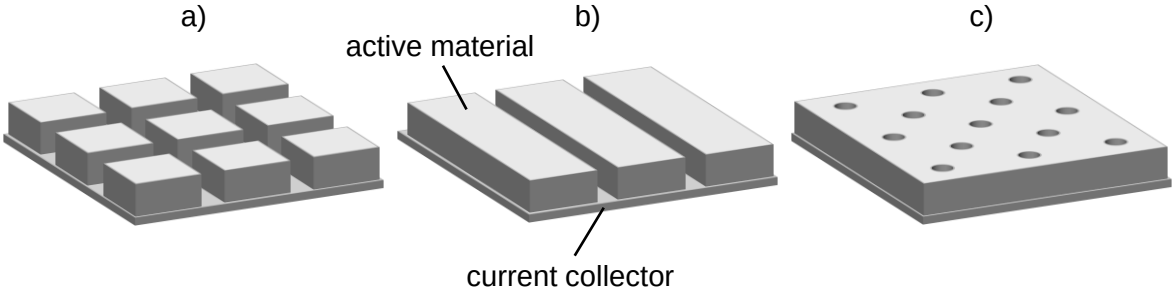

Figure 10: Schematic illustration of typical patterns for the structuring of electrodes; a) grid structure, b) line structure, c) hole structure

Laser structuring of cathodes

PRÖLL ET AL. (2015) and PRÖLL ET AL. (2014) produced four different types of $LiMn_2O_4$ cathodes by laser printing. Type 1 of the cathodes remained untreated, type 2 was calendered, type 3 was laser-structured without calendering, and type 4 was first calendered and then laser-structured. A grid was chosen as the structuring pattern. The authors used a femtosecond laser operating at a wavelength of 515 nm, a repetition rate of 200 kHz, a laser power of 25 mW, and a pulse duration of 350 fs. The different cathodes were installed in half cells (lithium metal as anode) and underwent various electrochemical tests. The calendered and laser-structured electrodes (type 4) showed the best results, both in terms of the C-rate capability and the capacity loss at the 35th cycle which was used as a measure for the cell aging.

A pulsed nanosecond laser and a femtosecond laser were used by SMYREK ET AL. (2015) and SMYREK ET AL. (2016) in order to generate cavities in NMC cathodes. They introduced both line and grid structures into the cathode coating and then conducted electrochemical tests in half cells versus lithium metal. The cells with laser-structured electrodes showed a higher specific capacity in the C-rate discharge tests than their unstructured counterparts. However, the loss of the NMC due to laser structuring, which results in a decrease in the energy density of the electrode, was not specifically mentioned.

In a subsequent study, the loss of cathode active material was quantified by RAKEBRANDT ET AL. (2017) to be in the range between 9 and 15 %. For structuring, a femtosecond laser was employed emitting laser pulses with a pulse duration of 380 fs, a wavelength of 515 nm, a repetition rate of 200 kHz, and an average power of 2 W. A pattern of parallel lines with a pitch distance of 200 µm was produced while applying scanning velocities in the range of 500 to 1500 mm/s. Three different electrode types were electrochemically characterized in C-rate discharge tests, each

of them with and without the induced line structures. For all three electrode types, an increased discharge capacity could be determined due to laser structuring, especially at higher discharge currents. Similar observations regarding the high current capability of NMC cathodes with laser-induced line structures were made by PARK ET AL. (2019) and ZHU ET AL. (2019).

PRÖLL (2014) investigated the laser structuring of NMC electrodes for his dissertation with a focus on the creation of capillary structures. To create the capillaries, line structures were introduced into the active material by directing the laser beam over the electrode at a continuous velocity. This way, an overlapping of the pulses was achieved (cf. sub-section 2.3.3). In addition to an improved high-current capability, PRÖLL (2014) observed an enhanced wettability with the electrolyte fluid. In lifetime tests, in which the formation of the cells was started immediately after the electrolyte filling, the cells with structured electrodes showed slower aging. This was attributed to a higher degree of wetting at the commencement time of the formation process. The improved wettability was also reported by PFLEGING & PRÖLL (2014) and PFLEGING ET AL. (2014). Furthermore, PRÖLL (2014) established a model hypothesis regarding the removal process of the electrode coating, in which he refers to preliminary work by SLOCOMBE & LI (2000) on the ablation of metal-polymer composites. This hypothesis states that the removal of the coating is not only due to the evaporation of the active material but also due to the thermal heating of the processing zone and its surroundings, which includes a fast heating of the binder. Since the binder evaporates at a much lower temperature, whole active material particles can be ejected without exceeding their evaporation or melting temperature. On the one hand, this results in a more efficient use of the introduced laser energy, since not all the active material is evaporated. On the other hand, it may result in structuring geometries that can be significantly larger than the laser beam diameter at the focal point. This theory was later referred to by PFLEGING ET AL. (2016) in a manuscript on laser-based electrode processing.

MANGANG ET AL. (2014), MANGANG ET AL. (2015), and MANGANG ET AL. (2016) studied the pulsed laser structuring of LFP cathodes. Based on the results of SMYREK ET AL. (2016), they found out that laser structuring resulted in an enhancement of the C-rate capability of LFP cathodes. In addition, they observed that the material removal rate varied depending on the laser beam source used (pulse durations 200 ns to 350 fs), with shorter pulses yielding an improved ablation efficiency. An increased melt formation on the structure flanks was found for longer laser pulses, while melt formation in the femtosecond range could be suppressed. The abovementioned results were summarized by PFLEGING (2018) and PFLEGING & GOTCU (2019).

A technological overview on applications of ultrafast laser processing was presented by MOTTAY ET AL. (2016). Battery applications, and especially the structuring of cathode materials were the focus of the review. The authors concluded that many future commercial applications will benefit from the progressing advancements in laser system technology, enhanced knowledge about laser-matter interaction, and the further development of high-speed beam deflection systems.

Laser structuring of anodes

Compared to the multitude of publications on laser structuring of the cathode, laser structuring of the anode has received much less attention to date. The focus of the existing work was on the structuring of silicon-containing anodes with the aim of compensating for the high volume expansion of the silicon during charging by creating void volumes within the electrode layer. For this purpose, silicon-graphite composite anodes were structured by ZHENG ET AL. (2017A), ZHENG ET AL. (2017B), ZHENG ET AL. (2018), and ZHENG ET AL. (2019A) using laser radiation. A grid structure was chosen so that the remaining "micro-pillars" could expand into the additionally created void volume. As a result, an improved C-rate capability could be achieved combined with a reduced degradation at the end of the cell testing. Additionally, ZHENG ET AL. (2019B) used laser-induced breakdown spectroscopy in order to experimentally determine the spatially resolved lithiation degree of the anodes, e.g. after a fast charging process.

Although PRÖLL (2014) focused on the laser-assisted modification of cathodes (cf. previous paragraph on the laser structuring on cathodes), he presented some investigations of cells with laser-structured graphite anodes as part of his dissertation. For structuring, a pattern of parallel lines with a 200 µm line spacing was chosen (PRÖLL 2014, p. 133). The applied nanosecond laser pulses (t_p = 200 ns) at a repetition rate of 80 kHz, a laser power of 8.5 W and a scanning velocity of 200 mm/s caused the removal of a significant share[4] of the graphite coating. In electrochemical tests in pouch cells with NMC cathodes, the cells with the laser-structured anodes failed quickly. Lithium-plating was suggested as the main reason for the failure, as some lithium ions coming from the cathode could not intercalate into the remaining graphite (PRÖLL 2014, p. 197). Due to the high material removal from the anode, the area-specific capacities of the anode and the cathode were no longer correctly matched. The work of PRÖLL (2014) shows that the share of removed material at the anode must remain very low in order to not considerably alter the ratio of the area-specific capacities of cathode and anode (also referred to as *balancing*). Alternatively,

[4] approx. 30%, estimation of the author of this thesis by analysis of Figure 6-80, p. 133 (PRÖLL 2014).

a higher anode loading could be deliberately applied prior to structuring in order to achieve the desired balancing after structuring. However, such approaches were not further pursued within the work described.

KIM ET AL. (2018) fabricated thick and highly compressed graphite anodes with three different loadings (1.15, 4.00, and 5.50 mAh/cm²), introduced pores by laser structuring, and assessed the C-rate capability during fast charging. A significant increase of the average specific capacity during charging was observed due to laser structuring, but only for the electrodes with the highest loading (5.50 mAh/cm²). Post-mortem analyses of the cells proved a more uniform lithium intercalation for laser-structured anodes.

YANG ET AL. (2019) provided process investigations regarding the laser ablation of graphite anodes with the aim to establish a relation between the laser pulse energy and the resulting ablation dimensions. Furthermore, they found that the graphite particle size has an influence on both the structure dimensions and the heat affected zone.

WATANABE ET AL. (2019) investigated whether a complete perforation of the anode and the cathode can be exploited to perform a pre-lithiation. The aim of this process is to avoid capacity reductions due to an irreversible lithium loss in the first charge and discharge cycle during formation. It was demonstrated that a perforation can facilitate the pre-lithiation process. Other effects of the perforation were not examined in this study.

Interim conclusion

The generation of structures in the microporous lithium-ion electrodes by means of laser radiation has received much attention in the scientific community in the last decade. The authors focused mainly on the modification of the cathode coating, and most of the common cathode active materials were considered. As structures, mostly lines were introduced, which in some cases overlapped forming grid structures (cf. Figure 10). To analyze the effects on the electrochemical behavior of the lithium-ion cells, discharge C-rate tests and cyclic voltammetry in half-cells with a metallic lithium anode were performed. The results consistently show an improved C-rate capability of cells with laser-structured cathodes, which is expressed by increased specific discharge capacities at high discharge currents. The findings are explained by an improved ion transport in the electrolyte enabled by the laser-induced cavities.

It should be noted that, in many publications, only the specific usable capacities during discharging are provided. This is problematic as the structuring of the cathode results in a loss of active material and thereby electrode capacity, while the electrode volume remains constant. In practice, laser structuring of the cathode may result in a gain in usable capacity at high discharge C-rates, but at the cost of a loss of the nominal capacity of the cell. In order to ensure comparability, the loss of active material and thus in the energy density of the electrode would have to be compensated, for example by reducing the porosity through higher compaction. So far, the current state of the art still lacks a sophisticated analysis that compares the potential benefits of structuring the cathode with the potential negative effects due to material removal.

Compared to the large number of studies aiming at the laser structuring of the cathode, the laser structuring of the anode has so far been considerably less intensively explored. This is remarkable, since graphite anodes typically have a higher tortuosity in the preferential direction of lithium transport than cathodes (cf. sub-sections 2.2.6 and 2.2.7) due to the flake-like shape of the graphite particles (EBNER ET AL. 2014). Thus, laser structuring can be expected to offer a particularly high potential to enhance the effective diffusion coefficient by reducing the electrode tortuosity (cf. eq. 2 - 14) and improving the ion transport upon charge and discharge. Until now, the state of the art for laser structuring of anodes has lacked experimental investigations on the fast charging performance of laser-structured anodes. Especially the occurrence of lithium-plating has not been adequately explored. Furthermore, although the approaches to explain the laser-induced improvements are plausible and intuitive, they lack a scientific model-based substantiation.

In this context, numerical simulation is of particular importance. It enables the calculation of the effects of morphological changes of the electrodes on the properties of the cell. Before the work in this research area is discussed in section 3.4, alternative processes for the structure generation in electrodes are considered in the following section.

3.3 Alternative electrode structuring processes

Laser structuring is only one of many potentially suitable processes for the creation of electrodes with 3D features such as line, grid, or hole structures. Various other concepts for the production of such electrodes can be found in the literature. Even

though most of the processes mentioned are still in an early development stage, they will be briefly discussed below.

In 2014, SAUTER (2012) from the Robert Bosch GmbH in Germany disclosed a patent on the structuring of electrodes, regardless of the structuring pattern and production process. The patent names a number of processes that can potentially be used to produce structured electrodes. These include the embossing of indentations with a mechanical tool, e.g. pre-structured rollers, drying the electrode slurry in such a way that drying cracks are formed which then serve as ion transport paths, and the layered build-up of electrodes in printing processes. Scientific publications exist for all of these techniques, some of which are mentioned hereafter.

KIM ET AL. (2007) used a laser printing process (laser direct write, LDW) to create discrete LCO electrode structures. LDW processes have been widely used in the production of micro batteries, but a transfer to large-format battery cells, e.g. for automotive applications, does not seem economically feasible at present.

BAE ET AL. (2013) iteratively co-extruded, assembled, and sintered LCO feed rods in order to create fine hole structures with hole diameters of approx. 6 µm. The channel spacing was adjustable down to 15 µm and improvements in electrode kinetics were achieved. BAE, et al. (2012) also patented a co-extrusion process in which electrode structures can be produced using a special print head. The potential of this technology was later analyzed by COBB & BLANCO (2014) and COBB & SOLBERG (2017) using numerical simulations (cf. section 3.4). Especially for high areal loadings of the electrodes, enormous improvements of the C-rate capability were numerically predicted. Publications on experimental work are not known. However, the technology is being developed commercially (PARC 2020).

LEE ET AL. (2018) manufactured electrodes with various NMC slurry formulations, so that cracks in the coating appeared during drying (so-called *mud-cracking*). These cracks were to serve as additional ion transport paths. Since the intended enhancements in the kinetic behavior of the electrodes could not be clearly demonstrated in cell tests and, in addition, premature aging of the cells was detected, the authors concluded that the electrical conductivity also needs to be examined for electrodes produced in this manner.

MAUREL ET AL. (2019) printed the electrodes for an LFP-graphite battery using Fused Deposition Modeling (FDM). In this initial study, the focus of the considerations was the fabrication of the printing filament, which must contain the electrochemically active materials and additives in order to obtain the required mechanical flexibility.

Due to its complexity, this process will not be able to compete with conventional processes in electrode production for large-format lithium-ion cells in the foreseeable future.

In the context of his dissertation on laser processing of cathode materials (cf. section 3.2), PRÖLL (2014) analyzed an embossing process using a profiled calender roll. This method, however, led to an excessive compaction of the structure flanks, since ultimately no active material is removed from the electrode but rather displaced towards adjacent areas. The displacement in the direction of the structure flanks locally reduced the porosity in these areas, which resulted in a blockage of the lithium transport routes. Therefore, PRÖLL (2014) questioned whether the desired effect of an electrochemical activation by a reduction of the tortuosity can be achieved by mechanical structuring methods.

Interim conclusion

Several different methods to generate structures in electrodes have been assessed in the scientific community. The variety and versatility of the processes examined underlines the importance of the matter. Especially the generative and additive processes (e.g. printing and extrusion) have a unique appeal, as they do not involve any loss of active material compared to subtractive processes, such as laser structuring. This can potentially lead to cost savings, even though, from today's perspective, the throughput times, and thus also the processing costs, do not appear to achieve competitiveness within a foreseeable future.

As described in section 2.3, developments in the field of laser technology continue to advance at a rapid pace. This applies both to the beam generation and the beam deflection. New pulsed beam sources with higher average powers are under continuous development and enable greater area processing rates. In the field of beam deflection, the technological advances allow for an increasingly high-precision and yet faster processing. Finally, the processing speed, the processing costs, the integrability into existing production plants, and the created technical benefit will decide upon whether structuring of the electrodes is economically feasible and which process will prevail in an industrial production scenario.

3.4 Modeling and numerical simulation of structured electrodes

Most of the work on the numerical simulation of the electrochemical processes in lithium-ion batteries with porous intercalation electrodes is based on the work of DOYLE ET AL. (1993) and FULLER ET AL. (1994). They developed a one-dimensional model, extended by a pseudo-dimension in the porous phase, to describe the concentration of ions in the particles of the active material and the electrolyte (cf. sub-section 2.2.4). This so-called *Newman model* consists of three domains (cathode, anode, and electrolyte) and two phases (solid and liquid), whereby electrical conduction only occurs in the solid phases of the anode and the cathode. The one-dimensional approach is enabled by defining an imaginary straight line orthogonally through the electrode-separator plane. In the electrode domains, it is assumed that both active material (represented by the radial pseudo-dimension) and electrolyte are present at each point. Therefore, the model is commonly designated as *homogenized* and *pseudo-two-dimensional* (p2D). The publications discussed in the following are based on the considerations by DOYLE ET AL. (1993) and FULLER ET AL. (1994), whereby the models were adapted for the respective batteries under consideration.

COBB & BLANCO (2014) and COBB & SOLBERG (2017) used the finite element method (FEM) software COMSOL Multiphysics® (COMSOL INC. 2020) in order to three-dimensionally depict the electrode structure that resulted from their newly developed co-extrusion process (cf. section 3.3). Spherical cathode material particles were implemented, resulting in isotropic diffusion properties within the electrode. The trenches caused by the extrusion process were assumed to be filled with the liquid electrolyte, thus showing a tortuosity of $\tau = 1$ in all spatial directions. Most model parameters were derived from literature.

NEMANI ET AL. (2015) developed a 2D model for the calculation of charge and mass transport processes in LCO-graphite batteries. The graphite anode featured a strong tortuosity anisotropy (cf. EBNER ET AL. (2014)) and the additionally introduced channel structures were implemented by assuming a tortuosity of $\tau = 1$ (for the definition see eq. 2 - 12 on p. 16) in both considered spatial dimensions. The model was used to carry out a purely numerical study, which led to the conclusion that many finely distributed structures are more beneficial for the electrode kinetics than a few coarse structures. For reasons of comparability, the volume taken up by the introduced pores was kept constant. Furthermore, NEMANI ET AL. (2015) found that a conical shape of the structures (opening towards the separator) resulted in higher C-rate capability enhancements than a cylindrical structure. This was attributed to the

increasing ionic current density close to the separator. Most of the model parameters were adopted from the scientific literature. An experimental model calibration or validation was not performed within the context of the described work. Furthermore, no production process was explored in order to create the structures.

Interim conclusion

The modeling of the electrochemical processes in lithium-ion cells has led to numerous publications over the last years. Most of the publications are based on the Newman model, which contains the fundamental cell-internal balance equations. The few existing research papers on the modeling of lithium-ion batteries containing electrodes with additional cavities were discussed above. These studies predict very encouraging effects of structuring, especially with respect to the enhanced ionic transport properties of the electrodes. So far, however, no experimentally calibrated or validated model exists that relates the numerical calculations to experimentally acquired data from cell analyses. This circumstance limits the applicability of the existing models and unveils the potential for further research.

3.5 Conclusion and need for action

Based on the fundamentals provided in chapter 2, chapter 3 described the state of the art in the field of structured electrodes for lithium-ion batteries. Section 3.2 provided a comprehensive overview of existing approaches for laser structuring of the electrodes. Various publications have been issued in this area of research in recent years. A large part of these works deals with laser structuring of the cathodes, while laser structuring of the anodes has been studied much less intensively. Although the underlying idea of a tortuosity reduction of the electrodes does not depend on whether structuring of the anode or the cathode is performed, the research gap in the field of anode laser structuring is significant. Especially since the anode is often characterized by a much higher tortuosity, the improvements due to the laser-induced pores at the anode should be substantial. Furthermore, only few considerations of the rapid charging capability of lithium-ion cells with laser-structured anodes exist. However, predominantly this area of research promises enormous potential, as the rapid charging capability of lithium-ion cells is one of their most crucial characteristics. Especially in the automotive sector, the fast charging capability is a very important criterion for customer acceptance and the market success of the lithium-ion

technology. The avoidance of lithium-plating (cf. sub-section 2.2.5) is a crucial prerequisite in this context.

Section 3.3 covered alternative electrode structuring processes. These processes usually serve the same goal of reducing the electrode tortuosity. The generative processes, such as printing or extrusion processes, appear particularly promising, as they potentially enable a structure creation without material loss. However, these processes are hardly compatible with the conventional, cost-efficient electrode production (cf. sub-section 2.2.8). Laser removal processes, on the other hand, already exhibit a high process speed due to the ever-rising power of the industrially available beam sources and rapid developments in the field of beam deflection. Since laser structuring can be carried out on conventional electrodes as an additional process step, the integration into the existing battery production process (cf. Figure 5) appears to be feasible. However, no research is currently known that has considered the scaling of the structuring process of electrodes beyond laboratory experiments and in which industrially relevant cells with laser-structured electrodes have been produced.

Section 3.4 provided a brief overview of existing work in the field of modeling and numerical simulation of lithium-ion batteries with structured electrodes. The presented work suggests significant enhancements of the lithium-ion transport properties by structuring. However, prior to the publication date of the papers prepared by the author in the context of this dissertation, no experimentally supported or validated model existed to describe the electrochemical effects of structured electrodes on intracellular processes.

The prevalent research deficit is summarized below. The following remarks refer to the state of the art at the respective time of the publications issued according to the research findings section (chapter 5) of this dissertation.

- Very few publications describing the potential of laser structuring of graphite anodes to enhance the performance of lithium-ion batteries exist. In particular, there is a lack of studies on the influence of hole structures, which are promising in that they lead to a low active material removal. Furthermore, there is a research deficit in the field of fast charging of lithium-ion cells with laser-structured anodes, especially with a focus on the occurrence of lithium-plating.
- The available models for the description of the cell-internal mass and charge transport are not able to precisely depict the processes in batteries with laser-

structured anodes. Experimental model calibration or validation approaches are not known to date.

- The accelerated electrolyte uptake of laser-structured electrodes has already been identified on a laboratory scale. However, the state of the art lacks investigations of this phenomenon under production-like conditions that allow an assessment of the quantitative potential of this technology, e.g. in terms of increasing the speed of the wetting process.
- Studies regarding the integration of the laser structuring process into battery production are scarce. For an economic industrialization, a high process speed is required. Since modern pulsed laser beam sources operate at increasingly high pulse repetition frequencies, the further development of powerful beam deflection systems is necessary.

The abovementioned unresolved issues justify the need for action and provide the basis for the research approach, which is presented in the following chapter and which was pursued over the course of this publication-based doctoral thesis.

4 Research Approach

4.1 Chapter overview

This chapter outlines the scientific objectives of this thesis and the pursued research approach, which led to the publications discussed in chapter 5. The state of the art described in chapter 3 serves as a foundation. In section 4.2, the overall objective is initially specified from which sub-objectives are derived. These sub-objectives constitute the framework for the methodical approach presented in section 4.3. The integration of the six publications, which form the research core of this work, into the methodology is also provided in this context.

4.2 Scientific objectives

The global objective of this thesis is to improve particular characteristics of lithium-ion batteries by introducing additional structures into the porous anode by means of pulsed laser radiation. The structures are intended to ease the lithium-ion transport through the anode, resulting in a reduction of overpotentials during fast charging and discharging (cf. sub-section 2.2.4). Expected effects include a higher usable capacity during discharging and a reduced occurrence of lithium-plating (cf. sub-section 2.2.5) during fast charging. These benefits are to be experimentally demonstrated and substantiated by a model in order to numerically derive quantitative insights regarding the intracellular processes. Production-related aspects, such as the reduction of the process time of the electrolyte wetting in cell production (cf. sub-section 2.2.8) and the rate of the structure generation itself, will also be considered. Five sub-objectives (SO) characterizing the need for action prior to this thesis (cf. section 3.5) can be derived and are listed below.

SO1: Qualification of the laser as a tool for beneficial anode structuring

The applicability of pulsed laser radiation to generate structures in graphite anodes is to be proven. A fundamental demonstration has to be provided that the structuring of the anode has a positive influence on the discharge C-rate capability.

SO2: Determination of performance improvements (charging and discharging)

The impact of laser structuring on various cell characteristics must be explored in further detail. Experimental investigations on the charging and discharging performance at different temperatures have to be carried out. The influence of the laser-induced structures on the occurrence of lithium-plating has to be examined.

SO3: Knowledge gain on the charge transport in laser structured anodes

A model of a structured anode is to be developed, on the basis of which electrochemical simulations can be carried out. The aim of these simulations is to gain an in-depth understanding of the charge carrier transport and to obtain quantitative information, e.g. on lithium concentration gradients. The model is intended to provide the basis for an application-specific electrode design.

SO4: Proof of accelerated electrolyte uptake under near-industrial production conditions

It must be examined whether the laser structuring of the electrodes can significantly accelerate the electrolyte wetting during cell production. For the investigations, the production conditions have to be close to the industrial practice.

SO5: Identification of required technological advances and measures for process acceleration

A production scenario is to be defined, which allows for an evaluation of the laser structuring process under technological and economic aspects. Challenges for increasing the process speed must be identified and addressed.

The research methodology ensuing from the sub-objectives is described in section 4.3 and schematically illustrated in Figure 11.

4.3 Methodology and integration of the publications

This section provides a classification of the publications elaborated in the course of the author's research activities on the basis of their thematic focus with regard to the research objectives formulated in section 4.2. The classification and integration of the publications into the methodology are summarized in Figure 11, while a more detailed description of the core research findings is provided in section 5.2.

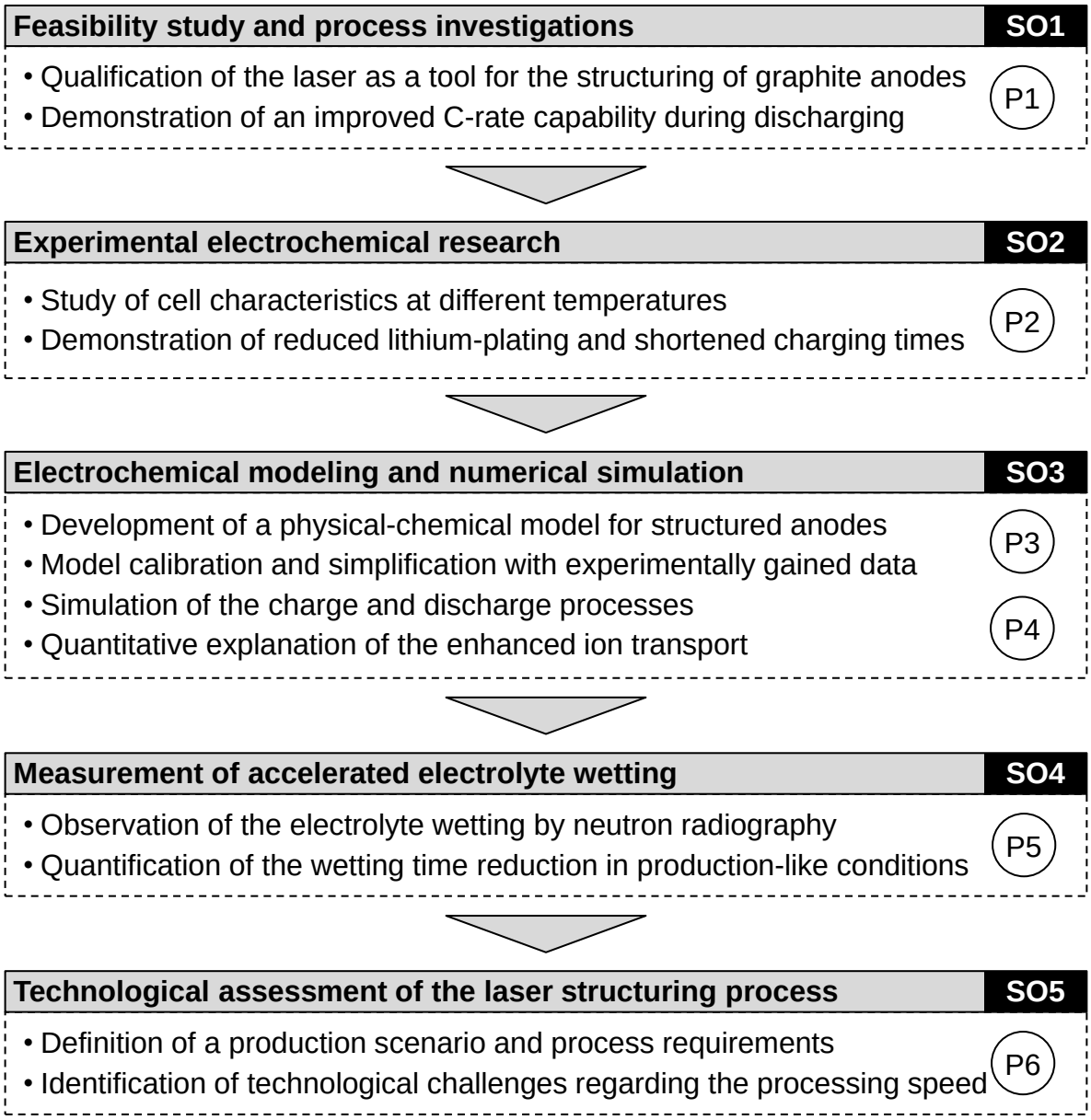

Figure 11: Methodical approach, conceptual classification, and thematic focus of the publications P1 to P6 with regard to the research sub-objectives (SO) defined in section 4.2

Feasibility study

Initially, process investigations for the laser structuring of graphite anodes are required. In this feasibility study, the laser has to be qualified as a suitable tool for the modification of the anode coating and advantageous process regimes for efficient laser structuring have to be identified. The material removal and the structuring pattern must be adjusted in such a way that the cell is still functional and no premature failure, e.g. due to lithium-plating, occurs. Finally, the positive effect of the anode structures on the C-rate capability of lithium-ion cells must be experimentally confirmed, providing the basis for the succeeding investigations. This feasibility study is represented by publication P1 as part of the methodical procedure shown in Figure 11 and addresses SO1, which was introduced in section 4.2.

Experimental electrochemical research

Subsequently, experimental investigations on the electrochemical characteristics of lithium-ion cells with laser-structured anodes compared to conventional cells must be carried out. A study using electrochemical impedance spectroscopy (EIS) (ORAZEM & TRIBOLLET 2017) is to be provided in order to compare the cell-internal resistances (cf. sub-section 2.2.4). Discharge rate tests must be presented with a focus on the performance at low temperatures. Special attention has to be paid to the experimental detection of lithium-plating during fast charging. These investigations are presented in the framework of publication P2 and address SO2.

Electrochemical modeling and numerical simulation

The publications P3 and P4 provide results that contribute to achieving SO3. First, a 3D FEM model of a lithium-ion battery containing laser-structured anodes has to be developed. The model can build on well-established approaches for the modeling of lithium-ion batteries (cf. sub-section 3.4). The geometric dimensioning of the structures implemented in the model should be based on the structures generated for P1. Electrochemical simulations of the discharge processes at different C-rates and a comparison with the experimentally obtained measurement data are to be performed. The results are to be used to acquire knowledge about the lithium concentration throughout the electrodes (e.g. at the end of a discharge process), which may provide a starting point for optimizing the electrode structures in future work. The procedure specified here was implemented as part of publication P3.

The knowledge gained from the 3D model is subsequently to be used to establish a simplified p2D model. Here, the reduction of the tortuosity due to laser structuring

can be taken into account by adjusting the effective transport parameters of the electrode (cf. sub-section 2.2.6). The aim is to reduce the computing times of the calculations allowing for the efficient simulation of a large parameter space. The focus of the subsequent numerical and experimental parameter study should be on the quantification of the discharge capacity improvement by laser structuring of the anode at different area loadings. In addition, the overpotential shares (ohmic, diffusion and activation overpotentials, cf. sub-section 2.2.4) are to be quantified for both the solid and the liquid phase. The development of the model discussed above was presented in publication P4.

Measurement of accelerated electrolyte wetting

In order to demonstrate the accelerated electrolyte uptake of laser-structured electrodes under near-production conditions, large format cells are to be produced. Since the progress of the electrolyte uptake in these cells is difficult to measure in situ, the cells are to be subjected to neutron radiography during wetting. This measuring technique was applied recently for the first time to measure the wetting degree of lithium-ion cells in production and offers the possibility to visualize the electrolyte distribution within the cell (KNOCHE ET AL. 2016). By evaluating the transient wetting degree, conclusions can be drawn about the fluid dynamic processes during electrolyte wetting. This work is described in publication P5 and contributes to the achievement of SO4.

Technological assessment of the laser structuring process

Based on a production scenario for electrodes, requirements for the processing rate of the laser structuring must be determined in publication P6 assessing the laser structuring process technologically and meeting the SO5. The requirements are to be derived from the feasibility study, embodied by P1, as well as from the insights of the electrochemical modeling investigations in P3 and P4. Based on this, specifications for the laser beam source and the laser beam deflection unit can be derived. The considerations aim at indicating the technological development requirements that must be met for the future industrial integration of the laser structuring process.

5 Research Findings

5.1 Chapter overview

Building on the methodical approach presented in section 4.3, this chapter presents the research findings obtained in the context of this work. The results are provided in the form of short recapitulations of the author's publications. After the short summary of each publication, the respective contributions of the authors are briefly reviewed. A classification of the core findings in reference to the state of the art is given in section 5.3.

5.2 Recapitulation of the imbedded publications

5.2.1 P1: Femtosecond laser structuring of graphite anodes for improved lithium-ion batteries: ablation characteristics and process design

In publication P1 "Femtosecond laser structuring of graphite anodes for improved lithium-ion batteries: Ablation characteristics and process design" (HABEDANK ET AL. 2018A), the basic approach of the structure generation in the anode with pulsed laser radiation was described. The structuring was performed using laser pulses with a pulse duration of 400 fs and a maximum pulse energy of 40 µJ. Such short pulses have the quality of inducing virtually no thermal damage to the surrounding material (cf. sub-section 2.3.4). First, investigations on the ablation of the anode coating were carried out. It was found that, even at the highest pulse energy of 40 µJ, several pulses were necessary to achieve significant structure depths in the approx. 50 µm thick coating. Subsequently, the depths of the generated structures were determined for 6, 10, 100, and 1000 laser pulses and correlated to the applied pulse energy per irradiated area. For this experiment, a low pulse repetition rate of 10 Hz was chosen in order to

avoid any optical interaction between the consecutively applied laser pulses and ejected ablation products. It was found that high pulse energies are crucial for an efficient ablation process. Low pulse energies led to a lower structure depth, even if the cumulated energy applied per structure was equalized by a higher number of pulses. In accordance with this trend, a disproportionally high number of additional pulses had to be applied to achieve a targeted structure depth of 40 µm increasing the overall energy input. Furthermore, it was discovered that the pulse repetition rate has a significant influence on the ablation depth. For the purpose of determining that, the structure depths were measured at repetition rates of 10 Hz, 100 Hz, 1 kHz, and 10 kHz. At high repetition rates, significantly lower ablation depths were observed. This was attributed to shielding effects caused by ablated particles and plasma. The studies on the repetition rate are of great importance for the practical process execution. Related considerations are addressed in publication P6 in sub-section 5.2.6. In order to consider workpiece-related impacts on the ablation process, the influence of the PVDF content of the electrode on the ablation depth was investigated. For this purpose, anodes with binder contents of 2, 5, and 8 % were manufactured and laser-structured. A lower binder content led to a significant increase in the process efficiency, as significantly higher structure depths could be achieved for identical process parameters. This trend was explained by the lower cohesive forces acting in the electrode at a reduced binder content and supports existing observations by SLOCOMBE & LI (2000). The authors discovered that in laser machining of granular composite materials containing a component with a low evaporation temperature (the PVDF binder in the case of the graphite electrode), entire particles are removed by thermal and shock-based effects. Accordingly, a complete vaporization of the graphite, which was evaluated e.g. by LENNER ET AL. (2009), HOFFMAN ET AL. (2014), and SINHA (2018), does not occur as even a comparatively low energy input leads to the creation of holes of considerable depth. Consequently, the binder content of the electrode is an important factor in the design of the laser structuring process.

Following the process investigations, three coin cells with structured anodes were manufactured and compared to three conventional cells in a discharge C-rate test. A pattern of hexagonally distributed holes with a distance of 70 µm was selected as the target structure. The depth of the structures was adjusted so that they nearly reached the current collector. The diameter of the structures at the anode surface was approx. 25 µm. The aim of the measurements was to fundamentally demonstrate the improvement of the discharge capacity at high currents by anode structuring, which was expected based on the theoretical considerations on electrode kinetics (cf. section 2.2). At low C-rates from C/10 to 1C, no significant variations in the discharge

capacity occurred, which suggested that no substantial damage to the remaining graphite was caused with regard to its functionality as an anode material (e.g. by thermal influences). This observation was confirmed in a cell aging study published in P3. At higher C-rates from 2C to 5C, an enhancement of up to 20 % in the discharge capacity was measured. This was attributed to lower cell resistances and reduced overpotentials.

Within the framework of P1, for the first time, the positive effects of laser-based anode structuring on the discharge capacity of lithium-ion cells at high C-rates were demonstrated. Process analyses served as a basis and provided insights into the ablation characteristics of porous graphite anodes. In the outlook section of P1, the need for an electrochemical simulation model was derived aiming at a deeper understanding of the effect of the anode structures. Such a model is presented in publication P3 (sub-section 5.2.3) and refined in publication P4 (sub-section 5.2.4). Furthermore, more detailed studies on the electrochemical properties of lithium-ion cells with laser-structured electrodes were proposed. These are addressed in publication P2 (sub-section 5.2.2).

Contributions of the authors

Jan Bernd Habedank, the author of this thesis, developed the idea for the laser structuring of graphite anodes. He planned the experiments and was responsible for the evaluation of the measurement data. Joseph Endres assisted within his master's thesis project in the execution of the experiments. The manuscript was written by Jan Bernd Habedank and edited by Joseph Endres, Patrick Schmitz, Heinz P. Huber, and Michael F. Zaeh. All authors discussed and commented on the findings. Jan Bernd Habedank presented the results in a talk at the International Congress on Lasers and Electro Optics (ICALEO) in Atlanta, GA, USA in 2017.

5.2.2 P2: Enhanced fast charging and reduced lithium-plating by laser-structured anodes for lithium-ion batteries

Publication P2 "Enhanced fast charging and reduced lithium-plating by laser-structured electrodes for lithium-ion batteries" (HABEDANK ET AL. 2019A) summarized experimental investigations which were carried out on the basis of publication P1 in order to provide a deeper insight into the effects of laser structuring of the anodes on electrochemical cell characteristics.

A laser emitting pulses with a duration of 150 ps was used to structure the anodes. Hexagonally arranged holes with a center distance of 100 µm were introduced into the anode. Electrochemical impedance spectroscopy (EIS) measurements were performed at temperatures of -15 °C, 0 °C and 25 °C for cells with laser-structured anodes and conventional reference cells. Three OCV levels (2.7 V, 3.7 V, and 4.2 V) were analyzed (cf. sub-section 2.2.4). The impedance of the lithium-ion cells with laser-structured anodes was lower than that of the reference cells. Building on the results from the publication P1, the current-dependent discharge capacity was investigated in C-rate tests at varying temperatures (-15 °C, 0 °C, and 25 °C). Since all charge and mass transport processes are slower at lower temperatures, the C-rate capability of all cells was generally inferior at lower temperatures, which is expressed in lower achievable discharge capacities. However, the cells with structured anodes showed a significantly improved capacity across the entire temperature spectrum compared to the conventional counterparts. The position and the level of the optimum of the capacity improvement by structuring were different for each temperature. The highest capacity increase at 25 °C was 9 % at a C-rate of 8C. At 0 °C, an increase of 21 % at 4C was observed. At -15 °C, an increase of 27 % at 2C was achieved. This demonstrates that, when evaluating the potential benefits of laser structuring, attention must be paid to the use scenarios of the lithium-ion battery.

The main focus of publication P2 was on the rapid charging characteristics and in particular the occurrence of lithium-plating. As explained in sub-section 2.2.5, lithium-plating denotes the deposition of metallic lithium on the anode and primarily occurs during fast charging of the battery, especially at low ambient temperatures. The detection of lithium-plating was carried out by evaluating the OCV curve after a charging process. If lithium-plating occurred during charging, a characteristic voltage plateau developed which persisted until the plated lithium re-intercalated into the graphite. The occurrence of lithium-plating became even more apparent when the differential voltage was considered, since a clear local minimum of the differential voltage denotes the end of the posterior re-intercalation process. The two temperature

levels of 0 °C and -15 °C were analyzed and different charging C-rates were applied. It was shown that, with conventional cells, significant lithium-plating already occurred during a charging process with 1C, which was expressed in a persistence of the characteristic voltage plateau after charging of approx. 30 minutes. Cells with laser-structured anodes showed hardly any evidence of lithium-plating for the same charging procedure. When charged with 2C, lithium-plating occurred in both cell types. However, the conventional cells were much more severely impacted. At a temperature of -15 °C, the positive effects due to laser structuring were considerably smaller. These measurements showed that at -15 °C, the ion transport processes in the electrolyte and the associated diffusion overpotentials no longer have a defining effect on lithium-plating.

Finally, the effect of structuring on the charging time was investigated when using a common CCCV (constant current constant voltage) charging protocol, where a constant current was applied until the upper cut-off voltage was reached (CC-phase). Then, this voltage was maintained until the current fell below a specified threshold (CV-phase). The charging time for the cells with laser-structured anodes was significantly shorter because the upper cut-off voltage (cf. Figure 3) was reached at a higher SOC, resulting in a shortened CV phase.

Publication P2 shows that laser structuring of the anodes of lithium-ion batteries potentially enables higher charging currents while maintaining the cell safety, especially in critical conditions regarding lithium-plating, e.g. at low temperatures.

Contributions of the authors

Jan Bernd Habedank planned, coordinated, and executed the experiments. Johannes Kriegler supported in the experiment execution within the framework of his master's thesis. Jan Bernd Habedank and Johannes Kriegler analyzed the experimental data and discussed the findings. The manuscript was written by Jan Bernd Habedank and edited by Johannes Kriegler and Michael F. Zaeh. All authors commented on the results.

5.2.3 P3: Increasing the discharge rate capability of lithium-ion cells with laser-structured graphite anodes: modeling and simulation

In publication P3 "Increasing the discharge rate capability of lithium-ion cells with laser-structured graphite anodes: modeling and simulation" (HABEDANK ET AL. 2018B), reference was made to the results of the publication P1. A simulation model was introduced, which numerically depicts the processes within a lithium-ion cell with laser-structured anodes.

The test data of the cells with conventional, unstructured anodes from P1 were first used for the experimental calibration of a p2D model, based on the work of DOYLE ET AL. (1993) and FULLER ET AL. (1994). On this foundation, a homogenized three-dimensional model was presented. The hexagonally arranged hole structures (cf. publication P1, sub-section 5.2.1) allowed for the simplification of the model due to the symmetry of the pattern, which was used as a means to reduce the computational effort. The model takes into account the mass and charge transport in the cell and the lithium transport in radially symmetrical particles (p2D approach, cf. section 3.4). The calibrated parameter set of the p2D model was transferred to the homogenized 3D model and used for the numerical calculation of the transient voltage curve for different C-rates.

The simulation results for the cells with structured anodes showed an excellent agreement with the experimentally acquired data, both in the transient voltage curves and in the measured discharge capacities. In accordance with P1, it was calculated that, at low C-rates, no significant influence of the structures on the discharge capacity is to be expected. This C-rate regime (C-rates at which laser structuring had a negligible impact) was designated as *stage 1*. Furthermore, a C-rate regime was identified in which the enhancements due to the structuring become particularly clear. This regime was subdivided into two stages. In *stage 2* there is an intensifying beneficial effect of the laser structuring up to a maximum, after which, in *stage 3*, the enhancements of the C-rate capability decline. This result was explained by a more detailed consideration of the lithium-ion concentration in both the liquid and the solid phases of the electrodes, allowing for an identification of the limiting mechanisms for the three stages. While ohmic losses and the kinetics of charge transfer dominate in *stage 1*, the overpotentials in the liquid phase gain importance in *stage 2* (cf. sub-section 2.2.4). The positive effect of the structures could thus be elucidated, as significantly lower concentration gradients were calculated in the liquid phase throughout the electrode. These, in turn, cause lower concentration gradients in the

solid phase, which suggests a fundamentally more homogeneous de-lithiation of the anode in the discharge process. In *stage 3*, i.e. at very high C-rates, the positive influences of the anode structures decrease. Here, limiting effects increasingly occur at the cathode, since an almost complete ion depletion of the electrolyte is achieved, which results in high ion transport resistances. In addition, the lithium concentration in the liquid phase of the anode increases significantly, which may lead to a reduction of the ionic conductivity of the electrolyte.

The developed model thus not only contributes to the precise representation of the processes in lithium-ion cells with structured electrodes, but can also serve as a basis for an optimization of the electrode structure. A modification of the cathode structure is explicitly encouraged within the framework of a future optimization process, as is the adaptation of the structuring pattern. Hereby, not only the structure distances can be changed, but also fundamentally different geometries, such as lattice or line structures, can be numerically examined with minor adjustments to the model.

In addition to the published model and the numerical studies, a lifetime study with NMC-graphite cells with structured and conventional anodes was presented within the framework of the publication P3. While the three cells with structured anodes still maintained more than 80 % of their original capacity after 1000 charge and discharge cycles, two of the three conventional cells had already degraded and only provided less than 70 % of their original capacity. Even if this study does not allow for statistically reliable statements about the aging behavior of cells with structured electrodes, the extended service life of the cells with laser-structured anodes was interpreted as an indication that the structuring does not cause long-term damage.

The results published in publication P3 on the modeling of lithium-ion cells with laser-structured anodes were further elaborated on in publication P4. These continuative developments are briefly summarized in the following sub-section 5.2.4.

Contributions of the authors

Jan Bernd Habedank proposed the development of a numerical model to evaluate the effects of anode structuring. He provided the experimental data, such as galvanostatic measurements, SEM images, and information about the structure dimensions. Ludwig Kraft performed the simulation studies and optimized the model parameters. Alexander Rheinfeld developed the homogenized 3D electrode model. Christina Krezdorn supported the model development within a student research project which was supervised by Jan Bernd Habedank. The data was analyzed by Jan Bernd Habedank, Ludwig Kraft, and Alexander Rheinfeld, who also elaborated the

manuscript together. Andreas Jossen and Michael F. Zaeh edited the manuscript. All authors discussed the findings and commented on the results.

5.2.4 P4: Modeling and simulation of pore morphology modifications using laser-structured graphite anodes in lithium-ion batteries

Publication P4 "Modeling and simulation of pore morphology modifications using laser-structured graphite anodes in lithium-ion batteries" (KRAFT ET AL. 2020) followed up on the results from publication P3. The homogenized 3D model from publication P3 was simplified to a p2D model in publication P4 by considering the laser structuring of the anode merely as an adjustment of the effective transport parameters, e.g. the tortuosity and the MacMullin number (cf. sub-section 2.2.6), compared to the conventional anode. The spatial dimensional model reduction led to a significantly lower computational effort, which allowed for a parameter study using batteries with varying electrode characteristics.

A total of eight different cells (four different loadings: L1 = 2.26 mAh/cm^2, L2 = 2.50 mAh/cm^2, L3 = 2.90 mAh/cm^2, and L4 = 3.82 mAh/cm^2, each laser-structured and unstructured) were assessed, both numerically and experimentally. First, the correlation described in section 2.2.7, meaning that a high area capacity of the electrodes leads to a reduction of the specific cell capacity at high discharge C-rates, was confirmed. For all four loadings, an increase in the specific discharge capacity due to laser structuring was determined, both numerically and experimentally. However, the C-rate regimes at which the improvements occurred were different for each loading: For higher loadings, the enhancements due to laser structuring (*stages 2* and *3*, see publication P3) were observed at lower C-rates, while for lower loadings, the enhancements occurred at higher C-rates. These observations are plausible, since electrodes with high loadings generally exhibit kinetic limitations due to overpotentials already at lower C-rates compared to electrodes with low loadings (cf. sub-section 2.2.4). Thus, the beneficial effects of laser structuring already appear at lower C-rates for electrodes with high loadings (high-capacity electrodes), enhancing their otherwise poor C-rate capability. The high degree of congruence between the experimentally determined and the numerically calculated values indicates a high model accuracy.

Subsequently, a purely numerical study was carried out to investigate the influence of different levels of tortuosity reduction, as they may be achieved by different structuring patterns. Starting from a reference value (τ = 8.5), the attainable discharge

capacity improvements for tortuosities from $\tau = 7.5$ to $\tau = 3.5$ were quantified. It was discovered that, with decreasing tortuosity, higher discharge capacity enhancements were achieved while the respective maximum enhancements tended towards higher C-rates.

A numerical analysis was then carried out with the aim of attributing the occurring overpotentials to their physical origin (cf. sub-section 2.2.4). First, a global analysis of the cell consisting of the overpotentials in the anode, the cathode, the separator, and the contact resistances was performed. A more detailed examination of the anode followed. A distinction was made between the ohmic overpotentials in the liquid and the solid phase, the diffusion overpotentials in the liquid and the solid phase, and the activation overpotentials (cf. sub-section 2.2.4). It was found that the improvements in the discharge capacity due to the laser structuring of the anode can be predominantly attributed to a reduction of the diffusion overpotentials in the liquid phase of the anode domain.

Publication P4 was concluded by a numerical investigation of the charging process, i.e. the lithiation of the anode, with a focus on lithium-plating. The potential difference between the solid and the liquid phase was used as a criterion for the occurrence of lithium-plating (cf. eq. 2 - 10, sub-section 2.2.5). It was determined that lithium-plating occurs at different charging C-rates and at different SOCs depending on the anode loading. An improvement of the effective transport parameters in the electrode, as achieved e.g. by laser structuring, showed a clearly positive influence on the lithium-plating sensitivity in the numerical study. Furthermore, it was found out that the structuring allowed for an increase in the charging C-rate, without risking lithium-plating. Depending on the loading, the maximum allowable C-rate was increased from 2.5C to 3.3C (L1), from 2.1C to 2.9C (L2), from 1.2C to 1.7C (L3), and from 0.7C to 0.9C (L4). In practice, this has the effect of proportionally shortening the battery's charging time in the CC charging phase. The numerical calculations thus confirmed the experimental observations of reduced lithium-plating from publication P2.

Contributions of the authors

Ludwig Kraft developed the idea of assessing the performance of lithium-ion cells with laser-structured anodes with different area-specific capacities. He planned and coordinated the acquisition of the data. Jan Bernd Habedank carried out the laser structuring process of the graphite anodes. The data was analyzed and interpreted by Ludwig Kraft and Jan Bernd Habedank. Alexander Frank and Alexander Rheinfeld

supported the overpotential analysis. The manuscript was written by Ludwig Kraft and edited by Jan Bernd Habedank and Andreas Jossen. All authors discussed the data and commented on the results.

5.2.5 P5: Rapid electrolyte wetting of lithium-ion batteries containing laser-structured electrodes: in situ visualization by neutron radiography

For publication P5 "Rapid electrolyte wetting of lithium-ion batteries containing laser-structured electrodes: in situ visualization by neutron radiography" (HABEDANK ET AL. 2019B), the influence of laser structuring on a subsequent production process, the electrolyte filling, was investigated. P5 was based on the concept presented by PFLEGING & PRÖLL (2014) to accelerate the wetting process of the electrodes by introducing capillaries into the electrodes using laser radiation. As discussed in sub-section 2.2.8, the electrolyte filling and the subsequent wetting phase are process steps in battery production which are associated with a high expenditure of time and costs.

For P5, the electrodes of large-format lithium-ion pouch cells (anode dimensions: 104 mm × 76 mm; cathode dimensions: 101 mm × 73 mm; varying thicknesses) were structured using pulsed laser radiation. In contrast to the publications P1 to P4, instead of a pattern of hexagonally arranged holes, grid structures with a rather large line spacing of 1.55 mm were introduced into both the anodes and the cathodes. Three different electrode types were produced: unstructured electrodes with a porosity of 30 %, unstructured electrodes with a porosity of 40 % and laser-structured electrodes with a porosity of 30 %. From these electrodes, multi-layer cell stacks were formed in which the separator was inserted by means of a Z-folding process (cf. sub-section 2.2.8). The pouch cell housing was left open on one side for electrolyte filling.

The electrolyte wetting was then examined by neutron radiography. This measuring method involves directing a neutron beam onto the object under investigation and recording the transmitted radiation with a detector (KNOCHE ET AL. 2016). Since the electrolyte liquid absorbs the neutron radiation more effectively than the other cell materials, the electrolyte-soaked cell areas appear dark on the recorded images. During the wetting process, radiographs were taken at defined time intervals to provide information about the temporal and local electrolyte distribution in the cell. Care was taken to ensure conditions as close as possible to industrial production standards. For this purpose, a fully automated electrolyte filling system was

constructed in which the electrolyte injection and the cell sealing occurred under vacuum. After sealing, the cells were exposed to ambient pressure.

The evaluation of the neutron radiographs revealed that the cells with laser-structured electrodes had wetted approx. twelve times as fast with electrolyte compared to the reference cells with 30 % electrode porosity. Due to the laser structuring, complete wetting was achieved after approx. 15 minutes, whereas the reference cells did not reach complete wetting within the entire observation period of 90 minutes. By linear extrapolation, a wetting time of approx. 180 minutes could be estimated. The cells with 40 % electrode porosity also showed accelerated electrolyte wetting, but approx. 90 minutes were required to achieve complete electrolyte infiltration. Thus, for the first time, it could be demonstrated under realistic production conditions that laser structuring can contribute to shortening the processing time of the cost-intensive wetting process.

Contributions of the authors

Jan Bernd Habedank developed the idea to monitor the wetting process of lithium-ion cells with laser-structured electrodes by neutron radiography. Together with Florian Günter, he was responsible for the experimental design and execution. Jan Bernd Habedank prepared the cell samples and performed the laser structuring. Nicolas Billot supported the practical performance of the experiments at the neutron source. Ralph Gilles and Tobias Neuwirth supervised the experiments at the neutron source. Jan Bernd Habedank and Florian Günter evaluated the measured data. The manuscript was written by Jan Bernd Habedank and edited by Florian Günter, Ralph Gilles, Gunther Reinhart, and Michael F. Zaeh. All authors discussed the data and commented on the results.

5.2.6 P6: Paving the way for industrial ultrafast laser structuring of lithium-ion battery electrodes by increasing the scanning accuracy

In publication P6 "Paving the way for industrial ultrafast laser structuring of lithium-ion battery electrodes by increasing the scanning accuracy" (HABEDANK ET AL. 2020) the laser structuring process of the anode was elucidated with regard to its industrial applicability. The results from the process investigations of publication P1 were used as a basis. The focus of the publication P6 was set on the upscaling of the structuring process with the aim of a conceptual integration into the production of lithium-ion electrodes (cf. sub-section 2.2.8).

For this purpose, a hypothetical roll-to-roll process in electrode production with a defined line speed of 20 m/min and an electrode width of 200 mm was assumed as the production scenario. A pattern of hexagonally arranged holes (cf. P1 to P4) with an equidistant hole spacing of 200 µm was presumed as the preferable target structure, in which one hole was created by six laser pulses (cf. publication P1). With the help of this baseline scenario, the required scanning speed and laser power were calculated. It was assumed that the structuring is carried out in repeated passes of a certain electrode area (cf. sub-sections 2.3.5 and 2.3.6). These estimates led to a high required laser power of 462.4 W, which is, however, attainable by modern pulsed beam sources. The required beam deflection velocities of more than 2000 meters per second pose a far greater challenge, assuming that only one laser beam source and one scanner is available. Such deflection velocities cannot be achieved by conventional galvanometer scanners (cf. sub-section 2.3.6) due to the inertia of the moving components (e.g. mirrors, see Figure 9). Instead, so-called polygon scanners must be used, in which the beam deflection is mostly performed by a polygon mirror wheel, rotating rapidly in one direction (cf. sub-section 2.3.6).

However, challenges arise in the precise positioning of the laser beam, which are due to the electronic control architecture and the communication between the laser beam source and the scanner sub-system. At such high beam deflection velocities, small temporal inaccuracies in the electronic signal transmission (so-called *temporal jitter*) cause significant spatial offsets (*spatial jitter*) in the application of the laser pulses. In conventional controllers, the temporal jitter lies in the range of several nanoseconds and is responsible for spatial inaccuracies of several tens of micrometers when the beam deflection velocities rise. With a pulse repetition rate of 20 MHz, for example, a processing speed of 4000 m/s is required to achieve a pulse spacing of 200 µm. In this example, the temporal jitter of 10 ns leads to an inaccuracy of the pulse application of up to 40 µm, which is in the order of magnitude of the focus diameter of the laser beam. As a result, precise machining is no longer possible at high deflection speeds with state-of-the-art scanner systems.

To alleviate these technical barriers, a novel electronic controller was developed by the industrial research partner ARGES GmbH[5] (Germany), which is capable of reducing the typically occurring inaccuracies in signal transmission by more than four orders of magnitude (from 10 ns to 0.5 ps). An oscilloscope was used to verify the increased accuracy of the signal transmission. These measurements were presented in the context of P6. Once this controller is integrated into a suitable laser-scanner-

[5] Since 2019, the ARGES GmbH is part of Novanta Inc.

system, a sufficiently accurate positioning of the laser beam can be achieved, even at high beam deflection velocities.

Contributions of the authors

Jan Bernd Habedank defined the technological requirements for the laser structuring process. Together with Daniel Schwab, he developed the concept for the roll-to-roll laser processing of the electrodes and derived the requirements for the laser scanner. Daniel Schwab and Bernhard Kiesbauer designed the control architecture for the synchronous control of the network participants (devices) in the overall system and provided the measurement data. The manuscript was written by Jan Bernd Habedank and edited by Michael F. Zaeh. All authors discussed the results. Jan Bernd Habedank presented the results at the International Congress on Lasers and Electro Optics (ICALEO) in Orlando, FL, USA in 2019.

5.3 Discussion of the findings

In this section, the results obtained and leading to the publications P1 to P6 are briefly discussed with a focus on their main contributions to the body of knowledge compared to the most relevant works from the state of the art. As shown in Figure 12, the results can be categorized according to the field of research in which they have led to knowledge gain or have contributed to technical innovations. These research fields are: *battery performance*, *laser processing*, and *battery production*. The publications in the field of battery performance can be further sub-classified according to their scientific approach (experimental study or model-based simulation). As described in the chapter on the state of the art, there are various technological approaches to electrode structuring (cf. section 3.3). This is taken into account in Figure 12 by the use of different background colors for the selected research contributions (grey for laser structuring and white for other approaches). Furthermore, a distinction is made concerning the electrode under investigation (anode or cathode).

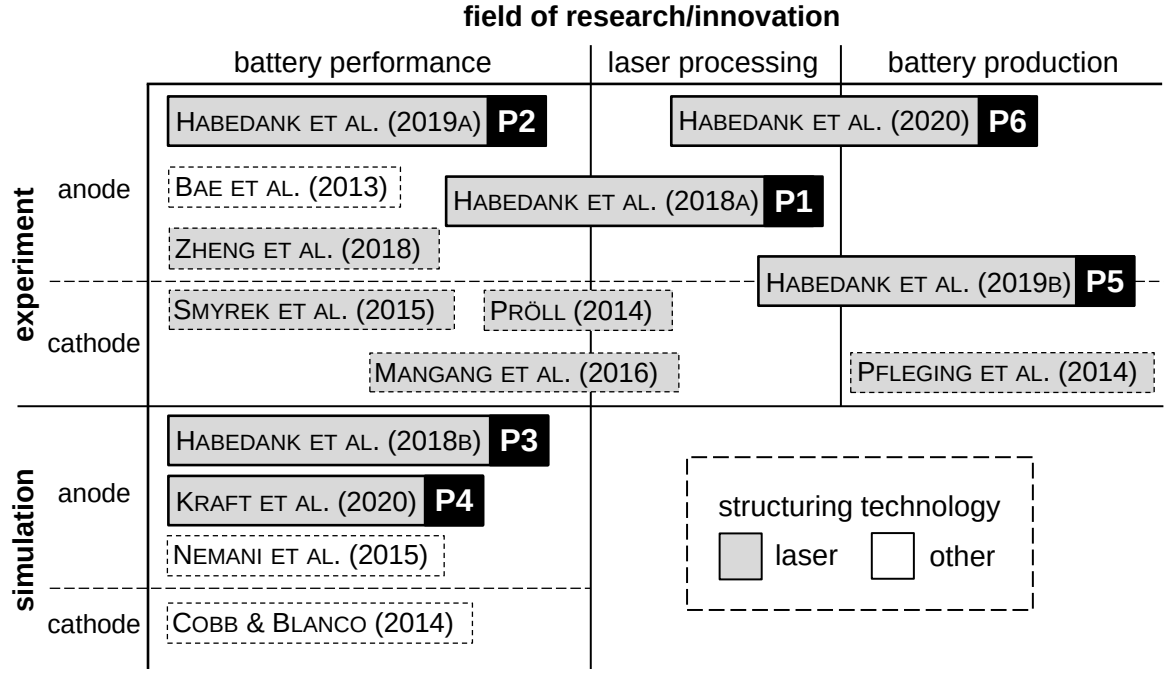

Figure 12: Classification of the publications P1 to P6, arranged according to their respective field of research/innovation and the type of work (experimental or simulation) considering the closest publications from the previous state of the art (cf. chapter 3)

The publication P1 of this dissertation can be mainly assigned to the research field *laser processing*, particularly the laser structuring of graphite anodes. From the explanations in section 3.2, it is apparent that the state of the art lacked studies on the influences of characteristic laser pulse features on the generation of drill structures in graphite anodes. In the works of PRÖLL (2014) and MANGANG ET AL. (2016), comparable approaches were considered, but with a focus on the modification of cathodes. These contain active materials which have entirely different ablation characteristics. Especially the considerations on the influence of the processing strategy and the binder content of the electrode on the ablation efficiency go beyond the state of the art, cf. sub-section 5.2.1. In P1, it was also experimentally proven for the first time that laser structuring of the anode enhances the C-rate capability during discharging, which is why it affects the research field of *battery performance* in Figure 12 as well. Until then, this effect had only been predicted by means of numerical simulations, but without suggesting a specific process for the structure generation and taking its characteristics into account (NEMANI ET AL. 2015). Thus, P1 meets the scientific sub-objective SO1 which was defined in section 4.2.

The publication P2 of this dissertation provided results that experimentally substantiated the benefits of anode laser structuring. Among the most important new

findings were the influence of the structuring on the temperature-dependent C-rate capability during discharge and the experimental proof of reduced lithium-plating during rapid charging of the cells. With regard to electrode structuring, these results go beyond the state of the art in the research field of *battery performance* (cf. Figure 12). The work of BAE ET AL. (2013) also addressed the generation of anode structures with the aim to enhance the battery performance, however by using an extrusion and sintering process. This process is not compatible with the established electrode production process of wet coating (cf. sub-section 2.2.8). In contrast, the structuring process considered in this thesis can be performed on conventionally produced electrodes. Thus, an easier integration into existing production plants can be presumed. The exemplary research of ZHENG ET AL. (2018) addressed the laser structuring of silicon-graphite composite anodes for lithium-ion batteries. A positive effect on the discharge capacity could be demonstrated as well. However, the charging characteristics and, in particular, the occurrence of lithium-plating were not considered by ZHENG ET AL. (2018). Due to the high volume expansion and the associated degradation during cycling, the use of high silicon shares in silicon-graphite anodes still poses a great challenge for the market dissemination of such cells. Thus, the scientific sub-objective SO2 is fulfilled, in which an investigation of various cell characteristics was required (cf. section 4.2).

The publications P3 and P4 contributed to a more profound understanding of the charge transport mechanisms in lithium-ion batteries with laser-structured electrodes. By means of numerical simulations, these publications provided new insights into the field of *battery performance*. Thematically related works are, for example, NEMANI ET AL. (2015) and COBB & BLANCO (2014) who also modelled electrochemical processes in lithium-ion cells with structured electrodes. P3 differs from the existing work in that a real structuring geometry (a laser borehole) was modelled three-dimensionally, using symmetry effects to limit the computational effort. Additionally, the established FEM model was, for the first time, calibrated using experimentally obtained measurement data. The simplification of the model setup presented in P4, taking into account the ion transport parameters affected by the structuring, combined with the presented overpotential analysis, also goes beyond the state of the art. Thus, the requirements formulated in the sub-objective SO3 in section 4.2 were met.

Based on laboratory-scale tests (individual electrode sheets) by PFLEGING ET AL. (2014), P5 demonstrated that laser structuring of electrodes can accelerate the electrolyte wetting process in cell production. The findings can thus be attributed to the broader research field *battery production*, cf. Figure 12. The investigations in P5

were carried out using pouch cells containing a multi-layer electrode stack that was assembled in a partially automated production process. By creating production-like conditions during electrolyte filling (automatic dosing, evacuation of the process chamber, and automatic sealing of the cells) and applying neutron radiography as measuring method, the wetting progress in cells with laser-structured electrodes could, for the first time, be determined in situ. The sub-objective SO4 (section 4.2) regarding the characterization of the impact of laser structuring on the electrolyte wetting was thereby fulfilled.

The contents of publication P6 can be allocated to the interface between the research fields of *laser processing* and *battery production* (cf. Figure 12). For the first time, a production scenario was specified in which, based on boundary conditions in battery production, requirements were set for a potential anode laser structuring process. Since these requirements were highly demanding for the beam deflection mechanism, a novel controller with an innovative architecture tailored for extreme beam deflection speeds was developed. This was a contribution to the development of advanced laser scanners that are suitable for high-precision and fast processing of large surfaces. Such laser scanners are by no means exclusively deployable for the structuring of electrodes but can also open up new potentials for other applications. Sub-objective SO5 regarding the identification of required technological advances for the industrial application of the structuring process (cf. section 4.2) was thus accomplished.

6 Summary and Outlook

Lithium-ion batteries are used as electrical energy storage systems in countless applications worldwide. Originating from the consumer electronics sector, they today serve, for example, as energy storage for various power tools and electric vehicles. But also the buffer storage of electrical energy generated by solar or wind power is increasingly performed by lithium-ion battery systems. Within a lithium-ion cell, lithium ions migrate back and forth from cathode to anode during charging and discharging while an electrical current passes through an external circuit (cf. sub-section 2.2.2). The conventional porous electrode structure limits the mass and charge transport during battery operation, which leads to the occurrence of overpotentials of different physical origins (cf. sub-section 2.2.4). A capacity loss during discharging, a limitation of the maximum current during charging, and lithium-plating (cf. sub-section 2.2.5) are among the undesired consequences.

The underlying idea of the research performed within this dissertation is to use pulsed laser radiation to locally remove active material from the anode so that additional lithium-ion transport paths are formed (cf. Figure 1). These are intended to promote the charge carrier flow though the electrode and reduce the internal cell resistance. Compared to competing processes, laser machining technology is highly developed and allows for large electrode areas to be processed in a short time. Future developments in laser scanning technology, e.g. advancements in the field of high-speed polygon scanners, will further enhance the applicability of laser technology for the precise and rapid structuring of large surfaces (cf. sub-section 2.3.6). In principle, however, alternative structuring methods (cf. section 3.3) also exhibit inherent potentials and may enable the effective structuring of electrodes in the future.

The explorative research approach followed in this thesis includes laser process investigations (cf. sub-section 5.2.1), electrochemical measurements and cell tests (cf. sub-section 5.2.2), the modeling of the electrochemical system with subsequent numerical simulations (cf. sub-sections 5.2.3 and 5.2.4), as well as analyses regarding production technology aspects (cf. sub-sections 5.2.5 and 5.2.6). An enhancement of

the state of the art could be attained in all these research fields (cf. section 5.3). In particular, the numerical depiction of the cell-internal processes is emphasized, as it contributes to a better comprehension of the influence of the electrode pore morphology on the cell operation. The knowledge acquired in this field can thus quickly be transferred to electrodes produced and structured by other techniques. In summary, the benefits of laser structuring of anodes identified in this work are

- an increase in the C-rate capability during discharge, which is expressed in an enhanced usable capacity Q at high discharge currents in a wide temperature range,
- reduced lithium-plating during fast charging of the battery under demanding conditions (e.g. low temperatures), potentially leading to reduced aging of the battery,
- shorter charging times by reducing the overpotentials and thus later attainment of the upper cut-off voltage in a CCCV charging process,
- and a significant reduction of the wetting time with the electrolyte fluid in cell production.

All the battery performance enhancements were explained and substantiated by electrochemical models, which were used to quantify the reduction of the emerging concentration gradients during cycling as well as the occurring overpotentials (cf. sub-section 2.2.4).

Citing the publications P2, P3, and P4 of this dissertation, CHEN ET AL. (2020) published a study on the fast charging of lithium-ion cells with laser-structured graphite anodes. An electrochemical model based on the ones developed in the publications P3 and P4 of this thesis was also presented. Several of the results obtained in the framework of this dissertation were confirmed by CHEN ET AL. (2020), e.g. the enhanced C-rate capability due to laser structuring and the reduced lithium-plating in fast charging procedures. The authors furthermore demonstrated that the decreased lithium-plating due to laser structuring significantly slowed down the cell aging. These confirmatory results by CHEN ET AL. (2020) underline the appeal of the approach pursued in this dissertation to enhance the performance characteristics of lithium-ion batteries.

Several aspects regarding the industrial laser structuring of electrodes have not been examined to date and remain to be addressed in future work, e.g. the hardware integration into existing production plants including the necessary laser safety as well as particle extraction and filtering systems. Especially the removal of potential

ablation residues from the electrode surface (cf. Figure 8) could be a challenge for large-area laser structuring, since the ablated material volume is of a considerable magnitude. A detailed evaluation regarding investment and process costs is also required. However, since the production costs of lithium-ion batteries are largely dominated by the costs of the electrode materials (especially the cathode) (WOOD ET AL. 2015), it can be assumed that the additional process step of laser structuring will only lead to a cost increase of a few percentage points (PFLEGING 2018). On the other hand, potential time and cost savings in the electrolyte filling process (cf. P5; sub-section 5.2.5) and improvements regarding the battery performance (cf. P1, P2, P3, and P4; sub-sections 5.2.1 to 5.2.4) will most likely justify the additional expenditure for electrode structuring.

All considerations within this work refer to conventional lithium-ion batteries, in which the electrodes are essentially planar. The lithium transport therefore follows a preferential direction (i.e. along the x-axis in Figure 4). In principle, however, other forms of electrodes are also conceivable, such as interdigitated cylindrical cathodes and anodes (Figure 13 a), interdigitated plate arrays of cathodes and anodes (Figure 13 b), rod arrays of cylindrical cathodes which are coated with an ionically conductive electrolyte and imbedded into an anode matrix (Figure 13 c), and sponge-like architectures, in which the cathode material is surrounded by a thin layer of electrolyte and the remaining volume is filled by the anode material (Figure 13 d) (LONG ET AL. 2004).

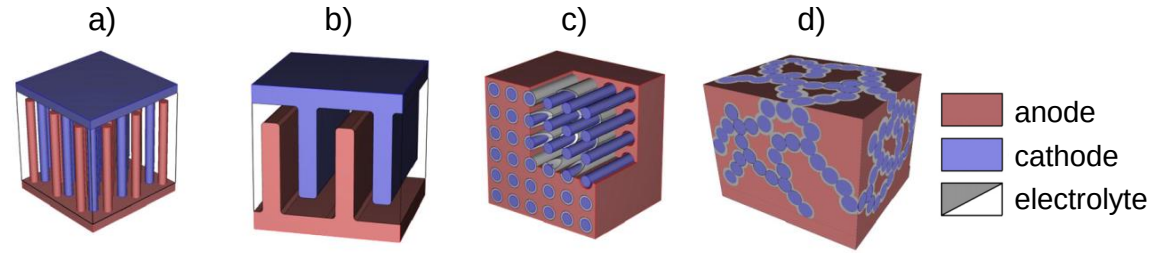

Figure 13: Exemplary 3D battery concepts; a) interdigitated cylindrical electrodes, b) interdigitated plate arrays of electrodes, c) rod arrays of cathodes in an anode matrix, d) sponge-like architectures with anode material surrounding the cathode (LONG ET AL. 2004, ZADIN ET AL. 2011)

In these electrode arrangements, the lithium transport no longer occurs one-dimensionally, but two- or three-dimensionally between interlocking electrodes. The concept of such 3D electrodes has been discussed in numerous publications. An overview of the manufacturing processes used to produce different types of 3D electrodes was given by OUDENHOVEN ET AL. (2011), ARTHUR ET AL. (2011) and

ROBERTS ET AL. (2011). Four years later, a review paper on the latest developments in the field of 3D micro batteries was published by FERRARI ET AL. (2015), again with a particular focus on the processes used to manufacture the complex interlocking microstructures. Considered processes are, for example, laser printing (KIM ET AL. 2007), electro deposition (OLTEAN ET AL. 2011), and the growth of nanowires (XIA ET AL. 2014). At present, all these processes are in a very early development stage, and a practical application of such batteries is currently considered merely in the field of MEMS. A scale-up of the production processes yielding battery sizes, as they are of interest in electromobility, is currently not considered realistic for cost and productivity reasons (FERRARI ET AL. 2015). Nevertheless, these approaches offer enormous potential to mitigate the conflict of objectives between a high energy density and a high power density of future lithium-ion batteries.

In addition to these further research activities regarding new battery concepts, the laser structuring process for graphite anodes, which was in the focus of this thesis, should be implemented in a pilot-scale battery production facility. Thereby, the effects of anode structuring on lithium-ion cells of an industrially established cell format or even entire energy storage systems can be explored. This step will lead to the next milestone towards the industrial application of the laser structuring of anodes for functionally enhanced lithium-ion batteries.

7 References

ANDRE ET AL. 2015

Andre, D.; Kim, S.-J.; Lamp, P.; Lux, S. F.; Maglia, F.; Paschos, O.; Stiaszny, B.: Future generations of cathode materials: an automotive industry perspective. J. Mater. Chem. A 3 (2015) 13, pp. 6709–6732.

ANTARTIS ET AL. 2015

Antartis, D.; Dillon, S.; Chasiotis, I.: Effect of porosity on electrochemical and mechanical properties of composite Li-ion anodes. Journal of Composite Materials 49 (2015) 15, pp. 1849–1862.

ARTHUR ET AL. 2011

Arthur, T. S.; Bates, D. J.; Cirigliano, N.; Johnson, D. C.; Malati, P.; Mosby, J. M.; Perre, E.; Rawls, M. T.;Prieto, Amy L.; Dunn, Bruce: Three-dimensional electrodes and battery architectures. MRS Bulletin 36 (2011) 7, pp. 523–531.

ATKINS & PAULA 2010

Atkins, P. W.; Paula, J.: Physical chemistry. 9th edn. New York: W.H. Freeman 2010. ISBN: 978-1429218122.

BAE ET AL. 2012

Property Right US 2014/0186700 A1 (Jul. 3, 2014). Palo Alto Research Center Incorporated. Pr.: 13/727,960, 2012. Bae, C.-J.; Shrader, E. J.; Cobb, C. L.: Advanced, high power and energy battery electrode manufactured by co-extrusion printing.

BAE ET AL. 2013

Bae, C.-J.; Erdonmez, C. K.; Halloran, J. W.; Chiang, Y.-M.: Design of battery electrodes with dual-scale porosity to minimize tortuosity and maximize performance. Advanced materials 25 (2013) 9, pp. 1254–1258.

Wherever an issue number is not indicated, it does not exist or is not known to the author of this thesis.

BALBUENA & WANG 2004

Balbuena, P. B.; Wang, Y.: Lithium-Ion Batteries: Published by Imperial College Press and distributed by World Scientific Publishing Co. 2004. ISBN: 978-1-86094-362-1.

BATTRION 2020

Battrion: Battrion AG. <https://www.battrion.com/> - visited on Aug. 8, 2020.

BILLAUD ET AL. 2016

Billaud, J.; Bouville, F.; Magrini, T.; Villevieille, C.; Studart, A. R.: Magnetically aligned graphite electrodes for high-rate performance Li-ion batteries. Nature Energy 1 (2016) 8, pp. 1–6.

BITSCH ET AL. 2016

Bitsch, B.; Gallasch, T.; Schroeder, M.; Börner, M.; Winter, M.; Willenbacher, N.: Capillary suspensions as beneficial formulation concept for high energy density Li-ion battery electrodes. Journal of Power Sources 328 (2016), pp. 114–123.

BLOMGREN 2017

Blomgren, G. E.: The Development and Future of Lithium Ion Batteries. Journal of The Electrochemical Society 164 (2017) 1, pp. A5019–A5025.

BRUGGEMAN 1935

Bruggeman, D. A.: Berechnung verschiedener physikalischer Konstanten von heterogenen Substanzen. I. Dielektrizitätskonstanten und Leitfähigkeiten der Mischkörper aus isotropen Substanzen. Annalen der Physik 416 (1935) 7, pp. 636–664.

BURNS ET AL. 2015

Burns, J. C.; Stevens, D. A.; Dahn, J. R.: In-Situ Detection of Lithium Plating Using High Precision Coulometry. Journal of The Electrochemical Society 162 (2015) 6, pp. A959–A964.

CHEN ET AL. 2020

Chen, K.-H.; Namkoong, M. J.; Goel, V.; Yang, C.; Kazemiabnavi, S.; Mortuza, S. M.; Kazyak, E.; Mazumder, J.;Thornton, K.; Sakamoto, J.; Dasgupta, N. P.: Efficient fast-charging of lithium-ion batteries enabled by laser-patterned three-dimensional graphite anode architectures. Journal of Power Sources 471 (2020), p. 228475.

CHICHKOV ET AL. 1996
Chichkov, B. N.; Momma, C.; Nolte, S.; Alvensleben, F.; Tünnermann, A.: Femtosecond, picosecond and nanosecond laser ablation of solids. Applied Physics A 63 (1996) 2, pp. 109–115.

COBB & BLANCO 2014
Cobb, C. L.; Blanco, M.: Modeling mass and density distribution effects on the performance of co-extruded electrodes for high energy density lithium-ion batteries. Journal of Power Sources 249 (2014), pp. 357–366.

COBB & SOLBERG 2017
Cobb, C. L.; Solberg, S. E.: Communication – Analysis of Thick Co-Extruded Cathodes for Higher-Energy-and-Power Lithium-Ion Batteries. Journal of The Electrochemical Society 164 (2017) 7, pp. A1339–A1341.

COMSOL INC. 2020
COMSOL INC.: COMSOL Multiphysics®. <https://www.comsol.com/> - visited on Aug. 11, 2020.

DANG ET AL. 2020
Dang, D.; Wang, Y.; Gao, S.; Cheng, Y.-T.: Freeze-dried low-tortuous graphite electrodes with enhanced capacity utilization and rate capability. Carbon 159 (2020), pp. 133–139.

DANIEL & BESENHARD 2011
Daniel, C.; Besenhard, J. O.: Handbook of Battery Materials. Weinheim, Germany: Wiley-VCH Verlag GmbH & Co. KGaA 2011.
ISBN: 9783527637188.

DE LOOR 2013
De Loor, R.: Polygon Scanner System for Ultra Short Pulsed Laser Micro-Machining Applications. Physics Procedia 41 (2013), pp. 544–551.

DEMIR ET AL. 2013
Demir, A. G.; Maressa, P.; Previtali, B.: Fibre Laser Texturing for Surface Functionalization. Physics Procedia 41 (2013), pp. 759–768.

DESBIENS & MASSON 2007
Desbiens, J.-P.; Masson, P.: ArF excimer laser micromachining of Pyrex, SiC and PZT for rapid prototyping of MEMS components. Sensors and Actuators A: Physical 136 (2007) 2, pp. 554–563.

DOYLE ET AL. 1993

Doyle, M.; Fuller, T. F.; Newman, J.: Modeling of Galvanostatic Charge and Discharge of the Lithium/Polymer/Insertion Cell. Journal of The Electrochemical Society 140 (1993) 6, pp. 1526–1533.

DU ET AL. 2012

Du, K.; Brüning, S.; Gillner, A.: High-power picosecond laser with 400W average power for large scale applications. In: Bachmann et al. (Ed.): Laser-based Micro- and Nanopackaging and Assembly. Proc. of SPIE Vol. 8244 (2012), pp. 82440P1–82440P10.

DUBESHTER ET AL. 2014

DuBeshter, T.; Sinha, P. K.; Sakars, A.; Fly, G. W.; Jorne, J.: Measurement of Tortuosity and Porosity of Porous Battery Electrodes. Journal of The Electrochemical Society 161 (2014) 4, pp. A599–A605.

DUBEY & YADAVA 2008

Dubey, A. K.; Yadava, V.: Laser beam machining – A review. International Journal of Machine Tools and Manufacture 48 (2008) 6, pp. 609–628.

EBNER ET AL. 2014

Ebner, M.; Chung, D.-W.; García, R. E.; Wood, V.: Tortuosity Anisotropy in Lithium-Ion Battery Electrodes. Advanced Energy Materials 4 (2014) 5, pp. 1–6.

EBNER & WOOD 2014

Ebner, M.; Wood, V.: Tool for Tortuosity Estimation in Lithium Ion Battery Porous Electrodes. Journal of The Electrochemical Society 162 (2014) 2, pp. A3064–A3070.

EICHLER & EICHLER 2015

Eichler, H. J.; Eichler, J.: Laser. Berlin, Heidelberg, Germany: Springer Vieweg 2015. ISBN: 978-3-642-41437-4.

ERDEY-GRÚZ & VOLMER 1930

Erdey-Grúz, T.; Volmer, M.: Zur Theorie der Wasserstoff Überspannung. Zeitschrift für Physikalische Chemie 150A (1930) 1, pp. 203–213.

FERRARI ET AL. 2015

Ferrari, S.; Loveridge, M.; Beattie, S. D.; Jahn, M.; Dashwood, R. J.; Bhagat, R.: Latest advances in the manufacturing of 3D rechargeable lithium microbatteries. Journal of Power Sources 286 (2015), pp. 25–46.

FULLER ET AL. 1994

Fuller, T. F.; Doyle, M.; Newman, J.: Simulation and Optimization of the Dual Lithium Ion Insertion Cell. Journal of The Electrochemical Society 141 (1994) 1, pp. 1–9.

GALLAGHER ET AL. 2015

Gallagher, K. G.; Trask, S. E.; Bauer, C.; Woehrle, T.; Lux, S. F.; Tschech, M.; Lamp, P.; Polzin, B. J.;Ha, Seungbum; Long, Brandon; Wu, Qingliu; Lu, Wenquan; Dees, Dennis W.; Jansen, Andrew N.: Optimizing Areal Capacities through Understanding the Limitations of Lithium-Ion Electrodes. Journal of The Electrochemical Society 163 (2015) 2, pp. A138–A149.

GAUTAM & PANDEY 2018

Gautam, G. D.; Pandey, A. K.: Pulsed Nd:YAG laser beam drilling: A review. Optics & Laser Technology 100 (2018), pp. 183–215.

GRAF 2013

Graf, C.: Kathodenmaterialien für Lithium-Ionen-Batterien. In: Korthauer, R. (Ed.): Handbuch Lithium-Ionen-Batterien. Berlin, Heidelberg, Germany: Springer Vieweg 2013, pp. 31–44. ISBN: 978-3-642-30652-5.

GULBINSKA 2014

Gulbinska, Malgorzata K. (Ed.): Lithium-ion battery materials and engineering. Current topics and problems from the manufacturing perspective. London: Springer 2014. ISBN: 978-1-4471-6547-7.

GÜNTER ET AL. 2018

Günter, F. J.; Habedank, J. B.; Schreiner, D.; Neuwirth, T.; Gilles, R.; Reinhart, G.: Introduction to Electrochemical Impedance Spectroscopy as a Measurement Method for the Wetting Degree of Lithium-Ion Cells. Journal of The Electrochemical Society 165 (2018) 14, pp. A3249–A3256.

GÜNTHER ET AL. 2016

Günther, T.; Billot, N.; Schuster, J.; Schnell, J.; Spingler, F. B.; Gasteiger, H. A.: The Manufacturing of Electrodes: Key Process for the Future Success of Lithium-Ion Batteries. Advanced Materials Research 1140 (2016), pp. 304–311.

HABEDANK ET AL. 2018a

Habedank, J. B.; Endres, J.; Schmitz, P.; Zaeh, M. F.; Huber, H. P.: Femtosecond laser structuring of graphite anodes for improved lithium-ion batteries: Ablation characteristics and process design. Journal of Laser Applications 30 (2018) 3, pp. 32205/1–32205/7.

HABEDANK ET AL. 2018b

Habedank, J. B.; Kraft, L.; Rheinfeld, A.; Krezdorn, C.; Jossen, A.; Zaeh, M. F.: Increasing the Discharge Rate Capability of Lithium-Ion Cells with Laser-Structured Graphite Anodes: Modeling and Simulation. Journal of The Electrochemical Society 165 (2018) 7, pp. A1563–A1573.

HABEDANK ET AL. 2019a

Habedank, J. B.; Kriegler, J.; Zaeh, M. F.: Enhanced Fast Charging and Reduced Lithium-Plating by Laser-Structured Anodes for Lithium-Ion Batteries. Journal of The Electrochemical Society 166 (2019) 16, pp. A3940–A3949.

HABEDANK ET AL. 2019b

Habedank, J. B.; Günter, F. J.; Billot, N.; Gilles, R.; Neuwirth, T.; Reinhart, G.; Zaeh, M. F.: Rapid electrolyte wetting of lithium-ion batteries containing laser structured electrodes: in situ visualization by neutron radiography. The International Journal of Advanced Manufacturing Technology 102 (2019) 9–12, pp. 2769–2778.

HABEDANK ET AL. 2020

Habedank, J. B.; Schwab, D.; Kiesbauer, B.; Zaeh, M. F.: Paving the way for industrial ultrafast laser structuring of lithium-ion battery electrodes by increasing the scanning accuracy. Journal of Laser Applications 32 (2020) 2, pp. 22053/1–22053/6.

HARRIS & LU 2013

Harris, S. J.; Lu, P.: Effects of Inhomogeneities – Nanoscale to Mesoscale – on the Durability of Li-Ion Batteries. The Journal of Physical Chemistry C 117 (2013) 13, pp. 6481–6492.

HARTNIG & SCHMIDT 2018

Hartnig, C.; Schmidt, M.: Electrolytes and conducting salts. In: Korthauer, R. (Ed.): Lithium-Ion Batteries: Basics and Applications. Berlin, Heidelberg, Germany: Springer 2018, pp. 59–74. ISBN: 978-3-662-53069-6.

HASELRIEDER ET AL. 2013
Haselrieder, W.; Ivanov, S.; Christen, D. K.; Bockholt, H.; Kwade, A.: Impact of the Calendering Process on the Interfacial Structure and the Related Electrochemical Performance of Secondary Lithium-Ion Batteries. ECS Transactions 50 (2013) 26, pp. 59–70.

HOFFMAN ET AL. 2014
Hoffman, J.; Chrzanowska, J.; Kucharski, S.; Moscicki, T.; Mihailescu, I. N.; Ristoscu, C.; Szymanski, Z.: The effect of laser wavelength on the ablation rate of carbon. Applied Physics A 117 (2014) 1, pp. 395–400.

HÜGEL & GRAF 2009
Hügel, H.; Graf, T.: Laser in der Fertigung. Strahlquellen, Systeme, Fertigungsverfahren. 2nd edn. Wiesbaden: Vieweg+Teubner/GWV Fachverlage GmbH Wiesbaden 2009. ISBN: 978-3-8351-0005-3.

HUGGINS 2009
Huggins, R.: Advanced batteries. Materials science aspects. 1st edn. Berlin, Germany: Springer 2009. ISBN: 978-0-387-76424-5.

JAEGGI ET AL. 2012
Jaeggi, B.; Neuenschwander, B.; Hunziker, U.; Zuercher, J.; Meier, T.; Zimmermann, M.; Selbmann, K. H.; Hennig, G.: Ultra-high-precision surface structuring by synchronizing a galvo scanner with an ultra-short-pulsed laser system in MOPA arrangement. In: Henning, G. et al. (Ed.): Laser Applications in Microelectronic and Optoelectronic Manufacturing (LAMOM) XVII. Proc. of SPIE 8243 (2012), pp. 82430/1–82430/11.

JAEGGI ET AL. 2013
Jaeggi, B.; Neuenschwander, B.; Meier, T.; Zimmermann, M.; Hennig, G.: High Precision Surface Structuring with Ultra-Short Laser Pulses and Synchronized Mechanical Axes. Physics Procedia 41 (2013) 0, pp. 319–326.

JARA ET AL. 2019
Jara, A. D.; Betemariam, A.; Woldetinsae, G.; Kim, J. Y.: Purification, application and current market trend of natural graphite: A review. International Journal of Mining Science and Technology 29 (2019) 5, pp. 671–689.

JOSSEN & WEYDANZ 2019
Jossen, A.; Weydanz, W.: Moderne Akkumulatoren richtig einsetzen. 2nd edn. Göttingen: Cuvillier 2019. ISBN: 3736999453.

KIM ET AL. 2007
Kim, H.; Auyeung, R. C.Y.; Piqué, A.: Laser-printed thick-film electrodes for solid-state rechargeable Li-ion microbatteries. Journal of Power Sources 165 (2007) 1, pp. 413–419.

KIM ET AL. 2014
Kim, H.; Sutto, T. E.; Piqué, A.: Laser materials processing for micropower source applications: a review. Journal of Photonics for Energy 4 (2014) 1, pp. 040992/1–040992/20.

KIM ET AL. 2018
Kim, Y.; Drews, A.; Chandrasekaran, R.; Miller, T.; Sakamoto, J.: Improving Li-ion battery charge rate acceptance through highly ordered hierarchical electrode design. Ionics 24 (2018) 10, pp. 2935–2943.

KITADA ET AL. 2016
Kitada, K.; Murayama, H.; Fukuda, K.; Arai, H.; Uchimoto, Y.; Ogumi, Z.; Matsubara, E.: Factors determining the packing-limitation of active materials in the composite electrode of lithium-ion batteries. Journal of Power Sources 301 (2016), pp. 11–17.

KNOCHE ET AL. 2016
Knoche, T.; Zinth, V.; Schulz, M.; Schnell, J.; Gilles, R.; Reinhart, G.: In situ visualization of the electrolyte solvent filling process by neutron radiography. Journal of Power Sources 331 (2016), pp. 267–276.

KNOCHE & REINHART 2015
Knoche, T.; Reinhart, G.: Electrolyte Filling of Large-Scale Lithium-Ion Batteries. Main Influences and Challenges for Production Technology. Applied Mechanics and Materials 794 (2015), pp. 11–18.

KOHLER ET AL. 2013
Kohler, R.; Proell, J.; Bruns, M.; Ulrich, S.; Seifert, H. J.; Pfleging, W.: Conical surface structures on model thin-film electrodes and tape-cast electrode materials for lithium-ion batteries. Applied Physics A 112 (2013) 1, pp. 77–85.

KOHLER 2014
Kohler, R.: Lasergestützte Strukturierung und Gefügemodifikation der Elektrodenmaterialien Lithiumcobaltoxid und Zinnoxid für Lithium-Ionen-Batterien. Diss. Karlsruher Inst. für Technologie. Aachen, Germany: Shaker 2014. ISBN: 978-3-8440-2804-1.

KORTHAUER 2018
Korthauer, R. (Ed.): Lithium-Ion Batteries: Basics and Applications. Berlin, Heidelberg, Germany: Springer 2018. ISBN: 978-3-662-53069-6.

KRAFT ET AL. 2020
Kraft, L.; Habedank, J. B.; Frank, A.; Rheinfeld, A.; Jossen, A.: Modeling and Simulation of Pore Morphology Modifications using Laser-Structured Graphite Anodes in Lithium-Ion Batteries. Journal of The Electrochemical Society 167 (2020) 1, p. 13506.

KRONTHALER ET AL. 2012
Kronthaler, M. R.; Schloegl, F.; Kurfer, J.; Wiedenmann, R.; Zaeh, M. F.; Reinhart, G.: Laser Cutting in the Production of Lithium Ion Cells. Physics Procedia 39 (2012), pp. 213–224.

KURZWEIL & DIETLMEIER 2015
Kurzweil, P.; Dietlmeier, O. K.: Elektrochemische Speicher. Wiesbaden, Germany: Springer Fachmedien 2015. ISBN: 978-3-658-10899-1.

KWADE ET AL. 2018
Kwade, A.; Haselrieder, W.; Leithoff, R.; Modlinger, A.; Dietrich, F.; Droeder, K.: Current status and challenges for automotive battery production technologies. Nature Energy 3 (2018) 4, pp. 290–300.

LANDESFEIND ET AL. 2016
Landesfeind, J.; Hattendorff, J.; Ehrl, A.; Wall, W. A.; Gasteiger, H. A.: Tortuosity Determination of Battery Electrodes and Separators by Impedance Spectroscopy. Journal of The Electrochemical Society 163 (2016) 7, pp. A1373–A1387.

LANDESFEIND 2018
Landesfeind, J.: Determination of Physical and Electrochemical Parameters for Lithium-Ion Batteries and Advanced Electrochemical Impedance Analysis. Diss. Technische Universität München. 2018. <https://mediatum.ub.tum.de/1437142> - visited on Aug. 11, 2020.

LANDESFEIND ET AL. 2018
Landesfeind, J.; Eldiven, A.; Gasteiger, H. A.: Influence of the Binder on Lithium Ion Battery Electrode Tortuosity and Performance. Journal of The Electrochemical Society 165 (2018) 5, pp. A1122–A1128.

LEE ET AL. 2013
Lee, D.; Patwa, R.; Herfurth, H.; Mazumder, J.: High speed remote laser cutting of electrodes for lithium-ion batteries: Anode. Journal of Power Sources 240 (2013), pp. 368–380.

LEE ET AL. 2018
Lee, B.-S.; Wu, Z.; Petrova, V.; Xing, X.; Lim, H.-D.; Liu, H.; Liu, P.: Analysis of Rate-Limiting Factors in Thick Electrodes for Electric Vehicle Applications. Journal of The Electrochemical Society 165 (2018) 3, pp. A525–A533.

LEGRAND ET AL. 2014
Legrand, N.; Knosp, B.; Desprez, P.; Lapicque, F.; Raël, S.: Physical characterization of the charging process of a Li-ion battery and prediction of Li plating by electrochemical modelling. Journal of Power Sources 245 (2014), pp. 208–216.

LEITZ ET AL. 2011
Leitz, K.-H.; Redlingshöfer, B.; Reg, Y.; Otto, A.; Schmidt, M.: Metal Ablation with Short and Ultrashort Laser Pulses. Physics Procedia 12 (2011), pp. 230–238.

LENNER ET AL. 2009
Lenner, M.; Kaplan, A.; Huchon, C.; Palmer, R. E.: Ultrafast laser ablation of graphite. Physical Review B 79 (2009) 18, pp. 184105/1–184105/11.

LEUTHNER 2018
Leuthner, S.: Lithium-ion battery overview. In: Korthauer, R. (Ed.): Lithium-Ion Batteries: Basics and Applications. Berlin, Heidelberg, Germany: Springer 2018, pp. 13–19. ISBN: 978-3-662-53069-6.

LI ET AL. 2014
Li, Z.; Huang, J.; Yann Liaw, B.; Metzler, V.; Zhang, J.: A review of lithium deposition in lithium-ion and lithium metal secondary batteries. Journal of Power Sources 254 (2014), pp. 168–182.

LIU ET AL. 1997
Liu, X.; Du, D.; Mourou, G.: Laser ablation and micromachining with ultrashort laser pulses. IEEE Journal of Quantum Electronics 33 (1997) 10, pp. 1706–1716.

LIU ET AL. 2010
Liu, J.; Kunz, M.; Chen, K.; Tamura, N.; Richardson, T. J.: Visualization of Charge Distribution in a Lithium Battery Electrode. The Journal of Physical Chemistry Letters 1 (2010) 14, pp. 2120–2123.

LIU ET AL. 2016
Liu, Q.; Du, C.; Shen, B.; Zuo, P.; Cheng, X.; Ma, Y.; Yin, G.; Gao, Y.: Understanding undesirable anode lithium plating issues in lithium-ion batteries. RSC Advances 6 (2016) 91, pp. 88683–88700.

LONG ET AL. 2004
Long, J. W.; Dunn, B.; Rolison, D. R.; White, H. S.: Three-Dimensional Battery Architectures. Chemical Reviews 104 (2004) 10, pp. 4463–4492.

LÜDERS ET AL. 2017
Lüders, C. von; Zinth, V.; Erhard, S. V.; Osswald, P. J.; Hofmann, M.; Gilles, R.; Jossen, A.: Lithium plating in lithium-ion batteries investigated by voltage relaxation and in situ neutron diffraction. Journal of Power Sources 342 (2017), pp. 17–23.

LUETKE ET AL. 2011
Luetke, M.; Franke, V.; Techel, A.; Himmer, T.; Klotzbach, U.; Wetzig, A.; Beyer, E.: A Comparative Study on Cutting Electrodes for Batteries with Lasers. Physics Procedia 12 (2011), pp. 286–291.

MACMULLIN & MUCCINI 1956
MacMullin, R. B.; Muccini, G. A.: Characteristics of porous beds and structures. AIChE Journal 2 (1956) 3, pp. 393–403.

MANEV ET AL. 1995
Manev, V.; Naidenov, I.; Puresheva, B.; Pistoia, G.: Effect of electrode porosity on the performance of natural Brazilian graphite electrodes. Journal of Power Sources 57 (1995) 1-2, pp. 133–136.

MANGANG ET AL. 2014
Mangang, M.; Pröll, J.; Tarde, C.; Seifert, H. J.; Pfleging, W.: Ultrafast laser microstructuring of $LiFePO_4$ cathode material. In: Klotzbach, U. et al. (Ed.): Laser-based Micro- and Nanoprocessing VIII. Proc. of SPIE Vol. 8968 (2014), pp. 89680M-1–89680M-9.

MANGANG ET AL. 2015

Mangang, M.; Gotcu-Freis, P.; Seifert, H. J.; Pfleging, W.: Electrochemical and kinetic studies of ultrafast laser structured $LiFePO_4$ electrodes. In: Klotzbach, U. et al. (Ed.): SPIE LASE. Proc. of SPIE Vol. 9351 (2015), pp. 93510K-1–93510K-12.

MANGANG ET AL. 2016

Mangang, M.; Seifert, H. J.; Pfleging, W.: Influence of laser pulse duration on the electrochemical performance of laser structured $LiFePO_4$ composite electrodes. Journal of Power Sources 304 (2016), pp. 24–32.

MARKS ET AL. 2011

Marks, T.; Trussler, S.; Smith, A. J.; Xiong, D.; Dahn, J. R.: A Guide to Li-Ion Coin-Cell Electrode Making for Academic Researchers. Journal of The Electrochemical Society 158 (2011) 1, pp. A51–A57.

MAUREL ET AL. 2019

Maurel, A.; Grugeon, S.; Fleutot, B.; Courty, M.; Prashantha, K.; Tortajada, H.; Armand, M.; Panier, S.; Dupont, Loïc: Three-Dimensional Printing of a $LiFePO_4$/Graphite Battery Cell via Fused Deposition Modeling. Scientific reports 9 (2019) 1, pp. 18031/1–18031/14.

MEIJER ET AL. 2002

Meijer, J.; Du, K.; Gillner, A.; Hoffmann, D.; Kovalenko, V. S.; Masuzawa, T.; Ostendorf, A.; Poprawe, R.; Schulz, W.: Laser Machining by short and ultrashort pulses, state of the art and new opportunities in the age of the photons. CIRP Annals 51 (2002) 2, pp. 531–550.

MISHRA & YADAVA 2015

Mishra, S.; Yadava, V.: Laser Beam MicroMachining (LBMM) – A review. Optics and Lasers in Engineering 73 (2015), pp. 89–122.

MOTTAY ET AL. 2016

Mottay, E.; Liu, X.; Zhang, H.; Mazur, E.; Sanatinia, R.; Pfleging, W.: Industrial applications of ultrafast laser processing. MRS Bulletin 41 (2016) 12, pp. 984–992.

NEMANI ET AL. 2015

Nemani, V. P.; Harris, S. J.; Smith, K. C.: Design of Bi-Tortuous, Anisotropic Graphite Anodes for Fast Ion-Transport in Li-Ion Batteries. Journal of The Electrochemical Society 162 (2015) 8, pp. A1415–A1423.

NEUENSCHWANDER ET AL. 2014

Neuenschwander, B.; Jaeggi, B.; Schmid, M.; Hennig, G.: Surface Structuring with Ultra-short Laser Pulses: Basics, Limitations and Needs for High Throughput. Physics Procedia 56 (2014) 0, pp. 1047–1058.

NEWMAN & THOMAS-ALYEA 2012

Newman, J.; Thomas-Alyea, K. E.: Electrochemical Systems. 3rd edn. Hoboken, New Jersey: John Wiley & Sons, Inc. 2012. ISBN: 978-0-471-47756-3.

NOVÁK ET AL. 1997

Novák, P.; Scheifele, W.; Winter, M.; Haas, O.: Graphite electrodes with tailored porosity for rechargeable ion-transfer batteries. Journal of Power Sources 68 (1997) 2, pp. 267–270.

NYMAN ET AL. 2010

Nyman, A.; Zavalis, T. G.; Elger, R.; Behm, M.; Lindbergh, G.: Analysis of the Polarization in a Li-Ion Battery Cell by Numerical Simulations. Journal of The Electrochemical Society 157 (2010) 11, pp. A1236–A1246.

OLTEAN ET AL. 2011

Oltean, G.; Nyholm, L.; Edström, K.: Galvanostatic electrodeposition of aluminium nano-rods for Li-ion three-dimensional micro-battery current collectors. Electrochimica Acta 56 (2011) 9, pp. 3203–3208.

ORAZEM & TRIBOLLET 2017

Orazem, M. E.; Tribollet, B.: Electrochemical impedance spectroscopy. 2nd edn. Hoboken, New Jersey: John Wiley & Sons Inc. 2017. ISBN: 978-1-118-52739-9.

OUDENHOVEN ET AL. 2011

Oudenhoven, J. F.; Baggetto, L.; Notten, P. H.: All-Solid-State Lithium-Ion Microbatteries: A Review of Various Three-Dimensional Concepts. Advanced Energy Materials 1 (2011) 1, pp. 10–33.

PARC 2020

PARC, a. X.: PARC, a Xerox Company. <https://www.parc.com/> - visited on Aug. 11, 2020.

PARK ET AL. 2019

Park, J.; Hyeon, S.; Jeong, S.; Kim, H.-J.: Performance enhancement of Li-ion battery by laser structuring of thick electrode with low porosity. Journal of Industrial and Engineering Chemistry 70 (2019), pp. 178–185.

PATWA ET AL. 2013

Patwa, R.; Herfurth, H.; Mueller, G.; Bui, K.: Laser drilling up to 15,000 holes/sec in silicon wafer for PV solar cells. In: Reutzel, E.W. (Ed.): Laser Material Processing for Solar Energy Devices II. Proc. of SPIE Vol. 8826 (2013), pp. 88260G1–88260G7.

PETTINGER ET AL. 2018

Pettinger, K.-H.; Kampker, A.; Hohenthanner, C.-R.; Deutskens, C.; Heimes, H.; Vom Hemdt, A.: Lithium-ion cell and battery production processes. In: Korthauer, R. (Ed.): Lithium-Ion Batteries: Basics and Applications. Berlin, Heidelberg, Germany: Springer 2018, pp. 211–226. ISBN: 978-3-662-53069-6.

PETZL & DANZER 2014

Petzl, M.; Danzer, M. A.: Nondestructive detection, characterization, and quantification of lithium plating in commercial lithium-ion batteries. Journal of Power Sources 254 (2014), pp. 80–87.

PFLEGING ET AL. 2014

Pfleging, W.; Kohler, R.; Pröll, J.: Laser generated microstructures in tape cast electrodes for rapid electrolyte wetting: new technical approach for cost efficient battery manufacturing. In: Koltzbach, U. et al. (Ed.): Laser-based Micro- and Nanoprocessing VIII. Proc. of SPIE Vol. 8968 (2014), pp. 89680B-1–89680B-8.

PFLEGING ET AL. 2016

Pfleging, W.; Zheng, Y.; Mangang, M.; Bruns, M.; Smyrek, P.: Laser processes and analytics for high power 3D battery materials. In: Heisterkamp, A. et al. (Ed.): Frontiers in Ultrafast Optics: Biomedical, Scientific, and Industrial Applications XVI. Proc. of SPIE Vol. 9740 (2016), pp. 974013-1–974013-9.

PFLEGING 2018

Pfleging, W.: A review of laser electrode processing for development and manufacturing of lithium-ion batteries. Nanophotonics 7 (2018) 3, pp. 1–25.

PFLEGING & GOTCU 2019

Pfleging, W.; Gotcu, P.: Femtosecond Laser Processing of Thick Film Cathodes and Its Impact on Lithium-Ion Diffusion Kinetics. Applied Sciences 9 (2019) 3588, pp. 1–10.

PFLEGING & PRÖLL 2014

Pfleging, W.; Pröll, J.: A new approach for rapid electrolyte wetting in tape cast electrodes for lithium-ion batteries. J. Mater. Chem. A 2 (2014) 36, pp. 14918–14926.

POPRAWE 2005

Poprawe, R.: Lasertechnik für die Fertigung. Grundlagen, Perspektiven und Beispiele für den innovativen Ingenieur. Berlin, Germany: Springer 2005. ISBN: 978-3-540-26435-4.

PRÖLL ET AL. 2013

Pröll, J.; Weidler, P. G.; Kohler, R.; Mangang, A.; Heißler, S.; Seifert, H. J.; Pfleging, W.: Comparative studies of laser annealing technique and furnace annealing by X-ray diffraction and Raman analysis of lithium manganese oxide thin films for lithium-ion batteries. Thin Solid Films 531 (2013) 0, pp. 160–171.

PRÖLL 2014

Pröll, J.: Lasergestützte Modifikation von Lithiummanganoxid und Lithiumnickelmangankobaltoxid. Diss. Karlsruher Institut für Technologie. Aachen, Germany: Shaker 2014. ISBN: 978-3-8440-3047-1.

PRÖLL ET AL. 2014

Pröll, J.; Kim, H.; Piqué, A.; Seifert, H. J.; Pfleging, W.: Laser-printing and femtosecond-laser structuring of $LiMn_2O_4$ composite cathodes for Li-ion microbatteries. Journal of Power Sources 255 (2014), pp. 116–124.

PRÖLL ET AL. 2015

Pröll, J.; Kim, H.; Mangang, M.; Seifert, H. J.; Piqué, A.; Pfleging, W.: Fs-laser microstructuring of laser-printed $LiMn_2O_4$ electrodes for manufacturing of 3D microbatteries. In: Klotzbach, U. et al. (Ed.): Laser-based Micro- and Nanoprocessing VIII. Proc. of SPIE Vol. 8968 (2015), pp. 896805-1–896805-6.

RAKEBRANDT ET AL. 2017

Rakebrandt, J.-H.; Smyrek, P.; Zheng, Y.; Seifert, H. J.; Pfleging, W.: Laser processing of thick $Li(NiMnCo)O_2$ electrodes for lithium-ion batteries. In: Klotzbach, U. et al. (Ed.): Laser-based Micro- and Nanoprocessing XI. Proc. of SPIE Vol 10092 (2017), pp. 100920M1–100920M7.

REINHART ET AL. 2013

Reinhart, G.; Zeilinger, T.; Kurfer, J.; Westermeier, M.; Thiemann, C.; Glonegger, M.; Wunderer, M.; Tammer, C.;Schweier, M.; Heinz, M.: Research and Demonstration Center for the Production of Large-Area Lithium-Ion Cells. In: Schuh, G. et al. (Ed.): Future Trends in Production Engineering. Berlin, Heidelberg, Germany: Springer 2013, pp. 3–12. ISBN: 978-3-642-24490-2.

ROBERTS ET AL. 2011

Roberts, M.; Johns, P.; Owen, J.; Brandell, D.; Edstrom, K.; El Enany, G.; Guery, C.; Golodnitsky, D.;Lacey, Matt; Lecoeur, Cyrille; Mazor, Hadar; Peled, Emanuel; Perre, Emilie; Shaijumon, Manikoth M.; Simon, Patrice; Taberna, Pierre-Louis: 3D lithium ion batteries – from fundamentals to fabrication. Journal of Materials Chemistry 21 (2011) 27, pp. 9876–9890.

ROOTS ANALYSIS 2019

Roots Analysis: Automotive Lithium-ion Battery Market: Global Opportunity and Trend Analysis, 2019-2030. <https://www.rootsanalysis.com/reports/view_document/automotive-lithium-ion-battery-market-global-opportunity-and-trend-analysis-2019-2030/273.html> - visited on Jan. 19, 2020.

SAUTER 2012

Property Right DE102012215921A1 (Mar. 13, 2014). Robert Bosch GmbH, 70469, Stuttgart, DE Pr.: H01M4/70, 2012. Sauter, U.: Battery e.g. lithium ion battery has porous layered electrode which is provided with several recesses at opposite side of electrode metal sheet.

SCHMIEDER 2016

Schmieder, B.: Laser cutting of graphite anodes for automotive lithium-ion secondary batteries: investigations in the edge geometry and heat affected zone. In: Bachmann, F. G. et al. (Ed.): Laser-based Micro- and Nanopackaging and Assembly VI. Proc. of SPIE Vol. 8244 (2016), pp. 82440R-1–82440R-7.

SCHRÖDER ET AL. 2017

Schröder, R.; Aydemir, M.; Seliger, G.: Comparatively Assessing different Shapes of Lithium-ion Battery Cells. Procedia Manufacturing 8 (2017), pp. 104–111.

SHENG ET AL. 2014

Sheng, Y.; Fell, C. R.; Son, Y. K.; Metz, B. M.; Jiang, J.; Church, B. C.: Effect of Calendering on Electrode Wettability in Lithium-Ion Batteries. Frontiers in Energy Research 2 (2014) 56, pp. 1–8.

SHIM & STRIEBEL 2003

Shim, J.; Striebel, K. A.: Effect of electrode density on cycle performance and irreversible capacity loss for natural graphite anode in lithium-ion batteries. Journal of Power Sources 119-121 (2003), pp. 934–937.

SINGH ET AL. 2015

Singh, M.; Kaiser, J.; Hahn, H.: Thick Electrodes for High Energy Lithium Ion Batteries. Journal of The Electrochemical Society 162 (2015) 7, pp. A1196–A1201.

SINHA 2018

Sinha, S.: Nanosecond laser ablation of graphite: A thermal model based simulation. Journal of Laser Applications 30 (2018) 1, 012008-1–012008-7.

SLOCOMBE & LI 2000

Slocombe, A.; Li, L.: Laser ablation machining of metal/polymer composite materials. Applied Surface Science 154-155 (2000), pp. 617–621.

SMYREK ET AL. 2015

Smyrek, P.; Pröll, J.; Rakebrandt, J.-H.; Seifert, H. J.; Pfleging, W.: Manufacturing of advanced Li(NiMnCo)O_2 electrodes for lithium-ion batteries. In: Klotzbach, U. et al. (Ed.): SPIE LASE. Proc. of SPIE Vol. 9351 (2015), pp. 93511D1–93511D8.

SMYREK ET AL. 2016

Smyrek, P.; Kim, H.; Zheng, Y.; Seifert, H. J.; Piqué, A.; Pfleging, W.: Laser printing and femtosecond laser structuring of electrode materials for the manufacturing of 3D lithium-ion micro-batteries. In: Gu, B. et al. (Ed.): SPIE LASE. Proc. of SPIE Vol. 9738 (2016), pp. 973806-1–972806-5.

SON ET AL. 2013

Son, B.; Ryou, M.-H.; Choi, J.; Kim, S.-H.; Ko, J. M.; Lee, Y. M.: Effect of cathode/anode area ratio on electrochemical performance of lithium-ion batteries. Journal of Power Sources 243 (2013) 0, pp. 641–647.

SONY 1991

SONY: Keywords to understanding Sony Energy Devices. <https://web.archive.org/web/20160304224245/http://www.sonyenergy-devices.co.jp/en/keyword/> - visited on Jan. 19, 2020.

STRIEBEL ET AL. 2004

Striebel, K.A.; Sierra, A.; Shim, J.; Wang, C.-W.; Sastry, A.M.: The effect of compression on natural graphite anode performance and matrix conductivity. Journal of Power Sources 134 (2004) 2, pp. 241–251.

THE ROYAL SWEDISH ACADEMY OF SCIENCES 2019

The Royal Swedish Academy of Sciences: Press release: The Nobel Prize in Chemistry 2019. <https://www.nobelprize.org/prizes/chemistry/2019/press-release/> - visited on Jan. 19, 2020.

THORAT ET AL. 2009

Thorat, I. V.; Stephenson, D. E.; Zacharias, N. A.; Zaghib, K.; Harb, J. N.; Wheeler, D. R.: Quantifying tortuosity in porous Li-ion battery materials. Journal of Power Sources 188 (2009) 2, pp. 592–600.

TRASK ET AL. 2014

Trask, S. E.; Li, Y.; Kubal, J. J.; Bettge, M.; Polzin, B. J.; Zhu, Y.; Jansen, A. N.; Abraham, D. P.: From coin cells to 400 mAh pouch cells: Enhancing performance of high-capacity lithium-ion cells via modifications in electrode constitution and fabrication. Journal of Power Sources 259 (2014), pp. 233–244.

UHLMANN ET AL. 2015

Uhlmann, C.; Illig, J.; Ender, M.; Schuster, R.; Ivers-Tiffée, E.: In situ detection of lithium metal plating on graphite in experimental cells. Journal of Power Sources 279 (2015), pp. 428–438.

VAN DER STRAETEN ET AL. 2018

van der Straeten, K.; Nottrodt, O.; Zuric, M.; Olowinsky, A.; Abels, P.; Gillner, A.: Polygon scanning system for high-power, high-speed microstructuring. Procedia CIRP 74 (2018), pp. 491–494.

VUORILEHTO 2018

Vuorilehto, K.: Materials and function. In: Korthauer, R. (Ed.): Lithium-Ion Batteries: Basics and Applications. Berlin, Heidelberg, Germany: Springer 2018, pp. 21–28. ISBN: 978-3-662-53069-6.

WALDMANN ET AL. 2015

Waldmann, T.; Kasper, M.; Wohlfahrt-Mehrens, M.: Optimization of Charging Strategy by Prevention of Lithium Deposition on Anodes in high-energy Lithium-ion Batteries – Electrochemical Experiments. Electrochimica Acta 178 (2015), pp. 525–532.

WATANABE ET AL. 2019

Watanabe, T.; Tsuda, T.; Ando, N.; Nakamura, S.; Hayashi, N.; Soma, N.; Gunji, T.; Ohsaka, T.; Matsumoto, Futoshi: An improved pre-lithiation of graphite anodes using through-holed cathode and anode electrodes in a laminated lithium ion battery. Electrochimica Acta 324 (2019) 134848, pp. 1–15.

WEYDANZ ET AL. 2018

Weydanz, W. J.; Reisenweber, H.; Gottschalk, A.; Schulz, M.; Knoche, T.; Reinhart, G.; Masuch, M.; Franke, J.; Gilles, R.: Visualization of electrolyte filling process and influence of vacuum during filling for hard case prismatic lithium ion cells by neutron imaging to optimize the production process. Journal of Power Sources 380 (2018), pp. 126–134.

WOEHRLE 2018

Woehrle, T.: Lithium-ion cell. In: Korthauer, R. (Ed.): Lithium-Ion Batteries: Basics and Applications. Berlin, Heidelberg, Germany: Springer 2018, pp. 101–111. ISBN: 978-3-662-53069-6.

WOOD ET AL. 2015

Wood, D. L.; Li, J.; Daniel, C.: Prospects for reducing the processing cost of lithium ion batteries. Journal of Power Sources 275 (2015), pp. 234–242.

WURM ET AL. 2018

Wurm, C.; Oettinger, O.; Wittkaemper, S.; Zauter, R.; Vuorilehto, K.: Anode materials for lithium-ion batteries. In: Korthauer, R. (Ed.): Lithium-Ion Batteries: Basics and Applications. Berlin, Heidelberg, Germany: Springer 2018, pp. 43–58. ISBN: 978-3-662-53069-6.

XIA ET AL. 2014

Xia, H.; Xiong, W.; Lim, C. K.; Yao, Q.; Wang, Y.; Xie, J.: Hierarchical TiO_2-B nanowire@α-Fe_2O_3 nanothorn core-branch arrays as superior electrodes for lithium-ion microbatteries. Nano Research 7 (2014) 12, pp. 1797–1808.

YANG ET AL. 2019

Yang, C.; Chen, K.-H.; Wang, Y.; Dasgupta, N.; Mazumder, J.: Improving Fast Charging Performance of Lithium-Ion Batteries Through Laser Patterning. ICALEO Conference Proceedings, Paper # BSEC 203. <http://icaleo.conferencespot.org/69130-lia-1.4567898/t006-1.4568717/f0056-1.4568730/0339-0501-000249-1.4568737/0339-0501-000249-1.4568738> - visited on Jan. 3, 2020 (2019).

YOSHIO ET AL. 2009

Yoshio, M.; Brodd, R. J.; Kozawa, A.: Lithium-Ion Batteries. New York, NY: Springer 2009. ISBN: 978-0-387-34444-7.

ZADIN ET AL. 2011

Zadin, V.; Brandell, D.; Kasemägi, H.; Aabloo, A.; Thomas, J. O.: Finite element modelling of ion transport in the electrolyte of a 3D-microbattery. Solid State Ionics 192 (2011) 1, pp. 279–283.

ZHANG 2020

Zhang, S. S.: Challenges and Strategies for Fast Charge of Li-Ion Batteries. ChemElectroChem 10.1002/celc.202000650 (2020), accepted article.

ZHENG ET AL. 2012a

Zheng, H.; Li, J.; Song, X.; Liu, G.; Battaglia, V. S.: A comprehensive understanding of electrode thickness effects on the electrochemical performances of Li-ion battery cathodes. Electrochimica Acta 71 (2012), pp. 258–265.

ZHENG ET AL. 2012b

Zheng, H.; Tan, L.; Liu, G.; Song, X.; Battaglia, V. S.: Calendering effects on the physical and electrochemical properties of $Li[Ni_{1/3}Mn_{1/3}Co_{1/3}]O_2$ cathode. Journal of Power Sources 208 (2012), pp. 52–57.

ZHENG ET AL. 2017a

Zheng, Y.; Smyrek, P.; Rakebrandt, J.-H.; Kübel, C.; Seifert, H. J.; Pfleging, W.: Fabrication and characterization of silicon-based 3D electrodes for high-energy lithium-ion batteries. In: Klotzbach, U. et al. (Ed.): Laser-based Micro- and Nanoprocessing XI, SPIE LASE. Proc. of SPIE Vol. 10092 (2017), pp. 100920L-1–100920L-8.

ZHENG ET AL. 2017b

Zheng, Y.; Smyrek, P.; Rakebrandt, J.-H.; Seifert, H. J.; Pfleging, W.; Kubel, C.: Silicon-based 3D electrodes for high power lithium-ion battery. IEEE International Conference on Manipulation, Manufacturing and Measurement on the Nanoscale (3M-NANO). Shanghai, China (2017), pp. 61–64.

ZHENG ET AL. 2018

Zheng, Y.; Seifert, H. J.; Smyrek, P.; Pfleging, W.: Development of Laser Structured Silicon-based Anodes for Lithium-ion Batteries. IEEE International Conference on Manipulation, Manufacturing and Measurement on the Nanoscale (3M-NANO). Hangzhou, China (2018), pp. 6–9.

ZHENG ET AL. 2019a

Zheng, Y.; Seifert, H. J.; Shi, H.; Zhang, Y.; Kübel, C.; Pfleging, W.: 3D silicon/graphite composite electrodes for high-energy lithium-ion batteries. Electrochimica Acta 317 (2019), pp. 502–508.

ZHENG ET AL. 2019b

Zheng, Y.; Pfäffl, L.; Seifert, H. J.; Pfleging, W.: Lithium Distribution in Structured Graphite Anodes Investigated by Laser-Induced Breakdown Spectroscopy. Applied Sciences 9 (2019) (20):4218, pp. 1–9.

ZHU ET AL. 2019

Zhu, P.; Seifert, H. J.; Pfleging, W.: The Ultrafast Laser Ablation of $Li(Ni_{0.6}Mn_{0.2}Co_{0.2})O_2$ Electrodes with High Mass Loading. Applied Sciences 9 (2019) (19):4067, pp. 1–15.

ZINTH ET AL. 2014

Zinth, V.; Lüders, C. von; Hofmann, M.; Hattendorff, J.; Buchberger, I.; Erhard, S.; Rebelo-Kornmeier, J.; Jossen, A.; Gilles, Ralph: Lithium plating in lithium-ion batteries at sub-ambient temperatures investigated by in situ neutron diffraction. Journal of Power Sources 271 (2014), pp. 152–159.

ZINTH ET AL. 2017

Zinth, V.; Lüders, C. von; Wilhelm, J.; Erhard, S. V.; Hofmann, M.; Seidlmayer, S.; Rebelo-Kornmeier, J.; Gan, W.;Jossen, Andreas; Gilles, Ralph: Inhomogeneity and relaxation phenomena in the graphite anode of a lithium-ion battery probed by in situ neutron diffraction. Journal of Power Sources 361 (2017), pp. 54–60.

References

Appendix

A1 List of supervised student research projects

In the course of this work, several student research projects were supervised by the author of this thesis in terms of content and organization. The supervision was performed at the Institute for Machine Tools and Industrial Management (*iwb*) of the Technical University of Munich. Some of the jointly gained insights have been incorporated into this dissertation and the publications described in section 5.2. The author of this dissertation would like to sincerely thank the students for the valuable discussions and the ideas that haven been developed during the collaboration.

Name of Student	**Title and date of student research project**
Scholz, R.	German (original): Machbarkeitsuntersuchung zur Strukturierung von Elektrodenmaterialien für Lithium-Ionen-Batterien English: Feasibility study for the structuring of electrode materials for lithium-ion batteries, submitted in August 2015
Mayer, S.	German (original): Elektrochemische Charakterisierung laserstrukturierter Kathoden für Lithium-Ionen-Batterien English: Electrochemical characterization of laser-structured cathodes for lithium ion batteries, submitted in March 2016
Mangold, M.	German (original): Prozessuntersuchungen zur Strukturierung von Aktivmaterialien für Lithium-Ionen-Batterien mit gepulster Laserstrahlung English: Process investigations on the structuring of active materials for lithium-ion batteries with pulsed laser radiation, submitted in March 2016

Paz, M.	English (original): Ablation Behaviour Investigation of Active Materials for Lithium-Ion Batteries with Pulsed Laser Radiation, submitted in September 2016
Piprek, T.	German (original): Untersuchungen zu den Eigenschaften von Lithium-Ionen-Zellen mit strukturierten Aktivmaterialbeschichtungen der Elektroden English: Studies on the properties of lithium-ion cells with structured active material coatings of the electrodes, submitted in October 2016
Krezdorn, C.	German (original): Lithium-Ionen-Zellen mit strukturierten Elektroden: Modellbildung und Simulation mittels COMSOL Multiphysics English: Lithium-ion cells with structured electrodes: modeling and simulation using COMSOL Multiphysics, submitted in November 2016
Endres, J.	German (original): Laserstrukturierung graphitischer Anoden zur Erhöhung der Entladetiefe eines Lithium-Ionen-Akkumulators English: Laser structuring of graphite anodes to increase the depth of discharge of a lithium-ion accumulator, submitted in April 2017
Ellsäßer, M.	German (original): Wirtschaftlichkeitsbewertung der Laserstrukturierung von Elektroden in Lithium-Ionen-Batterien English: Economic evaluation of laser structuring of electrodes for lithium-ion batteries, submitted in July 2017
Maciuga, T.	German (original): Laserstrukturierung von Graphit-Anoden zur Verbesserung der Schnellladefähigkeit von Lithium-Ionen-Akkumulatoren English: Laser structuring of graphite anodes to improve the fast charging capability of lithium-ion batteries, submitted in November 2017
Kriegler, J.	German (original): Laserstrukturierung von Graphit-Anoden zur Erhöhung der Schnellladefähigkeit von Lithium-Ionen-Batterien English: Laser structuring of graphite anodes to increase the fast charging capability of lithium-ion batteries, submitted in August 2018

A2 Publications of the author

The author's publications, which were elaborated in the course of writing this dissertation, are listed below in chronological order.

Publications imbedded into this dissertation

- **Habedank, J. B.**; Endres, J.; Schmitz, P.; Huber, H. P.; Zaeh, M. F.: Femtosecond laser structuring of graphite anodes for improved lithium-ion batteries: Ablation characteristics and process design. Journal of Laser Applications 30 (2018) 3, pp. 32205/1–32205/7. **Publication P1 of this dissertation.**

- **Habedank, J. B.**; Kraft, L. Rheinfeld, A. J. G.; Krezdorn, C.; Jossen, A.; Zaeh, M. F.: Increasing the Discharge Rate Capability of Lithium-Ion Cells with Laser-Structured Graphite Anodes: Modeling and Simulation. Journal of The Electrochemical Society, 165 (2018) 7, pp. A1563–A1573. **Publication P3 of this dissertation.**

- **Habedank, J. B.**; Guenter, F. J.; Billot, N.; Gilles, R.; Neuwirth, T.; Reinhart, G.; Zaeh, M. F.: Rapid electrolyte wetting of lithium-ion batteries containing laser-structured electrodes: in situ visualization by neutron radiography. The International Journal of Advanced Manufacturing Technology 102 (2019) 9–12, pp. 2769–2778. **Publication P5 of this dissertation.**

- **Habedank, J. B.**; Kriegler, J.; Zaeh, M. F.: Enhanced Fast Charging and Reduced Lithium-Plating by Laser-Structured Anodes for Lithium-Ion Batteries. Journal of The Electrochemical Society 166 (2019) 16, pp. A3940–A3949. **Publication P2 of this dissertation.**

- Kraft, L.; **Habedank, J. B.**; Frank, A.; Rheinfeld, A.; Jossen, A.: Modeling and Simulation of Pore Morphology Modifications using Laser-Structured Graphite Anodes in Lithium-Ion Batteries. Journal of The Electrochemical Society 167 (2020) 1, p. 13506. **Publication P4 of this dissertation.**

- **Habedank, J. B.**; Schwab, D. Kiesbauer, B. Zaeh, M. F.: Paving the Way for Industrial Ultrafast Laser Structuring of Lithium-Ion Battery Electrodes by Increasing the Scanning Accuracy. Journal of Laser Applications 32 (2020) 2, pp. 22053/1–22053/6. **Publication P6 of this dissertation.**

Other publications

- **Habedank, J. B.**: Produktionsforschung für Lithium-Ionen-Batterien – Innovationen für den Energiespeicher der Zukunft, translated title: Production research for lithium-ion batteries – innovations for the energy storage of the future. Automobiltechnologie in Bayern + e-Car (2015), pp. 36–38.

- **Habedank, J. B.**: Laserstrukturierung in der Batterieproduktion, translated title: Laser structuring in battery production. *iwb* newsletter 23 (2015) 3, pp. 7–8.

- **Habedank, J. B.**; Schmitz, P.; Zaeh, M. F.: Designing structured electrodes for Li-ion batteries. Poster, Advanced Battery Power Conference. March 28–30, 2017, Aachen, Germany.

- Schmitz, P.; **Habedank, J. B.**; Zaeh, M. F.: Spike laser welding for the electrical connection of cylindrical lithium-ion batteries. Journal of Laser Applications 30 (2018) 1, pp. 012004/1–012004/7.

- **Habedank, J. B.**; Metkar, A.; Schmitz, P.; Schnell, J.: Innovative Materialien und Produktionstechnik für die nächste Generation Lithium-Ionen-Zellen, translated title: Innovative materials and production technology for the next generation of lithium-ion cells. *iwb* newsletter, 25 (2018) 1, pp. 31–33.

- Kraft, L.; Rheinfeld, A.; **Habedank, J. B.**; Jossen, A.: Modeling of Lithium-Ion Cells with Laser-Structured Graphite Anodes. Poster, ECCM-ECFD. June 11–15, 2018, Glasgow, United Kingdom.

- Guenter, F. J.; **Habedank, J. B**.; Schreiner, D.; Neuwirth, T.; Gilles, R.; Reinhart, G.: Introduction to Electrochemical Impedance Spectroscopy as a Measurement Method for the Wetting Degree of Lithium-Ion Cells. Journal of The Electrochemical Society 165 (2018) 14, pp. A3249–A3256.

- **Habedank, J. B.**: Batterieproduktion in Deutschland, translated title: Battery production in Germany. *iwb* newsletter 25 (2018) 3, p. 5.

- **Habedank, J. B.**; Kraft, L.; Zaeh, M.F.: Laser Structuring of Anode Materials for Advanced Lithium-Ion Batteries. Poster, International Congress on Applications of Lasers and Electro Optics (ICALEO). October 14–18, 2018, Orlando, FL, USA.

- **Habedank, J.B.:** Femtosecond Laser Structuring of Graphite Anodes for Improved Lithium-Ion Batteries. LIA TODAY Special Edition (2018), pp. 22–23.

- Kraft, L.; Frank, A.; Rheinfeld, A.; **Habedank, J. B.**; Jossen, A.: Dependency of the Discharge Rate Capability on Electrode Thickness of Lithium-Ion Cells with Laser-Structured Graphite Anodes. Poster, 16th Symposium on Modeling and Experimental Validation of Electrochemical Energy Technologies (ModVal). March 12–13, 2019, Braunschweig, Germany.

Femtosecond laser structuring of graphite anodes for improved lithium-ion batteries: Ablation characteristics and process design

Jan Bernd Habedank, Joseph Endres, Patrick Schmitz, Michael F. Zaeh, Heinz P. Huber

Reproduced from:

Journal of Laser Applications 30 (2018) 3, pp. 32205/1–32205/7

Weblink: https://doi.org/10.2351/1.5040611

Femtosecond laser structuring of graphite anodes for improved lithium-ion batteries: Ablation characteristics and process design

Jan B. Habedank,[1] Joseph Endres,[1] Patrick Schmitz,[1] Michael F. Zaeh,[1] and Heinz P. Huber[2]
[1]*Technical University of Munich, 85748 Garching, Germany*
[2]*University of Applied Sciences Munich, 80335 Munich, Germany*

(Received 18 May 2018; accepted for publication 18 May 2018; published 14 June 2018)

Lithium-ion batteries are widely used as energy storage devices due to their high energy density and versatile applicability. Key components of lithium-ion batteries are electrically isolated electrodes and a liquid electrolyte solution which enables ion transport between the electrodes. Laser structuring of electrodes is a promising approach to enhance the high-current capability of lithium-ion batteries by reducing cell internal resistances, as a larger contact area of the active material with the electrolyte solution is created. In the work described here, lithium-ion battery anodes were structured by locally ablating small fractions of the coating using femtosecond laser pulses with infrared wavelengths. A study on ablation characteristics depending on different process parameters such as laser fluence and repetition rate was performed. Special focus was on the ablation efficiency, enabling an optimized process design. The influence of the electrode composition was taken into account by studying the ablation behavior at a varying binder content. Evenly distributed micro holes were chosen in order to keep active material removal at a minimum. To evaluate the effect of structured graphite anodes on the electrochemical properties of lithium-ion batteries, test cells were manufactured and galvanostatically cycled at different current rates. Results show improvements in high-current performance which is expressed by an increased discharge capacity yield. © *2018 Laser Institute of America*. https://doi.org/10.2351/1.5040611

Key words: laser structuring, electrodes, lithium-ion batteries, graphite

I. INTRODUCTION

Lithium-ion batteries are currently the dominant energy storage solution for consumer electronics and electric vehicles. Rapid developments in material science and engineering have led to significant gains in performance, reliability, and safety of battery-powered products at shrinking costs.[1] In order to meet future customer expectations in automotive applications, the energy content per battery volume and mass as well as power delivery have to be increased. These conflicting requirements are greatly influenced by the electrode attributes. The electrodes typically consist of a composite layer made of active material, binder, and conductive agents coated onto metallic current collector foils.[2] As only the electrochemically active materials contribute to the deployable capacity of a cell, the content of non-active material per areal dimension has to be reduced. This can be achieved by decreasing the content of binder and conductive agent, increasing the compression of the porous material matrix, or raising the coating thickness.[3] Electrodes with a higher coating thickness contain more energy; therefore, fewer electrodes are required to reach the nominal cell capacity. However, such electrodes with high active material loading struggle with an increased cell resistance in operation, leading to performance losses at higher charge and discharge currents. The resistance is mainly caused by a limited transport speed of the ions through the porous electrode layer and results in an early meeting of voltage limits, amplified heat generation, and faster initiation of degradation processes.[4] It has been demonstrated that structured electrodes can have a positive impact on cell performance at higher current rates.[5–8] Simulative and experimental approaches attribute this to an increase of reaction surface and reduced diffusion pathways through the tortuous electrode structure, facilitating ion transport.

Femtosecond laser processing has been widely introduced as a precise and flexible patterning method with a negligible thermal damage zone.[9,10] Laser structuring of electrodes is currently not used in industrial production of lithium-ion batteries. However, several research studies have been published on this matter. Pröll *et al.*,[11] Smyrek *et al.*,[12] and Mangang *et al.*[13] focused on cathode materials and were able to observe a notable increase in deployable mass-specific capacity at high-current rates. They used different pulsed laser sources with pulse durations in the range from nanoseconds (ns) to femtoseconds (fs). When treating porous cathode materials such as lithium-nickel-manganese-cobalt-oxide (NMC), they created grid or channel structures that were filled with electrolyte during cell assembly. Pfleging *et al.* were able to observe improvements in the electrolyte wetting time as the electrolyte liquid is soaked in more rapidly by capillary forces.[14] Lutey *et al.* performed a study on the ablation of different electrode coatings including graphite with nanosecond laser pulses and analyzed the incision depths at different translational velocities.[15] Schmieder developed an analytical model of laser ablation mechanisms with ns laser pulses.[16] The study focused on the cutting

process of electrodes, limiting the transferability of the results for structuring. Hoffman *et al.* studied the effect of the laser wavelength and fluence on the ablation of solid carbon surfaces.[17] To our knowledge, neither the effect of laser structuring of graphite anodes on the battery performance nor the ablation characteristics of porous graphite anodes with femtosecond laser radiation have been thoroughly analyzed yet. However, the structuring of graphite anodes should have a high potential, as graphite particles usually have a flake-like shape and tend to arrange in a parallel manner to the substrate foils due to production processes, creating particularly long and branched ion migration paths.[18] This behavior is displayed in Fig. 1 (top).

By creating laser induced pores, the effective lengths of the ion migration paths are reduced and thereby the internal cell resistance is decreased. Simulations indicate that the increase in cell performance by reduced cell resistance strongly depends on the structure dimensions. Nemani *et al.* identified an aspect ratio >1 (relation between structure diameter and depth) to be of high importance, suggesting structures with small diameters and large structure depths.[19] As state-of-the-art electrodes usually have coating thicknesses of 50–100 μm, the desired structure diameters are <50 μm with a structure depth of >50 μm. To achieve these dimensions, mechanical manufacturing processes are unsuitable, especially as a large number of structures have to be created in a short amount of time. Laser structuring appears to be highly suitable for the manufacturing of the desired structure dimensions.

II. OBJECTIVES AND APPROACH

As described above, laser structuring of graphite anodes is expected to have a great potential for improving the performance characteristics of lithium-ion batteries by shortening ion migration paths. In this work, a study regarding the ablation characteristics of the porous coating material of the electrode is presented. Several laser parameters such as peak fluence and pulse frequency as well as different electrode compositions were taken into account. A special focus was put on the ablation efficiency, as high ablation rates will be necessary for industrial electrode production. Test cells were manufactured to demonstrate the benefit of laser structuring of graphite anodes as well as to rule out any potential damage to the electrochemically active components.

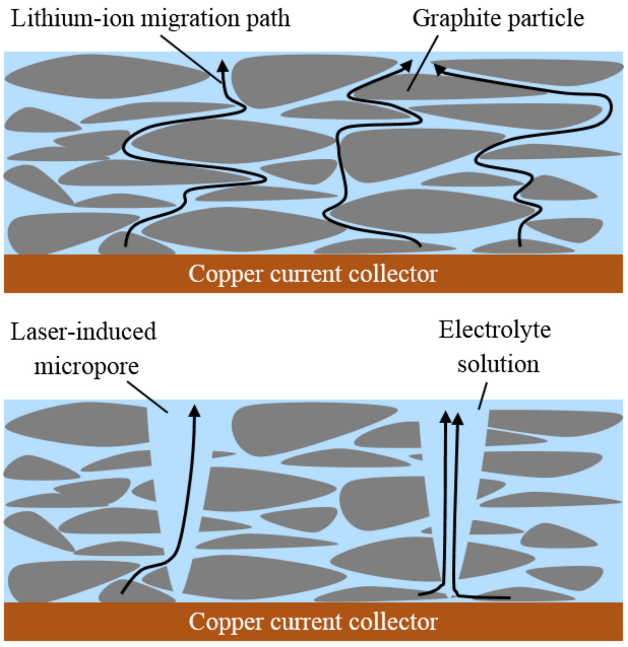

FIG. 1. Illustration of the lithium-ion flow through a graphite anode, top: unstructured electrode with long ion migration paths, bottom: structured electrode with short and direct ion migration paths.

III. MATERIALS AND METHODS

A. Electrode materials and fabrication

To ensure a high degree of comparability between separate ablation measurements, commercially available anodes with excellent homogeneity were chosen for the experiments. The material composition of the anodes was 92.5 wt. % graphite, 7.0 wt. % binder, and 0.5 wt. % conductive carbon coated onto both sides of a copper foil with a thickness of 10 μm. The coating thickness was 50 μm on both sides with a porosity of approximately 32%, resulting in a weight loading of 6.5 mg/cm^2 on each side. Other electrode characteristics as well as utilized production processes are unknown to the authors. For the studies on the ablation mechanisms with varying binder content as well as the production of test cells, tailored electrodes were manufactured. The anode ink was prepared by mixing 95.0 wt. % graphite (SGL Carbon) and 5.0 wt. % polyvinylidene fluoride (PVDF) with *N*-methyl-2-pyrrolidone (NMP, Sigma Aldrich) in a multi-step mixing process described in Günther *et al.*[20] The cathode ink contained 96.0 wt. % NMC (BASF), 2.0 wt. % PVDF, and 2.0 wt. % Carbon (C65, Timical). Mixing was performed in a planetary centrifugal vacuum mixer (Thinky ARV-310). Both inks were coated onto current collectors (anode: copper, cathode: aluminum) in a tape casting process and dried overnight at 50 °C to remove the NMP from the coating. After drying, the electrodes were compressed to a porosity of 35%. The resulting coating thickness after compression was 64 μm on average. Further details on the manufacturing process of electrodes can be found in Marks *et al.*[21]

B. Laser structuring and structure measurement

Laser structuring was performed using a pulsed femtosecond laser (Spirit® One™ 1040-8, Spectra-Physics) with a pulse duration τ_p of 400 fs and a wavelength λ of 1040 nm in ambient air. Specifications of the laser source such as the beam quality factor M^2 and the pulse energy E_p are presented in Table I.

TABLE I. Specifications of the laser source Spirit® One 1040-8.

λ (nm)	M^2	d_0 (μm)	τ_p (fs)	f_R (Hz)	E_p (μJ)
1040	1.2	17.2	400	10–10^4	max. 40

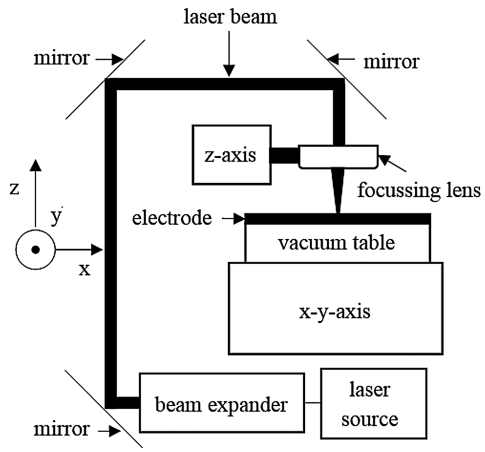

FIG. 2. Experimental setup for laser structuring of anodes.

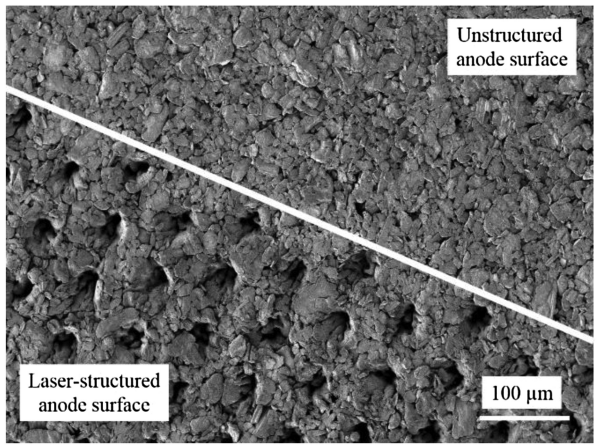

FIG. 3. Scanning electron microscopy image of a laser structured and an unstructured graphite anode surface.

The experimental setup is displayed in Fig. 2. The electrode was fixed using a vacuum clamping plate and moved in the *x*–*y*-plane in order to spatially distribute the structures. The laser beam was expanded before being focused on the electrode surface in order to achieve a small focus diameter.

The dimensions of the structures were measured using a confocal microscope (Leitz Ergoplan) and analyzed with the corresponding evaluation software (Gwyddion).

C. Cell assembly and testing

Coin cells were assembled in an argon filled glove box (M-Braun) with $H_2O < 0.1$ ppm and $O_2 < 0.1$ ppm. Prior to transferring the electrodes into the glovebox, they were dried overnight at 120 °C in a vacuum oven. All other cell components were dried overnight at 70 °C under vacuum. Two cell types were manufactured: reference cells with unstructured anodes and cells with structured anodes. The cathodes in all cells remained unstructured. Three cells of each type were produced to ensure statistical relevance. Cathode coins were 14 mm in diameter, anode coins 15 mm, and the glass microfiber separator (VWR, Type 691) 16 mm to ensure complete coverage of the cathode by the anode material and to avoid internal short circuits. Electrodes were matched to an area specific capacity ratio between anode and cathode of around 1.2 to 1. The electrolyte was LP572 (BASF) which consists of ethylene carbonate and ethyl-methyl-carbonate 3:7 with 1M lithium-hexafluorophosphate ($LiPF_6$) conductive salt and 2% vinylene carbonate.

After assembly, the cells went through formation by charging and discharging them three times at C/10 in a laboratory battery testing system (Basytec). The discharge capacity of the third cycle was defined as the theoretical capacity of the cell. To determine the rate capability, the cells were cycled from 4.2 to 3 V at increasing C-rates from C/10 to 5 C. Charging was done using a constant current constant voltage procedure with a charging current of C/10 for the corresponding discharge cycles with C/10, C/5, and C/2 and a charging current of C/2 for the corresponding discharge cycles with 1 C, 2 C, and 3 C. Discharging was performed using a constant current procedure.

IV. LASER ABLATION OF GRAPHITE ANODES

Separate holes with a distance of 70 μm and a structure diameter of approximately 25 μm were created and evenly distributed in a triangular pattern. However, due to the porous character of the electrode coating consisting of particles with different particle sizes, certain deviations in structure dimensions were observed. In contrast to line or grid structures, the hole pattern causes a large increase in electrode surface area while keeping the removal of active material at a minimum. An exemplary structure is displayed in Fig. 3 together with an image of the unstructured anode surface.

A. Peak fluence and number of repetitions

In order to evaluate the effect of the peak fluence

$$\Phi_0 = \frac{2 \cdot E_p}{r_0^2 \cdot \pi}, \tag{1}$$

and the number of applied pulses on the depth of the ablation craters, an analysis on ablation characteristics was performed. E_p is the pulse energy and r_0 is the radius of the laser beam in the focal plane. According to Nolte *et al.*, the ablation depth D can be described by Eq. (2), with the threshold fluence Φ_{th} and a scaling parameter δ:[22]

$$D = \delta^* \ln\left(\frac{\Phi_0}{\Phi_{th}}\right). \tag{2}$$

The experimental results are displayed in Fig. 4.

For each constant number of laser pulses, an increasing ablation depth D was observed when the peak fluence was increased. Also, a greater number of laser pulses with the same peak fluence led to an increased ablation depth. The parameters for the fit functions are presented in Table II. The fits were created using the least squares method.

However, a disproportionally large number of laser pulses n were needed to achieve a comparable ablation depth when the peak fluence was slightly decreased. This effect is

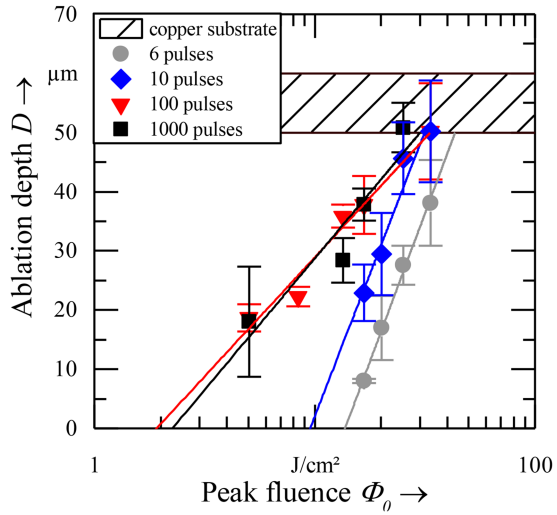

FIG. 4. Depths of ablation craters in graphite anodes for a varying number of applied pulses, standard deviations are displayed, $f_r = 10$ Hz, fits according to Table II.

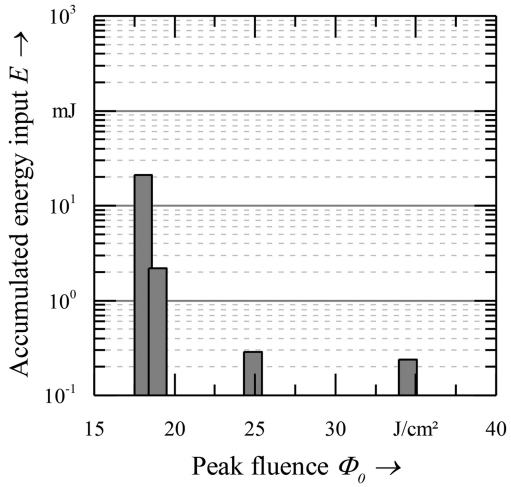

FIG. 5. Accumulated energy input E for a constant ablation depth of 40 μm into the graphite coating, $f_r = 10$ Hz.

presented in Fig. 5. The higher accumulated energy E that is introduced into the workpiece

$$E = n \cdot E_p = \frac{n \cdot \Phi_0 \cdot \pi \cdot r_0^2}{2}, \tag{3}$$

is an indication of the more inefficient ablation with smaller fluences.

The experiments were conducted with a pulse frequency of 10 Hz, in order to rule out effects that may occur due to heat accumulation, shielding by ablation products, or any other interaction between separate pulses. As the coating thickness of the electrode was approximately 50 μm, deeper penetration of the specimen could only be obtained by ablating a fraction of the copper current collector. This effect was not examined in further considerations.

It can be concluded that the single pulse fluence has a greater influence on the ablation depth than the accumulated energy that is introduced into the electrode over time. In order to accomplish a better process efficiency and short process times, large pulse fluences are essential. It has to be noted that even with the highest fluence applied, several pulses on the same spot were necessary to achieve significant structure depths >50% of the coating thickness. This brings up the question whether these pulses should be applied consecutively (forming one structure at a time) or in separate runs (structuring a certain electrode area repetitively). This issue is addressed in Sect. IV B.

TABLE II. Results for the logarithmic fits [Eq. (2)] displayed in Fig. 4.

Number of pulses (n)	δ (μm)	Φ_{th} (J/cm^2)
6	43.50	13.74
10	41.81	9.54
100	17.49	1.92
1000	19.31	2.26

B. Pulse fluence and repetition rate

For process design, it is crucial to evaluate the effects of an increasing pulse repetition rate on the process efficiency, especially as available industrial laser sources have been continuously gaining average power over the last years. Therefore, the influence of the pulse frequency at a varying peak fluence was determined. The number of applied pulses was 10 for all runs. The results are displayed in Fig. 6.

It becomes apparent that the pulse repetition rate has a significant influence on the amount of ablated material if all other process parameters remain constant. At low repetition rates (10 and 100 Hz), the influence of the repetition rate on the ablation depth was rather small. However, at higher rates,

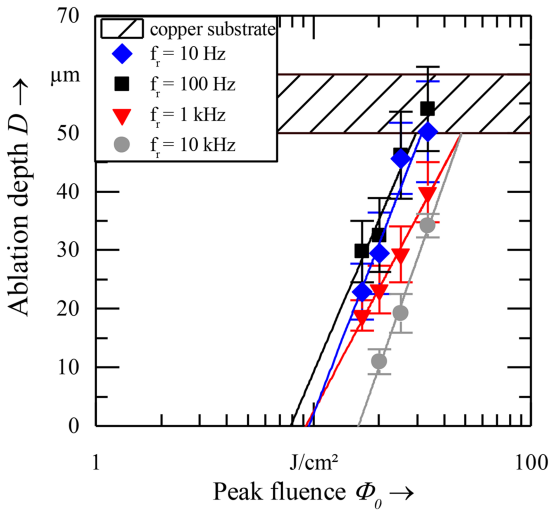

FIG. 6. Depths of ablation craters in graphite anodes for different pulse repetition rates, standard deviations are displayed, 10 pulses for all runs, fit according to Table III.

TABLE III. Results for the logarithmic fits [Eq. (2)] displayed in Fig. 6.

Repetition rate (f_r)	δ (μm)	Φ_{th} (J/cm^2)
10 Hz	41.81	9.54
100 Hz	37.63	7.86
1 kHz	30.33	9.25
10 kHz	45.74	16.11

the resulting ablation depth decreased significantly in case the pulses were applied on the same surface area. This may be attributed to heat accumulation or shielding effects caused by ablated graphite particles.

The parameters for the fit functions are presented in Table III. The fits were created using the least squares method.

In Fig. 7, the resulting structure depths are presented for different repetition rates from 10 Hz to 10 kHz. The peak fluence and the number of pulses were constant. If the structures were created one by one, a rise in repetition rate caused substantial losses in process efficiency. For a repetition rate of 10 kHz, an ablation depth of only 20 μm was observed, while at repetition rates <100 Hz, the ablation depth was approximately 45 μm, even though the energy input was identical.

As repetition rates below 100 Hz are much too slow for industrially relevant processes and at the same time large repetition rates cause laser ablation efficiency losses if structures are formed one at a time, the structures will have to be created in consecutive runs over a certain machining area. Thus, shielding effects can be avoided and the high pulse repetition rates of state-of-the-art laser sources combined with highly dynamic scanning optics can be exploited.

C. Influence of electrode composition on ablation

Additionally to the studies on the laser beam parameters such as peak fluence and repetition rate, an analysis of the influence of the electrode composition was carried out. Electrodes with a different content of PVDF binder were manufactured and laser structured with 10 laser pulses with a peak fluence of 33 J/cm^2 at a repetition rate of 1 kHz. The examined values of binder content were 2.0 wt. %, 5.0 wt. %, and 8.0 wt. %. The results are presented in Fig. 8. The ablation depth decreased significantly with an increasing binder content of the electrode. At 2.0 wt. % binder content approximately 37 μm of active material coating were removed compared to 18 μm at 5.0 wt. % and 14 μm at 8.0 wt. %. This indicates that small changes in binder content may lead to large alterations in ablation behavior of electrode material.

As the binder creates cohesion among the graphite particles, this result is highly plausible. If laser structuring of electrodes will gain importance in future electrode production, special attention should be paid to possible reductions in binder content or alternate binder types which could make ablation of the coating more effective.

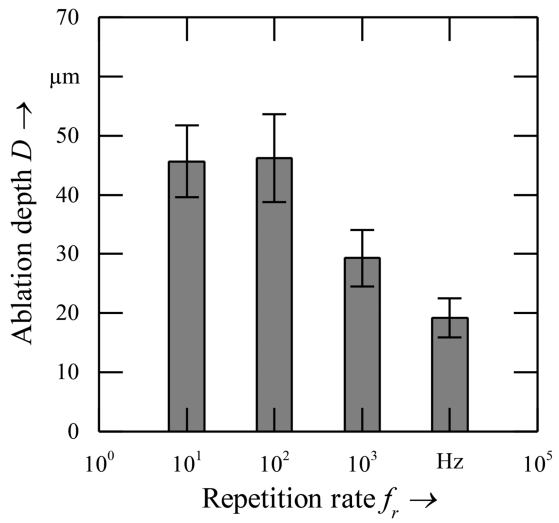

FIG. 7. Resulting ablation depths and standard deviations at different pulse repetition rates, 10 pulses per measurement point, $\Phi_0 = 25$ J/cm^2.

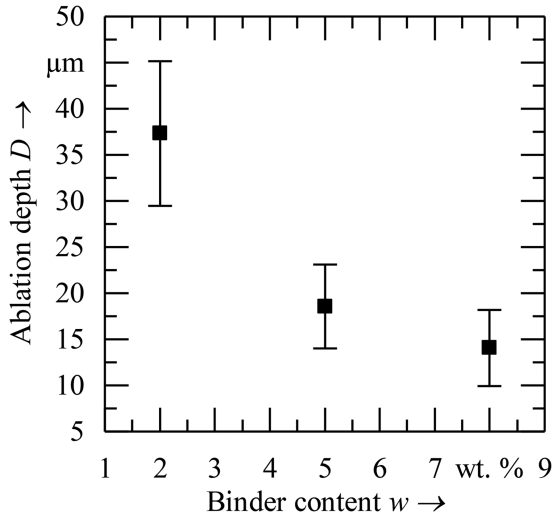

FIG. 8. Ablation depths and standard deviations of graphite anodes with a varying binder content, 10 pulses per measurement point, $\Phi_0 = 33$ J/cm^2, $f_r = 1$ kHz.

V. LI-ION CELLS WITH LASER STRUCTURED ANODES

To evaluate the beneficial effects of laser structuring of graphite anodes for lithium-ion batteries, test cells were manufactured. They were galvanostatically cycled at different C-rates from C/10 to 5 C. A C-rate of one represents a current that discharges the full capacity of a cell in one hour. The measured cell capacities at C/10 for the cells with unstructured anodes were 4.00, 3.69, and 3.90mAh. For structured anodes, the cell capacities were 4.00, 3.77, and 3.85 mAh, resulting in average capacities of 3.86 mAh for cells with unstructured anodes and 3.87 mAh with structured anodes. To facilitate a comparison between the cells, the discharge capacities were normalized with respect to the theoretical cell capacity. As the theoretical capacities of structured and unstructured cells and the electrode balancing are highly similar, this normalization is considered to not alter the results.

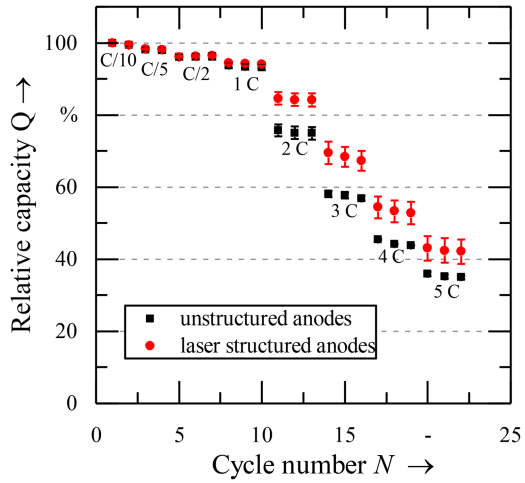

FIG. 9. Normalized discharge capacities and standard deviations of Li-ion coin cells with laser structured and unstructured anodes.

The results of the discharge rate test are presented in Fig. 9. The test indicated significant and substantial improvements in discharge capacity of approximately 20% for the cells with laser structured anodes compared to unstructured anodes for C-rates between 2 C and 5 C. At C-rates below 1 C, the reference cells and the cells with laser structured anodes showed almost equal performance. This indicates that no notable damage has been done to the surrounding active material particles by laser structuring, e.g., by creating a significant heat affected zone.

The improvements in the discharge characteristics of test cells with laser structured anodes can be attributed to reduced overpotentials and thereby decreased electrode polarization during discharge. The laser induced structures create lithium-ion migration paths that facilitate ion transport out of the electrode. In particular, the flake-like form of the graphite particles has repeatedly been suspected to slow down ion transport at high C-rates due to highly tortuous paths through the electrode's microstructure. This issue is partially overcome by laser structuring. It has to be noted that by laser structuring of anodes (in contrast to cathodes), the theoretical capacity of the cell is not decreased as the amount of active material on the cathode mainly determines the theoretical cell capacity. The active material loading on the cathode side is not changed, so if functional balancing of the electrodes is maintained, no reduction in theoretical capacity is created. This is of great importance, as commercial lithium-ion cells are operated in various current regimes and a capacity trade-off at varying C-rates is not likely to be accepted by customers.

VI. SUMMARY AND OUTLOOK

In this work, anodes for lithium-ion batteries were structured using femtosecond laser pulses. A detailed study on ablation characteristics was performed. A high laser peak fluence was identified to be more important for an efficient ablation process than the accumulated energy input into the electrode over time. High pulse repetition rates on the same electrode area should be avoided in order to circumvent shielding from ablation products. Lithium-ion cells with laser structured anodes were manufactured and tested. They outperformed their unstructured counterparts in terms of high-current capability, delivering a 20% higher discharge capacity at current rates >1 C. At low current rates, no reduction in capacity was detected. This makes laser structuring of anodes highly interesting for all high-current applications of lithium-ion batteries. The laser process may also contribute to the introduction of ultra-high energy density cells with thick electrodes, as a satisfactory C-rate capability is likely to be maintained. The authors will continue to work on optimizing structure design by electrochemical simulations, on experimental validation and also on the process scale up to prove the adaptability of the laser structuring process for large format lithium-ion batteries.

ACKNOWLEDGEMENTS

This work was financially supported by the German Federal Ministry of Economic Affairs and Energy (BMWi) under Grant No. 03ET6103F (SurfaLIB).

[1]A. Sakti, J. J. Michalek, E. R. Fuchs, and J. F. Whitacre, "A techno-economic analysis and optimization of Li-ion batteries for light-duty passenger vehicle electrification," J. Power Sources **273**, 966–980 (2015).
[2]R. Korthauer, *Handbuch Lithium-Ionen-Batterien* (Springer Berlin Heidelberg, Berlin, Heidelberg, 2013).
[3]H. Zheng, J. Li, X. Song, G. Liu, and V. S. Battaglia, "A comprehensive understanding of electrode thickness effects on the electrochemical performances of Li-ion battery cathodes," Electrochim. Acta **71**, 258–265 (2012).
[4]K. G. Gallagher, S. E. Trask, C. Bauer, T. Woehrle, S. F. Lux, M. Tschech, P. Lamp, B. J. Polzin, S. Ha, B. Long, *et al.*, "Optimizing areal capacities through understanding the limitations of lithium-ion electrodes," J. Electrochem. Soc. **163**, A138 (2015).
[5]S. Ferrari, M. Loveridge, S. D. Beattie, M. Jahn, R. J. Dashwood, and R. Bhagat, "Latest advances in the manufacturing of 3D rechargeable lithium microbatteries," J. Power Sources **286**, 25–46 (2015).
[6]M. Roberts, P. Johns, J. Owen, D. Brandell, K. Edstrom, G. El Enany, C. Guery, D. Golodnitsky, M. Lacey, C. Lecoeur, *et al.*, "3D lithium ion batteries—from fundamentals to fabrication," J. Mater. Chem. **21**, 9876 (2011).
[7]J. W. Long, B. Dunn, D. R. Rolison, and H. S. White, "Three-dimensional battery architectures," Chem. Rev. **104**, 4463–4492 (2004).
[8]M. Osiak, H. Geaney, E. Armstrong, and C. O'Dwyer, "Structuring materials for lithium-ion batteries: Advancements in nanomaterial structure, composition, and defined assembly on cell performance," J. Mater. Chem. A **2**, 9433 (2014).
[9]B. N. Chichkov, C. Momma, S. Nolte, A. Tünnermann, "Femtosecond, picosecond and nanosecond laser ablation of solids," Appl. Phys. A **63**, 109 (1996).
[10]X. Liu, D. Du, and G. Mourou, "Laser ablation and micromachining with ultrashort laser pulses," IEEE J. Quantum Electron. **33**, 1706–1716 (1997).
[11]J. Pröll, H. Kim, A. Piqué, H. J. Seifert, and W. Pfleging, "Laser-printing and femtosecond-laser structuring of LiMn2O4 composite cathodes for Li-ion microbatteries," J. Power Sources **255**, 116–124 (2014).
[12]P. Smyrek, J. Pröll, J.-H. Rakebrandt, H. J. Seifert, and W. Pfleging, in *SPIE LASE*, edited by U. Klotzbach, K. Washio, C. B. Arnold (SPIE, 2015), p. 93511D.
[13]M. Mangang, J. Pröll, C. Tarde, H. J. Seifert, and W. Pfleging, in *SPIE LASE*, edited by U. Klotzbach, K. Washio, C. B. Arnold (SPIE, 2014), p. 89680M.
[14]W. Pfleging, R. Kohler, and J. Pröll, "Laser generated microstructures in tape cast electrodes for rapid electrolyte wetting: new technical approach for cost efficient battery manufacturing," in *SPIE LASE*, edited by U. Klotzbach, K. Washio, C. B. Arnold (SPIE, 2014), p. 89680B.

[15]A. H. A. Lutey, A. Fortunato, A. Ascari, S. Carmignato, and L. Orazi, in *ASME 2014 International Manufacturing Science and Engineering Conference Collocated with the JSME 2014 International Conference on Materials and Processing and the 42nd North American Manufacturing Research Conference, Detroit, MI, June 9–13, 2014* (ASME, 2014).
[16]B. Schmieder, in *SPIE LASE*, edited by U. Klotzbach, K. Washio, C. B. Arnold (SPIE, 2015), p. 93511C.
[17]J. Hoffman, J. Chrzanowska, S. Kucharski, T. Moscicki, I. N. Mihailescu, C. Ristoscu, and Z. Szymanski, "The effect of laser wavelength on the ablation rate of carbon," Appl. Phys. A **117**, 395–400 (2014).
[18]M. Ebner, D.-W. Chung, R. E. García, and V. Wood, "Tortuosity anisotropy in lithium-ion battery electrodes," Adv. Energy Mater. **4**, 1301278 (2014).
[19]V. P. Nemani, S. J. Harris, and K. C. Smith, "Design of bi-tortuous, anisotropic graphite anodes for fast ion-transport in Li-ion batteries," J. Electrochem. Soc. **162**, A1415 (2015).
[20]T. Günther, N. Billot, J. Schuster, J. Schnell, F. B. Spingler, and H. A. Gasteiger, "The manufacturing of electrodes: Key process for the future success of lithium-ion batteries," AMR **1140**, 304–311 (2016).
[21]T. Marks, S. Trussler, A. J. Smith, D. Xiong, and J. R. Dahn, "A guide to Li-ion coin-cell electrode making for academic researchers," J. Electrochem. Soc. **158**, A51 (2011).
[22]S. Nolte, C. Momma, H. Jacobs, A. Tünnermann, B. N. Chichkov, B. Wellegehausen, and H. Welling, "Ablation of metals by ultrashort laser pulses," J. Opt. Soc. Am. B **14**, 2716–2722 (1997).

Enhanced Fast Charging and Reduced Lithium-Plating by Laser-Structured Anodes for Lithium-Ion Batteries

Jan Bernd Habedank, Johannes Kriegler, Michael F. Zaeh

Journal of The Electrochemical Society 166 (2019) 16, pp. A3940–A3949

Weblink: https://iopscience.iop.org/article/10.1149/2.1241915jes/meta

Enhanced Fast Charging and Reduced Lithium-Plating by Laser-Structured Anodes for Lithium-Ion Batteries

Jan Bernd Habedank, [z] **Johannes Kriegler, and Michael F. Zaeh**

Technical University of Munich, Institute for Machine Tools and Industrial Management, 85748 Garching, Germany

Within this paper we report on a lithium-ion battery with laser-structured graphite anodes, alleviating current drawbacks of lithium-ion batteries such as the reduced discharge capacity at high C-rates and the on-set of lithium-plating during fast charging. These issues are intensified at low temperatures, as reaction and diffusion kinetics decelerate, which is why a focus of the presented work lies on low temperature performance. Electrochemical impedance spectroscopy was used to show a reduction in the impedances of cells with laser-structured anodes in comparison to their conventional counterparts. The discharge capacity retention at high C-rates was enhanced by up to 27% compared to conventional cells, proving potential for high power applications. For the cells with laser-structured anodes, the on-set of lithium-plating at 0°C was observed at higher charging C-rates by analyzing the voltage relaxation after charging. At −15°C, a smaller amount of plated lithium was detected, even though lithium-plating could not be entirely avoided. Laser structuring also enabled shorter charging times, as the upper cutoff voltage was reached at a higher SOC. The results point out that laser structuring of the anode improves the fast charging capability of lithium-ion cells, especially under demanding operating conditions.

 [DOI: 10.1149/2.1241915jes]

Manuscript submitted August 22, 2019; revised manuscript received October 31, 2019. Published November 26, 2019.

Lithium-ion batteries (LIBs) are the key-components for the success of electric vehicles and a sustainable energy economy. Their performance is highly dependent on the charge and mass transport kinetics between the porous electrodes.[1] At low temperatures, the cell internal resistances rise due to a decreasing ionic conductivity of the liquid electrolyte, sluggish charge transfer processes on the interfacial area between the active material and the electrolyte, and slow lithium diffusion within the active material.[2] The increasing resistances result in high overpotentials and electrode polarization during cell operation.[3] For discharge, the consequences are a reduced deployable capacity and an amplified heat generation. However, high overpotentials during charging can cause the deposition of metallic lithium (Li-plating) onto the anode surface, specifically when the anode surface potential falls below 0 V.[4] Li-plating has been reported to accelerate the ageing of the LIB[5] and presents severe safety risks due to dendrite formation.[6] Among others, a low anode-to-cathode capacity ratio, low temperatures, high charging rates, and overcharging favor the deposition of metallic lithium, as these factors have an effect on the anode kinetics and the diffusion rate.[2] Thus, the charging currents have to be strictly limited, especially at low temperatures. While in laboratory cells the individual electrode potentials can be measured by applying reference electrodes, the detection of Li-plating in commercial full cells is challenging. The Li-plating process is partially reversible and some of the deposited lithium re-intercalates into the graphite when a relaxation phase occurs after charging. During this period, a distinctive voltage plateau can be observed, making the on-set of Li-plating detectable with nondestructive electrochemical methods.[7] Similar observations were made when skipping the relaxation phase and examining the voltage in the discharge process after fast-charging at low temperatures instead.[8] In this case, the plated lithium mostly dissolves into the electrolyte before it re-intercalates into the anode (Li-stripping).[9] By analyzing the differential voltage during this Li-stripping process,[10] the identification of previously plated lithium can be further facilitated.[11]

Conventional electrodes of LIBs consist of active material particles, binders and conductive agents which are coated onto metallic current collector foils. While there are many possible chemistries for the cathode, such as $LiCoO_2$, $LiFePO_4$ or $LiNi_xMn_yCo_zO_2$ (NMC, $x + y + z = 1$), the majority of anodes in commercially available cells are made of carbon (mostly graphite). In cell production, the electrode constituents form a porous layer with a tortuous void volume which is filled by the liquid electrolyte. The effect of the porous microstructure on the ion transport is commonly described by the MacMullin number N_M

$$N_M = \frac{\kappa}{\kappa_{eff}} \quad [1]$$

which provides a relation between the ionic conductivity κ and the effective conductivity κ_{eff} through the porous media. From a geometrical perspective, the tortuosity τ

$$\tau = \frac{d_{path}}{d} \quad [2]$$

is a characteristic value for describing the ion transport restraint of the porous electrode microstructure, where d_{path} is the actual transport path of an ion through the electrode and d is the direct path between the point of de-intercalation and intercalation while charging or discharging.[12] The tortuosity τ has been reported to have a major influence on diffusion and concentration overpotentials within the electrode structure.[12] As the lithium transport into and out of the electrode is impeded, large concentration gradients are formed, creating a strongly inhomogeneous charge carrier distribution.[13] This effect predominantly occurs in anodes containing flake-like graphite particles[14] which are commonly used as anode material in LIBs due to their lower cost compared to spherical graphite, which is roughly three times more expensive due to high scrap rates in spherical graphite production.[15] Due to the calendering process in LIB production, the preferential orientation of the graphite flakes is parallel to the current collector and perpendicular to the diffusion direction through the electrode.[16] This generates a spatial tortuosity anisotropy and creates particularly long diffusion pathways d_{path} through the electrode.[17] Among many other parameters,[18] the ionic resistance within LIB electrodes can be assessed in situ by measuring the cell impedance using electrochemical impedance spectroscopy (EIS),[19] enabling a calculation of the tortuosity.[12] By measuring the impedance of cells at different states of charge (SOC) and temperatures, conclusions concerning the kinetics of lithium ions within the electrodes can be drawn.[20–22] Impedance spectra for LIB are represented in the form of Nyquist plots and typically consist of two partially overlapping semicircles and a straight sloping line in the low frequency region.[23,24] As the effective impedances of cathode and anode in full cells cannot be precisely distinguished, the recorded EIS spectra represent the total impedance of the electrochemical cell. The size of the semicircles provides information about the magnitude of the resistances resulting from the charge transfer processes between the electrodes and the electrolyte as well as the passing through the solid electrolyte interface (SEI).[25] When measuring at very low frequencies, the resulting quasi-linear slope can be related to the solid-state diffusion processes within the active material particles.[26,27] At low

[z]E-mail: jan.habedank@iwb.mw.tum.de

temperatures[20,21,24] and low SOCs,[27,28] the charge transfer resistances within the cell rise, resulting in an increase in the overall impedance, which can be seen in the EIS spectra.

One promising way for enhancing the lithium transport in LIBs is the creation of three-dimensional (3D) electrode structures, aiming at a reduction of the average electrode tortuosity τ. Thereby the effective diffusion of lithium in the electrolyte D_{eff} can be increased according to

$$D_{eff} = \frac{\varepsilon}{\tau} D_0 \quad [3]$$

where ε is the electrode porosity and D_0 is the diffusion coefficient of lithium in the liquid electrolyte. The 3D-structures can be created by laser pulses which precisely remove a small fraction of the coating. It has been reported that the shortened ion transport pathways lead to a reduced cell resistance and thereby improve the discharge rate capability compared to conventional unstructured electrodes.[29,30] This effect was computationally analyzed in a numerical model, precisely depicting the structure arrangement and dimensions.[30] The introduction of additional pores by laser radiation offers a high flexibility regarding the structure type (e.g. grid, line, or hole structures) and the respective spacing between the structures. Also, the dimensions of each individual structure can be adjusted.[29] Generally speaking, more particles are removed close to the surface of the electrode, resulting in conical structures which narrow toward deeper parts of the electrode.[31] The size and the distribution of the structures have a strong effect on the cell-internal resistance[32] and, thus, the electrochemical performance. When evaluating structure geometries that lead to a comparable total amount of removed electrode material, finer structures have proven to be more beneficial than coarser structures.[33] In contrast to other concepts such as co-extruded[34] or sintered[35] as well as 3D-printed electrodes,[36] the laser structuring process can be applied to conventionally coated electrodes. From a production point of view, establishing the laser structuring process in the industrial fabrication of LIBs shows higher potential for in-line implementation (roll-to-roll processing) into the existing production chain and is associated with lower cost. Cost calculations with regard to laser structuring of electrodes based on scenarios by Wood et al.[37] even predict potential savings in LIB production which may surpass the additional costs due to laser machinery, maintenance, and operation.[38] These potential savings result from a reduction in the electrolyte wetting time[39] and the application of electrodes with a higher areal loading and energy density.

Objectives and Approach

As described in the introductory section, Li-plating is one of the major obstacles in the development of LIBs with fast-charging capability. This paper presents a new approach to electrode design in order to reduce the cell impedance and, thus, the overpotentials during charging and discharging. The generation of structures in the anode by means of short laser pulses (pulse duration 150 ps) aims at improving the ion transport between anode and cathode (Fig. 1).

As structures, holes in a hexagonal pattern with a center point distance of 100 µm were created. The laser process was designed to achieve an aspect ratio of the structures of >1.5, which is defined by the ratio of the structure depth over the structure diameter at the electrode surface. Based on previously published data, the hexagonal hole pattern represents the best geometric structure to balance the conflict between the removal of active material and the reduction of the anode tortuosity.[30,31] By analyzing the electrochemical impedance spectra at temperatures of −15°C, 0°C, and 25°C, the impedances of coin cells containing laser-structured anodes (S1 and S2) were compared to their conventional counterparts (R1 and R2). Subsequently, the effects of the structuring on the discharge C-rate capability were examined. In the next step, the charging behavior was analyzed with a special focus on the detection of Li-plating. For this purpose, the voltage relaxation after charging at C-rates from 0.1C to 2C and ambient temperatures of −15°C, 0°C, and 25°C was monitored and indications of Li-plating were observed. Finally, the charging durations required to fully charge the LIBs were assessed in order to evaluate the potential for improvements in fast charging under demanding low-temperature conditions. In Fig. 1a and Fig. 1b, the internal setup of a LIB with laser-structured graphite anodes and conventional unstructured NMC cathodes is illustrated. Fig. 1c shows a top-view scanning electron microscopy (SEM) image of a laser-structured graphite anode as well as a close-up image of a single laser-induced hole structure. More detailed information on the materials and processes used can be found in the subsequent Materials and Methods section.

Materials and Methods

Materials.—All coin cell components including the coated electrode materials were purchased from commercial sources to ensure a high comparability of the base materials (type 2032 coin cell cases, springs, and spacers: MTI Corporation, USA; glass fiber separator: Type 691, VWR, USA; cathodes: Umicore NV/SA, Belgium; anodes: SEI Corporation, Japan). The electrode characteristics, as provided by the electrode manufacturers, are presented in Table I. Further details on the precise material types (e.g. type of binder, type of conductive carbon) and the respective production processes were not disclosed to the authors for reasons of confidentiality.

Laser structuring of the anodes.—A pulsed Nd:YAG fiber laser (YLPP-1-150V-30, IPG Photonics Corporation, USA) with discrete tunable pulse durations from 150 ps to 5 ns was used to generate the

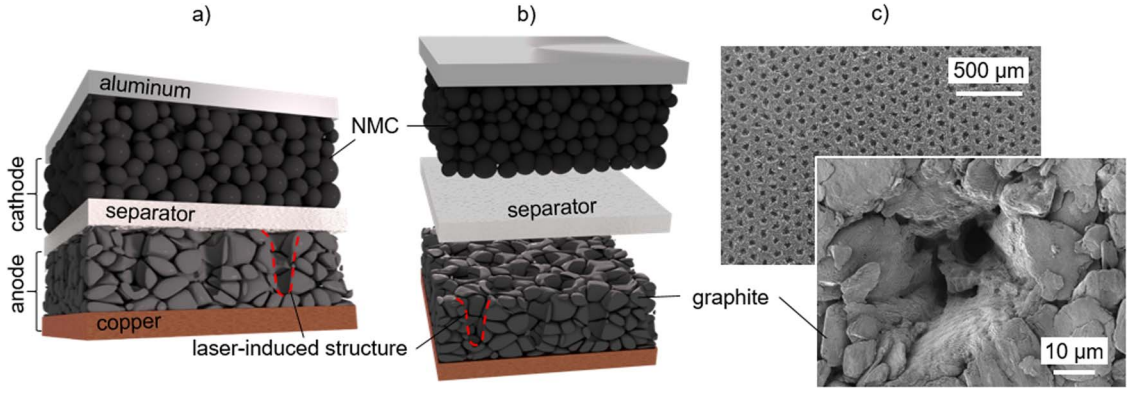

Figure 1. Schematic set-up of a lithium-ion cell with laser-structured graphite anodes; a) illustration of the assembled cell b) exploded view of the cell with a hexagonally arranged hole pattern; c) Top-view SEM-image of a graphite anode with laser-induced structures with a centre spacing of 100 µm and close-up SEM-image of one single structure; the cavities tend to narrow toward the current collector showing a conical shape; due to the porous and non-uniform nature of the electrode coating each structure shape is unique.

Table I. Electrode specifications.

	Cathode	Anode
Active material	NMC (1/1/1)	Graphite
	93.0 wt%	92.5 wt%
Conductive carbon	3.0 wt%	0.5 wt%
Binder	4.0 wt%	7.0 wt%
Feature		
Capacity loading	2.748 mAh/cm^2	3.606 mAh/cm^2
Weight loading	20.38 mg/cm^2	12.99 mg/cm^2
Loading deviation	± 2.5%	± 3.0%
Packing density	2.08 g/cm^3	1.038 g/cm^3
Porosity	approx. 32%	approx. 32%
Electrode thickness	69 µm	70 µm
Thickness deviation	± 2 µm	± 2 µm

microstructures by local selective ablation of the anode material. The ablated particles were removed by a suction nozzle. The pulse duration was set to 150 ps with a pulse repetition frequency of 1200 kHz, an average power of 3 W, and a processing time of 0.45 ms per structure. The laser beam was deflected by scanning optics (Racoon 21, ARGES, Germany) and focused by an F-theta lens (S4LFT0080/126, Sill Optics, Germany) with a focal length of 80 mm. Thereby, a mean focal diameter of 27.1 µm was achieved over the full power range of the laser system and determined using a beam measuring system (MicroSpotMonitor, Primes, Germany). A scanning electron microscope (JCM-600, JEOL, Germany) was used to measure the structure diameter at the top of the electrode. An average structure diameter of approx. 40 µm on the electrode surface was observed, while the structures narrowed toward deeper segments of the electrode (cp. Fig. 1). The depth of the structures was measured with a laser scanning microscope (VK 9710, Keyence, Germany) and accounted for over 90% of the total electrode thickness, occasionally revealing the current collector. No significant changes in the mechanical properties of the electrodes were observed. This was attributed to the low heat input by the short-pulse laser radiation. Thus, the binder, which is responsible for the cohesion of the electrode, was not detectably vaporized or degraded beyond the actual structure diameter. All subsequent handling processes in the assembly of the coin cells could be carried out unaltered.

Cell assembly and formation.—The coin cells (type 2032) were assembled in a dry room (dew point < −40°C). Before cell assembly, the electrodes were dried for 12 hours at 120°C in a vacuum oven. All other cell components were dried overnight at 60°C in an oven within the dry room atmosphere. Two cell types were manufactured: reference cells with conventional anodes and conventional cathodes, and cells with laser-structured anodes and conventional cathodes. The circular cathode electrodes were 14 mm in diameter while the anode coins were 15 mm in diameter to ensure a complete coverage of the cathodes by the anodes. The diameter of the glass microfiber separator was 16 mm to avoid internal short circuits. The conventional electrodes had an area specific capacity ratio between anode and cathode of approx. 1.31, while the cells comprising structured electrodes showed a capacity ratio of approx. 1.24 due to anode material removal. The electrolyte (LP572, BASF, Germany) consisted of ethylene carbonate (EC) and ethyl-methyl-carbonate (EMC) in a ratio of 3:7 with 1 M lithium-hexaflourophosphate ($LiPF_6$) and 2% vinylene carbonate (VC). After assembly, the cells went through formation by charging and discharging them five times at approx. 0.1C in a laboratory battery testing system (CTS, BaSyTec, Germany). The measured capacity in the last formation cycle was used for referencing purposes, i.e. to define an individual nominal capacity for each cell. During formation, no negative influence on the initial capacity by laser structuring was observed as all the nominal cell capacities showed a negligible standard deviation of 0.048 mAh around a mean capacity of 2.93 mAh, see Table II.

Table II. Coulombic efficiencies (CE) of the first and second formation cycle and nominal cell capacities after the fifth formation cycle.

Cell name	CE cycle 1	CE cycle 2	Capacity after formation
R1	87.54%	99.17%	2.96 mAh
R2	87.59%	98.65%	2.85 mAh
S1	86.74%	98.30%	2.92 mAh
S2	86.86%	98.44%	2.97 mAh

In particular, no indications of a significantly increased SEI formation were detected as the coulombic efficiencies (CE) in the first and second formation cycles do not deviate strongly (Table II). This may be explained by the fact that, although the macroscopic and therefore exposed surface area of the electrode was enhanced, graphite particles were ultimately removed by the laser ablation process. These removed graphite particles were therefore not subject to SEI formation. A variation of the material system or the structure geometry could change the ratio of the counteracting influences regarding SEI formation described above. Further studies on SEI formation will be performed to substantiate this interpretation of the measurement data.

Electrochemical impedance spectroscopy.—For the EIS measurements, a potentiostat (Interface 5000E, Gamry Instruments, USA) was used. Before every measurement, a rest period of >1 h was applied to avoid a falsification of the results by cell polarization. Every measurement started with the recording of the OCV, which was performed for 15 s. Subsequently, the impedance was recorded in the frequency range from 100 kHz to 1 Hz with 10 measurement points per decade.

Discharge rate capability tests.—To determine the discharge rate capability, the cells were cycled between 2.7 V and 4.2 V at different temperatures and increasing C-rates (Fig. 3). At a temperature of 25°C, the maximum C-rate was set to 10C, while at 0°C and −15°C the maximum C-rate was set to 5C in order to avoid excessive stress and cell ageing. Charging was done using a constant-current/constant-voltage (CCCV) procedure. For the corresponding discharge rates up to 1C, an equal charging current was used in the CC phase. For discharge cycles >1C, the charging current was held constant at 1C to avoid premature ageing and Li-plating. The CV phase was terminated when the charging current fell below 0.01C. No rest period between charging and discharging was applied. Discharging was performed using a constant current (CC) procedure.

Detection of Li-plating.—The tests for the detection of Li-plating were based on the identification of voltage plateaus in a relaxation phase after CCCV charging. In the CC phase, different currents were applied and also the termination criteria for the CV phase were adjusted. In case of the 0.1C and 0.5C charging current in the CC phase, a 0.05C cutoff current in the CV phase was chosen, while in case of the 1C and 2C charging currents in the CC phase, a 0.2C cutoff current in the CV phase was applied. The latter termination criterion for the CV phase was used in order to achieve comparable durations of the CV phases. Equal termination criteria would have resulted in very long CV phases for the faster charging processes (1C and 2C), which would have strongly altered the significance of the results with regard to Li-plating as lithium re-intercalation also would have happened during the CV phase.

Influence of Laser Structuring on Cell Impedance

In Fig. 2, the Nyquist plots obtained from EIS measurements of LIBs with laser-structured anodes (S1, S2) and conventional anodes (R1, R2) at an OCV of 3.7 V are presented. Three ambient temperatures of 25°C, 0°C and −15°C were analyzed. Please note that the presented measurements do not aim at quantitative statements or

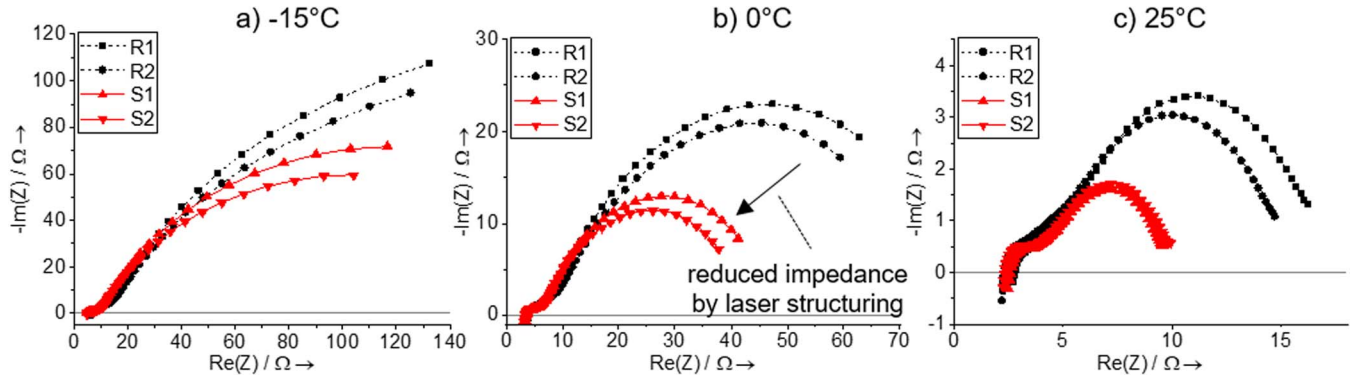

Figure 2. Electrochemical Impedance Spectra in a measurement frequency range of 100 kHz to 1 Hz, recorded at an OCV of 3.7 V and temperatures of a) −15°C, b) 0°C, and c) 25°C for laser-structured (S1, S2) and reference cells (R1, R2); a significant reduction in the impedance at all measured temperatures was achieved by laser structuring; due to the high impedance at a temperature of −15°C the second semi-circle is only visible partly in the applied frequency regime.

models for the electrochemical processes within the cell but at a qualitative comparison of the impedances of the two different cell types at varying temperatures. As the properties of the cathodes as well as other cell parameters were kept constant in all cells, the variances in the EIS spectra can only be attributed to the additional laser-induced macroscopic pores in the anodes.

As described in the introductory section of this paper, at very low frequencies, the impedance spectra of intercalation battery electrodes represent the transport of charge carriers in the solid phases.[40] As the graphite microstructure and, thus, the solid-state diffusion characteristics were not altered, the low frequency domain (< 1 Hz) was not considered in the presented experiments. Please also note the different scales of the individual Nyquist plots. In accordance with the literature, an increased impedance with decreasing temperature was observed. This can be attributed to slower lithium diffusion kinetics and higher charge transfer resistances within the cells. When analyzing Fig. 2c (25°C), the characteristic Nyquist plot for LIBs consisting of two semicircles can be identified. The first semicircle is significantly smaller than the second for both laser-structured and conventional cells. A reduction of the temperature to 0°C (Fig. 2b) led to an overall increase of the impedance, while the general shape of the graph was maintained. The impedance increased even further when the temperature was lowered to −15°C (Fig. 2a). While at 0°C both semicircles are still visible, at −15°C, the second semicircle is truncated due to the minimum applied measuring frequency of 1 Hz (the slight curvature of the plots in the direction of lower frequencies indicates that the second half circle only starts here). For all plots it becomes apparent that the impedance of cells with laser-structured anodes was considerably lower than that of cells with conventional electrodes. While no significant influence on the high frequency resistance (HFR) was noticed, the impedances in the semi-circle region of the Nyquist plots were significantly lower. This range is usually attributed to charge transfer processes, which comprise the lithium transport from the liquid into the solid phase and vice versa. Smaller semi-circles therefore mean that this charge transfer is associated with lower resistance, which may have various possible origins. On the one hand, the structuring results in a higher mean porosity, which in turn provides a better accessibility of the graphite particles for the charge transfer. Since the additional pores open toward the electrode surface due to their characteristic shape, the average porosity is further decreased in proximity of the electrode surface. This gradient in porosity additionally enhances the abovementioned effect. These findings indicate that laser structuring may have a positive influence on the charge transport behavior and, thus, on the fast charging and discharging performance of the cell. As already indicated above, a detailed modelling of the complex resistances will be carried out in future work in order to investigate the origin of the impedance reduction more closely. However, since this paper mainly aims to outline the potentials of the laser structuring of the anode with regard to fast charging, we only provide comparative observations here.

Enhanced Discharge Rate Capability

In the previous section, significantly reduced impedances for the laser-structured electrodes were determined by EIS. The amount of charge provided by lithium-ion cells during discharge depends on the discharge current. This interrelation has its origin in the cell-internal resistances. A reduction in these resistances therefore leads to an increase in the amount of charge provided. To quantify the influence of structuring, discharge rate tests were performed on cells with conventional anodes and the results were compared to cells with laser-structured anodes at different temperatures (25°C, 0°C, −15°C) (Fig. 3). To ease the comparison, the provided discharge capacities were normalized to the value measured at a low discharge rate of 0.1C in the first discharge cycle after cell formation. Since both the conventional and the laser-structured cells showed only a very small deviation in capacity (cp. Table II), we do not consider the validity of the results as falsified by the normalization. Low temperatures generally limit the rate capability as charge and mass transport processes decelerate. The measurements presented here are in agreement with this relationship. At all temperatures, enhancements in rate capability were observed due to laser structuring. The level of improvement through laser structuring varied in strong dependence of the temperature. At 25°C, a maximum increase of approx. 9% in the delivered charge could be achieved by anode structuring. At 0°C the maximum increase was approx. 21% compared to unstructured cells, while at −15°C the maximum improvement was approx. 27%. Depending on the temperature, these maxima were measured at different C rates. While the best results at −15°C were already observed at 2C, the maxima at 0°C and at 25°C were shifted toward 4C and 8C respectively. This trend is shown in Fig. 3d. Moreover, an explicit maximum of improvement in C-rate capability was observed at all temperatures and the achievable improvements decreased again at very high C-rates. This indicates that the positive impact of anode structuring is visible at temperature and material specific discharge rates. At even higher C-rates, other limitations predominate and the associated homogenization of the charge carrier distribution in the electrolyte and in the electrode decreases.

It should be noted that the removal of a small fraction of the graphite coating (reduction of the ratio between anode and cathode capacity from 1.31 to 1.24, see materials and methods section) results in a lower mass loading of the anode, which should generally lead to a slightly improved C-rate capability, even without the structures. Investigations to distinguish between the influence of mass loading reduction and the benefit of the structures by precise adjustment of the electrode parameters are currently underway and will be published shortly. However, previously published work on the electrochemical simulation of pore morphology modifications by laser structuring indicates that the

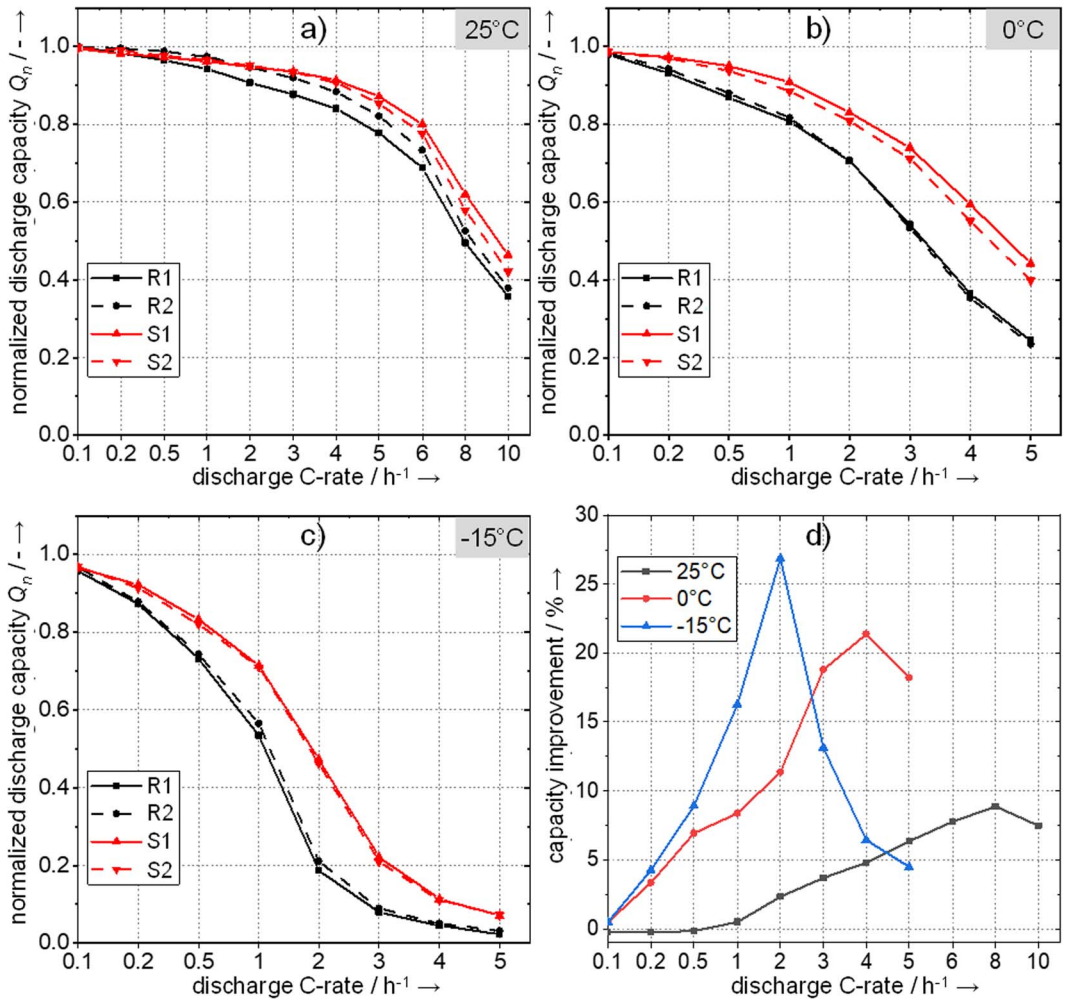

Figure 3. Normalized discharge capacities of laser-structured (S1, S2) and reference cells (R1, R2) at different C-rates for temperatures of a) 25°C, b) 0°C, and c) −15°C; in d), the mean improvements of the available capacity achieved by laser structuring are displayed.

electrode structure itself has a decisive influence on the cell performance.[31] Also note, that anode overbalancing is typically used to prevent the occurrence of Li-plating. However, in the following section, we show that despite lower anode overbalancing, the structuring results in reduced Li-plating during fast charging. Laser structuring may therefore be a solution for eliminating the need for excessive overbalancing in future cell design.

Reduction of Lithium-Plating

As described in the introduction to this paper, there are several ways to electrochemically detect the occurrence of Li-plating in full cells. The measurement method described below to detect Li-plating was adapted from Uhlmann et al.[7] and is illustrated in Fig. 4. The voltage relaxation of the full cell during a rest period after CCCV charging is considered. Depending on whether or not metallic lithium is plated at the anode during the charging process, there are clearly distinguishable relaxation voltage curves.[41]

If no Li-plating occurs, the voltage converges quasi-exponentially against a threshold value. This relaxation has its origin in the homogenization of the cell polarization in the electrodes and in the electrolyte. However, if Li-plating occurs during charging, these homogenization processes are superimposed by lithium re-intercalation in the relaxation phase (de-plating). The metallic lithium adhering to the anode surface decomposes and intercalates into the anode within a specific timespan that correlates with the amount of plated lithium. Since this process takes place at a different potential level, a characteristic transient voltage plateau emerges, compare Fig. 4. The voltage curves presented in Fig. 5 show the relaxation after previous charging (CCCV) at a temperature of 0°C for the two structured and the two conventional cells. These environmental conditions already pose a challenge for rapid charging, but at the same time are close to application in the field of electric mobility. At a temperature of 25°C, either no Li-plating could be provoked or detected during these tests (charging up to 2C). Within preliminary tests, it could be shown that with a further increase of the charging current the upper cutoff voltage of 4.2 V was reached very quickly. Since the cells still had a very low SOC at that time, only a small amount of lithium had been transferred to the anode at all. However, since Li-plating occurs particularly at high SOCs (due to the approximation of the anode potential toward 0 V vs. lithium at high degrees of lithiation), no Li-plating could be detected. Therefore, the fast charge measurements at 25°C will not be discussed further.

Fig. 5a shows the voltage curve after a 0.1C charge, Fig. 5b after a 0.5C charge, Fig. 5c after a 1C charge, and Fig. 5d after a 2C charge. For the two slower charging processes, the termination criterion of the CV phase was when the charge current fell below 0.05C, while for the two faster charging processes, the termination criterion of the CV phase was set to 0.2C. As the re-intercalation of lithium also occurs during the CV phase prior to the rest period, the latter termination criterion was chosen so that all CV phases lasted for a similar amount of time. Thus, even while fast charging, a significant re-intercalation of lithium during the CV phase could be avoided, which ensures the comparability of the results. After a 0.1C charge (Fig. 5a), both the structured and the

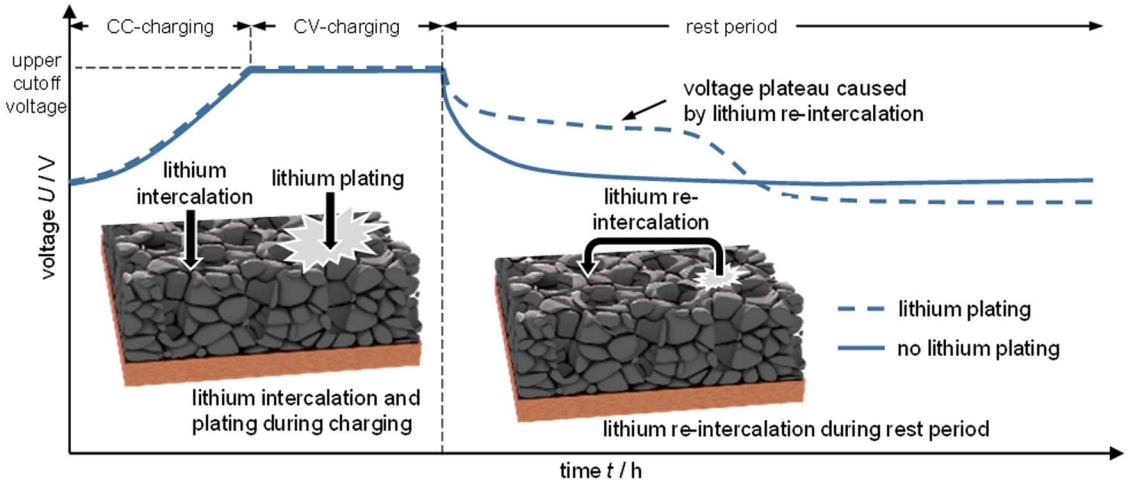

Figure 4. Schematic illustration of the Li-plating process with the corresponding voltage profile; in the rest period subsequent to charging, a voltage plateau is visible if Li-plating occurred during the previous charging process; this plateau forms due to the re-intercalation of the plated lithium into graphite, which takes place on a different potential level.

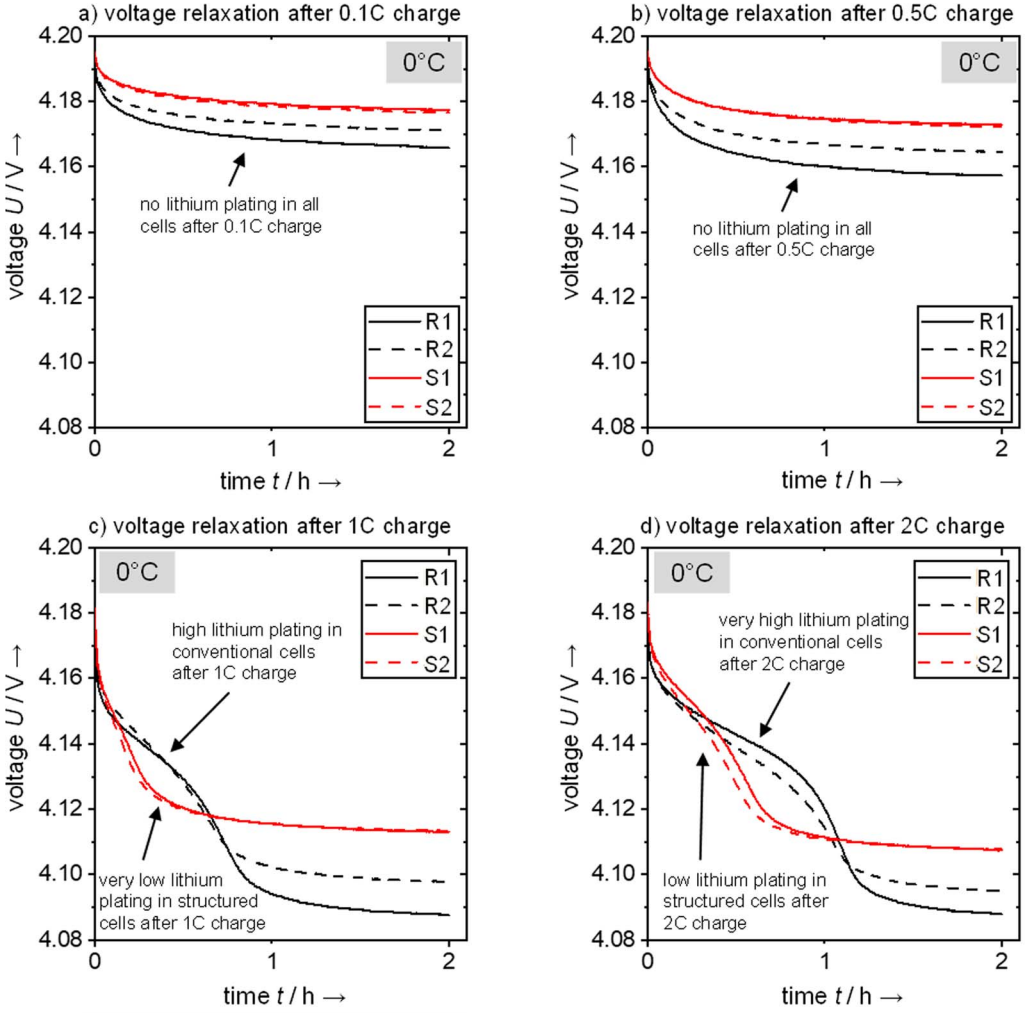

Figure 5. Voltage relaxation of conventional and laser-structured cells after CCCV charging at 0°C; in the CC phase different currents were applied: a) 0.1C current in CC phase, 0.05C cutoff current in CV phase; b) 0.5C current in CC phase, 0.05C cutoff current in CV phase; c) 1C current in CC phase, 0.2C cutoff current in CV phase; d) 2C current in CC phase, 0.2C cutoff current in CV phase; the on-set of Li-plating was observed at significantly higher charging C-rates for laser-structured cells than for conventional cells taken from the voltage plateau caused by lithium re-intercalation; at very high charging C-rates, Li-plating is strongly reduced; voltage relaxation is generally lower for laser-structured cells, indicating a better fast charging capability.

unstructured cells showed a voltage curve indicating that no Li-plating occurred during charging. However, a small difference of the final voltage after relaxation could be measured. While the OCV of the structured cells relaxed toward a voltage of approx. 4.18 V, this value was 4.17 V for the unstructured cells. This indicates that already at low charge currents of only 0.1C a stronger polarization occurred in the conventional cells and that this polarization could be reduced by laser structuring. The course of the voltage during relaxation after a charge with a current of 0.5C (Fig. 5b) was very similar. No indications of Li-plating were observed. For charging with a current of 1C (Fig. 5c), significant differences in the voltage curves were visible. While the cells with laser-structured anodes maintained a quasi-exponential voltage relaxation, the conventional cells showed a distinct voltage plateau. This plateau lasted for about 30 minutes before the voltage relaxed against a final OCV in the range between 4.08 V and 4.10 V indicating the occurrence of Li-plating during charging. Furthermore, the duration of the persistence of the plateau gives an indication about the severity of Li-plating. The longer the period of re-intercalation, the more lithium was metallically deposited during the charging process. A charging current of 1C at 0°C which already led to strong Li-plating for the conventional cells was still uncritical for laser-structured cells. This demonstrates the high potential of laser structuring, as safety risks and ageing originating from Li-plating are reduced, which suggests that increased charging currents may be used in fast-charging applications. Li-plating was observed for both cell types at a charging current of 2C (Fig. 5d), whereby the amount of deposited lithium varied significantly. The re-intercalation plateau was present for more than one hour for the conventional cells, whereas it was considerably shortened (approx. 30 minutes) for the structured cells.

The effects described above become even more pronounced when the time derivative of the voltage curve is depicted. The corresponding differential voltage curves are shown in Fig. 6. The end of the voltage plateau, which is expressed as a change in the slope of the voltage curve (cp. Fig 5), then appears as a local minimum and thus allows quantification of the completion of the lithium re-intercalation. In accordance to the slopes in Fig. 5a and Fig. 5b no pronounced minima are visible after charging with 0.1C and 0.5C. On the contrary, Fig. 6c clearly shows that a small amount of metallic lithium was plated, leading to a local minimum in the case of the structured cells after a 1C charge. However, the degree of the Li-plating of the unstructured cells is distinctly higher. Similar characteristics can be observed after a 2C charge.

At a temperature of −15°C, all charge and mass transport processes are significantly slower. Preliminary tests showed that charging with

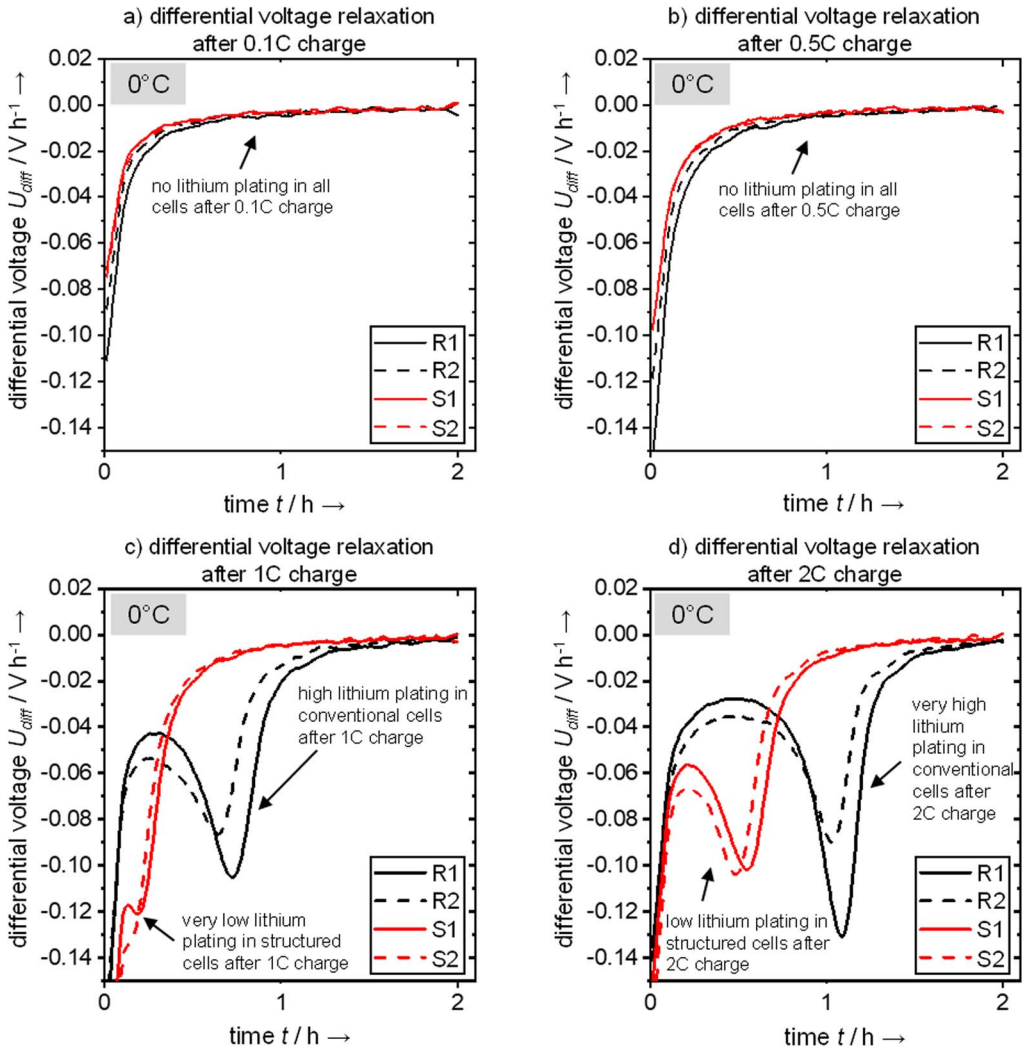

Figure 6. Differential voltage U_{diff} of conventional and laser-structured cells after CCCV charging at 0°C; in the CC phase different currents were applied: a) 0.1C current in CC phase, 0.05C cutoff current in CV phase; b) 0.5C current in CC phase, 0.05C cutoff current in CV phase; c) 1C current in CC phase, 0.2C cutoff current in CV phase; d) 2C current in CC phase, 0.2C cutoff current in CV phase; the on-set of Li-plating is observed at significantly higher charging C-rates for laser-structured cells than for conventional cells taken from the local minimum of U_{diff} caused by lithium re-intercalation; at 2C charging rate, Li-plating is strongly reduced expressed by the shorter re-intercalation time.

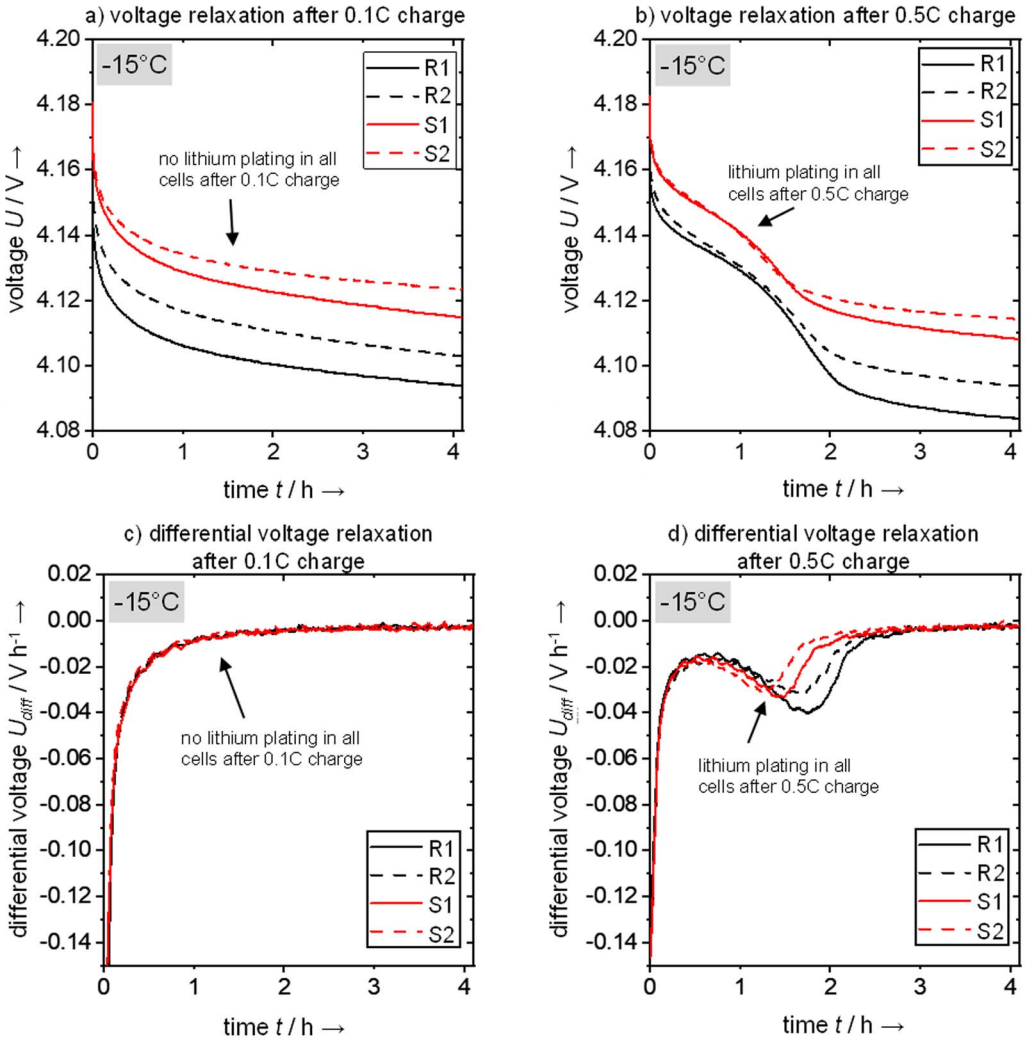

Figure 7. Voltage relaxation (a, b) and corresponding differential voltage relaxation (c, d) of conventional and laser-structured cells after charging with different currents at −15°C; the beneficial effects of laser structuring seen at 0°C are far less pronounced at −15°C indicating that other shares of the cell resistance become dominant.

1C and 2C lead to a fast increase in cell voltage and to a premature reach of the upper cutoff voltage. Thereby, no SOC higher than 50% could be reached in the CC phase. In this SOC range, no evidence of Li-plating was detectable. The authors attribute this to the low SOC of the cells at which Li-plating is unlikely to occur. Therefore, only the relaxation processes after 0.1C and 0.5C charging are described below. The results are presented together with the time derivative of the voltage curves in Fig. 7. It becomes evident that at a charging current of 0.1C, Li-plating did not occur in either the conventional cells or the cells with structured anodes. This conclusion can be drawn from the voltage relaxation (Fig. 7a) as well as the time derivative (Fig. 7c), where no local minimum is apparent. When charged with 0.5C, both cell types showed indications of Li-plating, expressed by the distinctive voltage plateaus (Fig. 7b) and the respective local minima in the differential voltage curves (Fig. 7d). Again, the trend toward reduced Li-plating of the structured cells can be observed, but less pronounced than at an ambient temperature of 0°C. Apparently, the reduction of the internal resistance by structuring is not as effective at −15°C. This may indicate that other cell internal processes, e.g. lithium diffusion within the graphite particles or at the phase boundaries between the electrolyte and the active materials, have a limiting effect. Thus, the ion transport in the electrolyte within the tortuous electrode structure no longer appears to be the limiting process. It should be noted that the re-intercalation process generally takes much longer at −15°C. After charging with 0.5C the re-intercalation takes approx. 1.5 hours for the structured cells and approx. 2 hours for the conventional cells. More detailed measurements with a higher resolution in the examined charging rates are required to determine the C-rate at which Li-plating first occurs at −15°C for both cell types.

Improvement of Fast Charging

As described in the previous sections, laser structuring reduces the mean tortuosity of the anode, resulting in lower overpotentials and lithium concentration gradients during charging and discharging. The lower overpotentials imply that the upper cutoff voltage during CC charging is reached at a higher SOC for cells with laser-structured anodes for a given charging current. As a result, the duration of the subsequent CV phase is reduced since a smaller amount of charge is necessary to reach an SOC of 100%. The respective charging times in the CC and CV phase were measured for the four cells S1, S2, R1, and R2. The results are shown in Fig. 8 for an ambient temperature of 0°C.

The laser structuring of the anodes and the associated change in the CC/CV ratio led to a significantly reduced time to achieve an SOC of 100%. While the conventional cells needed about 2.4 hours to be fully charged at a charge current of 0.5C, the structured cells required only 2.0 hours (Fig. 8a). To further investigate this, the SOC at which the

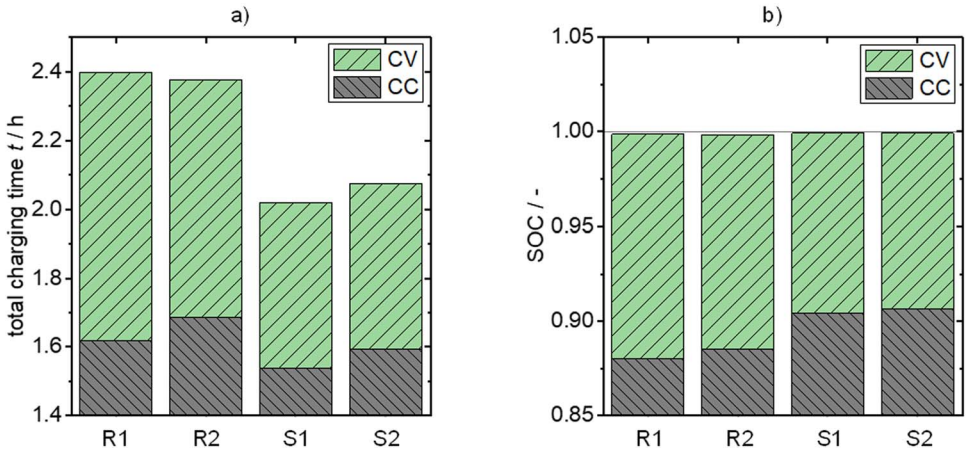

Figure 8. a) Charging times separated into the CC phase and the CV phase for laser-structured and conventional cells; b) achieved SOC separated into CC phase and CV phase. CC charging was 0.5C at 0°C. A reduction in charging time from approx. 2.4 h down to approx. 2.0 h was achieved, since higher SOCs were reached in the CC phase, reducing the remaining charging capacity for the CV phase significantly. An SOC of nearly 100% was achieved for all cells. No Li-plating occurred in the cells (cp. Fig. 5 and Fig. 6).

CV phase begins was examined (Fig. 8b). The results show that the CV phase does not start before an SOC of approx. 90% compared to approx. 88% for the conventional cells. Since the charge current drops rapidly at the beginning of the CV phase, substantially more time is required to reach the final SOC of 100%. This comparison proves that the laser structuring of anodes can have a significant positive influence on the charging time of lithium-ion cells, even in operating conditions that do not cause Li-plating.

Conclusions and Future Work

In this publication, the influence of laser structuring of the graphite anodes on the operating characteristics of LIBs was assessed. By using electrochemical impedance spectroscopy it was shown that the cell impedance and specifically the charge transfer resistance was significantly reduced by laser structuring. This was attributed to a reduced mean tortuosity that facilitated lithium transport as well as an increased mean porosity which provided a higher surface area for charge transfer. The laser structuring had a positive effect on both the discharge and charge process of the cell. For discharging, it was demonstrated that the amount of capacity and therefore energy provided was distinctly increased. This effect was particularly pronounced at low temperatures. The maximum improvements in deployable capacity were observed at varying discharge C-rates depending on the ambient temperature. At this point we would like to point out once again that some of these improvements were due to the slight reduction in the active material loading of the anode due to laser structuring. However, previously published work in the field of electrochemical simulation suggests that a directional porosity intentionally created by laser structuring has further positive impact.[31,33] In addition, the rapid charging behavior of the two cell types was investigated. A special focus was placed on the detection of Li-plating at different ambient temperatures and charging rates. Analyzing the OCV behavior after charging indicated that Li-plating could be avoided or strongly reduced by laser structuring. With a view to an automotive application, this may provide the possibility to carry out charging processes of the vehicle faster at low temperatures without the risk of provoking Li-plating. Furthermore, reduced charging times were measured, even under charging conditions uncritical with regard to Li-plating. The increased fast charging capability of the cells through the modification of the electrode design offers considerable potential for automotive applications. Particularly considering the trend toward higher energy densities of the electrodes, e.g. through higher densification or higher active material layer thicknesses, laser structuring can be an important approach for maintaining electrodes with high current capability. In future work, the authors will focus on the quantitative and locally resolved measurement of Li-plating in LIBs with laser-structured anodes. This includes both measurements with reference electrodes for monitoring the individual electrode potentials and post-mortem investigations. Furthermore, lifetime tests will be performed describing the effects of reduced Li-plating on the cyclic ageing of the cells. Ultimately, the scaling of the laser structuring process toward economic structuring speeds is required.

Acknowledgments

This work was financially supported by the German Federal Ministry of Education and Research (BMBF) under grant number 03CP0081 (ExZellTUM II) as well as the German Federal Ministry of Economic Affairs and Energy (BMWi) under grant number 03ET6103F (SurfaLIB). The authors gratefully acknowledge the support. The authors also thank Gamry Instruments for the loan of the potentiostat. There are no conflicts to declare.

ORCID

Jan Bernd Habedank https://orcid.org/0000-0003-2057-7037

References

1. K. G. Gallagher, S. E. Trask, C. Bauer, T. Woehrle, S. F. Lux, M. Tschech, P. Lamp, B. J. Polzin, S. Ha, B. Long, Q. Wu, W. Lu, D. W. Dees, and A. N. Jansen, *J. Electrochem. Soc.*, **163**, A138 (2015).
2. Q. Liu, C. Du, B. Shen, P. Zuo, X. Cheng, Y. Ma, G. Yin, and Y. Gao, *RSC Adv.*, **6**, 88683 (2016).
3. F. Jiang and P. Peng, *Scientific Reports*, **6**, 32639 (2016).
4. X.-G. Yang, Y. Leng, G. Zhang, S. Ge, and C.-Y. Wang, *Journal of Power Sources*, **360**, 28 (2017).
5. M. Broussely, P. Biensan, F. Bonhomme, P. Blanchard, S. Herreyre, K. Nechev, and R. J. Staniewicz, *Journal of Power Sources*, **146**, 90 (2005).
6. V. Zinth, C. von Lüders, M. Hofmann, J. Hattendorff, I. Buchberger, S. Erhard, J. Rebelo-Kornmeier, A. Jossen, and R. Gilles, *Journal of Power Sources*, **271**, 152 (2014).
7. C. Uhlmann, J. Illig, M. Ender, R. Schuster, and E. Ivers-Tiffée, *Journal of Power Sources*, **279**, 428 (2015).
8. M. C. Smart, B. V. Ratnakumar, L. Whitcanack, K. Chin, M. Rodriguez, and S. Surampudi, *IEEE Aerosp. Electron. Syst. Mag.*, **17**, 16 (2002).
9. M. C. Smart and B. V. Ratnakumar, *J. Electrochem. Soc.*, **158**, A379 (2011).
10. M. Petzl and M. A. Danzer, *Journal of Power Sources*, **254**, 80 (2014).
11. S. Schindler, M. Bauer, M. Petzl, and M. A. Danzer, *Journal of Power Sources*, **304**, 170 (2016).
12. J. Landesfeind, J. Hattendorff, A. Ehrl, W. A. Wall, and H. A. Gasteiger, *J. Electrochem. Soc.*, **163**, A1373 (2016).
13. V. Zinth, C. von Lüders, J. Wilhelm, S. V. Erhard, M. Hofmann, S. Seidlmayer, J. Rebelo-Kornmeier, W. Gan, A. Jossen, and R. Gilles, *Journal of Power Sources*, **361**, 54 (2017).

14. A. Nyman, T. G. Zavalis, R. Elger, M. Behm, and G. Lindbergh, *J. Electrochem. Soc.*, **157**, A1236 (2010).
15. A. D. Jara, A. Betemariam, G. Woldetinsae, and J. Y. Kim, *International Journal of Mining Science and Technology*, **29**, 671 (2019).
16. T. Günther, N. Billot, J. Schuster, J. Schnell, F. B. Spingler, and H. A. Gasteiger, *AMR*, **1140**, 304 (2016).
17. M. Ebner, D.-W. Chung, R. E. García, and V. Wood, *Adv. Energy Mater.*, **4**, 1301278 (2014).
18. D. D. Macdonald, *Electrochimica Acta*, **51**, 1376 (2006).
19. F. J. Günter, J. B. Habedank, D. Schreiner, T. Neuwirth, R. Gilles, and G. Reinhart, *J. Electrochem. Soc.*, **165**, A3249 (2018).
20. T. Momma, M. Matsunaga, D. Mukoyama, and T. Osaka, *Journal of Power Sources*, **216**, 304 (2012).
21. S. S. Zhang, K. Xu, and T. R. Jow, *Electrochimica Acta*, **49**, 1057 (2004).
22. M. Itagaki, K. Honda, Y. Hoshi, and I. Shitanda, *Journal of Electroanalytical Chemistry*, **737**, 78 (2015).
23. D. Andre, M. Meiler, K. Steiner, C. Wimmer, T. Soczka-Guth, and D. U. Sauer, *Journal of Power Sources*, **196**, 5334 (2011).
24. S. S. Zhang, K. Xu, and T. R. Jow, *Electrochemistry Communications*, **4**, 928 (2002).
25. M. Itagaki, N. Kobari, S. Yotsuda, K. Watanabe, S. Kinoshita, and M. Ue, *Journal of Power Sources*, **135**, 255 (2004).
26. C. H. Chen, J. Liu, and K. Amine, *Journal of Power Sources*, **96**, 321 (2001).
27. P. L. Moss, G. Au, E. J. Plichta, and J. P. Zheng, *Journal of Power Sources*, **155**, A986 (2008).
28. G. Ning, B. Haran, and B. N. Popov, *Journal of Power Sources*, **117**, 160 (2003).
29. J. B. Habedank, J. Endres, P. Schmitz, M. F. Zaeh, and H. P. Huber, *Journal of Laser Applications*, **30**, 32205 (2018).
30. J. B. Habedank, L. Kraft, A. Rheinfeld, C. Krezdorn, A. Jossen, and M. F. Zaeh, *J. Electrochem. Soc.*, **165**, A1563 (2018).
31. L. Kraft, J. B. Habedank, A. Frank, A. Rheinfeld, and A. Jossen, *J. Electrochem. Soc.*, **167**, 13506 (2020).
32. R. Morasch, B. Suthar, J. B. Habedank, J. Landesfeind, M. F. Zaeh, and H. A. Gasteiger, ModVal (2018).
33. V. P. Nemani, S. J. Harris, and K. C. Smith, *J. Electrochem. Soc.*, **162**, A1415 (2015).
34. C. L. Cobb and M. Blanco, *Journal of Power Sources*, **249**, 357 (2014).
35. C.-J. Bae, C. K. Erdonmez, J. W. Halloran, and Y.-M. Chiang, *Advanced Materials*, **25**, 1254 (2013).
36. M. S. Saleh, J. Li, J. Park, and R. Panat, *Additive Manufacturing*, **23**, 70 (2018).
37. D. L. Wood, J. Li, and C. Daniel, *Journal of Power Sources*, **275**, 234 (2015).
38. W. Pfleging, *Nanophotonics*, **7**, 13 (2018).
39. J. B. Habedank, F. J. Günter, N. Billot, R. Gilles, T. Neuwirth, G. Reinhart, and M. F. Zaeh, *Int J Adv Manuf Technol*, **102**, 2769 (2019).
40. J. Song and M. Z. Bazant, *J. Electrochem. Soc.*, **160**, A15 (2013).
41. C. von Lüders, V. Zinth, S. V. Erhard, P. J. Osswald, M. Hofmann, R. Gilles, and A. Jossen, *Journal of Power Sources*, **342**, 17 (2017).

Increasing the Discharge Rate Capability of Lithium-Ion Cells with Laser-Structured Graphite Anodes: Modeling and Simulation

Jan Bernd Habedank, Ludwig Kraft, Alexander Rheinfeld, Christina Krezdorn, Andreas Jossen, Michael F. Zaeh

Journal of The Electrochemical Society 165 (2018) 7, pp. A1563–A1573

Weblink: https://iopscience.iop.org/article/10.1149/2.1181807jes

Increasing the Discharge Rate Capability of Lithium-Ion Cells with Laser-Structured Graphite Anodes: Modeling and Simulation

Jan B. Habedank,[1,=] Ludwig Kraft,[2,=,*,z] Alexander Rheinfeld,[2,=,*] Christina Krezdorn,[1] Andreas Jossen,[2] and Michael F. Zaeh[1]

[1]*Institute for Machine Tools and Industrial Management, Technical University of Munich (TUM), Munich, Germany*
[2]*Institute for Electrical Energy Storage Technology, Technical University of Munich (TUM), Munich, Germany*

A physical-chemical model is suggested, which is able to describe the enhanced discharge rate capability of lithium-ion cells by using laser-structured graphite anodes. Recently published test data of coin cells comprising unstructured and structured graphite anodes with $LiNi_{1/3}Co_{1/3}Mn_{1/3}O_2$ cathodes is used for the presented purpose of modeling, simulation and validation. To minimize computational demand, a homogenized three-dimensional model of a representative hole structure is developed, accounting for charge and mass transport throughout the cell layers and one-dimensional diffusion within radial-symmetric particles. First, a standard pseudo-two-dimensional model is calibrated against rate capability test data of coin cells with unstructured anodes. The calibrated parameter set is transferred to the three-dimensional model in order to simulate the transient voltage response and the discharged capacity depending on the applied C-rate. The simulation data shows excellent agreement with experimental data for both cell types. Three stages of rate capability enhancement are identified showing an improved relative capacity retention of 11−24% at 3C. Experimental and simulation data reveal a restricted C-rate window, which can be positively affected by the structuring process, whereas both shape and pattern of the structuring process can be further optimized with the model.
 [DOI: 10.1149/2.1181807jes]

Manuscript submitted March 26, 2018; revised manuscript received May 4, 2018. Published May 23, 2018.

Lithium-ion batteries (LIBs) are the predominant energy storage solution for consumer electronics, electric vehicles and stationary energy storage devices. However, especially LIBs with high energy densities struggle to deliver sufficient energy at high discharge rates.[1] This rate limitation is caused by internal cell resistances of diverse origins, which has recently been reported to be dominated by the ionic resistance in the liquid electrolyte for common LIB electrode morphologies and operation strategies.[2,3] The electrodes of LIBs typically consist of active material particles mixed with binders and conductive agents and are coated onto metallic current collector foils. The pores of the electrodes and the electronically insulating separator are filled with the electrolyte solution, enabling ion transport between the electrodes. In most automotive LIBs, lithium nickel cobalt manganese oxide $Li(Ni_xCo_yMn_z)O_2$ (NMC) is employed as the cathode active material due to its high specific capacity and voltage level vs. Li/Li^+. For nearly all commercially available cells, graphite is used as the anode active material. Natural graphite particles have a flake-like shape, which makes them align parallel to the current collector foil during the coating and the subsequent calendering process. This particle orientation implies a strong tortuosity anisotropy within the graphite anodes, creating particularly long diffusion pathways for Li-ion transport through the electrode.[4] This results in large Li-ion concentration gradients within the electrode at high charge and discharge rates, causing concentration overpotentials and, consequently, a premature approach of the voltage limits resulting in an insufficient usage of the available capacity.[3]

Previously, it has been demonstrated that structured electrodes can have a positive impact on the cell's performance at higher current rates.[5] Multiple fabrication processes have been introduced, such as co-extrusion of the active material[6] and combinations of extrusion and sintering processes.[7] Many of the battery concepts involve a three-dimensional (3D) cell setup, in which the electrodes interlock on a micro or nano scale, creating a large reaction surface area and excellent charge transfer characteristics.[8] As laser-based manufacturing processes have been gaining importance in the processing industry over the past decades, particular attention has been given to laser-structuring of state-of-the-art electrodes. This concept involves high-precision ablation of a small fraction of the active material from the initial coating, generating additional diffusion pathways, which are solely filled with electrolyte. Significant improvements in rate capability were observed for laser-structured cathodes, e.g. consisting of lithium manganese oxide $LiMn_2O_4$,[9] as well as for graphite anodes.[10]

A few simulation-based approaches have been published in the past, explaining the improved rate capability for structured cathodes[6,11] and anodes[12] due to the reduced overall tortuosity of the electrodes. Based on the structuring process, a more homogeneous active material utilization is achieved and overpotentials are reduced during operation. To the knowledge of the authors, no experimentally validated physical-chemical model of LIBs with structured graphite anodes has been presented so far. Such a model, however, is needed to optimize the geometry of the superimposed structure while taking manufacturing constraints into account. In the work presented here, a homogenized 3D model of an NMC/graphite cell with laser induced microstructures within the anode is introduced taking one-dimensional (1D) diffusion within the solid particles into account. The adapted 3D+1D electrochemical model is based on Newman's pseudo two-dimensional (p2D) model of a LIB[13] accounting for both theories of porous electrodes and concentrated solutions.[14] The presented model is implemented and solved with the aid of a commercially available finite element method (FEM) tool. Geometrical features of the electrodes are matched to previously measured data.[10] Most relevant material parameters, such as the open circuit potentials of the used materials, were determined experimentally. The model is utilized to not only predict the transient voltage curves for discharge rates from C/5 to 10C and the derived capacity at the end of discharge, but also to determine Li-ion concentration gradients throughout the cell representing the cause of overpotentials during operation. The simulation results show excellent accordance with experimental data collected during the considered rate capability tests. Based on these results, the presented model can be used for optimizing a superimposed electrode structure, allowing for further improvements in terms of rate capability of LIBs.

Experimental

In this section, the experimental procedures for electrode fabrication, laser-structuring of the anodes as well as cell assembly and testing are described.

Electrode fabrication.—The components for the electrode inks were mixed with N-methyl-2-pyrrolidone (NMP, Sigma-Aldrich, USA) in a planetary vacuum mixer (Thinky Mixer ARV-310, Thinky, USA) for 10 min at ambient pressure and temperature. The graphite

=These authors contributed equally to this work.
*Electrochemical Society Student Member.
zE-mail: ludwig.kraft@tum.de

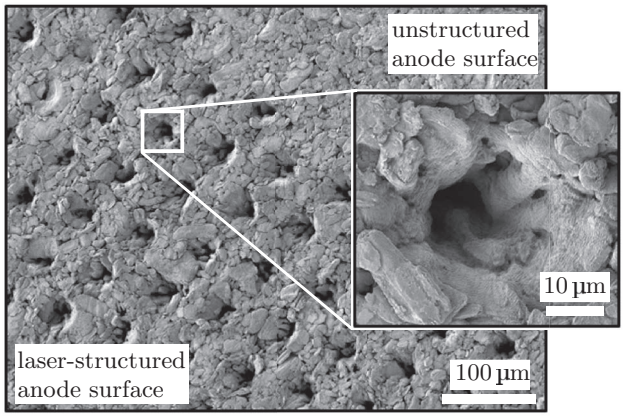

Figure 1. SEM image of a laser-structured anode with structured and unstructured parts.

ink contained 95 wt% graphite (SGL Carbon, Germany) and 5 wt% polyvinylidene fluoride (PVDF, Kynar, Arkema, France). The NMC ink was made of 96 wt% $LiNi_{1/3}Co_{1/3}Mn_{1/3}O_2$ (BASF, Germany), 2 wt% PVDF and 2 wt% conductive carbon (C65, Timcal, Switzerland). Slot die coating was performed in an industrial roll-to-roll coating machine (Coatema, Germany) equipped with an infrared dryer at a coating speed of 1 m min^{-1}. Subsequently, the coatings were calendered to a final porosity of approximately 35%. After calendering, the average coating thickness was 64 µm for both anode and cathode.

Laser-structuring of anodes.—For laser-structuring, a femtosecond laser (Spirit One 1040-8, Spectra-Physics, USA), operating at an infrared wavelength of $\lambda = 1040$ nm with a pulse duration τ_p of 400 fs was used. Only the anodes were structured, the NMC cathodes remained pristine as a larger effect on the overall tortuosity can be achieved in comparison. The beam diameter d_0 in the focal plane (on the electrode surface) was 17.2 µm and the peak fluence Φ_0 was 33.6 J cm^{-2}. The repetition rate f_{rep} used for ablation was 1 kHz and a pulse number $n = 100$ was applied to achieve an average structure depth d_s of approximately 52 µm and an average structure diameter of approximately 20 µm at the electrode's surface, measured with a confocal microscope. Toward deeper parts of the electrode (close to the current collector), the structures narrowed. The structures were spatially distributed in a hexagonal shape with a lateral length of 70 µm, resulting in approximately 20400 structures per cm^2. The ablated fraction of the coating materials for the chosen process parameters was around 5 wt% of the composite electrode material, determined by weighing electrodes before and after structuring. For more details on the experimental setup, the reader is referred to Habedank et al.[10] An image of the resulting structure distribution and geometry gained by means of scanning electron microscopy (SEM) is presented in Fig. 1. It becomes apparent, that the laser-induced structures are not uniformly shaped as the electrode consists of particles of different sizes and shapes. The local electrode conditions thus play a decisive role in the resulting characteristics of the structure.

Half cell assembly and open circuit potentials.—The open circuit potential curves of the utilized unstructured graphite and NMC electrodes were measured in 2032 type coin cells vs. a lithium metal electrode. The half cells were assembled in an argon filled glove box (M. Braun Inertgas-Systeme, Germany) with $H_2O < 0.1$ ppm and $O_2 < 0.1$ ppm. Each cell was filled with 150 µl of electrolyte (LP57, BASF, Germany), containing ethylene carbonate (EC) and ethyl-methyl-carbonate (EMC) in a ratio of 3:7 (by weight) with 1 M lithium-hexaflourophosphate ($LiPF_6$). As a separator, a glass microfiber sheet (Type 691, VWR, USA) was employed. In its uncompressed state, the separator has a thickness of 260 µm. Due to the compression during cell assembly, the separator thickness was estimated to be 200 µm.[15] For the measurement of the quasi open circuit potential as a function of the degree of lithiation, the cells were charged and discharged three times at rates of C/50 in a dry room at a controlled temperature of 20°C between 4.3 V and 2.9 V (NMC) and between 1.6 V and 0.05 V (graphite). In order to derive representative open circuit potential curves from this procedure, an averaging between lithiation (NMC) and delithiation (graphite) of the considered working electrode was carried out for all three C/50 cycles. The averaged open circuit potential curves that were used for modeling and simulation are shown in Fig. A1 in the Appendix. The individual cell capacities for specifying the applied C/50 current were calculated by determining the coating mass assuming mass specific capacities of 150 mAh g^{-1} for NMC and 360 mAh g^{-1} for graphite.

Full cell fabrication.—Three 2032 type coin cells with unstructured anodes and three coin cells with laser-structured anodes were assembled analogously to the half cell assembly described in the previous section. As common practice for Li-ion cells, the areal capacities of the graphite anodes were slightly overdimensioned compared to the NMC cathodes in order to account for irreversible losses during formation and to avoid anode potentials below 0 V, which would result in an undesired Li-plating reaction during charge. In the case presented here, an overdimensioning factor of approximately 1.2 of the pristine anode was chosen so that Li-plating could be avoided at all times during cycling. As only 5 wt% of the coating was removed during the laser-structuring process, this overdimensioning was considered sufficient so that Li-plating during charging could also be avoided in this case. As the mass loading of the pristine graphite anodes was kept constant, the structuring process inevitably resulted in a change in the capacity balancing of the electrodes. This effect needs to be taken into account especially during modeling and simulation and will be further discussed in the modeling section. As the electrolyte, LP572 (BASF, Germany) was used, which consists of EC and EMC in a gravimetric mixing ratio of 3:7 with 1 M $LiPF_6$ conductive salt and 2 wt% vinylene carbonate (VC). As the full cell test data has already been published elsewhere,[10] no further details on the cell fabrication procedure are discussed here. The focus of the work presented here lies on model validation by means of this experimental test data, which is why only essential information is given. Material and fabrication parameters relevant for modeling and simulation purposes are listed in the Appendix of this paper.

Formation procedure.—All cells went through a formation procedure of three charge and discharge cycles at a C-rate of C/10 in order to sufficiently form the solid electrolyte interphase (SEI) on the surface of the graphite particles before the subsequent rate capability test was carried out. Charging was conducted using a constant current/constant voltage (CCCV) operation with a cutoff current of C/20 and discharging was performed in a constant current (CC) procedure within a voltage window of 4.2 V to 3.0 V at a constant temperature of 20°C.

Rate capability test.—After formation, the cells underwent a rate capability test at a controlled temperature of 20°C whereas the applied current was derived from the capacity of the cell after the last formation cycle at C/10. The area-specific values for the adapted C/10 discharge current are shown in Table I for each individual cell considered in this study. As can be seen from this table, all cells investigated in this work showed comparable areal capacities with only slight deviations between the samples. This was considered to be of major importance in order to allow for a straightforward comparison in absolute capacity retention. Higher C-rates are a multiple of the corresponding C/10 discharge current. Charging was carried out following a CCCV procedure and discharging was performed in a CC procedure within a voltage window between 4.2 V and 3.0 V from C/10 to 10C. The constant voltage (CV) phase during charge was terminated when a charging current smaller than C/20 was reached. Charging currents were C/10 and C/5 for the corresponding discharge cycles of C/10 and C/5, respectively. After that, a charging current of C/2 was applied.

Table I. C/10 discharge currents matched to cell capacities of coin cells comprising unstructured and structured anodes.

		Discharge current in mA cm^{-2}
Unstructured anode	Cell 1	0.2399
	Cell 2	0.2535
	Cell 3	0.2597
	Average	0.2510
Structured anode	Cell 4	0.2597
	Cell 5	0.2445
	Cell 6	0.2501
	Average	0.2514

The resulting discharge rate capability is shown in Fig. 2. As can be seen from this figure, all investigated cells show quite comparable behavior. The cells containing structured anodes show an even more reproducible behavior compared to the cells with unstructured anodes. As can be clearly seen from the experiments in Fig. 2, the structuring process results in an overall improvement of the cell's absolute capacity retention, which becomes dominant beyond 2.5 mA cm^{-2} or 1C and fades again before 25 mA cm^{-2} or 10C. This effect will be further evaluated in the following sections.

Cyclic aging test.—Subsequent to the rate capability tests, the six coin cells comprising unstructured and structured anodes underwent a cycling test of 1000 cycles. The cells were charged with a CCCV procedure following a charging current of 1C until the cutoff voltage of 4.2 V and a cutoff current of C/5 in the CV phase. The discharge was carried out with a CC phase at a 1C discharge current until a cutoff voltage of 3.0 V. Similar to the rate capability tests, the ambient temperature was set to 20°C. The capacity retention of the first CC discharge cycle was used as a reference. The capacity fade of each cell as a result of cyclic aging is displayed in Fig. 3.

Modeling

In accordance with the homogenized p2D modeling approach for porous microstructures developed by Newman, Doyle and Fuller,[13,14,16] the model presented here consists of an anode, a separator, and a cathode domain in which both charge and mass transport are accounted for. The governing equations rely on porous electrode and concentrated solution theories and are listed in the appendix for the reader's convenience. Relevant model parameters representing the investigated coin cells are summarized in Table AI in the appendix. The Newman model originally considers a 1D representation through the layers of the electrochemical cell which is coupled to a second dimension representing radial-symmetric active material particles (i.e. 1D+1D, hence p2D). This approach has proven to be valid if the cell shows a homogeneous behavior in the second and third in-plane dimension which allows to neglect gradients in these dimensions as the cell behavior is dominated by through-plane charge and mass transport.[17,18] Only if these gradients cannot be ruled out due to e.g. the non-ideal spatial configuration of the current collectors and the positioning of the corresponding tabs, further means of model development need to be considered.[19,20]

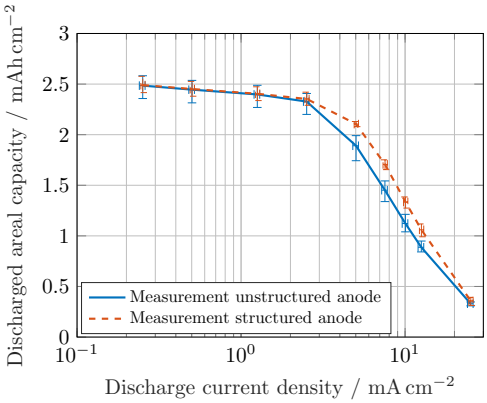

Figure 2. Measured area-specific discharge capacity as a function of applied current density of coin cells comprising unstructured and structured anodes.

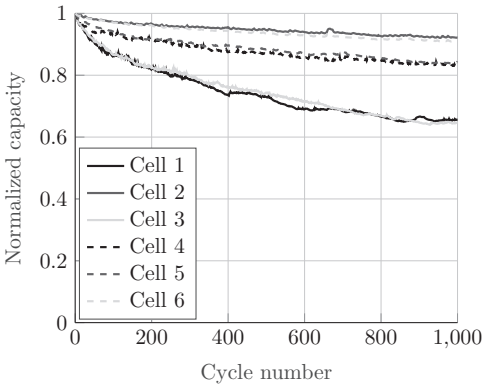

Figure 3. Normalized capacity retention during cycling of cells comprising unstructured anodes (Cell 1, Cell 2 and Cell 3) and structured anodes (Cell 4, Cell 5 and Cell 6).

In the case presented here, 1D and 2D models cannot be used to appropriately describe the hole structure created by the laser ablation process as gradients are expected to occur due to the spatial distribution of the superimposed structure. Furthermore, as already stated in the laser-structuring section, the hole structure is not uniform throughout the entire electrode but is highly dependent on the size and shape of the particles which are affected by the ablation process resulting in a rather coarse hole structure when visually comparing the holes one by one. In order to account for a representative hole structure on the one hand and in order to limit computational effort on the other hand, a homogenized 3D representation of the electrode layers is considered which is coupled to the aforementioned additional radial dimension representing the active material particles. This simplification follows the same line of thought initially suggested by the Newman group in order to efficiently describe porous insertion materials. If the electrode is large enough in terms of its planar dimensioning, every location along an electrode's normal vector can be represented by one particle that will be in contact with the surrounding electrolyte leading to the p2D approach, which is widely accepted and applied. The same principle accounts for a representative hole structure describing the general behavior of the structured electrode. Following this idea, there will be a particle at every location within the representative 3D structure which will be in contact with the surrounding electrolyte at this very location. Furthermore, a generalized or simplified hole structure representing the 20400 holes per cm^2 can be introduced. The specified differential equations have to be consequently solved in all three spatial dimensions of the homogenized 3D cell setup which implies:

$$\nabla := \left(\frac{\partial}{\partial x}, \frac{\partial}{\partial y}, \frac{\partial}{\partial z} \right) \quad [1]$$

Due to the increased spatial discretization effort, 3D models tend to have larger degrees of freedom (DOF), which inevitably causes a higher computational demand and, hence, longer computing times. To minimize the computational effort for solving the set of partial differential equations, the modeled electrode section takes most advantage of symmetry planes representing the structuring pattern. The definition of the modeled geometry is shown in Fig. 4. The laser ablation process creates holes in a hexagonal pattern as can be seen from Fig. 1. The x-direction of the modeled section represents the direction perpendicular to the layers of the cell following the same notation

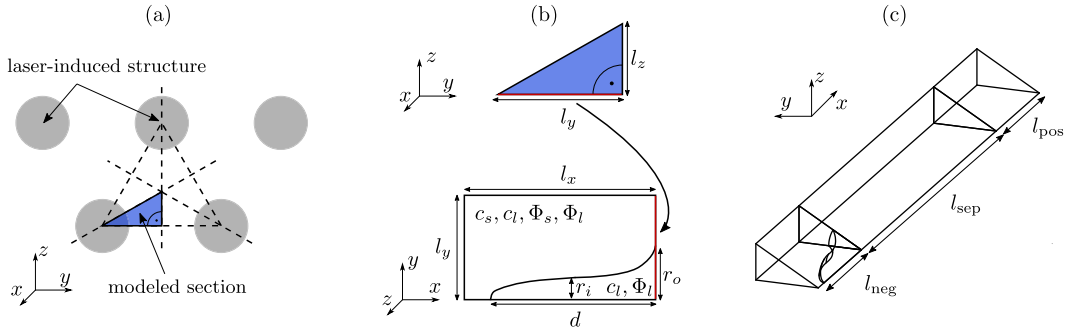

Figure 4. Definition of the modeled geometry using symmetry characteristics of the laser-structured anode. Representative anode surface (a), anode cross section (the state variables solved per domain are the solid and liquid phase Li-ion concentration c_s and c_l and the solid and liquid phase potential Φ_s and Φ_l, respectively) (b) and final 3D geometry implemented in the FEM tool (c).

as the original Newman model. As the holes are homogeneously distributed across the cell, a triangular section of the structured anode is sufficient to describe the entire cell behavior, see Fig. 4a. In this case, a 30° sector of the hexagonal structuring pattern is specified. The cross section of the anode is shown in Fig. 4b with l_x, l_y and l_z representing the length in x-, y- and z-direction, respectively. In this case, l_x is equal to the thickness of the negative electrode l_{neg}. The distance between the centers of two adjacent holes accounts for $2l_y$. The inner radius of the hole is described by r_i, the outer radius by r_o and the depth by d. As the structures are not perfectly cylindrical, the shape was built by using a cubic Bézier curve

$$B(t) = (1-t)^3 P_0 + 3(1-t)^2 t P_1 + 3(1-t)t^2 P_2 + t^3 P_3 \qquad [2]$$

The Bézier curve runs in the interval $0 \leq t \leq 1$. It starts at P_0 for $t = 0$ and terminates in the last control point for $t = 1$. Each control point P_n is defined by its x_n and y_n component, the shape of the curve was controlled by the weighting coefficients w_1 and w_2. The control points are provided in Table II.

$$P_n = \begin{pmatrix} x_n \\ y_n \end{pmatrix}, \; n = 0, 1, 2, 3 \qquad [3]$$

All remaining parameters are listed in the Appendix in Table AI. The resulting idealized 3D geometry is displayed in Fig. 4c. The volume fraction of the modeled hole is 5.1% of the initial anode volume, which is in good agreement with the results of the laser-structuring process. To account for a reduced anode volume, the initial degree of lithiation of the unstructured anode was increased from $0.78 \cdot c_{s,\,max,\,neg}$ (see Table AI) to $0.82 \cdot c_{s,\,max,\,neg}$ for the structured anode which represents this relative decrease. The thicknesses of the separator l_{sep} and the positive electrode l_{pos} are added to the geometry in x-direction.

The presented model of the Li-ion cell was implemented in the FEM-based software platform *COMSOL Multiphysics 5.3*. In order to depict the geometrical features of the hole, a high spatial discretization around the hole boundaries was chosen resulting in approximately 30000 DOF which need to be solved during computation. For comparison, a 3D model of an unstructured cell with a similar spatial discretization along the x-axis results in approximately 9000 DOF. For describing the unstructured cell, a classic p2D model with around 2000 DOF was chosen in order to save computing time.

Table II. x and y components of the four control points.

	x_n	y_n
P_0	$l_{neg} - d$	0
P_1	$l_{neg} - d$	$r_i w_1$
P_2	l_{neg}	$r_i w_2$
P_3	l_{neg}	r_o

In order to describe charge and mass transport in the porous microstructures of a Li-ion cell, a correction of the electrolyte's transport properties is necessary. An often used correction factor is the Bruggeman exponent which was empirically determined for porous structures formed of spherical particles. Recent research findings showed that the Bruggeman correction often underestimates the limitation of the transport properties especially in graphite electrodes formed of platelet-like particles.[4,21–24] In order to evaluate effective transport parameters, the tortuosity τ of the porous electrode structure needs to be known, which can be defined as the ratio of the direct path length to the effective path length of ion transport

$$D_{l,\,eff} = D_l \frac{\varepsilon_l}{\tau} = \frac{D_l}{N_M} \qquad [4]$$

$$\kappa_{eff} = \kappa \frac{\varepsilon_l}{\tau} = \frac{\kappa}{N_M} \qquad [5]$$

with D_l representing the diffusion coefficient in the liquid phase (i.e. the electrolyte), κ its conductivity and ε_l the volume fraction of the electrolyte, also known as the porosity of the porous structure. The ratio of the tortuosity to the volume fraction is also known as the Mac-Mullin number N_M.[24–26] Ebner et al. further demonstrated that the electrode's tortuosity for spherical particles (e.g. NMC) shows an isotropic behavior, but for cylindrical (e.g. lithium cobalt oxide $LiCoO_2$ (LCO)) and platelet-shaped particles (e.g. graphite), an anisotropy of tortuosity can be observed that cannot be neglected when considering charge and mass transport in all spatial dimensions of an electrode.[4] Especially the through-plane tortuosity of graphite τ_x is significantly higher than the in-plane tortuosity (with $\tau_y = \tau_z$). In order to account for this effect, an anisotropic tortuosity was implemented in the graphite anode with $\tau_x = 8$ and $\tau_y = \tau_z = 2.5$.[4] The separator and the NMC cathode were considered to inhibit an isotropic tortuosity of $\tau_x = \tau_y = \tau_z = 1.2$ and $\tau_x = \tau_y = \tau_z = 1.7$, respectively (see Table AI).

Results and Discussion

In this section, the data gained from the rate capability tests carried out for this work is presented and then discussed with the aid of simulation studies derived from the developed modeling approach. The results of the cyclic aging experiments carried out after the rate capability tests are discussed at the end of the section.

Effects of structuring on rate capability.—All rate capability tests were carried out as described in the experimental section at C/10, C/5, C/2, 1C, 2C, 3C, 4C, 5C and 10C at an ambient temperature of 20°C. As the coulombic efficiency of the C/10 cycles after the formation procedure was only 99.1% on average, this data is not considered in the further process of this work. The authors believe that the process of formation was not completely finished at this stage, which might falsify the observed trends if taken into consideration here. From the

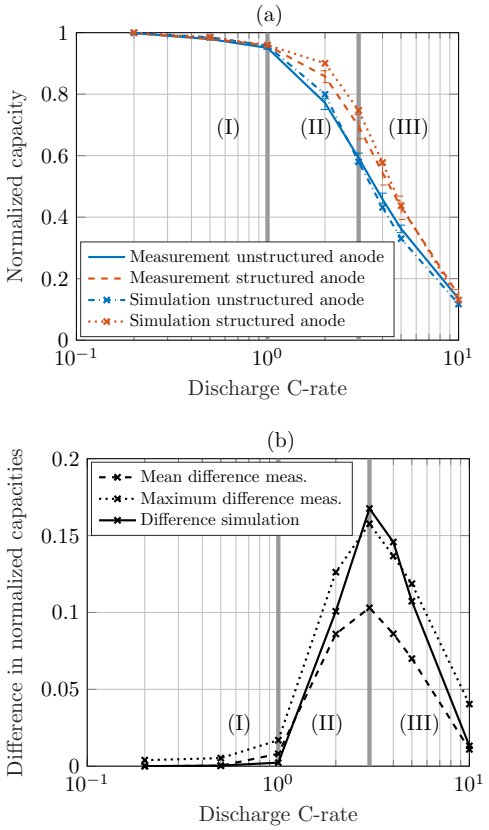

Figure 5. Comparison of measured and simulated C/5-normalized discharge rate capability of coin cells comprising unstructured and structured anodes (a) and observed difference in normalized discharge rate capability (b) within the three stages (I), (II) and (III).

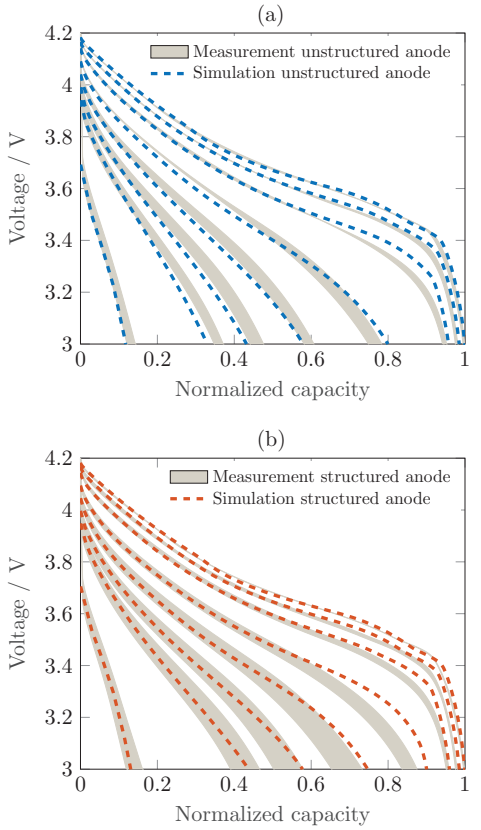

Figure 6. Comparison of measured and simulated discharge voltage curves as a function of C/5-normalized capacity for coin cells comprising unstructured (a) and structured anodes (b) for C-rates of C/5, C/2, 1C, 2C, 3C, 4C, 5C, and 10C (from right to left).

C/5 cycles onwards, all cycles showed efficiencies above this value rising toward 99.7%. Therefore, all further observations were focused on C-rates larger than C/10.

In Fig. 2, the mean area-specific discharged capacity is shown as a function of applied current density. As indicated by the error bars, a variation in both directions occurs, whereas the variation in applied current follows the notation presented in Table I, which is based on the derived capacity at the end of the carried out formation cycles. The cathode samples used for building the coin cells were chosen in such way, that the loading of the capacity limiting electrode, i.e. the cathode, was very similar for both unstructured and structured cells (see experimental section). This approach resulted in a highly reproducible area-specific capacity of approximately 2.5 mAh cm^{-2} at low current densities for all cells considered within this study, which guarantees a most straightforward comparison of the results gained from the rate capability tests. For the reader's convenience, besides area-specific values (see Fig. 2), also the capacity retention normalized to the C/5 discharge rate (see Fig. 5a) and the difference in normalized capacity retention (see Fig. 5b) is shown in this work. When looking into the difference in normalized capacity retention, the impact of electrode structuring can be categorized in three different stages depending on the applied C-rate and increase in derived capacity. The area-specific energy density is not shown here, as the voltage level only merely varies between coin cells with structured and unstructured anodes. Therefore, the area-specific capacity and area-specific energy density as a function of applied C-rate show very similar characteristics in this work. As the volume of the anode does not change with the structuring process, the volumetric energy density of the cell directly follows this trend. Based on the lower density of the electrolyte compared to the composite anode, the overall weight of the electrolyte soaked anode is reduced by approximately 3%. This will slightly improve the gravimetric energy density of the full cell. For all applied currents, the coin cells comprising structured anodes generally showed a larger discharged capacity compared to their unstructured counterpart, as can be seen in Fig. 2. In the case presented in this study, this effect suddenly becomes dominant at discharge current densities above 2.5 mA cm^{-2} or 1C reaching its peak impact around 7.5 mA cm^{-2} or 3C and steadily declines at current densities above this value as shown in Fig. 5b. As can also be seen from Figs. 2 and 5a, there is a rather gentle decrease of the discharged capacity with increasing current density up to 2.5 mA cm^{-2} or 1C, which then becomes more pronounced up to 7.5 mA cm^{-2} or 3C and then finally decreases again in its steepness. In order to understand the interplay of mechanisms leading to this effect, the presented model was applied. For this purpose, a standard p2D Newman model was considered first, in order to match the parameter set to the results of the rate capability tests with cells comprising unstructured anodes. As shown in Figs. 5a and 6a, the relative decline in capacity retention with rising C-rate at the end of the discharge as well as the transient characteristics of the voltage response during discharge can be depicted very well with the parameter set given in the Appendix.

This parameter set was then transferred to the 3D representation of the homogenized structured electrode model. With a simulated hole diameter of roughly 20 µm, 80% of penetration depth and 70 µm of distance between the centers of the holes, the rate capability tests performed on cells comprising structured anodes could also be depicted very well. Again, this accounts for both the absolute and the relative decline in discharged capacity with rising C-rate at the end of the discharge procedure (see Fig. 5a) as well as the transient characteristics of the voltage response during discharge (see Fig. 6b).

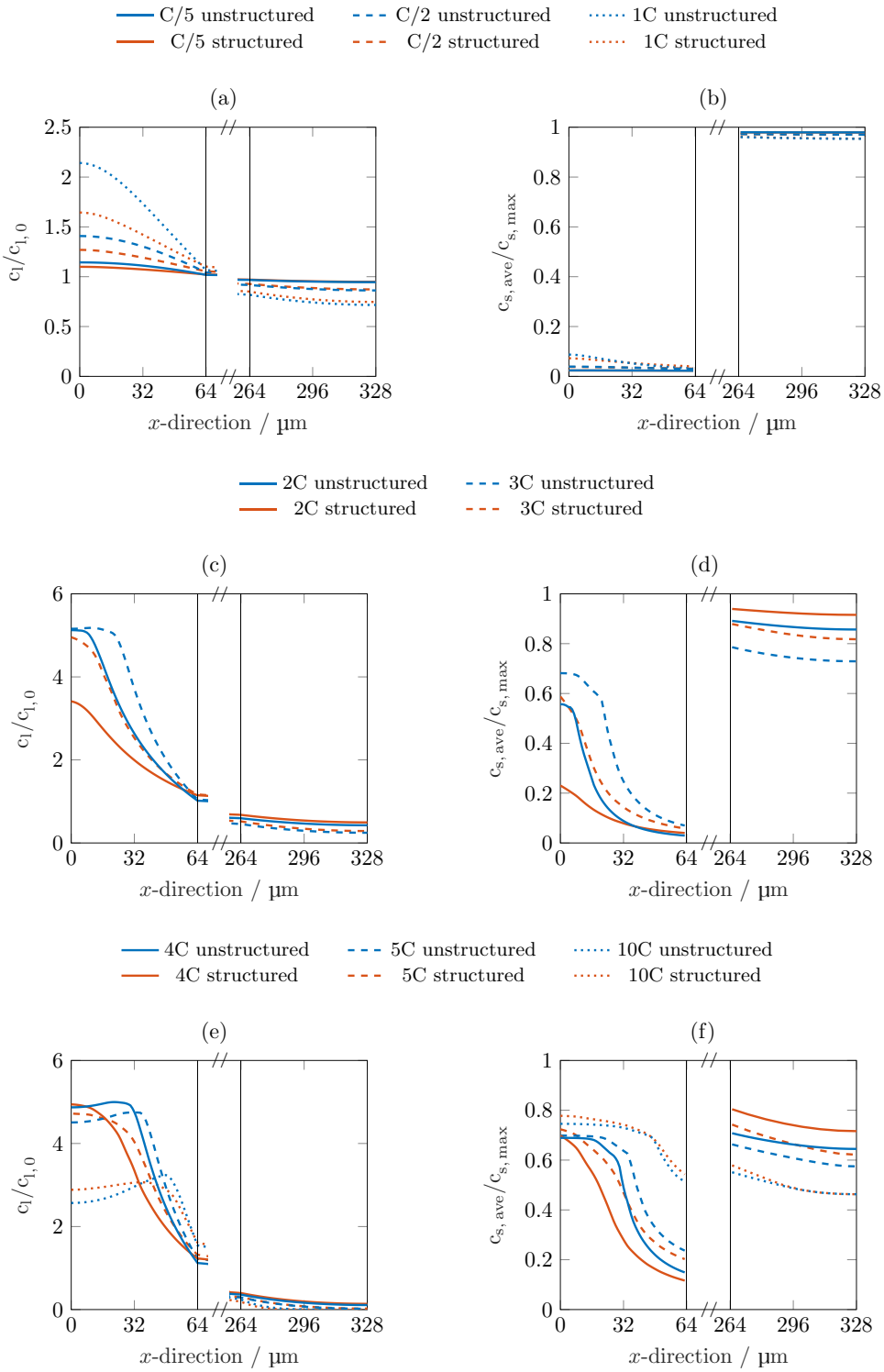

Figure 7. Li-ion concentration in both liquid (left) and solid phase (right) averaged along y- and z-direction at the end of the corresponding discharge step; solid phase concentration accounts for the mean concentration within the particle dimension.

Mechanisms of rate limitation.—When looking into Fig. 5a, the C-rates of C/5, C/2 and 1C are almost not affected by the structuring process. Also, the similar trend of the decline in discharged capacity hints at a limiting effect which is not influenced by the structuring process and consequently charge and mass transport in the liquid phase. This assumption can be proven when looking into Figs. 7a and 7b. The spatial distribution in liquid phase concentration at the end of the discharge procedure is almost identical for both the unstructured and structured cells with rising gradients between the anode and cathode for increasing C-rate. The same holds true for the spatial distribution in solid phase concentration. The utilization of the electrodes is constantly above 90% with almost no gradients along the thickness of the electrodes. At C-rates of 1C and below, this observation leads to the assumption that the capacity retention is mainly influenced by an increased potential drop based on ohmic losses and charge transfer kinetics with increasing C-rate. From 2C onwards, a

more homogeneous liquid phase concentration can be observed for the cells with structured anodes compared to those with unstructured anodes with lower maximum values, which positively influences the transport properties of the electrolyte (see Fig. 7c). This results in a considerably homogenized solid phase concentration along the electrode with lower mean values on the anode side which leads to higher overall solid phase concentrations on the cathode side at the end of the discharge procedure (see Fig. 7d). At C-rates of 4C and above, the homogenizing influence of laser beam structuring on both the liquid and the solid phase concentration is considerably diminished as shown in Figs. 7e and 7f. At these C-rates, the limiting influence in the liquid phase on the cathode side becomes increasingly dominant, reaching almost a complete depletion of Li-ions, which results in large overpotentials related to charge transfer kinetics (see Fig. 7e). In addition, the liquid phase concentration within the anode domain rises above 4 mol l^{-1} which significantly reduces both its conductivity and diffusivity resulting in large ohmic and diffusion based overpotentials. The electrolyte conductivity is reduced to 35% and the diffusivity to 14% at 4 mol l^{-1} compared to the values at the initial liquid Li-ion concentration of 1 mol l^{-1}. In order to improve the rate capability of the cell at these high discharge rates, further modifications need to be considered such as different electrolytes with enhanced transport properties at such high levels of Li-ion concentration or an additional structuring of the cathode to avoid a complete depletion of Li-ions.

These observations suggest a classification of the influence of laser beam structured anodes on the rate capability of the cells: At low C-rates, electrode morphology plays only a minor role in capacity retention making laser beam structuring obsolete in general, i.e. stage (I) between 0.1C and 1C in this case. At moderate C-rates, the effect of anode morphology and related effective transport properties becomes dominant, showing the largest benefit of laser beam structured anodes, i.e. stage (II) between 1C and 3C in this case. At high C-rates, not only the anode morphology is mainly influencing the occuring overpotentials, but also the electrolyte's inherent transport properties as well as the morphology of the separator and cathode are becoming increasingly important approaching a depletion of the electrolyte near the cathode current collector, i.e. stage (III) between 3C and 10C in this case. It is worth mentioning here, that the chosen glass fiber separator is not representative for commercial Li-ion cells, where separators are used which are about a magnitude thinner (i.e. approximately 10–30 µm). The glass fiber separator was used in this case due to ease of handling and comparability between half cell and full cell measurements. For the here presented results, this circumstance should only have a mere influence on the investigated rate capability as the overpotentials within the separator are dominated by the effective transport properties of the electrolyte, resembling an effective path-length of ion movement. The chosen glass fiber separator shows a MacMullin number of approximately 1.7 in its compressed state of 200 µm, which results in an effective path-length for the Li-ions of 340 µm. A standard polyolefin based separator with a thickness of 25 µm and a porosity of 40% inhibits a MacMullin number between 10 to 15,[24] resembling an effective path-length of 250–375 µm, which is very comparable to the chosen glass fiber separator.

In order to not only evaluate the through-plane but also the in-plane penetration depth of the structuring procedure, the 3D spatial distribution of Li-ion concentration in the solid and liquid phase was studied at the end of a 3C discharge step. For this purpose, five cut planes were introduced along the thickness of the structured anode (compare Fig. 4c) at a constant distance of 16 µm between them (see Figs. 8a and 8b). Looking into the spatial distribution of both the liquid and solid phase concentration, a fairly homogeneous coloring of the cut planes can be observed, whereby the coloring level is mainly dominated by the through-plane distribution in Li-ion concentration. This implies that the concentration gradients along the hole's axis are generally larger than the concentration gradients along the hole's radial direction.

Near the interface between the anode and the separator (i.e. planes V and IV), there is only little variation in Li-ion concentration throughout the cut planes in both the liquid and the solid phase. This tendency is confirmed when looking into the normalized liquid and solid phase concentration along the hypotenuse symmetry axis of the considered triangular electrode domain (see Figs. 8c and 8d). Furthermore, we observe an increasing gradient from the bulk material between the holes to the center of the hole with increasing distance to the separator along the depth of the holes (i.e. planes III and II). In case of the liquid phase concentration, the spatial distribution within the unstructured part of the electrode (i.e. plane I) becomes fairly homogeneous again, however, at significantly elevated levels of concentration. This jump becomes especially apparent when looking into the level of liquid phase Li-ion concentration within the hole (i.e. at $y = z = 0$ within planes V, IV and III) compared to the unstructured part of the electrode (i.e. at $y = z = 0$ within plane I). A similar trend in the solid phase concentration can be observed, whereas a considerable gradient in Li-ion concentration remains near the current collector in the range of a third to a half of the total through-plane concentration difference, which can be explained by the comparably slow diffusion-based equalization process within the solid phase compared to the liquid phase.[17] These observations imply that the penetration depth of the structuring process not only varies for the liquid and solid phase concentration but is highly dependent on the size and the depth of the hole as well as the distance between the holes. These results suggest that the size, the depth and the shape of the hole itself as well as the structuring pattern can be optimized in order to obtain an improved rate capability within a certain operating window and price range.

Cyclic aging behavior.—From the overall cycling behavior displayed in Fig. 3, no distinct indication can be observed that coin cells comprising structured or unstructured graphite anodes show superior aging characteristics. What is more, the developing spread between the cells might be a result of the manual cell assembly process or partial deterioration during the rate capability tests with high C-rates. Nevertheless, all cells comprising structured anodes reveal a capacity retention above 83% after 1000 cycles, whereas two cells with unstructured anodes already showed a capacity fade toward 65%. This leads to the conclusion that the laser-structuring process of the graphite anodes has no negative impact on the cyclic aging behavior of the coin cells. If coin cells comprising structured anodes even show an enhanced aging behavior needs to be evaluated by means of further measurements including more cells and cells that did not undergo a rate capability test before the carried out aging study.

Conclusions

Within this work, a combination of experimental and simulation-based evaluation of laser-beam structured graphite electrodes for enhancing the discharge rate capability of a NMC/graphite Li-ion cell was presented. As the experimental basis of this work, coin cells with a constant loading of approximately 2.5 mAh cm^{-2} were manufactured, whereas the NMC cathode was the capacity limiting electrode and the pristine graphite anode was oversized by approximately 20% in capacity so that the laser beam ablation of roughly 5 wt% did not result in an elevated risk of Li-plating during cycling. For simulation purposes, a representative homogenized microstructure model of the considered laser-beam-structured graphite electrode was developed and validated against rate capability tests, which were performed on both coin cells with unstructured and structured graphite electrodes.[10] In a first step, the underlying physical and chemical model parameters were adapted toward the unstructured coin cells with the aid of a standard p2D Newman-type model resulting in an excellent agreement between experimental and simulated rate capability tests. This parameter set was then transferred to the homogenized 3D+1D microstructure model, forming a representative triangular section of the structuring pattern making most use of symmetry planes in order to minimize computational effort. Due to the inevitably higher spatial discretization effort around the hole geometry, which was qualitatively approximated by a cubic Bézier curve toward SEM pictures, the computational demand

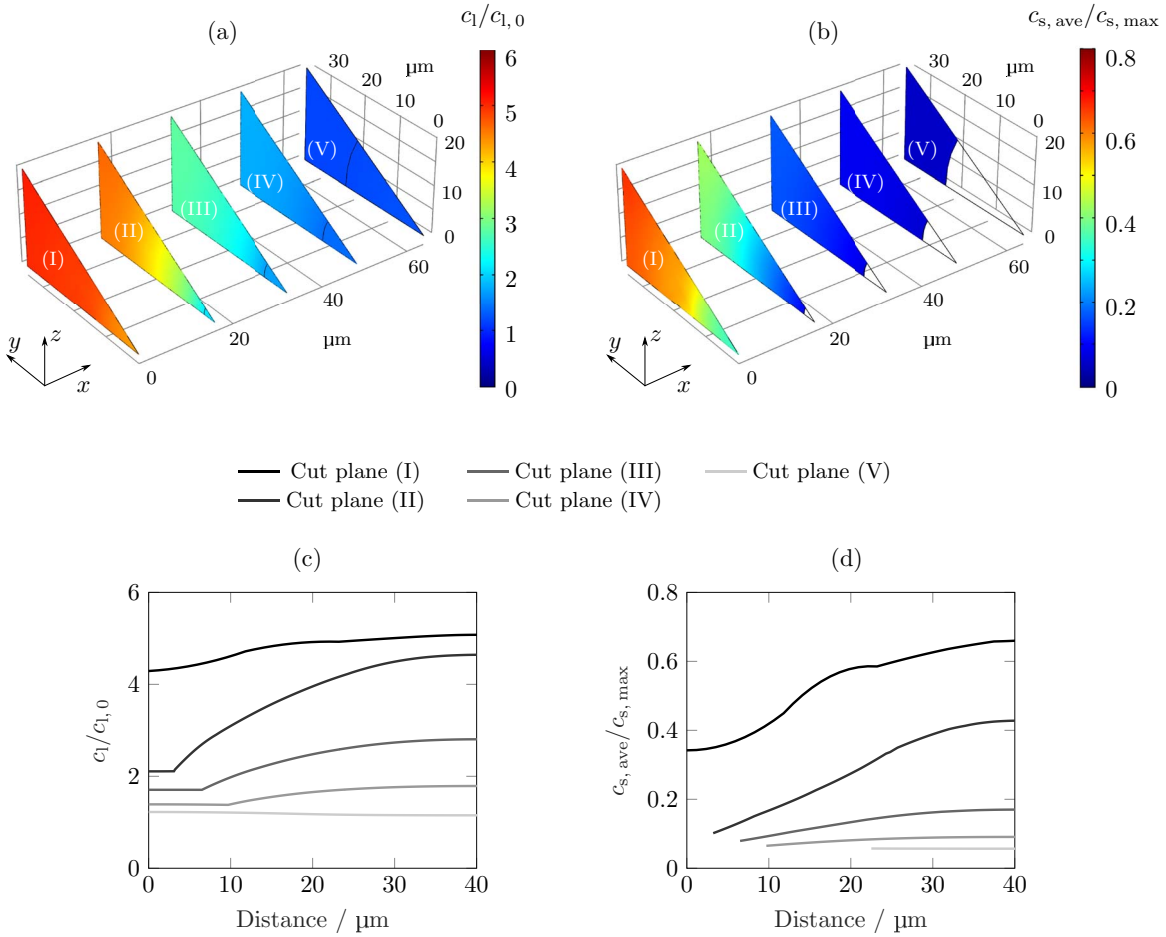

Figure 8. Liquid (a) and solid phase (b) Li-ion concentration on defined cut planes (I), (II), (III), (IV) and (V) (distance in x-direction: 0 μm, 16 μm, 32 μm, 48 μm and 64 μm, respectively) and liquid (c) and solid phase (d) Li-ion concentration along hypotenuse of cut planes at the end of a 3C discharge step within the structured graphite anode.

increased by a factor of approximately 15 compared to a standard p2D model (30000 DOF vs. 2000 DOF).

Simulated rate capability tests, which were carried out with the aid of the parametrized structured electrode model, were validated against experimental data showing again excellent agreement in terms of the transient voltage decline during discharge as well as the observed reduced capacity retention with increasing C-rate. It was shown, that for the electrode morphologies and materials considered in this case, the maximum benefit of structuring the graphite electrode was around a discharge rate of 3C. At low discharge rates, there is merely an influence of the structuring process (here up to 1C), which then suddenly changes at 2C rising toward its maximum impact at 3C of gaining between 10% and 15% in capacity compared to cells without structured graphite anodes at C/5. This corresponds to a relative improvement of capacity retention of 11–24% at 3C, at which the minimum and maximum capacity retention of the structured cells at 3C are related to the mean capacity retention of the unstructured cells at 3C. Beyond 3C, the impact of the structuring process declines again, however, at a comparably lower rate. This implies, that there forms a certain C-rate region in which the use of structured electrodes can considerably enhance a cell's rate capability forming an optimum. In other words, structured electrodes do not necessarily come with an overall improvement in rate capability of Li-ion cells at all applied currents as mass transport limitations within the electrolyte are still dominating at large currents despite the locally homogenized distribution in Li-ion concentration (e.g. overall electrolyte depletion in the NMC cathode[3]). When looking into the simulated spatial Li-ion concentration in the liquid and the solid phase at the end of discharge, the effect of the structuring process on the rate limitation becomes apparent. At low C-rates (i.e. C/5, C/2 and 1C or stage (I)), the structuring process has almost no influence on the solid phase concentration in both anode and cathode. Consequently, the amount of discharged capacity is rather limited by an increasing polarization due to ohmic losses and charge transfer kinetics instead of transport limitations in the liquid electrolyte. At higher C-rates (i.e. 2C and 3C or stage (II)), the homogenized liquid phase concentration has a more dominant impact on the distribution in liquid and solid phase concentration especially in the graphite anode which results in higher degrees of utilization within both electrodes. When further increasing the discharge rate (i.e. 4C, 5C and 10C or stage (III)), the positive impact of electrode structuring on the homogeneity of liquid phase concentration fades, which then results in a similarly inhomogeneous utilization of the graphite anode. What also becomes apparent is that the level in liquid phase concentration within the cathode generally decreases with increasing C-rate which is based on the ongoing depletion of the electrolyte resulting in increased charge transfer overpotentials. Similarly, the liquid phase concentration within the anode becomes excessively high ($> 4\,\mathrm{mol\,l^{-1}}$), which significantly reduces the inherent transport properties of the electrolyte, resulting in large ohmic and diffusion based overpotentials. This effect cannot be significantly influenced by a structuring of the anode but needs further modifications such as using enhanced electrolytes or including an additional structuring of the cathode.

The results shown in this work imply that not only the anode structuring process can enhance the discharge rate capability of the entire cell in a certain range but also that modeling and simulation

can help to understand the underlying mechanisms and interactions resulting in this enhancement. By evaluating the through-plane and in-plane distribution in Li-ion concentration throughout the electrodes, the ideal hole size, geometry and pattern can be identified in order to maximize the rate capability within a limited operating window. By further considering the costs of the electrode structuring process and also of the excess electrolyte within the holes, a cost-effective rate capability enhancement can be achieved. This can be best explained when considering Fig. 5b, where the peak location, height and width of the curve can be altered by changing the size, the shape and the pattern of the superimposed structure. In order to be able to reliably optimize the structure, inherent transport properties of the applied electrolyte need to be characterized well throughout the entire concentration range occurring during operation before salt precipitation takes place (i.e. beyond 4 mol l^{-1} in this case). The same holds true for a thorough characterization of the anisotropic electrode morphology. Further work will focus on this optimization procedure, not only for the graphite anode, but also for the NMC cathode during both discharge and charge operation for various electrode loadings. Furthermore, the model error accompanied with the homogenization of the microstructure will be evaluated and investigated in terms of means of a further model order reduction.

Acknowledgment

This work was financially supported by the German Federal Ministry of Education and Research (BMBF) under grant number 03XP0081 (ExZellTUM II) and 03XP0027G (MiBZ).

Appendix

In the experimental section, the open circuit potential measurements of the half cells were described. In Fig. A1, the derived curves are plotted as a function of degree of lithiation.

The developed model is based on the subsequent equations. For a more detailed description, the reader is referred to the work of the Newman group.[13,14,16] The most relevant model parameters used in this work are listed in Table AI. The mass balance is applied in the porous intercalation electrodes

$$\varepsilon_l \frac{\partial c_l}{\partial t} = \nabla \left(D_{l,\,\mathrm{eff}} \nabla c_l - \frac{i_l t_+}{F} \right) + \frac{3\varepsilon_s}{r_p} j_n \qquad [A1]$$

where ε_l is the porosity or the liquid phase fraction of the electrode domain, $D_{l,\,\mathrm{eff}}$ the effective diffusivity, i_l the ionic current density, F the Faraday constant, ε_s the solid phase fraction, r_p the particle radius and j_n the pore wall flux. In the separator, there is no charge transfer reaction taking place, hence, the mass balance simplifies to

$$\varepsilon_l \frac{\partial c_l}{\partial t} = \nabla \left(D_{l,\,\mathrm{eff}} \nabla c_l - \frac{i_l t_+}{F} \right) \qquad [A2]$$

The ionic current density accounts for the interaction between the different species in the electrolyte which is why the activity dependence is essential

$$i_l = -\kappa_{\mathrm{eff}} \nabla \Phi_l + \frac{2\kappa_{\mathrm{eff}} RT}{F} \left(1 + \frac{\partial \ln f_\pm}{\partial \ln c_l} \right) (1 - t_+) \nabla \ln c_l \qquad [A3]$$

with κ_{eff} being the effective ionic conductivity, Φ_l the potential in the liquid phase and R the ideal gas constant. At high C-rates the Li-ion concentration in the electrolyte can locally become very low due to transport limitations. To prevent the concentration from becoming zero or even negative, which causes instability of the model, a kinetic modification introduced by the Newman group[27] was implemented. The Butler-Volmer equation, which describes the charge transfer between the solid and the liquid phase on the particle surface is divided by a limitation term with $c_{\mathrm{lim}} = 1\ \mathrm{mol\,m^{-3}}$

$$j_n = \frac{i_0}{F} \frac{\exp\left(\frac{\alpha_a F}{RT}\eta\right) - \exp\left(-\frac{\alpha_c F}{RT}\eta\right)}{1 + \frac{c_{\mathrm{lim}}}{c_l} \exp\left(-\frac{\alpha_c F}{RT}\eta\right)} \qquad [A4]$$

α_a and α_c are the anodic and cathodic charge-transfer coefficients. The exchange current density i_0 is defined as

$$i_0 = F k_c^{\alpha_a} k_a^{\alpha_c} (c_{s,\,\max} - c_s)^{\alpha_a} c_s^{\alpha_c} \left(\frac{c_l}{c_{l,\,\mathrm{ref}}} \right)^{\alpha_a} \qquad [A5]$$

with $c_{l,\,\mathrm{ref}} = 1\ \mathrm{mol\,m^{-3}}$. $c_{s,\,\max}$ is the maximum Li-ion concentration in the solid phase and k_a and k_c are the anodic and cathodic reaction rates, respectively. The overpotential η is defined as a subtraction of the potential of the liquid phase Φ_l and the equilibrium voltage E_{eq} from the potential of the solid phase Φ_s

$$\eta = \Phi_s - \Phi_l - E_{\mathrm{eq}} \qquad [A6]$$

Finally, the following boundary conditions have to be maintained

$$\left. \frac{\partial c_l}{\partial x} \right|_{x=0 \& x=L} = 0 \qquad [A7]$$

$$\left. \frac{\partial \Phi_l}{\partial x} \right|_{x=0 \& x=L} = 0 \qquad [A8]$$

with $L = l_{\mathrm{neg}} + l_{\mathrm{sep}} + l_{\mathrm{pos}}$.

$$\left. \frac{\partial \Phi_s}{\partial x} \right|_{x=0 \& x=L} = -\frac{i_s}{\sigma} \qquad [A9]$$

with i_s being the electric current density.

$$\left. \frac{\partial \Phi_s}{\partial x} \right|_{x=l_{\mathrm{neg}} \& x=l_{\mathrm{neg}}+l_{\mathrm{sep}}} = 0 \qquad [A10]$$

$$\nabla i_l = -\nabla i_s \qquad [A11]$$

$$\left. \frac{\partial c_s}{\partial r} \right|_{r=0} = 0 \qquad [A12]$$

$$\frac{\partial c_s}{\partial r} = D_s \left(\frac{\partial^2 c_s}{\partial r^2} + \frac{2}{r} \frac{\partial c_s}{\partial r} \right) \qquad [A13]$$

$$-D_s \left. \frac{\partial c_s}{\partial r} \right|_{r=r_p} = j_n \qquad [A14]$$

In literature, only a few electrolytes used in Li-ion cells have been characterized adequately so that they can be used for the purpose of model parameterization.[27–31] Necessary characteristics are diffusivity, ionic conductivity and activity dependence of the electrolyte. These characteristics depend on the Li-ion concentration and on the

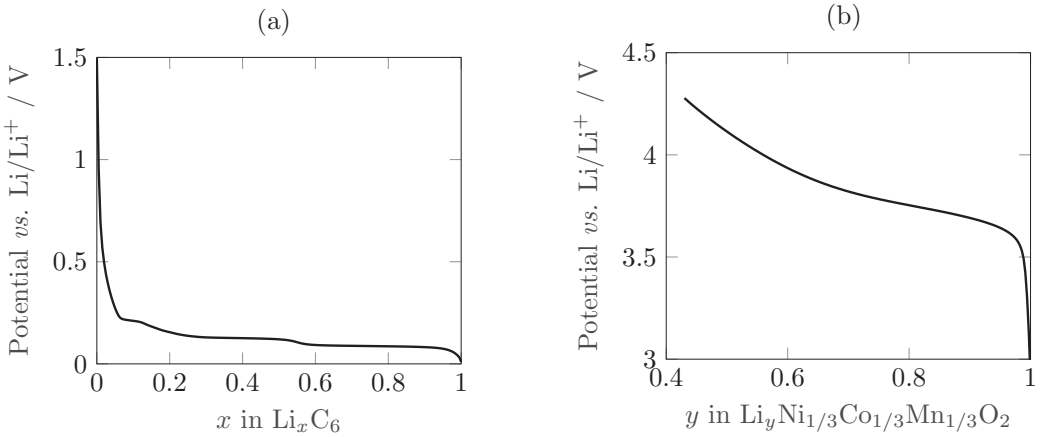

Figure A1. Open circuit potential curves for the graphite anode (a) and the NMC cathode (b) considered in this work.

Table AI. Model parameters used within this work; superscript *m* indicates measured values, *e* indicates estimated values (* value derived from D50 mass-median-diameter from datasheet, ** value derived from weight ratio of electrode composition); numeric values and magnitudes of parameters chosen in this study were referenced to literature where applicable.

Parameter	Anode	Separator	Cathode
Geometry			
Thickness l	64 µm ^{m}	200 µm[15]	64 µm ^{m}
Particle radius r_p	5 µm *		5.5 µm *
Solid phase fraction ϵ_s	0.59 **		0.52 **
Liquid phase fraction ϵ_l	0.32 ^{m}	0.7 ^{e}	0.35 ^{m}
Tortuosity through-plane τ_x	8[4]	1.2 ^{e}	1.7[4]
Tortuosity in-plane $\tau_{y,z}$	2.5[4]	1.2 ^{e}	1.7[4]
Thermodynamics			
Equilibrium voltage E_{eq}	Fig. A1a		Fig. A1b
Maximum lithium concentration $c_{s,max}$	32000 mol m^{-3}[32,33]		50000 mol m^{-3}[33]
Initial state of charge $\frac{c_{s,0}}{c_{s,max}}$	0.78 ^{e}		0.43 ^{e}
Kinetics			
Anodic reaction rate k_a	1×10^{-9} m s^{-1}[27]		1×10^{-9} m s^{-1}[27]
Cathodic reaction rate k_c	1×10^{-9} m s^{-1}[27]		1×10^{-9} m s^{-1}[27]
Anodic charge-transfer coefficient α_a	0.5[32,34]		0.5[32,34]
Cathodic charge-transfer coefficient α_c	0.5[32,34]		0.5[32,34]
Transport			
Solid diffusivity D_s	1×10^{-14} m^{2}s^{-1}[27,32]		1.8×10^{-13} m^{2}s^{-1}[33,35]
Solid conductivity σ	100 S m^{-1}[21,36]		10 S m^{-1}[35,36]

Parameter	Hole
Inner radius r_i	7.5 µm ^{m}
Outer radius r_o	22.5 µm ^{m}
Depth d	$0.8 \cdot l_{neg}$ ^{m}
Weighting factor w_1	1.1
Weighting factor w_2	0.6
Distance $2l_y$	70 µm ^{m}

Parameter	Electrolyte
Electrolyte diffusivity D_l	Eq. A15
Electrolyte conductivity κ_{fit}	Eq. A17
Activity dependence $\frac{\partial \ln f_\pm}{\partial \ln c_l}$	Eq. A18
Transport number t_+	0.4[27]

Parameter	Global
Temperature T	293.15 K ^{m}
Ohmic contact resistance R_Ω	1.3×10^{-3} Ωm^2 ^{e}

temperature, which is kept constant in this case. Due to various electrolyte compositions, the resulting curves differ slightly but overall show a similar trend.

The electrolyte diffusion coefficient and the electrolyte ionic conductivity were adopted according to Mao et al.[27] The corresponding unit for the following characteristic electrolyte functions is mol l^{-1} for the Li-ion concentration c_l and K for the temperature T

$$D_l = 5.34 \times 10^{-10} \exp(-0.65 c_l) \exp\left(\frac{2000(T-298)}{298T}\right) f \quad [A15]$$

$$\kappa = (0.0911 + 1.9101 c_l - 1.052 c_l^2 + 0.1554 c_l^3) \exp\left(\frac{1690(T-298)}{298T}\right) \quad [A16]$$

The electrolyte diffusion coefficient was slightly reduced by multiplying a factor $f = 0.85$. Mao et al.[27] used a polynomial fitting function for the ionic conductivity that is only valid in a certain concentration range. For concentrations above 3 mol l^{-1}, the conductivity starts to increase again due to the considered cubic fitting function. As larger Li-ion concentrations were observed in this work, the following fit was used, which is based on Eq. A16 with a constant temperature $T = 293.15$ K

$$\kappa_{fit} = 2.034 \left(\frac{c_l}{2.512}\right)^{0.55} \exp\left(-\left(\frac{c_l}{2.512}\right)^{1.55}\right) \quad [A17]$$

The effective diffusivity and ionic conductivity can be determined using the correction presented in Eqs. 4 and 5. The electrolyte activity dependence was taken from Valøen and Reimers[28] as it was neglected by Mao et al.[27]

$$\frac{\partial \ln f_\pm}{\partial \ln c_l} = \frac{0.601 - 0.24 c_l^{0.5} + 0.982 c_l^{1.5}(1 - 0.0052(T-294))}{1 - t_+} - 1 \quad [A18]$$

The equation contains a dependence of the transport number t_+, which was set constant, see Table AI.

ORCID

Jan B. Habedank http://orcid.org/0000-0003-2057-7037
Ludwig Kraft http://orcid.org/0000-0003-4324-426X
Alexander Rheinfeld http://orcid.org/0000-0003-0995-7266

References

1. M. Singh, J. Kaiser, and H. Hahn, "Thick Electrodes for High Energy Lithium Ion Batteries," *Journal of the Electrochemical Society*, **162**, A1196 (2015).
2. A. Nyman, T. G. Zavalis, R. Elger, M. Behm, and G. Lindbergh, "Analysis of the Polarization in a Li-Ion Battery Cell by Numerical Simulations," *Journal of The Electrochemical Society*, **157**, A1236 (2010).
3. K. G. Gallagher, S. E. Trask, C. Bauer, T. Woehrle, S. F. Lux, M. Tschech, P. Lamp, B. J. Polzin, S. Ha, B. Long, Q. Wu, W. Lu, D. W. Dees, and A. N. Jansen, "Optimizing Areal Capacities through Understanding the Limitations of Lithium-Ion Electrodes," *Journal of The Electrochemical Society*, **163**, A138 (2015).
4. M. Ebner, D.-W. Chung, R. E. García, and V. Wood, "Tortuosity Anisotropy in Lithium-Ion Battery Electrodes," *Advanced Energy Materials*, **4**, 1 (2014).
5. M. Osiak, H. Geaney, E. Armstrong, and C. O'Dwyer, "Structuring materials for lithium-ion batteries: Advancements in nanomaterial structure, composition, and defined assembly on cell performance," *Journal of Materials Chemistry*, **A 2**, 9433 (2014).

6. C. L. Cobb and M. Blanco, "Modeling mass and density distribution effects on the performance of co-extruded electrodes for high energy density lithium-ion batteries," *Journal of Power Sources*, **249**, 357 (2014).
7. C.-J. Bae, C. K. Erdonmez, J. W. Halloran, and Y.-M. Chiang, "Design of battery electrodes with dual-scale porosity to minimize tortuosity and maximize performance," *Advanced materials*, **25**, 1254 (2013).
8. S. Ferrari, M. Loveridge, S. D. Beattie, M. Jahn, R. J. Dashwood, and R. Bhagat, "Latest advances in the manufacturing of 3D rechargeable lithium microbatteries," *Journal of Power Sources*, **286**, 25 (2015).
9. J. Pröll, H. Kim, A. Piqué, H. J. Seifert, and W. Pfleging, "Laser-printing and femtosecond-laser structuring of $LiMn_2O_4$ composite cathodes for Li-ion microbatteries," *Journal of Power Sources*, **255**, 116 (2014).
10. J. B. Habedank, J. Endres, P. Schmitz, H. P. Huber, and M. F. Zaeh, "Femtosecond laser structuring of graphite anodes for improved lithium-ion batteries: Ablation characteristics and process design," *Journal of Laser Applications* (2018) (accepted for publication) 2018.
11. C. L. Cobb and S. E. Solberg, "Communication—Analysis of Thick Co-Extruded Cathodes for Higher-Energy-and-Power Lithium-Ion Batteries," *Journal of The Electrochemical Society*, **164**, A1339 (2017).
12. V. P. Nemani, S. J. Harris, K. C. Smith, and Design of Bi-Tortuous, "Anisotropic Graphite Anodes for Fast Ion-Transport in Li-Ion Batteries," *Journal of The Electrochemical Society*, **162**, A1415 (2015).
13. J. Newman and K. E. Thomas-Alyea, *Electrochemical Systems*, 3rd ed.; John Wiley & Sons, Inc.: Hoboken, New Jersey, 2004.
14. M. Doyle, T. F. Fuller, and J. Newman, "Modeling of Galvanostatic Charge and Discharge of the Lithium/Polymer/Insertion Cell," *Journal of the Electrochemical Society*, **140**, 1526 (1993).
15. J. Landesfeind, D. Pritzl, and H. A. Gasteiger, "An Analysis Protocol for Three-Electrode Li-Ion Battery Impedance Spectra: Part I. Analysis of a High-Voltage Positive Electrode," *Journal of the Electrochemical Society*, **164**, A1773 (2017).
16. T. F. Fuller, M. Doyle, and J. Newman, "Simulation and Optimization of the Dual Lithium Ion Insertion Cell," *Journal of the Electrochemical Society*, **141**, 1 (1994).
17. F. M. Kindermann, P. J. Osswald, G. Ehlert, J. Schuster, A. Rheinfeld, and A. Jossen, "Reducing Inhomogeneous Current Density Distribution in Graphite Electrodes by Design Variation," *Journal of The Electrochemical Society*, **164**, E3105 (2017).
18. F. M. Kindermann, P. J. Osswald, S. Klink, G. Ehlert, J. Schuster, A. Noel, S. V. Erhard, W. Schuhmann, and A. Jossen, ", Measurements of lithium-ion concentration equilibration processes inside graphite electrodes," *Journal of Power Sources*, **342**, 638 (2017).
19. S. V. Erhard, P. J. Osswald, J. Wilhelm, H. E. Hoster, and A. Jossen, "Simulation and Measurement of Local Potentials of Modified Commercial Cylindrical Cells: II: Multi-Dimensional Modeling and Validation," *Journal of The Electrochemical Society*, **162**, A2707 (2015).
20. S. V. Erhard, et al. Simulation and Measurement of the Current Density Distribution in Lithium-Ion Batteries by a Multi-Tab Cell Approach," *Journal of The Electrochemical Society*, **164**, A6324 (2017).
21. M. Doyle and J. Newman, "Comparison of Modeling Predictions with Experimental Data from Plastic Lithium Ion Cells," *Journal of the Electrochemical Society*, **143**, 1890 (1996).
22. K. K. Patel, J. M. Paulsen, and J. Desilvestro, "Numerical simulation of porous networks in relation to battery electrodes and separators," *Journal of Power Sources*, **122**, 144 (2003).
23. I. V. Thorat, D. E. Stephenson, N. A. Zacharias, K. Zaghib, J. N. Harb, and D. R. Wheeler, "Quantifying tortuosity in porous Li-ion battery materials," *Journal of Power Sources*, **188**, 592 (2009).
24. J. Landesfeind, J. Hattendorff, A. Ehrl, W. A. Wall, and H. A. Gasteiger, "Tortuosity Determination of Battery Electrodes and Separators by Impedance Spectroscopy," *Journal of The Electrochemical Society*, **163**, A1373 (2016).
25. R. B. MacMullin and G. A. Muccini, "Characteristics of porous beds and structures," *AIChE Journal*, **2**, 393 (1956).
26. M. J. Martínez, S. Shimpalee, and J. W. van Zee, "Measurement of MacMullin Numbers for PEMFC Gas-Diffusion Media," *Journal of the Electrochemical Society*, **156**, B80 (2009).
27. J. Mao, W. Tiedemann, and J. Newman, "Simulation of temperature rise in Li-ion cells at very high currents," *Journal of Power Sources*, **271**, 444 (2014).
28. L. O. Valøen and J. N. Reimers, "Transport Properties of $LiPF_6$-Based Li-Ion Battery Electrolytes," *Journal of the Electrochemical Society*, **152**, A882 (2005).
29. A. Nyman, M. Behm, and G. Lindbergh, "Electrochemical characterisation and modeling of the mass transport phenomena in $LiPF_6$–EC–EMC electrolyte," *Electrochimica Acta*, **53**, 6356 (2008).
30. M. Guo and R. E. White, "A distributed thermal model for a Li-ion electrode plate pair," *Journal of Power Sources*, **221**, 334 (2013).
31. H. Lundgren, M. Behm, and G. Lindbergh, "Electrochemical Characterization and Temperature Dependency of Mass-Transport Properties of $LiPF_6$ in EC:DEC," *Journal of the Electrochemical Society*, **162**, A413 (2014).
32. P. Ramadass, B. Haran, P. M. Gomadam, R. White, and B. N. Popov, "Development of First Principles Capacity Fade Model for Li-Ion Cells," *Journal of The Electrochemical Society*, **151**, A196 (2004).
33. S. Tippmann, D. Walper, L. Balboa, B. Spier, and W. G. Bessler, "Low-temperature charging of lithium-ion cells part I: Electrochemical modeling and experimental investigation of degradation behavior," *Journal of Power Sources*, **252**, 305 (2014).
34. M. Doyle and Y. Fuentes, "Computer Simulations of a Lithium-Ion Polymer Battery and Implications for Higher Capacity Next-Generation Battery Designs," *Journal of The Electrochemical Society*, **150**, A706 (2003).
35. M. Park, X. Zhang, M. Chung, G. B. Less, and A. M. Sastry, "A review of conduction phenomena in Li-ion batteries," *Journal of Power Sources*, **195**, 7904 (2010).
36. K. Smith and C.-Y. Wang, "Power and thermal characterization of a lithium-ion battery pack for hybrid-electric vehicles," *Journal of Power Sources*, **160**, 662 (2006).

Modeling and Simulation of Pore Morphology Modifications using Laser-Structured Graphite Anodes in Lithium-Ion Batteries

Ludwig Kraft, Jan Bernd Habedank, Alexander Frank, Alexander Rheinfeld, Andreas Jossen

Journal of The Electrochemical Society 167 (2020) 1, p. 13506

Weblink: https://iopscience.iop.org/article/10.1149/2.0062001JES

Modeling and Simulation of Pore Morphology Modifications using Laser-Structured Graphite Anodes in Lithium-Ion Batteries

Ludwig Kraft, [1,*,z] **Jan B. Habedank,** [2] **Alexander Frank,** [1] **Alexander Rheinfeld,** [1] **and Andreas Jossen** [1]

[1] *Institute for Electrical Energy Storage Technology, Technical University of Munich (TUM), Munich, Germany*
[2] *Institute for Machine Tools and Industrial Management, Technical University of Munich (TUM), Munich, Germany*

The energy density of lithium-ion batteries can be enhanced by using thicker and denser electrodes, which leads to transport limitations in the electrolyte within the porous structures. A pore morphology modification of the electrodes can counteract this limitation mechanism and provide higher rate capabilities of the cells. In this work, graphite anodes are structured with a picosecond laser in order to create transport pathways for the lithium-ions and allow for enhanced penetration of the electrodes. Experimental data from graphite/NMC-111 coin cells with varying areal capacities are used for the development and parameterization of an electrochemical model. The modified pore morphology of the structured electrodes is represented in the model by an adapted tortuosity, which results in lower lithium-ion concentration gradients and reduced diffusion polarization in the electrolyte. The effect of electrode thickness and tortuosity on limiting mechanisms is analyzed via simulation studies in order to derive the impact of structured electrodes. As a result, improved discharge as well as charge rate capability appears beside enhanced safety features such as increased tolerance versus hazardous lithium-plating during fast charging scenarios.
 [DOI: 10.1149/2.0062001JES]

Manuscript submitted June 11, 2019; revised manuscript received August 1, 2019. Published September 23, 2019. *This paper is part of the JES Focus Issue on Mathematical Modeling of Electrochemical Systems at Multiple Scales in Honor of Richard Alkire.*

Lithium-ion batteries are the prevailing energy storage system for electric vehicles, stationary energy devices, mobile applications and power tools.[1] Especially electric vehicles require increasing energy densities to offer a satisfactory driving range for customers.[2,3] While solid state technologies are under ongoing development, they face a lot of challenges and cannot provide the required energy density, current capability and cycling stability.[4] Therefore, lithium-ion batteries comprising porous electrodes filled with liquid electrolyte are still the state-of-the-art technology.

One way to increase the energy density is the use of new active materials,[2,3,5] e.g. combining a nickel-rich lithium nickel manganese cobalt oxide (NMC-811) cathode with a silicon/graphite anode.[6] The performance of an existing active material can also be enhanced by nanostructuring methods[7–10] or by changing the electrode formulation, composed of active material, binder and carbon black.[11–16] Another option lies in an optimized cell design in order to increase the share of active material and reduce the share of passive parts like current collectors, tab connectors or the housing.[17] Thicker and denser electrodes offer an opportunity to increase the required energy density independently of the used active material, but face issues when they are stressed with higher currents.[13,18–21] One major contributor are mass transport limitations in the electrolyte.[21–25]

Electrode pore morphology modifications provide a potential to overcome limitations arising from thicker and denser electrodes.[13,26–28] The path length, the lithium-ions have to travel in the electrolyte through the porous electrode, is defined by the thickness, the porosity and the tortuosity.[17,29] Primarily, high charge/discharge currents lead to a poor battery performance, as the overpotentials increase and the full capacity cannot be utilized.[28] Depending on the application and the desired requirements, current research focuses on improving the properties of anode[30–32] and cathode[33–37] composites by a modification of their structure. Besides an increased battery performance, an introduction of macro channels or pores into the electrode can lead to a reduced wetting time during the cell manufacturing process.[13,38]

The focus in this work lies on modified graphite anodes using a laser-structuring process.[31] It will be demonstrated, that lithium-ion cells comprising structured graphite anodes not only provide a higher discharge rate capability,[39] but also exhibit an opportunity to tackle issues concerning fast charging.[40] While the discharge performance, determined by the maximum discharge current, of state-of-the-art lithium-ion batteries is at a practical level for most applications, fast charging capability of energy storage systems is becoming more and more important. If the energy density of lithium-ion batteries cannot be increased to a satisfactory level, especially electric vehicles rely on fast charging capability to overcome range anxiety of potential customers.

Experimental data gained from measurements on graphite/NMC-111 coin cells comprising unstructured and structured graphite anodes with varying thicknesses are used for the development of an electrochemical pseudo two-dimensional (p2D) model. With the aid of simulation studies, the influence of the electrode pore morphology on the charging and discharging behavior is analyzed and design criteria of electrodes are provided.

Experimental

Electrode fabrication.—A rotation-revolution mixer (Speedmixer DAC 3000, Hauschild Engineering, Germany) was used to mix the components for the electrode inks with N-methyl-2-pyrrolidone (NMP, Sigma-Aldrich, USA) at ambient pressure and temperature. The cathode ink contained 96 wt% $LiNi_{1/3}Co_{1/3}Mn_{1/3}O_2$ (NMC-111) (BASF, Germany), 2 wt% polyvinylidene fluoride (PVDF, Kynar, Arkema, France) and 2 wt% conductive carbon (C65, Timcal, Switzerland). In terms of the anode, 95 wt% graphite (SGL Carbon, Germany) and 5 wt% PVDF were used. Doctor blade coating was performed in an industrial roll-to-roll coating machine (Coatema, Germany) equipped with an infrared dryer at a coating speed of 0.5 m min^{-1}. Four different anode and cathode coating thicknesses were prepared and subsequently calendered in order to achieve a final porosity of approximately 35%. The anode and cathode composition remained constant for each coating. The resulting electrode thicknesses accounted for 71 µm, 79 µm, 90 µm and 116 µm for coatings 1 to 4, respectively.

Laser-structuring of anodes.—For the electrode pore morphology modification, picosecond laser pulses from an Ytterbium fiber laser (YLPP-1-150V-30, IPG Photonics, USA) at infrared wavelengths were locally employed to ablate small fractions of the composite material and induce hole-like structures into the anode coatings. The cathode coatings as well as the current collectors of both electrodes remained pristine. The structuring process parameters were adjusted so that the holes reached down to the copper current collector, which resulted in an ablated fraction of around 5 to 10 wt% of the composite electrode material, depending on the electrode thickness, determined by

*Electrochemical Society Student Member.
[z]E-mail: ludwig.kraft@tum.de

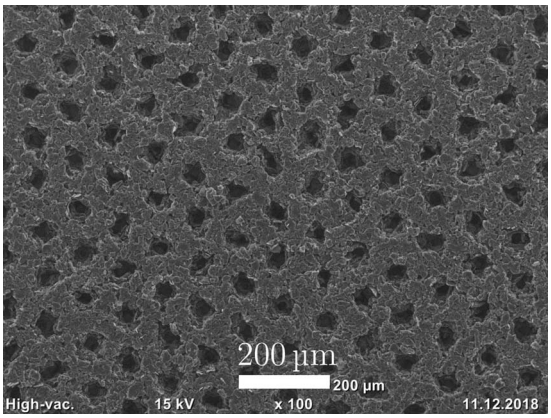

Figure 1. SEM image of a laser-structured graphite anode.

weighing the electrode sheets before and after structuring. The structures were spatially distributed in a hexagonal pattern with a lateral length of 100 µm. As more particles are removed in the structuring process close to the surface of the coating, the structures are not perfectly cylindrical. On the surface, the hole diameter was around 25 to 35 µm, but the structures narrowed toward the deeper parts of the electrode. The structuring process was performed with an average laser power of 10 W, a pulse repetition frequency of 1.2 MHz, a pulse energy of 8.33 µJ and an irradiation time of 0.6 ms per structure. The focal diameter of the laser beam was approximately 25 µm, measured with a high-precision beam diagnostics device (MicroSpotMonitor, PRIMES, Germany). For the deflection of the laser beam, scanning optics (Racoon 21, ARGES, Germany) were used. A scanning electron microscope (SEM) image of a laser-structured graphite anode is displayed in Fig. 1. For a more detailed description of the experimental setup for laser-structuring as well as process analyses, the reader is referred to our previous work.[31,38]

Coin cell assembly.—Coin cells of the type 2032 were assembled in an argon filled glove box (M. Braun Inertgas-Systeme, Germany) at purity (H_2O < 0.1 ppm, O_2 < 0.1 ppm). The cathode coins were punched at a diameter of 14 mm, the anode coins at a diameter of 15 mm. A glass microfiber sheet (Type 691, VWR, USA) with a diameter of 16 mm was used as separator. In its uncompressed state, the separator has a thickness of 260 µm. Due to the compression during cell assembly, the separator thickness is estimated to be around 200 µm.[41] The used glass fiber separator shows a high porosity and low tortuosity, compare Table AI, resulting in a MacMullin number of approximately 1.7. Separators used in commercial lithium-ion cells are thinner (15–30 µm) but exhibit a higher MacMullin number (5–15), which in turn results in a comparable effective path-length for the lithium-ions.[42] Particularly for the assembling of laboratory cells, these glass fiber separators provide a better ease of handling and serve as an electrolyte reservoir that prevents the cell from drying out during cycling.[43,44] Each cell was filled with 100 µl of electrolyte (LP57, BASF, Germany), containing ethylene carbonate (EC) and ethyl-methyl-carbonate (EMC) in a ratio of 3:7 (by weight) with 1 M lithium-hexaflourophosphate ($LiPF_6$). The assembly included two aluminum spacers, each with a thickness of 1 mm in order to fill the housing caps, a wave spring and an insulation ring.

Six coin cells – three cells with unstructured anodes and three with structured anodes – were assembled for each of the four loadings as shown in Table I. The cell capacities used for the formation procedure were calculated by determining the coating mass and assuming mass specific capacities of 150 mAh g^{-1} for NMC-111 and 360 mAh g^{-1} for graphite. The areal capacity of the anode coatings was overbalanced by approximately 20% compared to the capacity of the cathode coatings in order to have a N/P ratio greater than unity and to avoid lithium-plating during charging. The structured anodes still remained overbalanced since the loss of material during the ablation process only accounts for approximately 5–10 wt% of the coating. For a more even balancing, the anodes with more active material due to manufacturing tolerances were used for the structuring process. Additionally, cathodes with less active material, determined by weighing, were paired with anodes with less active material, i.e. the structured ones.

Formation procedure and rate capability test.—After assembly, all cells went through a formation procedure of three charge and discharge cycles at a constant current (CC) of C/10 related to their calculated capacity within a voltage window between 4.2 V and 3.0 V after the first charge. A detailed overview of the measurement procedures is given in Table II. All measurements were performed with a CTS battery test system (BaSyTec, Germany) in a custom-built climate chamber with a controlled ambient temperature of 25°C . The insulated climate chamber uses peltier devices for thermoelectric cooling to control the temperature, similar to the test chamber described by Rheinfeld et al.[45] After formation, a C/20 charge/discharge cycle was used to determine the nominal capacity of each coin cell, listed as average values of a set of three cells in Table I.

In the rate capability test, the cells were charged with a CC phase followed by a constant voltage (CV) phase, which remained unaltered, independent of the applied discharge current. Between each charge and discharge cycle a pause of 1 h was kept to allow for relaxation of the cells. In the discharge procedure, the cells with loading 1 and 2 were discharged with C/5, C/2, 1C, 2C, 3C, 4C, 5C and 10C. To have a better resolution, discharge currents of 1.5C, 2.5C, 3.5C, 4.5C and 6C were added for loading 3 and 4. The results of the rate capability test are shown in Fig. 2. The discharge capacities were referenced to the area of the cathode coins of 1.54 cm^2. Marginal deviations in the final

Table I. Characterization of the four loadings comprising unstructured and structured anodes.

Loading	Anode type	Abbreviation	Measured capacity[I]	Electrode thickness[II]	Modeled areal capacity[III]	Anode tortuosity
1	unstructured	L1U	3.54 mAh	71 µm	2.26 mAh cm^{-2}	5.5
	structured	L1S	3.42 mAh	71 µm	2.26 mAh cm^{-2}	3.5
2	unstructured	L2U	3.90 mAh	79 µm	2.50 mAh cm^{-2}	5.5
	structured	L2S	3.80 mAh	79 µm	2.50 mAh cm^{-2}	3.5
3	unstructured	L3U	4.57 mAh	90 µm	2.90 mAh cm^{-2}	8.5
	structured	L3S	4.33 mAh	90 µm	2.90 mAh cm^{-2}	5.5
4	unstructured	L4U	6.00 mAh	116 µm	3.82 mAh cm^{-2}	8.5
	structured	L4S	5.77 mAh	116 µm	3.82 mAh cm^{-2}	6.5

[I]average cell capacity determined by the C/20 discharge cycle.
[II]accounts for both, anode (l_{neg}) and cathode thickness (l_{pos}).
[III]derived from the averaged measured capacities and normalized to the cathode area of 1.54 cm^2.

Table II. Measurement procedures applied to the coin cells.

Procedure	Charge	Discharge	Cycles
Formation	CC @ C/10 until $U \geq 4.2$ V	CC @ C/10 until $U \leq 3.0$ V	3
Capacity check	CC @ C/20 until $U \geq 4.2$ V CV @ 4.2 V until $I \leq$ C/100	CC @ C/20 until $U \leq 3.0$ V	1
Rate capability test	CC @ C/2 until $U \geq 4.2$ V CV @ 4.2 V until $I \leq$ C/100	CC @ I_L* until $U \leq 2.7$ V	3 (for each I_L)

CC - constant current, CV - constant voltage.
*$I_{L1,L2}$ = C/5, C/2, 1C, 2C, 3C, 4C, 5C, 10C for loading 1 and 2.
$I_{L3,L4}$ = C/5, C/2, 1C, 1.5C, 2C, 2.5C, 3C, 3.5C, 4C, 4.5C, 5C, 6C, 10C for loading 3 and 4.

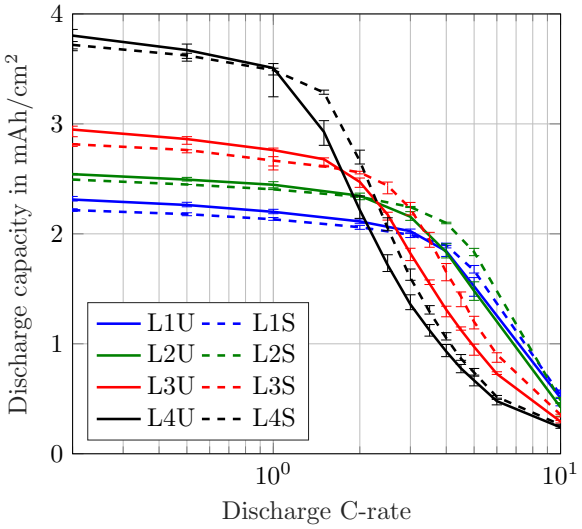

Figure 2. Measured area-specific discharge capacity of coin cells comprising unstructured and structured anodes for C-rates from C/5 to 10C.

coating thicknesses appeared in the range of manufacturing tolerances and led to slight deviances in the measured coin cell capacities.

Modeling

In our previous work, a homogenized 3D model of a representative hole structure was used to describe a structured anode.[39] Simulation results of lithium-ion concentrations in both the electrolyte and the active material helped to understand and clarify occurring inhomogeneities due to the structuring. Among the main findings were the reduced concentration gradients in the liquid electrolyte in the through-plane direction of the cell, which in turn led to the increased discharge rate capability. Moreover, it is difficult to represent the geometric shape of the induced holes in a 3D model. Each hole has a slightly different shape depending on the particles that were removed by the laser ablation process, compare to Fig. 1. In this work, a p2D model according to Doyle, Fuller and Newman[46,47] is used, which consists of the three 1D domains anode, separator and cathode, defined by their thickness l_{neg}, l_{sep} and l_{pos}, respectively. The governing equations are listed in the appendix in Table AII and the parameterization is shown in Table AI. Note, that reducing the spatial dimensions of the electrode to the through-plane dimension holds a simplification of the complex electrode structure. However, the 1D model comes with faster computational speed and is able to adequately describe the processes and limitations in the through-plane direction, which are the main contributors to the determinant cell performance.[39]

In 1D models the geometry does not account for porous structures, as is the case for the electrodes and the separators in a state-of-the-art lithium-ion battery with liquid electrolyte. Hence, an adaption is needed to appropriately represent the prolonged transport pathways in porous structures. This plays an important role, especially when high currents are applied to the cell and the limitation mechanisms in the electrolyte have a major contribution. To account for the morphology of porous structures in 1D models, the electrolyte transport parameters are modified by using a correction term to express the effective diffusivity $D_{l,eff}$ and conductivity κ_{eff} as shown in Eq. 1. An often used term in modeling is the Bruggeman correction,[5,48–52] where the factor α_{Brugg} was calculated to be 1.5 for materials with ideal spherical particles of identical size.[53] Since the electrode particles are not ideally spherical, e.g. natural graphite is platelet-shaped, and are not of the same size, a Bruggeman correction of $\alpha_{Brugg} = 1.5$ just states a lower limit for the correction factor.[17,29,54,55] The MacMullin number N_M, which can be defined as the ratio of the tortuosity τ and the porosity ε_l (Eq. 2) is another possible correction factor.[56]

$$\Psi_{l,eff} = \varepsilon_l^{\alpha_{Brugg}} \Psi_l = \frac{\varepsilon_l}{\tau} \Psi_l = \frac{\Psi_l}{N_M} \quad [1]$$

$$N_M = \frac{\tau}{\varepsilon_l} \quad [2]$$

No matter which correction term is used, a change in the factor will significantly influence the transport properties and thereby the cell behavior. The structuring process modifies the electrode pore morphology and enhances the lithium-ion transport in the electrolyte which has a positive effect on the capacity retention in a certain range of discharge currents.[39] Based on the parameter set of the cells comprising unstructured anodes, a reduction of the MacMullin number is utilized to describe the behavior of the cells comprising structured anodes. Thus, either a reduction in the electrode's tortuosity or an increase in the porosity will improve the local transport properties. However, an increase in the porosity has a higher influence because it directly affects the mass balance

$$\varepsilon_l \frac{\partial c_l}{\partial t} = -\nabla N_l + R_l \quad [3]$$

Regarding the discharge of the cell, i.e. the delithiation of the anode, a higher anode porosity means that there is more space for the lithium-ions in the pore volume and the absolute lithium-ion concentration in the electrolyte c_l is lowered. The lithium-ion concentration in turn has a crucial effect on the electrolyte transport properties, see Table AI.

In this work, the tortuosity was adapted in the model to represent the pore morphology change by the structuring process of the graphite anode. In order to maintain comparability between the different loadings, the sensitivity analysis in this work investigates varying tortuosities only and neglects the alternation of porosity, which may be correlated with a change in tortuosity. The discharge rate behavior of the loadings was adjusted via the electrode thickness and the anode tortuosity, all other modeling parameters remained unaltered. Tortuosity measurements via impedance spectroscopy or 3D tomography offer information about the electrode morphology.[21,29,55,57,58] The tortuosities used in this work are based on values found in the literature, where platelet-shaped natural graphite exhibits comparatively high through-plane values.[29,55] The parameters for the characterization of the different loadings are listed in Table I, whereas the general

model parameters are listed in Table AI. The electrode thickness is the same for the anode (l_{neg}) and the cathode (l_{pos}).

The temperature was set constant to 25°C in the model, owing to the low cell capacities compared to the high heat capacity of the coin cell setup. All measurements were performed at the same ambient temperature, so even for the highest cell capacity of 6 mAh and a discharge current of 10C, no temperature rise was detected. All C-rates used in the simulation studies are referenced to the modeled areal capacities in Table I, which were averaged and remained constant for each loading to allow a better comparison between unstructured and structured anodes.

Overpotential analysis.—The p2D model was implemented in the commercial FEM solver *COMSOL Multiphysics 5.3a*. According to Nyman et al.,[22] the total cell polarization can be ascribed to local potentials and concentrations solved in the p2D model and is composed of the following six sub-processes, the equations are listed in Table AIII:

- Diffusion polarization in the liquid phase
- Diffusion polarization in the solid phase
- Ohmic potential drop in the liquid phase
- Ohmic potential drop in the solid phase
- Activation overpotential
- Contact resistance

The limitation mechanisms in the simulation studies are analyzed via using this implicit characterization method based on the actually solved concentrations and potentials in time and over the electrode thickness. In the separator domain, only diffusion polarization and ohmic potential drop in the electrolyte occur, as there is no active material and no reaction takes place. The contact resistance $R_{contact}$ cannot be ascribed to a single domain and is therefore listed separately in the later analysis. In the model, the cell voltage is corrected by the voltage drop resulting from the contact resistance ($R_{contact} \cdot i_{app}$).

Lithium-plating indication.—Charging a lithium-ion cell can induce lithium-plating on the surface of the graphite anode particles, particularly at low temperatures and high charging currents.[59] Up to a certain extent, this reaction is reversible and the plated metallic lithium gets oxidized either by intercalating into the graphite particles during relaxation or by stripping/dissolution in an subsequent discharge cycle.[60,61] However, part of this reaction remains irreversible and plated lithium tends to form dendrites that can penetrate the separator and cause severe safety problems.[62]

With an equilibrium potential of 0 V vs. Li^0/Li^+, the necessary condition of the lithium-plating reaction is an overpotential of $\eta_{Li} \leq 0\,V$.[52,63–65] The lateral electrode dimensions and the tab positions can cause an inhomogeneous distribution of the current density and therefore result in different local potentials.[6] Besides, both the anode and the cathode properties and the balancing of the two electrodes play an important role for the likelihood of lithium-plating.[64] Regarding the used 1D model, the lithium-plating reaction is presumably most pronounced at the anode/separator interface and the local potential criterion $\Phi_s - \Phi_l \leq 0\,V$ can be interpreted as an indicator for lithium-plating during a charging procedure.[6] Based on this criterion, various fast charging scenarios were evaluated in the later simulations.

Results and Discussion

Model validation and simulation.—For validation of the developed model, the data from Fig. 2 is normalized to the C/5 discharge capacity of each loading and compared to the simulation results, which is shown in Fig. 3a. By normalization of the the discharge capacity, it is more obvious that the lower loadings can withstand higher C-rates. The curves shift from the highest loading L4U to the lowest loading L1U on the very right side. The curves of the cells comprising structured anodes (dashed lines) all bend at higher C-rates so that these lie right of their unstructured counterparts of the same

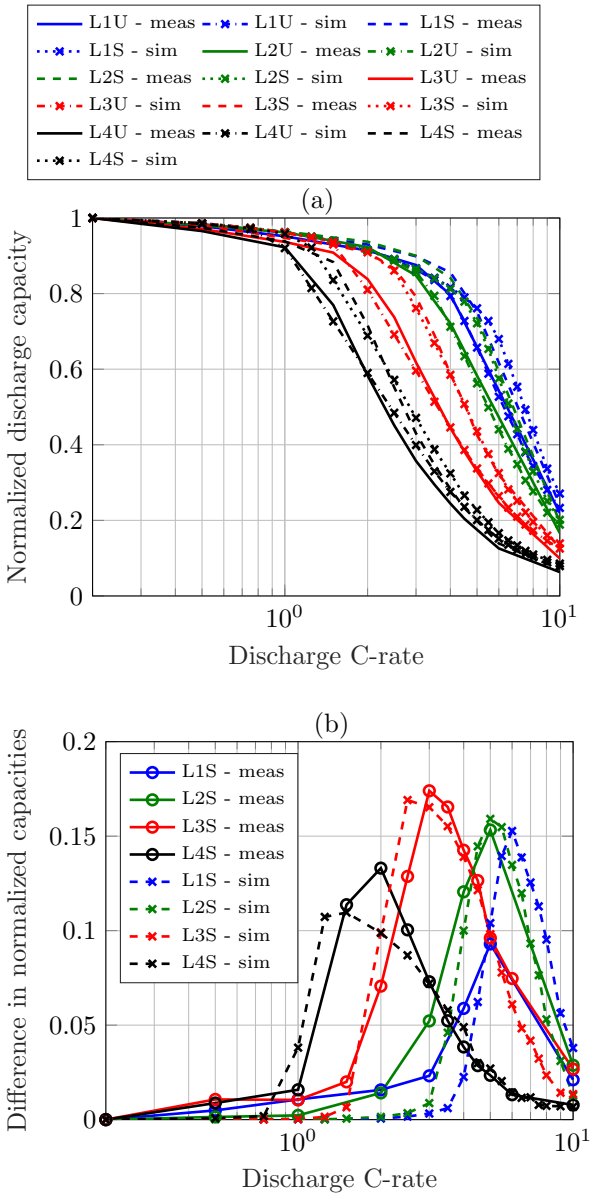

Figure 3. (a) Comparison of measured and simulated C/5-normalized discharge rate capability of coin cells comprising unstructured and structured anodes and (b) observed difference in normalized discharge rate capability.

loading (solid lines). The simulation results represented by the dash-dotted lines for the unstructured electrodes and the dotted lines for the structured electrodes are in good agreement with the measurement data.

The validation of the measured and simulated discharge voltage curves is shown in the appendix in Fig. A1. The gray shaded areas represent the margin of the measured discharge voltages of each set of coin cells for the specified loading. The experimental and simulated rate capability tests covered a wide span of discharge C-rates, for validation of the voltage profiles, the C-rates C/5, 2C, 5C and 10C were selected. In the simulations, only the electrode thickness, the applied current density and the anode tortuosity were adapted to the different loadings and the measurement data is in very good agreement with the simulation results.

The benefit of the structuring process appears in the difference in normalized capacities of the cells comprising structured and unstructured anodes, see Fig. 3b. A categorization in three different stages is visible: for low applied C-rates there is no improvement induced by the

structuring process, for medium C-rates the improvement increases and reaches a maximum and for higher C-rates it diminishes when other limitations become more pronounced. A detailed explanation of the three stages can also be found in our previous work.[39] The location of the maximum determines the range of C-rates where the structuring process has a positive impact. The pore morphology change of the graphite anode leads to an enhanced transport of lithium-ions and a reduction of concentration gradients in the electrolyte. Thereby, the cutoff voltage for the discharge process is reached at a later moment and more capacity can be discharged from the cell. For higher loadings the maximum shifts toward lower C-rates, for lower loadings it shifts toward higher C-rates. Even for the low loading L1 with 2.26 mAh cm^{-2} there is a 15% increase in capacity retention for a discharge rate of 6C. Note, that for loading L1 and L2 the cells were discharged with 5C and then 10C with no further steps in between, so the maximum of L1 was most likely not reached precisely. Modeling and simulation is often used to extend and refine the fundamental data of use case scenarios, such as the variation of discharge C-rates to determine the location of the maximum improvement in capacity retention in this work. The shape of the capacity difference, given by the location and the value of the maximum, will be analyzed with a simulation study next.

The influence of the structuring process as a function of electrode thickness is studied based on the parameter set of loading L1. In this study, an increase in electrode thickness increases the loading, so the discharge current is adapted to the changed loading. Choosing moderate values, the tortuosity of the unstructured anodes is set to 5.5 and the tortuosity of the structured anodes to 3.5. The thickness of the electrodes is increased by 25% in each step ranging from 71 µm to 173 µm. The results are displayed in Fig. 4a. As expected, an increase in the electrode loading causes the maximum to shift toward lower C-rates. The maximum improvement is just slightly affected by the electrode thickness. For thin electrodes with 71 µm thickness there is a 15% capacity enhancement compared to 18% for thick electrodes with 173 µm thickness.

On the other hand, the tortuosity improvement by a pore morphology modification highly affects the maximum enhancement in capacity retention as can be seen in Fig. 4b. This simulation study is based on parameter set L4 that features high tortuosity values. Starting from a tortuosity of 8.5 for the unstructured anode, the tortuosity of the structured anode is reduced by steps of 1 down to 3.5. The electrode thickness and the resulting discharge currents remained constant. The lower the tortuosity of the porous anode, the higher the improvement in capacity retention. The C-rate where the maximum is reached slightly shifts toward higher discharge currents, in this case from around 1.25C up to 2.5C. Note, an electrode porosity of 0.35 results in a tortuosity of 1.7 by using the Bruggeman correlation with $\alpha_{Brugg} = 1.5$. This in turn would lead to an increased discharge capacity of around 45% in this use case scenario. So the morphology of a composite electrode has to be carefully assessed when deriving correction terms for modeling purposes.

Overpotential analysis.—Regarding local polarization within the electrode stack, such as the anode, separator and cathode domain, the overall cell polarization is derived based on the aforementioned implicit overpotential analysis (as described in the modeling section) and outlined in the following to investigate the limiting mechanisms during discharge processes with increasing C-rates.

Based on the parameter set L2U, the initial conditions of the simulation were set to a fully charged state at a cell voltage of 4.2 V. Similar to the rate capability test listed in Table II, the cells were discharged with a CC procedure with C-rates ranging from C/5 to 10C until a cutoff voltage of 2.7 V was reached. The individual overpotentials were temporally averaged over each discharge cycle and then ascribed to one domain based on their occurrence. In Fig. 5a the relative contribution to the cell polarization is shown (they sum up to 1). While the anode contribution is declining for increasing discharge C-rates, it constitutes the major contribution to the total cell polarization up to 7C. This can be explained by the high tortuosity on the one hand and the fact that the

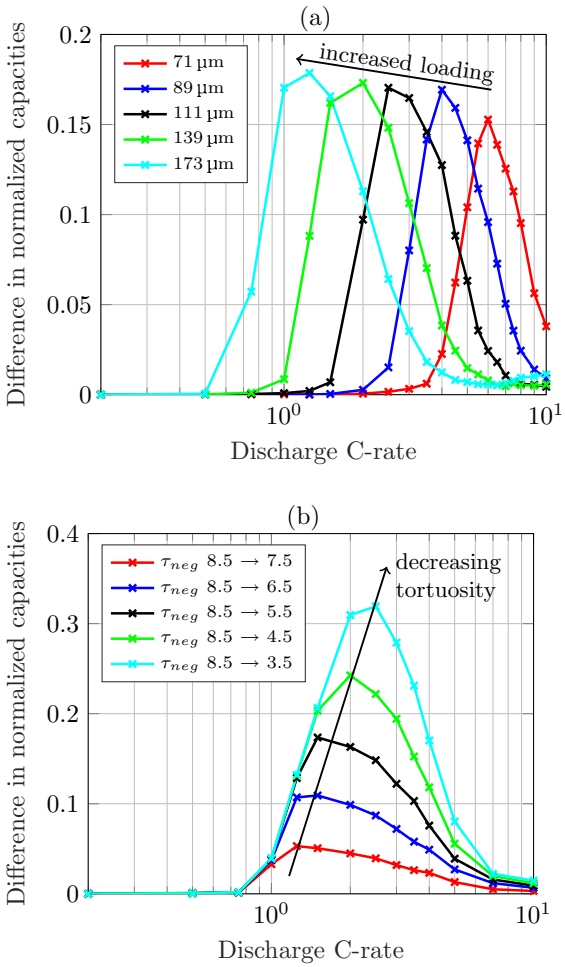

Figure 4. Simulated difference in normalized discharge rate capability of (a) cells with increased loading by increasing the electrode thickness based on parameter set of L1 and (b) cells with decreasing anode tortuosity and constant electrode thickness based on parameter set L4.

anode is the limiting electrode for the discharge process on the other hand. This will be explained in detail in the upcoming part. The cathode and contact contribution overtake the anode at 8C. Since the contact resistance is purely ohmic, the overpotential increases linearly with the applied discharge current. The separator only plays a minor role as only the diffusion polarization and ohmic potential drop in the liquid phase contribute in this domain. To get a better understanding of the impact of the overpotential, the absolute values are plotted in Fig. 5b for selected C-rates. For low discharge currents, e.g. C/5, the absolute cell overpotential is very low, hence its origin is less important. For 1C the total cell overpotential rises to around 100 mV and almost reaches 800 mV for a 10C discharge with the given parameterization set of the p2D model. With medium currents, the dominating anode contribution shows an opportunity to improve the cell design. Therefore, the anode overpotentials are investigated in detail depending on their driving force.

By excluding the contact resistance, the polarization in the anode can be categorized into five groups, namely the diffusion polarization and the ohmic potential drop in the solid and liquid phase and the activation overpotential. In order to investigate the influence of the change in anode pore morphology on the arising overpotentials, the parameter sets L2U and L2S were compared in the simulations. An overview of the absolute anode overpotentials for discharge currents ranging from C/5 to 10C is shown in Fig. 6. For the depicted pair of bars at each simulated discharge C-rate, the left one represents the results for the unstructured and the right one for

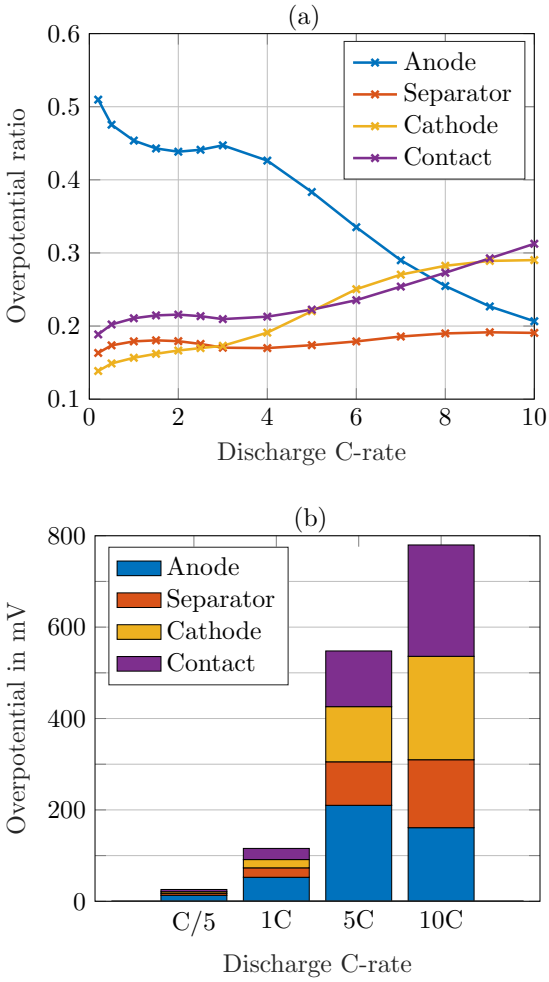

Figure 5. (a) Relative and (b) absolute distribution of cycle-averaged overpotentials of parameter set L2U assigned to the domains anode, separator and cathode and the contact resistance for discharge C-rates from C/5 to 10C.

the structured anode comprising the L2U and L2S parameterization, respectively.

The ohmic potential drop in the solid phase is barely visible which is referred to a high electrical conductivity in natural graphite of around 100 S m^{-1}.[66–70]

The ohmic potential drop in the electrolyte is also very low, with a minor contribution at very high C-rates. With the given parameter set of this work, the electrolyte conductivity κ lies around 1 S m^{-1} for moderate lithium-ion concentrations of 1000 mol m^{-3}, see also electrolyte transport parameters in Table AI. The conductivity of the bulk electrolyte can be measured with a turn-key conductivity sensor[29] and is therefore a well determined electrolyte property. A detailed overview of different electrolyte properties used for modeling purposes, including the conductivity, is given by Rheinfeld et al.[71] In their work the conductivity of five different electrolytes ranges from 0.8 to 1.2 S m^{-1} (at 1000 mol m^{-3} and 25°C). Even with the calculation of the effective conductivity κ_{eff} (see Eq. 1), in our case, the liquid current density i_l is too low to cause a high potential drop in the electrolyte.

The major contributors to the cell overpotential, as can be seen in Fig. 6, are the diffusion polarization in the solid and liquid phase and the activation overpotential. The diffusion polarization in the solid phase is calculated by the difference of the equilibrium potential on the surface of the particles and the average equilibrium potential (equations listed in Table AIII). During the end of discharge, the anode lithiation level x in Li_xC_6 tends toward zero and the corresponding equilibrium voltage $E_{eq,neg}$ reveals increasing potential gradients the more lithium is extracted, which in turn causes the reach of the cell discharge cutoff voltage of 2.7 V. Hence, a low lithium-ion concentration on the particle surface generates a high polarization in the solid phase, especially at the end of discharge.

The activation overpotential is affected by the kinetics as described by the Butler-Volmer equation, e.g. a higher exchange current density i_0 would result in lower overpotentials η (and vice versa) to reach the same surficial molar flux, as defined by the boundary conditions (see electrode kinetics in Table AII). Due to the nonlinear characteristics of the Butler-Volmer equation, a rise in the discharge current does not result in a proportional rise in the activation overpotential. It slightly increases with increasing discharge C-rates. The exchange current density is calculated by the anodic and cathodic reaction rates and the local lithium-ion concentrations. The lithiation process of the

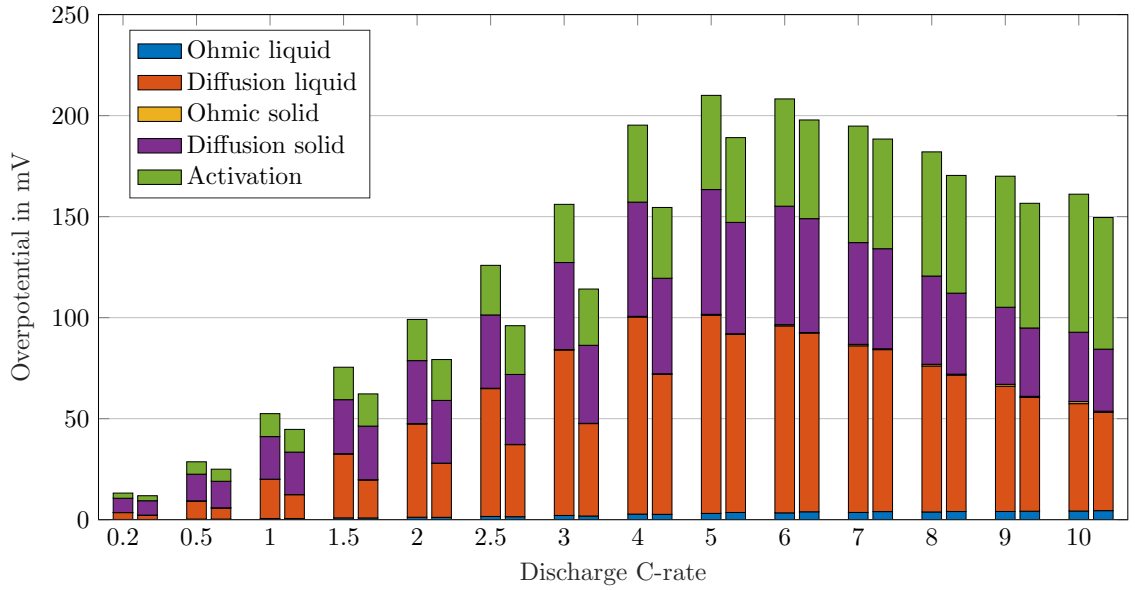

Figure 6. Cycle-averaged anode overpotentials for discharge C-rates from C/5 to 10C. For each pair of bars at a given C-rate the left bar corresponds to the overpotentials of the unstructured anode (L2U) and the right bar of the structured anode (L2S).

active material is either limited by the liquid phase concentration c_l tending toward zero (electrolyte depletion) or the surface concentration of the particles $c_{s,surf}$ reaching the maximum concentration $c_{s,max}$. The delithiation process is limited if the surface concentration of the particles reaches zero. In either case the exchange current density is diminished and the activation overpotential rises. The determination of the kinetic reaction rates is not trivial and not many values can be found in literature. A lot of publications use the reaction rates as fitting parameters[51,72–74] or set the exchange current density to a constant value,[67,68] which makes the reaction rates unnecessary. Generally, high reaction rates result in low activation overpotentials and low reaction rates in high activation overpotentials. Lin et al.[75] list a range of 10^{-12} to 10^{-9}m s^{-1} for the reaction rates of anodes and cathodes. Based on a sensitivity analysis conducted in this work, the reaction rates were estimated to 6×10^{-11} m s^{-1}, which is within the given range by Lin et al.[75]

The diffusion polarization in the liquid phase is the biggest contributor in the anode domain. Its driving force are the lithium-ion concentration gradients in the electrolyte. As explained in the modeling section, the effective electrolyte diffusivity is strongly affected by the porous electrode structure and calculated with the tortuosity and porosity. The high anode tortuosity lowers the effective diffusivity and increases the concentration gradients. Spatially resolved concentration gradients can be found in our previous work.[31] The resulting overpotential of the diffusion in the liquid phase of the unstructured anode reaches a maximum of around 100 mV at 5C and amounts to almost half the overpotential arising in the anode. By structuring the graphite anode, the modeled tortuosity is lowered from 5.5 for loading L2U to 3.5 for L2S. The maximum in capacity retention for this structuring process also occurs at a discharge C-rate of 5C, which corresponds to a peak in the liquid diffusion polarization. The structuring process enhances the transport in the electrolyte and mainly reduces the overpotentials caused by the diffusion polarization. A maximum reduction in anode overpotential of 42 mV is reached at 3C with 36 mV from liquid diffusion polarization.

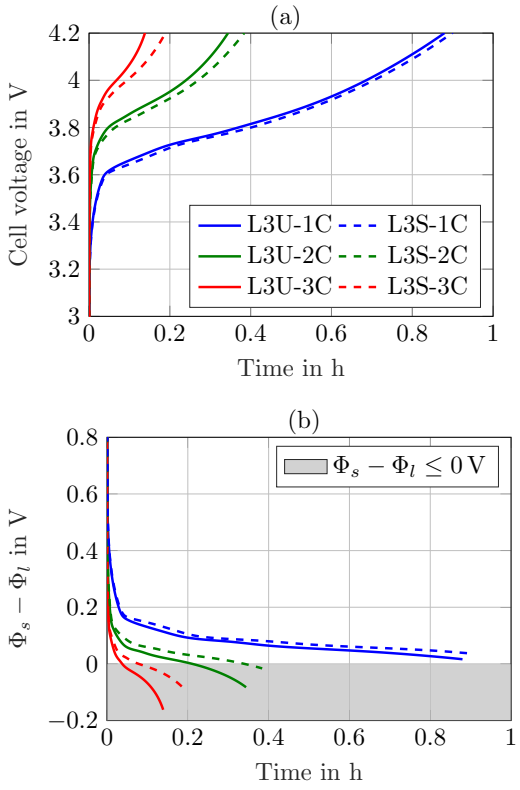

Figure 7. (a) Simulated cell voltage and (b) potential difference $\Phi_s - \Phi_l$ at anode/separator interface for charging currents 1C, 2C and 3C based on parameter set L3.

Fast charging scenario.—In the previous sections, it was demonstrated that lithium-ion cells comprising structured graphite electrodes provide an increased discharge rate capability in a certain range of C-rates by reducing electrolyte concentration gradients and overpotentials. Based on the parameterization that was validated against discharge rate capability tests, a fast charging scenario was simulated.

Therefore, the initial lithium-ion concentrations in both the anode and the cathode were adapted (compare Table AI) in order to represent a fully discharged cell with an initial cell voltage of 2.7 V. The simulations were carried out with a CC charge of 1C, 2C and 3C until a cutoff voltage of 4.2 V was reached, no CV phase was added to the charging procedure. In Fig. 7 the cell voltage and the potential difference at the anode/separator interface are plotted for loading L3. The charged capacities and the lithium-plating indication for all loadings are listed in Table III.

Note, that the gray shaded area for the potential drop in Fig. 7b just gives an indication of possible lithium-plating at the anode. The simulations were carried out under isothermal conditions ($T = 25°$C), which might hold true for a coin cell with low power losses. A heating of the cell would result in enhanced electrolyte transport properties,

Table III. Charged capacity and lithium-plating indication during fast charging scenarios.

	ΔCapacity[I]			ΔSOC[II]			ΔSOC Li-plating[III]			
Loading	1C	2C	3C	1C	2C	3C	1C	2C	3C	Maximum C-rate[IV]
L1U	3.27 mAh	2.97 mAh	2.60 mAh	94.0%	85.2%	74.5%	-	-	59.8%	2.5C
L1S	3.29 mAh	3.02 mAh	2.71 mAh	94.6%	86.7%	78.0%	-	-	-	3.3C
L2U	3.60 mAh	3.21 mAh	2.68 mAh	93.5%	83.4%	69.5%	-	-	44.0%	2.1C
L2S	3.63 mAh	3.29 mAh	2.88 mAh	94.4%	85.6%	74.9%	-	-	74.3%	2.9C
L3U	3.93 mAh	3.07 mAh	1.86 mAh	88.0%	69.0%	41.6%	-	42.2%	11.2%	1.2C
L3S	4.02 mAh	3.43 mAh	2.53 mAh	89.9%	76.9%	56.9%	-	68.0%	23.5%	1.7C
L4U	4.61 mAh	2.46 mAh	1.06 mAh	77.9%	41.7%	18.0%	64.3%	14.7%	6.1%	0.7C
L4S	4.80 mAh	3.03 mAh	1.35 mAh	81.7%	51.5%	23.0%	79.8%	23.8%	7.6%	0.9C

[I]CC charging from 2.7 V to a cutoff voltage of 4.2 V.
[II]referenced to the nominal capacities determined by the corresponding loading in Table I.
[III]ΔSOC when Li-plating is provoked, determined by $\Phi_s - \Phi_l$ at anode/separator interface.
[IV]maximum charging C-rate without Li-plating.

reduced lithium-ion concentration gradients and lower overpotentials that counteract lithium-plating. The simulation study just provides a hint for possible lithium-plating and the effects of the electrode pore morphology modification on charging procedures.

In the simulation in Fig. 7a during the 1C charge of both L3U and L3S, almost 90% of the cell capacity can be charged, the benefit of the structuring is marginal. In the cell voltage there is no option to assess the anode potential and it looks like the structured anodes just give a small benefit in the charged capacity in the end. For a 2C charge however, the reduction in overpotentials can be clearly seen in Fig. 7b, where the potential drop for the structured anodes lies well above the the one for unstructured anodes. After 12 min of charging, the unstructured anode reaches a potential that could invoke lithium-plating, while the structured anode reaches the critical potential only shortly before the end of charge (compare SOC in Table III). This effect is even more pronounced for a 3C charge, where both potential curves lie well below 0 V shortly after applying the charging current. This is a clear indication of possible lithium-plating and the charging current is too high for this cell setup. Regarding the charged capacity for a 3C charging rate, the cells comprising structured anodes reach a 15% higher SOC until the cutoff voltage is exceeded. So not only for discharging, but also for charging procedures the modified electrode pore morphology shows distinct advantages in an overpotential reduction.

An assessment of the other three loadings, as listed in Table III, reveals that for loading L1 with an electrode thickness of 71 μm the structuring shows little benefits regarding the charged capacity. Just at the end of a 3C charge, the potential drop of L1S is a little less and the lithium-plating criterion is not fulfilled. For loading L2 with thicker electrodes, more capacity can be charged and the advantages of structured anodes increase. Especially for a 3C charge, with structured anodes there is almost no lithium-plating provoked compared to the unstructured ones. A comparison of the charged capacities of loading L4 and Fig. 3b reveals, that there is also a range for charging currents with a maximum benefit. The 1C charge adds 3.3% in capacity, the 2C charge 9.8% and the 3C charge 5.0%. At lower charging currents, the concentration gradients are reduced and the pore morphology change has little or no influence. With increasing charging currents, a maximum benefit arises and diminishes again when other limitations come into place. However, for the thick electrodes in the case of L4 (116 μm), all three charging currents would possibly provoke lithium-plating and the current should be reduced for both the cells with unstructured and structured anodes. Just the amount of plated lithium could be less with structured anodes.

In order to assess the maximum charging C-rate for each loading, a simulation study with incremental C-rates with a step size of 0.1C was carried out. The results are listed in the last column in Table III. In each case, the potential difference $\Phi_s - \Phi_l$ at the anode/separator interface would stay slightly above 0 V at the end of charge. The cells comprising structured anodes can withstand higher C-rates for all loadings. With increasing electrode thickness, the maximum charging C-rate has to be reduced. The C-rates are derived from the modeled areal capacities in Table I, a conversion of the C-rates to current densities, due to the changed loading, leads to the same trend. Based on the charged capacities with the maximum C-rate of the cells with unstructured anodes, the C-rates with structured anodes that lead to the same charged capacity can be calculated. The simulated pore morphology modification would allow higher charging currents so that the charged capacity stays the same in the end for the cells comprising unstructured and structured anodes of each loading. This leads to a reduced charging time of around 10% for loadings L1 and L2, 17% for L3 and 13% for L4, respectively. On top of the shorter charging time, the distance to the lithium-plating threshold is higher for the structured anodes and thereby the cell safety enhanced.

Conclusions

An electrochemical model was developed and validated against experimental data gained from lithium-ion cells comprising unstructured and structured graphite anodes. The areal capacities of the cells were varied by changing the electrode thickness, the electrode composition and the porosity remained constant within the manufacturing tolerances. The simulation results are well in line with the discharge rate capability measurements.

The loading of the cell, defined by the electrode thickness, determines the C-rates where the structuring process provides a benefit in capacity retention, which was around 10–18% for the measured cells. The location and shape of this benefit is given by the electrode thickness and the tortuosity reduction. With increasing electrode thickness, the maximum benefit shifts to lower C-rates (and vice versa) and the tortuosity reduction specifies the maximum itself, i.e. a lower tortuosity yields a higher rate capability.

In order to understand the limiting mechanisms, an overpotential analysis was conducted that revealed the anode as a major contributor. Especially the diffusion polarization in the electrolyte limits the performance for medium C-rates. Through modification of the pore morphology, a reduction in the anode tortuosity can be achieved, which results in a reduction of concentration gradients and the accompanying overpotentials and more capacity can be discharged from the cell.

A fast charging scenario for the different loadings revealed that the reduced overpotentials through electrode structuring provide an approach for preventing lithium-plating at the anode. In the fast charging simulation studies, a reduction of the charging time of 10–17% was achieved while keeping the anode potential in a safe area above the lithium-plating threshold.

In this work, laser-structuring was used to modify the electrode pore morphology of graphite anodes and the generated effects were investigated. In conclusion, the tortuosity should be well considered regarding electrode and cell design and simulation studies can support the overall process. Future work will focus on the optimization of the electrode structure, defined by the geometrical dimensions of the induced holes and the amount of structures, i.e. the structure pattern. Tortuosity measurements are necessary in order to identify the change in electrode pore morphology generated by the structuring process. Furthermore, simulations could be used to provide a guideline for an optimal structure for a given set of electrodes, adjusted to the desired performance improvement within the physical bounds of tortuosity reduction.

Acknowledgment

This work was financially supported by the German Federal Ministry of Education and Research (BMBF) under grant number 03XP0081 (ExZellTUM II). The authors thank Johannes Sturm for his critical feedback.

Appendix

The comparison of the measured and simulated discharge voltage curves for all loadings comprising unstructured and structured anodes is displayed in Fig. A1. The representative voltage curves for the discharge C-rates of C/5, 2C, 5C and 10C were selected for validation.

An overview of the most relevant model parameters is shown in Table AI. The electrolyte diffusivity D_l and conductivity κ were taken from Mao et al.[76] However, Mao et al. used a polynomial fitting function for the electrolyte conductivity which is only valid for concentrations below 3000 mol m^{-3}. At higher concentration levels, the conductivity starts to increase, so a correction for extrapolation at highly saturated electrolytes from Rheinfeld et al.[71] was used instead. The electrolyte activity dependence was extracted from Valøen and Reimers.[77] All three functions describing the electrolyte expect the concentration to be in mol m^{-3}.

The differential algebraic equations of the p2D model are listed in Table AII. In order to prevent local lithium-ion concentrations from becoming zero or even negative and thus cause instability, a modification of the Butler-Volmer equation introduced by Mao et al.[76] was implemented.

The equations for calculating the polarization of the different sub-processes are stated in Table AIII. The total current per cross-sectional area i_{tot} is calculated via an integration

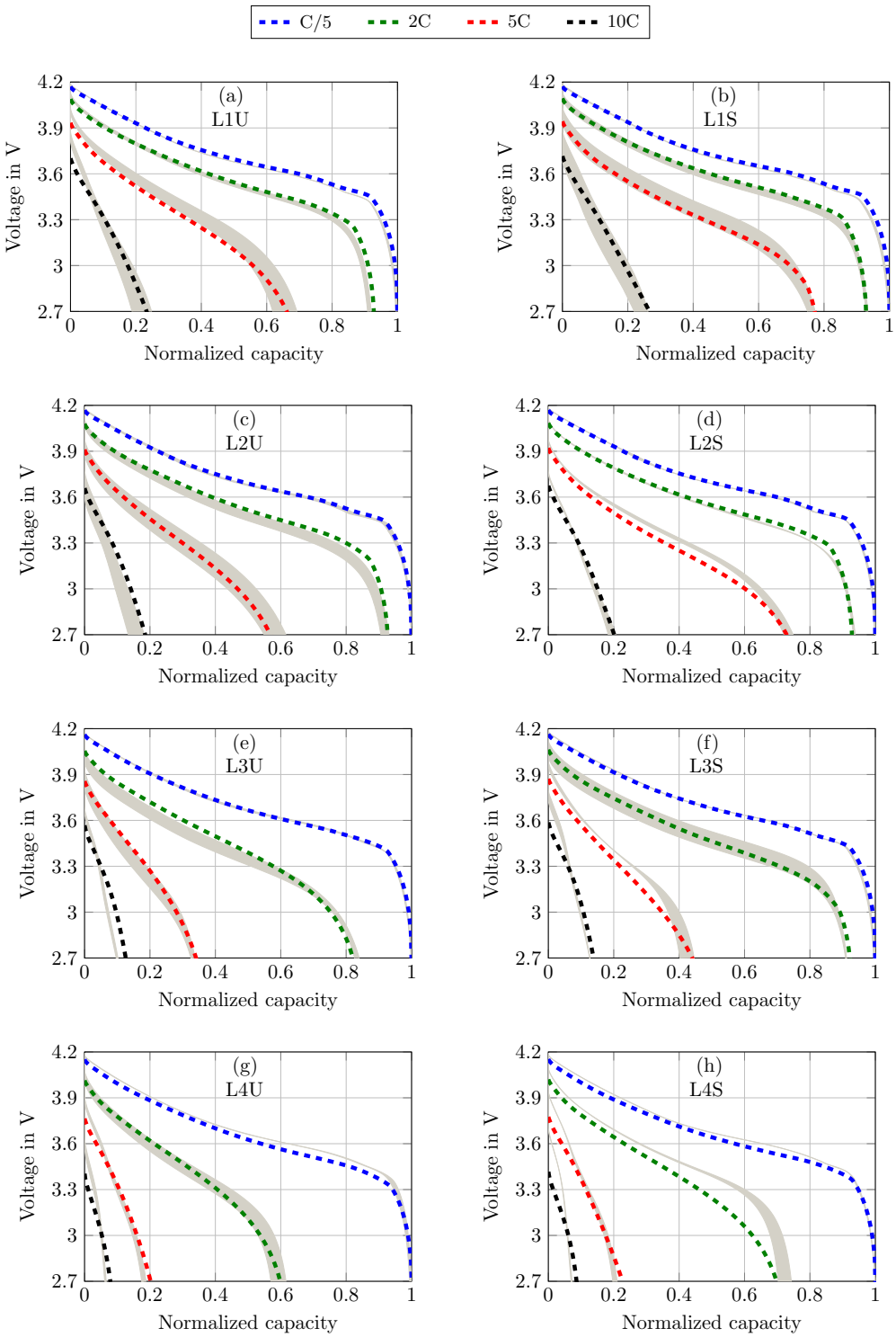

Figure A1. Comparison of measured (gray shaded areas) and simulated discharge voltage curves, normalized to their C/5 capacity for C-rates C/5, 2C, 5C and 10C. The cells comprising unstructured anodes are depicted in (a), (c), (e) and (g) for loadings L1U, L2U, L3U and L4U and the cells comprising structured anodes are depicted in (b), (d), (f) and (h) for loadings L1S, L2S, L3S and L4S, respectively.

of the local current density on the particle surface i_{loc} – as given by the Butler-Volmer equation – multiplied with the specific interfacial area a (ratio of active material surface to volume)

$$i_{tot} = \int_{x_1}^{x_2} a i_{loc} dx \qquad [A1]$$

In order to calculate the average cell polarization, the integration boundaries x_1 and x_2 are chosen to 0 and $L = l_{neg} + l_{sep} + l_{pos}$, respectively. Polarization based on spatial integral values refers to the relevant domains of anode, separator and cathode and the corresponding boundary values in the x-dimension. For a profound explanation of the method and the set of equations, the reader is referred to the original publication of Nyman et al.[22]

Table AI. Model parameters used within this work; numeric values and magnitudes of parameters chosen in this study were referenced to literature where applicable.

Parameter	Anode	Separator	Cathode
Geometry			
Thickness l	Table I	200 µm[41]	Table I
Particle radius r_p	5 µm [I]		5.5 µm [I]
Solid phase fraction ε_s	0.53 [II]		0.5 [II]
Liquid phase fraction ε_l	0.35 [m]	0.7 [e]	0.35 [m]
Tortuosity τ	Table I	1.2 [e]	1.8[55]
Thermodynamics			
Equilibrium voltage E_{eq}	Ref. 31		Ref. 31
Maximum lithium concentration $c_{s,max}$	32000 mol m^{-3}[73]		50000 mol m^{-3}[73]
Lithiation at 100% SOC $\frac{c_{s,100}}{c_{s,max}}$	0.71 [e]		0.43 [e]
Lithiation at 0% SOC $\frac{c_{s,0}}{c_{s,max}}$	0.003 [e]		0.91 [e]
Kinetics			
Anodic reaction rate k_a	6×10^{-11} m s^{-1} [e]		6×10^{-11} m s^{-1} [e]
Cathodic reaction rate k_c	6×10^{-11} m s^{-1} [e]		6×10^{-11} m s^{-1} [e]
Anodic charge-transfer coefficient α_a	0.5[67]		0.5[67]
Cathodic charge-transfer coefficient α_c	0.5[67]		0.5[67]
Transport			
Solid diffusivity D_s	1×10^{-14} m^2 s^{-1}[76]		1.8×10^{-13} m^2 s^{-1}[73]
Solid conductivity σ	100 S m^{-1}[68]		10 S m^{-1}[68]

Parameter	Electrolyte
Electrolyte diffusivity D_l	$5.34 \times 10^{-10} \exp\left(-0.65 \frac{c_l}{1000}\right) \exp\left(2000 \frac{T-298}{298T}\right)$[76] in m^2 s^{-1}
Electrolyte conductivity κ	$729.9912 \exp\left(\frac{-1690}{T}\right) \left(\frac{c_l}{2050}\right)^{0.75} \exp\left(-\left(\frac{c_l}{2050}\right)^{1.75}\right)$[71] in S m^{-1}
Activity dependence $\frac{\partial \ln f_{\pm}}{\partial \ln c_l}$	$\frac{0.601-0.24(c_l/1000)^{0.5}+0.982(c_l/1000)^{1.5}(1-0.0052(T-294))}{1-t_+} - 1$[77]
Transport number t_+	0.38[77]

Parameter	Global
Temperature T	298.15 K [m]
Ohmic contact resistance $R_{contact}$	9.75×10^{-4} Ωm^2 [e]

m measured value, *e* estimated value.
[I] derived from D50 mass-median-diameter from datasheet.
[II] derived from weight ratio of electrode composition.

Table AII. Differential algebraic equations of the p2D model according to Doyle, Fuller and Newman[46] including an adaption for the Butler-Volmer equation from Mao et al.[76]

Type	Equations
Mass balance	$\varepsilon_l \frac{\partial c_l}{\partial t} = \frac{\partial}{\partial x}\left(D_{l,eff} \frac{\partial c_l}{\partial x} + \frac{i_l (1-t_+)}{F}\right)$
	$\varepsilon_s \frac{\partial c_s}{\partial t} = \frac{1}{r^2} \frac{\partial}{\partial r}\left(D_s r^2 \frac{\partial c_s}{\partial r}\right)$
Potentials	$\frac{\partial \Phi_l}{\partial x} = -\frac{i_l}{\kappa_{eff}} + \frac{2RT}{F}(1-t_+)\left(1 + \frac{d\ln f_{\pm}}{d\ln c_l}\right)\frac{\partial \ln c_l}{\partial x}$
	$\frac{\partial \Phi_s}{\partial x} = -\frac{i_{app}-i_l}{\sigma_s}$ with $i_{app} = i_s + i_l \quad \forall x, t$
Charge balance	$\frac{\partial i_l}{\partial x} + \frac{\partial i_s}{\partial x} = 0$ with $\frac{\partial i_s}{\partial x} = -\frac{3\varepsilon_s}{r_p} F j_n$
Electrode kinetics	$j_n = \frac{i_0}{F} \frac{\exp\left(\frac{\alpha_a F \eta}{RT}\right) - \exp\left(-\frac{\alpha_c F \eta}{RT}\right)}{1 + \frac{1\text{mol m}^{-3}}{c_l} \exp\left(-\frac{\alpha_c F \eta}{RT}\right)}$
	$\eta = \Phi_s - \Phi_l - E_{eq}$
	$i_0 = F k_c^{\alpha_a} k_a^{\alpha_c} \left(c_{s,max} - c_{s,surf}\right)^{\alpha_a} \left(c_{s,surf}\right)^{\alpha_c} \left(\frac{c_l}{1\text{mol m}^{-3}}\right)^{\alpha_a}$

Table AIII. Polarization analysis by Nyman et al.[22]

Polarization source	Equation
Diffusion polarization liquid phase	$\frac{1}{i_{tot}} \int_{x_1}^{x_2} \frac{2RT}{c_l F}(1 + \frac{\partial \ln f_{\pm}}{\partial \ln c_l})(1-t_+)\frac{\partial c_l}{\partial x} i_l dx$
Diffusion polarization solid phase	$\frac{1}{i_{tot}} \int_{x_1}^{x_2} a i_{loc}(E_{eq,surf} - E_{eq,ave}) dx$
Ohmic potential drop liquid phase	$\frac{1}{i_{tot}} \int_{x_1}^{x_2} \frac{i_l^2}{\kappa_{eff}} dx$
Ohmic potential drop solid phase	$\frac{1}{i_{tot}} \int_{x_1}^{x_2} \frac{i_s^2}{\sigma_{eff}} dx$
Activation overpotential	$\frac{1}{i_{tot}} \int_{x_1}^{x_2} a i_{loc}(\Phi_s - \Phi_l - E_{eq,surf}) dx$
Contact resistance	$i_{app} \cdot R_{contact}$

List of symbols

Symbol	Description	Unit
a	Specific interfacial area	m^{-1}
c	Concentration	mol m^{-3}
D	Diffusion coefficient	m^2 s^{-1}
E_{eq}	Equilibrium potential	V
F	Faraday constant	96 485 As mol^{-1}
$f_{\pm}$	Activity coefficient	-
i	Current density	A m^{-2}
j_n	Pore-wall flux	A $m^{-2}s^{-1}$
l	Thickness	m
N_l	Ion flux density	mol $m^{-2}s^{-1}$
N_M	MacMullin number	-
r_p	Particle radius	m
r	r-coordinate in p2D model	m
R	Universal gas constant	8.314 J mol^{-1} K^{-1}
$R_{contact}$	Contact resistance	Ω m^2
R_l	Reaction term	mol $m^{-3}s^{-1}$
t	Time	s
t_+	Transport number	-
T	Temperature	K
x	x-coordinate in p2D model	m

Greek

α_{Brugg}	Bruggeman correction term	-
ε	Volume fraction	-
κ	Electrolyte conductivity	S m^{-1}
τ	Tortuosity	-
σ	Solid phase conductivity	S m^{-1}
Φ	Electrical potential	V
Ψ	Transport property in porous media	-

Subscripts

a	anodic reaction (oxidation)
app	applied
ave	average
c	cathodic reaction (reduction)
eff	effective (transport parameter correction)
l	liquid phase/electrolyte
loc	local
max	maximum
neg	negative electrode/anode
pos	positive electrode/cathode
s	solid phase/active material
sep	separator
$surf$	surface
tot	total

ORCID

Ludwig Kraft https://orcid.org/0000-0003-4324-426X
Jan B. Habedank https://orcid.org/0000-0003-2057-7037
Alexander Frank https://orcid.org/0000-0001-8069-2948
Alexander Rheinfeld https://orcid.org/0000-0003-0995-7266
Andreas Jossen https://orcid.org/0000-0003-0964-1405

References

1. M. A. Hannan, M. M. Hoque, A. Mohamed, and A. Ayob, Review of energy storage systems for electric vehicle applications: Issues and challenges, *Renewable and Sustainable Energy Reviews*, **69**, 771 (2017).
2. O. Gröger, H. A. Gasteiger, and J.-P. Suchsland, Review—Electromobility: Batteries or Fuel Cells? *Journal of the Electrochemical Society*, **162**, A2605 (2015).
3. D. Andre, S.-J. Kim, P. Lamp, S. F. Lux, F. Maglia, O. Paschos, and B. Stiaszny, Future generations of cathode materials: An automotive industry perspective, *Journal of Materials Chemistry A*, **3**, 6709 (2015).
4. K. Kerman, A. Luntz, V. Viswanathan, Y.-M. Chiang, and Z. Chen, Review—Practical Challenges Hindering the Development of Solid State Li Ion Batteries, *Journal of The Electrochemical Society*, **164**, A1731 (2017).
5. Y. Wu, W. Wang, J. Ming, M. Li, L. Xie, X. He, J. Wang, S. Liang, and Y. Wu, An Exploration of New Energy Storage System: High Energy Density, High Safety, and Fast Charging Lithium Ion Battery, *Advanced Functional Materials*, **29**, 1805978 (2019).
6. J. Sturm, A. Rheinfeld, I. Zilberman, F. B. Spingler, S. Kosch, F. Frie, and A. Jossen, Modeling and simulation of inhomogeneities in a 18650 nickel-rich, silicon-graphite lithium-ion cell during fast charging, *Journal of Power Sources*, **412**, 204 (2019).
7. S. Goriparti, E. Miele, F. de Angelis, E. Di Fabrizio, R. Proietti Zaccaria, and C. Capiglia, Review on recent progress of nanostructured anode materials for Li-ion batteries, *Journal of Power Sources*, **257**, 421 (2014).
8. M. Osiak, H. Geaney, E. Armstrong, and C. O'Dwyer, Structuring materials for lithium-ion batteries: Advancements in nanomaterial structure, composition, and defined assembly on cell performance, *Journal of Materials Chemistry A*, **2**, 9433 (2014).
9. A. M. Dreizler, N. Bohn, H. Geßwein, M. Müller, J. R. Binder, N. Wagner, and K. A. Friedrich, Investigation of the Influence of Nanostructured LiNi 0.33 Co 0.33 Mn 0.33 O 2 Lithium-Ion Battery Electrodes on Performance and Aging, *Journal of The Electrochemical Society*, **165**, A273 (2018).
10. R. A. Adams, A. N. Mistry, P. P. Mukherjee, and V. G. Pol, Materials by Design: Tailored Morphology and Structures of Carbon Anodes for Enhanced Battery Safety, *ACS applied materials & interfaces*, **11**, 13334 (2019).
11. G. Liu, H. Zheng, X. Song, and V. S. Battaglia, Particles and Polymer Binder Interaction: A Controlling Factor in Lithium-Ion Electrode Performance, *Journal of The Electrochemical Society*, **159**, A214 (2012).
12. H. Zheng, J. Li, X. Song, G. Liu, and V. S. Battaglia, A comprehensive understanding of electrode thickness effects on the electrochemical performances of Li-ion battery cathodes, *Electrochimica Acta*, **71**, 258 (2012).
13. W. Pfleging, A review of laser electrode processing for development and manufacturing of lithium-ion batteries, *Nanophotonics*, **7**, 549 (2018).
14. R. Morasch, J. Landesfeind, B. Suthar, and H. A. Gasteiger, Detection of Binder Gradients Using Impedance Spectroscopy and Their Influence on the Tortuosity of Li-Ion Battery Graphite Electrodes, *Journal of The Electrochemical Society*, **165**, A3459 (2018).
15. B. L. Trembacki, A. N. Mistry, D. R. Noble, M. E. Ferraro, P. P. Mukherjee, and S. A. Roberts, Editors' Choice—Mesoscale Analysis of Conductive Binder Domain Morphology in Lithium-Ion Battery Electrodes, *Journal of The Electrochemical Society*, **165**, E725 (2018).
16. A. N. Mistry, K. Smith, and P. P. Mukherjee, Secondary-Phase Stochastics in Lithium-Ion Battery Electrodes, *ACS applied materials & interfaces*, **10**, 6317 (2018).
17. S. Malifarge, B. Delobel, and C. Delacourt, Determination of Tortuosity Using Impedance Spectra Analysis of Symmetric Cell, *Journal of The Electrochemical Society*, **164**, E3329 (2017).
18. M. Singh, J. Kaiser, and H. Hahn, Thick Electrodes for High Energy Lithium Ion Batteries, *Journal of the Electrochemical Society*, **162**, A1196 (2015).
19. T. Danner, M. Singh, S. Hein, J. Kaiser, H. Hahn, and A. Latz, Thick electrodes for Li-ion batteries: A model based analysis, *Journal of Power Sources*, **334**, 191 (2016).
20. N. Dufour, M. Chandesris, S. Geniès, M. Cugnet, and Y. Bultel, Lithiation heterogeneities of graphite according to C-rate and mass-loading: A model study, *Electrochimica Acta*, **272**, 97 (2018).
21. S. Malifarge, B. Delobel, and C. Delacourt, Experimental and Modeling Analysis of Graphite Electrodes with Various Thicknesses and Porosities for High-Energy-Density Li-Ion Batteries, *Journal of The Electrochemical Society*, **165**, A1275 (2018).
22. A. Nyman, T. G. Zavalis, R. Elger, M. Behm, and G. Lindbergh, Analysis of the Polarization in a Li-Ion Battery Cell by Numerical Simulations, *Journal of The Electrochemical Society*, **157**, A1236 (2010).
23. K. G. Gallagher, S. E. Trask, C. Bauer, T. Woehrle, S. F. Lux, M. Tschech, P. Lamp, B. J. Polzin, S. Ha, B. Long, Q. Wu, W. Lu, D. W. Dees, and A. N. Jansen, Optimizing Areal Capacities through Understanding the Limitations of Lithium-Ion Electrodes, *Journal of The Electrochemical Society*, **163**, A138 (2015).
24. F. L. E. Usseglio-Viretta, A. Colclasure, A. N. Mistry, K. P. Y. Claver, F. Pouraghajan, D. P. Finegan, T. M. M. Heenan, D. Abraham, P. P. Mukherjee, D. Wheeler, P. Shearing, S. J. Cooper, and K. Smith, Resolving the Discrepancy in Tortuosity Factor Estimation for Li-Ion Battery Electrodes through Micro-Macro Modeling and Experiment, *Journal of The Electrochemical Society*, **165**, A3403 (2018).
25. A. N. Mistry and P. P. Mukherjee, Probing spatial coupling of resistive modes in porous intercalation electrodes through impedance spectroscopy, *Physical chemistry chemical physics : PCCP*, **21**, 3805 (2019).
26. S. Ferrari, M. Loveridge, S. D. Beattie, M. Jahn, R. J. Dashwood, and R. Bhagat, Latest advances in the manufacturing of 3D rechargeable lithium microbatteries, *Journal of Power Sources*, **286**, 25 (2015).
27. E. R. Reale and K. C. Smith, Capacitive Performance and Tortuosity of Activated Carbon Electrodes with Macroscopic Pores, *Journal of The Electrochemical Society*, **165**, A1685 (2018).
28. J. Li, X. Liang, R. Panat, and J. Park, Enhanced Battery Performance through Three-Dimensional Structured Electrodes: Experimental and Modeling Study, *Journal of The Electrochemical Society*, **165**, A3566 (2018).
29. J. Landesfeind, A. Ehrl, M. Graf, W. A. Wall, and H. A. Gasteiger, Direct Electrochemical Determination of Thermodynamic Factors in Aprotic Binary Electrolytes, *Journal of The Electrochemical Society*, **163**, A1254 (2016).
30. V. P. Nemani, S. J. Harris, and K. C. Smith, Design of Bi-Tortuous, Anisotropic Graphite Anodes for Fast Ion-Transport in Li-Ion Batteries, *Journal of The Electrochemical Society*, **162**, A1415 (2015).
31. J. B. Habedank, J. Endres, P. Schmitz, M. F. Zaeh, and H. P. Huber, Femtosecond laser structuring of graphite anodes for improved lithium-ion batteries: Ablation characteristics and process design, *Journal of Laser Applications*, **30**, 032205 (2018).
32. Q. Cheng and Y. Zhang, Multi-Channel Graphite for High-Rate Lithium Ion Battery, *Journal of The Electrochemical Society*, **165**, A1104 (2018).
33. C. L. Cobb and M. Blanco, Modeling mass and density distribution effects on the performance of co-extruded electrodes for high energy density lithium-ion batteries, *Journal of Power Sources*, **249**, 357 (2014).

34. J. Pröll, H. Kim, A. Piqué, H. J. Seifert, and W. Pfleging, Laser-printing and femtosecond-laser structuring of $LiMn_2O_4$ composite cathodes for Li-ion microbatteries, *Journal of Power Sources*, **255**, 116 (2014).
35. C. L. Cobb and S. E. Solberg, Communication—Analysis of Thick Co-Extruded Cathodes for Higher-Energy-and-Power Lithium-Ion Batteries, *Journal of The Electrochemical Society*, **164**, A1339 (2017).
36. B. Delattre, R. Amin, J. Sander, J. de Coninck, A. P. Tomsia, and Y.-M. Chiang, Impact of Pore Tortuosity on Electrode Kinetics in Lithium Battery Electrodes: Study in Directionally Freeze-Cast $LiNi_{0.8}Co_{0.15}A_{l0.05}O_2$ (NCA), *Journal of the Electrochemical Society*, **165**, A388 (2018).
37. T. Tsuda, N. Ando, S. Nakamura, Y. Ishihara, N. Hayashi, N. Soma, T. Gunji, T. Tanabe, T. Ohsaka, and F. Matsumoto, Improvement of high-rate discharging performance of $LiFePO_4$ cathodes by forming micrometer-sized through-holed electrode structures with a pico-second pulsed laser, *Electrochimica Acta*, **296**, 27 (2019).
38. J. B. Habedank, F. J. Günter, N. Billot, R. Gilles, T. Neuwirth, G. Reinhart, and M. F. Zaeh, Rapid electrolyte wetting of lithium-ion batteries containing laser structured electrodes: in situ visualization by neutron radiography, *The International Journal of Advanced Manufacturing Technology*, **102**, 2769 (2019).
39. J. B. Habedank, L. Kraft, A. Rheinfeld, C. Krezdorn, A. Jossen, and M. F. Zaeh, Increasing the Discharge Rate Capability of Lithium-Ion Cells with Laser-Structured Graphite Anodes: Modeling and Simulation, *Journal of The Electrochemical Society*, **165**, A1563 (2018).
40. A. M. Colclasure, A. R. Dunlop, S. E. Trask, B. J. Polzin, A. N. Jansen, and K. Smith, Requirements for Enabling Extreme Fast Charging of High Energy Density Li-Ion Cells while Avoiding Lithium Plating, *Journal of the Electrochemical Society*, **166**, A1412 (2019).
41. J. Landesfeind, D. Pritzl, and H. A. Gasteiger, An Analysis Protocol for Three-Electrode Li-Ion Battery Impedance Spectra: Part I. Analysis of a High-Voltage Positive Electrode, *Journal of the Electrochemical Society*, **164**, A1773 (2017).
42. J. Landesfeind, J. Hattendorff, A. Ehrl, W. A. Wall, and H. A. Gasteiger, Tortuosity Determination of Battery Electrodes and Separators by Impedance Spectroscopy, *Journal of The Electrochemical Society*, **163**, A1373 (2016).
43. F. M. Kindermann, P. J. Osswald, S. Klink, G. Ehlert, J. Schuster, A. Noel, S. V. Erhard, W. Schuhmann, and A. Jossen, Measurements of lithium-ion concentration equilibration processes inside graphite electrodes, *Journal of Power Sources*, **342**, 638 (2017).
44. T. Teufl, D. Pritzl, S. Solchenbach, H. A. Gasteiger, and M. A. Mendez, State of Charge Dependent Resistance Build-Up in Li- and Mn-Rich Layered Oxides during Lithium Extraction and Insertion, *Journal of the Electrochemical Society*, **166**, A1275 (2019).
45. A. Rheinfeld, S. Kosch, S. V. Erhard, P. J. Osswald, B. Rieger, and A. Jossen, Electro-Thermal Modeling of Large Format Lithium-Ion Pouch Cells: A Cell Temperature Dependent Linear Polarization Expression, *Journal of the Electrochemical Society*, **163**, A3046 (2016).
46. M. Doyle, T. F. Fuller, and J. Newman, Modeling of Galvanostatic Charge and Discharge of the Lithium/Polymer/Insertion Cell, *Journal of the Electrochemical Society*, **140**, 1526 (1993).
47. T. F. Fuller, M. Doyle, and J. Newman, Simulation and Optimization of the Dual Lithium Ion Insertion Cell, *Journal of the Electrochemical Society*, **141**, 1 (1994).
48. X. Lin, J. Park, L. Liu, Y. Lee, A. M. Sastry, and W. Lu, A Comprehensive Capacity Fade Model and Analysis for Li-Ion Batteries, *Journal of the Electrochemical Society*, **160**, 1701 (2013).
49. R. Fu, S.-Y. Choe, V. Agubra, and J. Fergus, Development of a physics-based degradation model for lithium ion polymer batteries considering side reactions, *Journal of Power Sources*, **278**, 506 (2015).
50. L. Xia, E. Najafi, Z. Li, H. J. Bergveld, and M. Donkers, A computationally efficient implementation of a full and reduced-order electrochemistry-based model for Li-ion batteries, *Applied Energy*, **208**, 1285 (2017).
51. W. A. Appiah, J. Park, S. Byun, I. Cho, A. Mozer, M.-H. Ryou, and Y. M. Lee, A coupled chemo-mechanical model to study the effects of adhesive strength on the electrochemical performance of silicon electrodes for advanced lithium ion batteries, *Journal of Power Sources*, **407**, 153 (2018).
52. D. Ren, K. Smith, D. Guo, X. Han, X. Feng, L. Lu, M. Ouyang, and J. Li, Investigation of Lithium Plating-Stripping Process in Li-Ion Batteries at Low Temperature Using an Electrochemical Model, *Journal of The Electrochemical Society*, **165**, A2167 (2018).
53. D. A. G. Bruggeman, Berechnung verschiedener physikalischer Konstanten von heterogenen Substanzen. I. Dielektrizitätskonstanten und Leitfähigkeiten der Mischkörper aus isotropen Substanzen, *Annalen der Physik*, **416**, 636 (1935).
54. I. V. Thorat, D. E. Stephenson, N. A. Zacharias, K. Zaghib, J. N. Harb, and D. R. Wheeler, Quantifying tortuosity in porous Li-ion battery materials, *Journal of Power Sources*, **188**, 592 (2009).
55. M. Ebner, D.-W. Chung, R. E. García, and V. Wood, Tortuosity Anisotropy in Lithium-Ion Battery Electrodes, *Advanced Energy Materials*, **4**, 1 (2014).
56. R. B. MacMullin and G. A. Muccini, Characteristics of porous beds and structures, *AIChE Journal*, **2**, 393 (1956).
57. B. Suthar, J. Landesfeind, A. Eldiven, and H. A. Gasteiger, Method to Determine the In-Plane Tortuosity of Porous Electrodes, *Journal of The Electrochemical Society*, **165**, A2008 (2018).
58. J. Landesfeind, M. Ebner, A. Eldiven, V. Wood, and H. A. Gasteiger, Tortuosity of Battery Electrodes: Validation of Impedance-Derived Values and Critical Comparison with 3D Tomography, *Journal of the Electrochemical Society*, **165**, A469 (2018).
59. Z. Li, J. Huang, B. Yann Liaw, V. Metzler, and J. Zhang, A review of lithium deposition in lithium-ion and lithium metal secondary batteries, *Journal of Power Sources*, **254**, 168 (2014).
60. V. Zinth, C. von Lüders, M. Hofmann, J. Hattendorff, I. Buchberger, S. Erhard, J. Rebelo-Kornmeier, A. Jossen, and R. Gilles, Lithium plating in lithium-ion batteries at sub-ambient temperatures investigated by in situ neutron diffraction, *Journal of Power Sources*, **271**, 152 (2014).
61. C. von Lüders, V. Zinth, S. V. Erhard, P. J. Osswald, M. Hofmann, R. Gilles, and A. Jossen, Lithium plating in lithium-ion batteries investigated by voltage relaxation and in situ neutron diffraction, *Journal of Power Sources*, **342**, 17 (2017).
62. R. Zhu, J. Feng, and Z. Guo, In Situ Observation of Dendrite Behavior of Electrode in Half and Full Cells, *Journal of the Electrochemical Society*, **166**, A1107 (2019).
63. S. Hein and A. Latz, Influence of local lithium metal deposition in 3D microstructures on local and global behavior of Lithium-ion batteries, *Electrochimica Acta*, **201**, 354 (2016).
64. A. N. Mistry, K. Smith, and P. P. Mukherjee, Electrochemistry Coupled Mesoscale Complexations in Electrodes Lead to Thermo-Electrochemical Extremes, *ACS applied materials & interfaces*, **10**, 28644 (2018).
65. C. von Lüders, J. Keil, M. Webersberger, and A. Jossen, Modeling of lithium plating and lithium stripping in lithium-ion batteries, *Journal of Power Sources*, **414**, 41 (2019).
66. M. Doyle and J. Newman, Comparison of Modeling Predictions with Experimental Data from Plastic Lithium Ion Cells, *Journal of the Electrochemical Society*, **143**, 1890 (1996).
67. M. Doyle and Y. Fuentes, Computer Simulations of a Lithium-Ion Polymer Battery and Implications for Higher Capacity Next-Generation Battery Designs, *Journal of The Electrochemical Society*, **150**, A706 (2003).
68. K. Smith and C.-Y. Wang, Power and thermal characterization of a lithium-ion battery pack for hybrid-electric vehicles, *Journal of Power Sources*, **160**, 662 (2006).
69. S. G. Stewart, V. Srinivasan, and J. Newman, Modeling the Performance of Lithium-Ion Batteries and Capacitors during Hybrid-Electric-Vehicle Operation, *Journal of the Electrochemical Society*, **155**, A664 (2008).
70. M. Park, X. Zhang, M. Chung, G. B. Less, and A. M. Sastry, A review of conduction phenomena in Li-ion batteries, *Journal of Power Sources*, **195**, 7904 (2010).
71. A. Rheinfeld, J. Sturm, A. Noel, J. Wilhelm, A. Kriston, A. Pfrang, and A. Jossen, Quasi-Isothermal External Short Circuit Tests Applied to Lithium-Ion Cells: Part II. Modeling and Simulation, *Journal of the Electrochemical Society*, **166**, A151 (2019).
72. M. Safari and C. Delacourt, Modeling of a Commercial Graphite/LiFePO4 Cell, *Journal of the Electrochemical Society*, **158**, A562 (2011).
73. S. Tippmann, D. Walper, L. Balboa, B. Spier, and W. G. Bessler, Low-temperature charging of lithium-ion cells part I: Electrochemical modeling and experimental investigation of degradation behavior, *Journal of Power Sources*, **252**, 305 (2014).
74. S. V. Erhard et al., Simulation and Measurement of the Current Density Distribution in Lithium-Ion Batteries by a Multi-Tab Cell Approach, *Journal of The Electrochemical Society*, **164**, A6324 (2017).
75. N. Lin, X. Xie, R. Schenkendorf, and U. Krewer, Efficient Global Sensitivity Analysis of 3D Multiphysics Model for Li-Ion Batteries, *Journal of The Electrochemical Society*, **165**, A1169 (2018).
76. J. Mao, W. Tiedemann, and J. Newman, Simulation of temperature rise in Li-ion cells at very high currents, *Journal of Power Sources*, **271**, 444 (2014).
77. L. O. Valøen and J. N. Reimers, Transport Properties of LiPF6-Based Li-Ion Battery Electrolytes, *Journal of the Electrochemical Society*, **152**, A882 (2005).

Rapid electrolyte wetting of lithium-ion batteries containing laser structured electrodes: in situ visualization by neutron radiography

Jan Bernd Habedank, Florian J. Günter, Nicolas Billot, Ralph Gilles, Tobias Neuwirth, Gunther Reinhart, Michael F. Zaeh

Reproduced from:

The International Journal of Advanced Manufacturing Technology 102 (2019) 9–12, pp. 2769–2778

Weblink: https://link.springer.com/article/10.1007/s00170-019-03347-4

The International Journal of Advanced Manufacturing Technology
https://doi.org/10.1007/s00170-019-03347-4

ORIGINAL ARTICLE

Rapid electrolyte wetting of lithium-ion batteries containing laser structured electrodes: in situ visualization by neutron radiography

Jan Bernd Habedank[1] · Florian J. Günter[1] · Nicolas Billot[1] · Ralph Gilles[2] · Tobias Neuwirth[2] · Gunther Reinhart[1] · Michael F. Zaeh[1]

Received: 11 May 2018 / Accepted: 17 January 2019

Abstract
Lithium-ion batteries are widely used as energy storage devices due to their high energy density and versatile applicability. Their dissemination in the mobility sector is presently limited by their high manufacturing costs. The electrolyte wetting process is one major cost driver, as process times of hours or even days are necessary to ensure complete electrolyte impregnation. In this contribution, multilayer pouch cells comprising three different types of electrodes were manufactured and filled with the electrolyte liquid while being subject to in situ neutron radiography. Two different electrode porosities were compared, as well as laser structured electrodes with additionally created micro channels, aiming at an acceleration of the wetting process. With the powerful tool of neutron radiography, it is possible to visualize and determine very precisely the wetting time, which was significantly shorter for the batteries with electrodes of higher porosity. Laser structuring of the electrodes accelerated the wetting process even further, reducing the time to complete wetting by at least one order of magnitude. These findings present great potential for the reduction of the processing time and thereby the manufacturing costs of lithium-ion batteries.

Keywords Lithium-ion battery · Laser structuring · Neutron imaging · 3D electrodes · Electrolyte filling

1 Introduction

Lithium-ion batteries (LIBs) are the dominant energy storage solution for consumer electronics and electric vehicles. Rapid developments in material science and engineering have led to significant gains in performance, reliability, and safety of LIB-powered products at shrinking costs [1]. In order to meet future customer expectations in automotive applications, the costs of the battery cells have to decrease even further. Manufacturing costs—especially those associated with the time-consuming electrolyte wetting and the following formation process—make up for a significant share of the total costs of LIBs and have great potential to be reduced by process optimization [2].

1.1 Challenges of the electrolyte filling process

The electrolyte filling and subsequent wetting process are among the bottlenecks in LIB production, as a certain amount of the liquid electrolyte solution has to be dispensed into a sealed and secluded cell volume, which is mostly occupied by the cell stack. The cell stack consists of electrodes and separator sheets stacked or wound together, whereas the electrodes themselves consist of composite layers of active materials, binders, and conductive agents coated on metallic current collector foils [3]. These foils are impermeable for liquids and therefore act as an infiltration barrier for the electrolyte. Thus, the volume to be filled (the pores of the electrodes and the separators) is not easily accessible for the liquid. Additionally, the pores are initially filled with gas, which firstly has to be removed in order to enable electrolyte infiltration. Different pressure cycles have proven to accelerate the electrolyte intake and are therefore used in industrial cell production [4, 5]. With increasing size of the available LIBs in the market, process knowledge gains importance, as production rejects due to insufficient product quality become more expensive per piece. At the same time, the complexity of the electrolyte dosing process increases as the ratio between the pore

✉ Jan Bernd Habedank
jan.habedank@iwb.mw.tum.de

[1] Institute for Machine Tools and Industrial Management (iwb), Technical University Munich, Boltzmannstr. 15, 85748 Garching, Germany

[2] Heinz Maier-Leibnitz Zentrum (MLZ), Technical University Munich, Lichtenbergstr. 1, 85748 Garching, Germany

Published online: 06 February 2019

volume (electrodes and separator) and the void volume between the cell stack and the casing rises. This may require a process design consisting of multiple dosing and wetting steps [6]. In order to reduce the amount of gas remaining in the pores, the cell is evacuated to a pressure slightly above the vapor pressure of the electrolyte liquid. After dosing, the electrolyte liquid wets the surfaces superficially and from there intrudes into the porous media by diffusion and capillary forces. When enough liquid has diffused into the pores, dosing can be repeated until the target electrolyte amount is reached. Subsequently the cell is sealed and exposed to atmospheric pressure. The residual gas in the porous media is compressed according to the ideal gas law. The pore volume filled with electrolyte $V_{\mathrm{pores,el}}$ is then the difference between the pore volume of the electrode V_{pores} and the compressed gas volume $\Delta V_{\mathrm{pores,gas}}$:

$$V_{\mathrm{pores},el} = V_{\mathrm{pores}} - \Delta V_{\mathrm{pores,gas}} = V_{\mathrm{pores}} - \frac{m_{\mathrm{gas}} \cdot R \cdot T_{\mathrm{amb}}}{p_{\mathrm{amb}} - p_{\mathrm{evac}}} \tag{1}$$

with R being the specific gas constant, m_{gas}, the mass of the residual gas, T_{amb}, the ambient temperature, p_{amb}, the ambient pressure and p_{evac}, the pressure after evacuation. One way to enhance the energy density and the specific energy of LIBs is to reduce the porosity of the electrodes while maintaining a constant active material loading per electrode area [7, 8]. The electrode porosity ε is defined by the ratio of the pore volume V_{pores} and the total volume of the porous electrode $V_{\mathrm{electrode}}$:

$$\varepsilon = \frac{V_{\mathrm{pores}}}{V_{\mathrm{electrode}}} \tag{2}$$

This porosity reduction is achieved in a rolling process (calendering) and is part of the industrial LIB production process. However, low electrode porosities may impair the wettability of the electrodes, as the average pore sizes are reduced and surface sealing can occur, impeding the penetration of the liquid into the electrode pores [9]. Although studies on the influence of porosity on the wettability of the electrodes of LIB exist [9, 10], very little is known about the influence of the prevailing production conditions, e.g., the changing pressure levels during electrolyte filling and wetting. Also, the multilayer cell stack setup can be assumed to have a significant influence on the dissemination of the liquid, as the interfaces between the cell layers create additional capillary planes [4]. The wetting process has recently been visualized for the first time by neutron radiography in pouch cells [4] and hard case cells [11]. In these studies, LIBs were irradiated with a neutron beam and the transmitted neutron radiation was recorded with a neutron detector. As most of the battery components, except for the electrolyte liquid, show high neutron transmission due to a low mass attenuation coefficient of the neutrons [12], the temporal and 2D-spatial distribution of the electrolyte could be visualized under realistic production conditions [4]. This measurement technique presents unique possibilities for the development of further process knowledge, providing a basis for optimization of the cell and electrode design.

1.2 Laser structuring of electrodes

Laser structuring of the electrodes of LIBs has attracted considerable attention in the recent past, having potential for advancements of many aspects of LIBs. It was indicated that the deployable specific capacity of LIBs with laser structured cathodes could be increased at high current rates [13]. Similar results were shown for anode materials, such as graphite [14]. This effect was attributed to shortened diffusion paths, creating a better degree of electrochemical accessibility of all electrode segments, especially those close to the current collectors [13, 15, 16]. Drawbacks of laser structuring of electrodes have also been addressed. As a fraction of active material is removed from the electrode by laser radiation, the areal capacity of the electrode and thereby the deployable capacity at low currents is slightly decreased. However, this effect can be minimized by reducing the width of the capillary structures [17]. A study on the influence of laser-induced structures on the wetting process of single electrode sheets showed notable improvements in the wetting time. Capillary forces were identified as the main drivers for the accelerated electrolyte uptake [18].

1.3 Approach and objective

In the work presented here, neutron radiography was applied to large footprint LIBs containing electrodes with different properties of the active material layers, in order to determine the influence of electrode characteristics on the spatial and temporal distribution of the electrolyte liquid during electrolyte wetting. The wetting process in the examined pouch cells is much more complex than the wetting of single electrode sheets. Furthermore, the low pressure during electrolyte dosing and the subsequent sealing and venting procedures create entirely different conditions for the spreading liquid. The goal of the presented work is to outline the potential of laser structuring for the acceleration of the wetting process under realistic production conditions as well as to compare the potential benefits to other measures, e.g., an increased porosity of the electrodes. Possible trade-offs arising from the removed active material fraction will be discussed and are subject of ongoing further investigations.

2 Experimental

2.1 Cell production

Three pouch bag cells, each consisting of five anodes and four cathodes (double-sided coating) were produced at the Technical University of Munich on fully automated machines:

- One cell with *conventional* electrodes with an electrode porosity of 30% (cell a))
- One cell with *conventional* electrodes with an electrode porosity of 40% (cell b))
- One cell with *laser structured* electrodes with an electrode porosity of 30% (cell c))

Electrode production was performed in a cleanroom (ISO 6) and cell assembly in a dry room (dew point < − 55 °C). The anode ink was prepared by mixing 95 wt.% graphite (SGL) and 5 wt.% Polivinylidendiflouride (PVDF, Kynar) with 1-Methyl-2-pyrrolidon (NMP, Sigma Aldrich) in a multi-step mixing process described in [19]. The cathode ink contained 96 wt.% lithium-nickel-manganese-cobalt-oxide (NMC, BASF), 2 wt.% PVDF and 2 wt.% carbon (C65, Timcal), and NMP. Mixing was performed in a planetary centrifugal mixer (DAC 3000, Hauschild Engineering). Both inks were coated on both sides of metallic current collector foils (anode: copper, 14 μm thickness, cathode: aluminum, 15 μm thickness) in a roll-to-roll tape cast process and dried in an infrared dryer (Coatema). The areal capacity of the anodes was by a factor of 1.2 higher than the capacity of the cathodes, resulting in area specific capacities of 2.0 mAh cm^{-2} for the cathodes and 2.4 mAh cm^{-2} for the anodes. The target porosities P were achieved in a calendering process. Therefore, the required thicknesses D of the electrode layers without the current collector foils were calculated according to

$$P = \frac{D - W\left((x1/\rho1) + \left(x2/\rho2\right) + \left(x3/\rho3\right)\right)}{D} \tag{3}$$

where W is the measured mass of the coating per area and $x1$, $x2$, and $x3$ are the percentage shares of active material (NMC/graphite), PVDF, and C65. $\rho1$, $\rho2$, and $\rho3$ are the respective densities, which were derived from literature as follows: NMC 4.75 g cm^{-3}, C65 2.00 g cm^{-3}, PVDF 1.76 g cm^{-3}, graphite 2.26 g cm^{-3} [20]. For a target porosity of 30% (cell a) and cell c)), the anode thickness was 107 μm and the cathode thickness was 109 μm, whereas for a target porosity of 40% (cell b)), the anode thickness was 126 μm and the cathode thickness was 125 μm. The fulfillment of these target values was confirmed by measurements with a digital micrometer (Series 293, Mitutoyo). Subsequently, the electrode sheets were cut in a remote laser cutting process to a format of 101 mm × 73 mm (cathode) and 104 mm × 76 mm (anode), see Fig. 2. Afterwards, the laser structuring process was performed for one cell with 30% electrode porosity (cell c), which is presented in more detail in section 2.2. The commercial separator (Celgard 2325) was z-folded between the electrodes to ensure electrical insulation and wrapped around the cell stack for mechanical stability. The current collector foils were joined in a first ultrasonic welding process and subsequently connected to the cell tabs in a second ultrasonic welding process. The complete cell stacks were packaged into deep drawn pouch bag foils, leaving one side open for the electrolyte filling process.

2.2 Laser structuring

For laser structuring, an infrared pulsed fiber laser (YLPP-1-150 V-30, IPG Photonics) combined with a high speed optical scanning head (ARGES, Racoon 21) and a telecentrical focusing lens was used. Important beam characteristics are listed in Table 1.

The laser beam coming from the source was guided through an optical fiber into the remote amplifier, from where the unfocussed beam was directed into the scanning optics, where the laser beam was deflected by two mirrors in the x/y-plane and focussed on the electrode surface. The focal distance between the lens and the electrode surface was 80 mm. The electrode was fixed using a vacuum table. The experimental setup is presented in Fig. 1.

A grid structure consisting of horizontal and vertical lines with a pitch distance of 1.55 mm was chosen as the electrode structure, in order to enable electrolyte flow through the capillaries in both directions of the electrode plane. The line scanning speed was 600 mm/s for both anode and cathode, resulting in an applied line energy E_{line} of 50 J m^{-1}. The cell stack setup and an illustration of the applied structure pattern are displayed in Fig. 2.

Structuring was performed in ambient air at ambient pressure. The ablated material was removed by a suction nozzle. Further details of the resulting electrode morphology are presented in section 3.1.

Table 1 Laser beam parameters for structuring

Wavelength λ in nm	Beam quality factor M^2	Focus diameter d_0 in μm	Pulse duration τ_p in ps	Pulse repetition rate f_R in kHz	Pulse energy E_p in μJ
1060	2.0	25	150	600	50

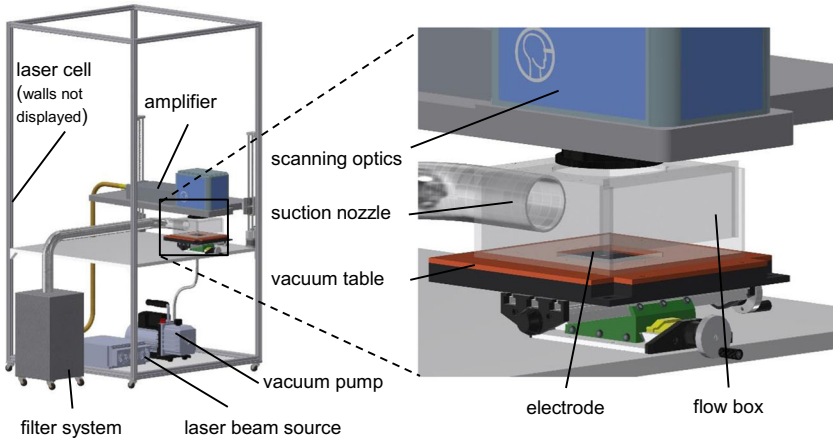

Fig. 1 Schematic illustration of the experimental setup for laser structuring of the electrodes

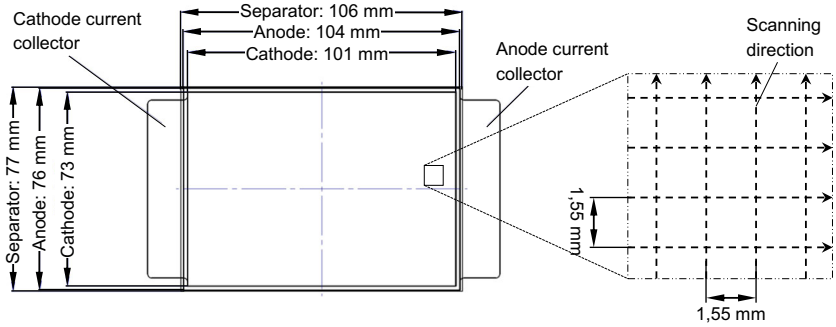

Fig. 2 Schematic illustration of the multilayer cell stack (left) and the applied laser structuring pattern (right)

2.3 Experimental setup for electrolyte filling and wetting

The filling and radiography experiments were conducted at the ANTARES imaging instrument at the Heinz Maier-Leibnitz Zentrum (MLZ) in Garching near Munich, Germany [21, 22]. Electrolyte filling was performed using a custom-designed installation, mainly consisting of a vacuum chamber, a sealing bar, and the required valves and filling assets (see Fig. 3a). The entire installation was placed in front

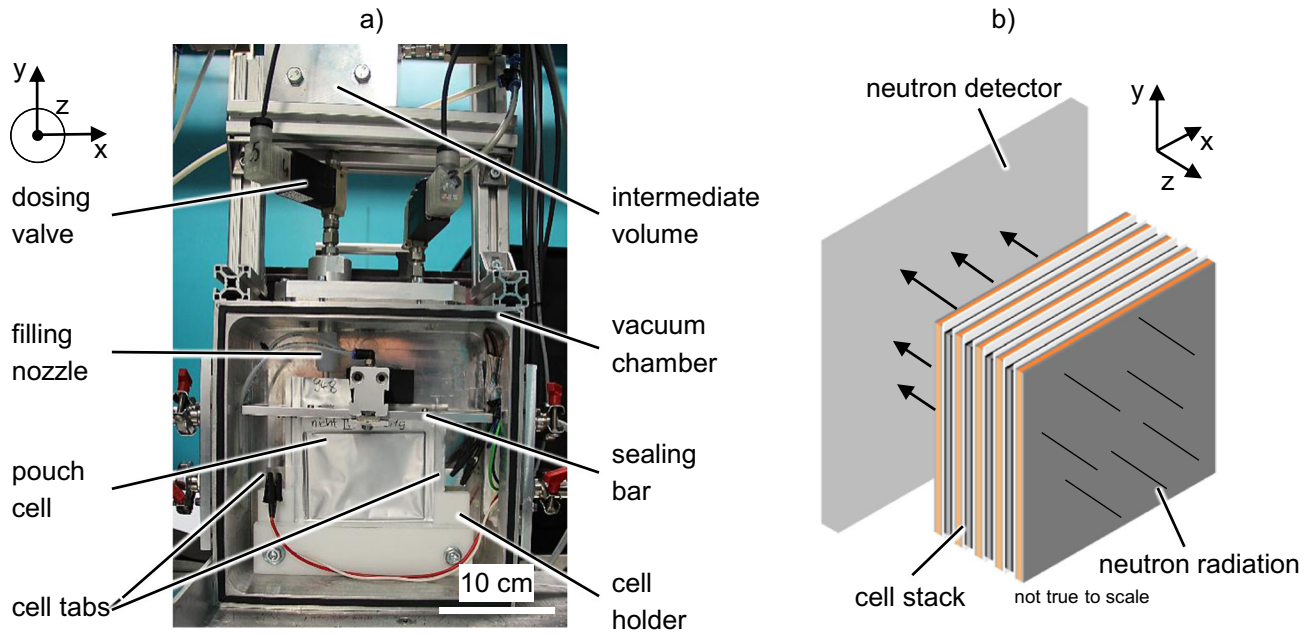

Fig. 3 **a** Electrolyte filling installation in front of the neutron detector at the ANTARES imaging instrument. **b** Schematic illustration of the neutron flow through the cell stack in the *z*-direction

of a neutron detector which recorded the transmitted neutrons, as shown in Fig. 3b.

The pouch cell was placed in a cell holder in a vertical orientation with the open side facing upwards. The filling nozzle was positioned, so that the liquid could flow directly into the cell. The electrolyte (LP572, BASF) consisted of ethylene carbonate (EC) and ethyl-methyl-carbonate (EMC) in a mixing ratio of 3:7 with 1 M lithium-hexaflourophosphate ($LiPF_6$) and 2% vinylene carbonate (VC). An electrolyte amount of 6.0 ml was pre-dosed with a dosing device (Dosino 800, Metrohm) into an intermediate volume. At the same time, the aluminum vacuum chamber was evacuated down to a pressure p_{evac} of 50 mbar. By opening the valve between the previously evacuated vacuum chamber and the intermediate dosing volume at ambient pressure, the electrolyte liquid was sucked into the pouch cell via the filling nozzle. Due to the large free space between the cell stack and the pouch foil, one dosing step was sufficient for the described experiments. Shortly after the injection of the electrolyte liquid, the cells were hermetically sealed at p_{evac} before the vacuum chamber was flooded with air until reaching ambient pressure. After venting, the sealed cell containing the electrolyte liquid was kept at constant ambient pressure and constant temperature of 25 °C for the wetting process and a total observation time of 90 min.

2.4 Imaging and signal processing

Before the filling experiments, five dark field images I_{df} were recorded with a closed neutron shutter in order to obtain the static background signal from the detector. Prior to each filling experiment, one neutron image of each empty cell I_{ref} positioned in the vacuum chamber was recorded. The following neutron images were acquired within the wetting timespan of 90 min. The size of one radiography image was 1300 × 2048 pixels. The images were later cropped to the size of the cell stack. The effective size of one pixel was 73 μm × 73 μm. The spatial resolution of the radiographies was approximately 150 μm, being a combination of the geometrical resolution defined by the L/D ratio of 500 used in this experiment, the blurring due to the scintillator thickness (100 μm), and the effective pixel size. For the acquisition of one image, the neutron shutter was opened for 3 s, irradiating the sample with a neutron flux density $\Phi_n = 6.4 \cdot 10^7 \mathrm{cm}^{-2} s^{-1}$. The electrolyte flow in the cell during wetting was slow enough to avoid a significant motion blur within this time period. In order to reduce the amount of measurement data and to keep the radioactive activation of the samples and the experimental setup low, the imaging rate was reduced towards the end of the measurement timespan: for the first 15 min, one image was taken every 15 s, for the next 45 min, one image was taken every 45 s, and for the remaining 30 min, the time between the images was 120 s, as displayed in Fig. 4.

For further signal processing, the images of the empty cells were used to computationally eliminate the signals originating from the cell components, the cell holder, and the vacuum chamber, visualizing only the electrolyte liquid. The final transmission images T_i were calculated in *Matlab* by

$$T_i = \frac{I_i - I_{\mathrm{median,df}}}{I_{\mathrm{ref}} - I_{\mathrm{median,df}}} \tag{4}$$

with I_i being the image of the filled cell and $I_{\mathrm{median,df}}$ the median of the dark field images. A time stamp was assigned to each image starting with the image taken just before the electrolyte injection. As the wetted parts of the cell appeared darker due to the higher neutron absorption of the electrolyte, the wetting degree of the cell could be determined by using a grayscale threshold: The pixels darker than the threshold value were attributed to the wetted fraction of the cell, whereas brighter pixels were assigned to the dry parts [4].

3 Results and discussion

3.1 Characterization of the electrodes

The different electrodes for the three cell types were examined using a scanning electron microscope (SEM). In Fig. 5, images of all incorporated electrode types are displayed. The difference in porosity between the electrodes of cell a) and cell b) is clearly visible, as the graphite and NMC particles are compressed much more in cell a), resulting in smaller pore sizes. By laser structuring (cell c)), the active material on the anode was completely removed in the irradiated sections of the electrode, leaving the blank copper foil and creating the

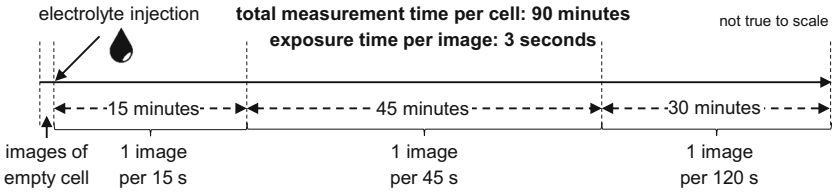

Fig. 4 Measurement sequence for neutron image acquisition

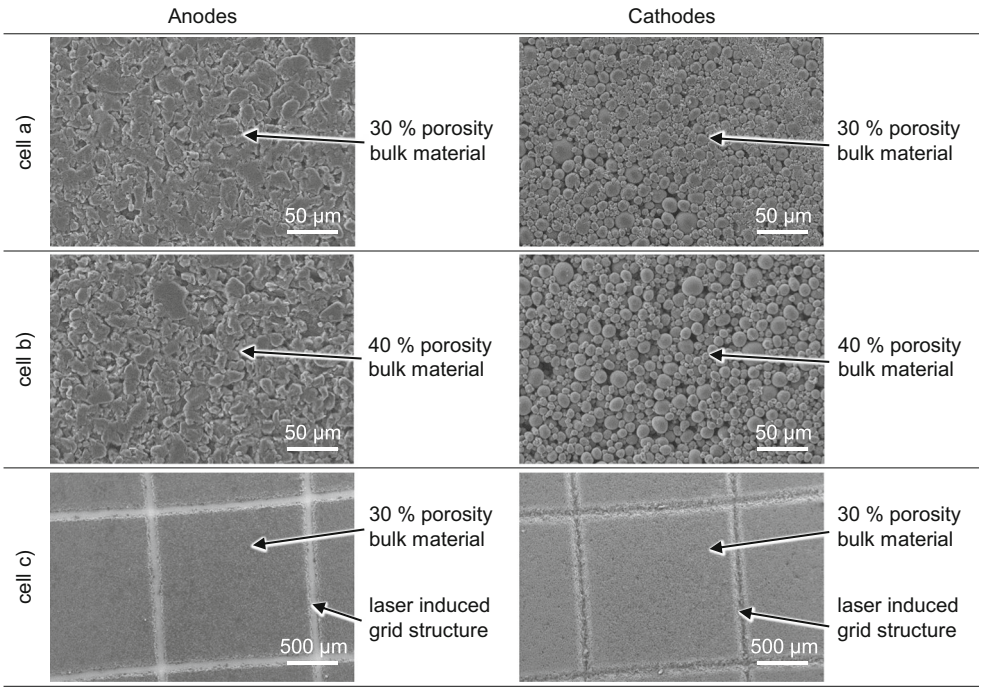

Fig. 5 SEM-images of the different electrodes for the cells with 30% electrode porosity (type a)), 40% porosity (type b)), and 30% porosity with additional laser induced structures (type c))

aspired micro capillaries for more rapid electrolyte intake and distribution within the cell stack. With the applied structuring process, capillary widths of 60–80 µm and a depth of 46.5 µm (100% of single-sided coating thickness) were created, leading to a removal of approx. 10% of the active material on the electrode.

On the cathode side, the coating was not entirely removed in the irradiated sections, merely locally revealing small parts of the aluminum foil. In other areas, active material residues on the current collector were observed. This hints at different ablation characteristics of the two coating types. Ongoing studies will create a deeper understanding of the laser ablation process of the different electrodes.

3.2 Analysis of electrolyte intake

In Fig. 6, neutron radiography images of the three cells are displayed, all recorded precisely 270 s after the electrolyte injection. The image on the left shows cell a), which comprises conventional electrodes with 30% porosity, the image in the middle is of cell b) with conventional electrodes with a porosity of 40%, and the image on the right is of cell c) with electrodes of 30% porosity and additional laser structures. The darker parts of the images represent the sections already wetted with electrolyte, while the brighter parts represent the dry areas. At this observation time, all cells have been sealed, and the vacuum chamber has been flooded with air, exerting pressure on the cell stack. Striking differences of the wetting progress become apparent. After 270 s of wetting time, cell a) still exhibits large dry sections that have not been in touch with the electrolyte solution. On the sides and on the bottom of the cell stack, large amounts of still unused excess electrolyte can be localized, which was drawn into the inner parts of the cell stack later during the wetting process. As previously described in [4], the propagation of the electrolyte mainly proceeds from the bottom and the sides of the cell stack, creating a U-shaped liquid front. Compared to cell a), the wetting progress of cell b) is already more advanced at the time of observation, as the bright parts of the image in the inner parts of the cell stack as well as the amount of remaining electrolyte on the bottom of the cell are considerably smaller. The higher electrode porosity seems to have a positive impact on the electrolyte intake and the distribution rate. This can be attributed to the larger pores which create a generally more open electrode structure with more access and distribution paths for the fluid. The wetting progress of cell c) is even further advanced, leaving only a very small section of the cell stack without electrolyte. The remaining liquid towards the bottom of the cell stack has almost completely been soaked up by the cell stack at this point in time.

With a spatial image resolution of 150 µm, a more detailed observation of the microscopic wetting process was not possible and only the macroscopic acceleration of the fluid dispersion could be observed. The effect within the capillaries will be studied by the authors in more detail in future work in order to further reduce the amount of removed active material from the electrodes and identify an ideal structuring geometry. In Fig. 7, the relative wetted area of the three different cells determined by the grayscale threshold method is displayed as a function of time.

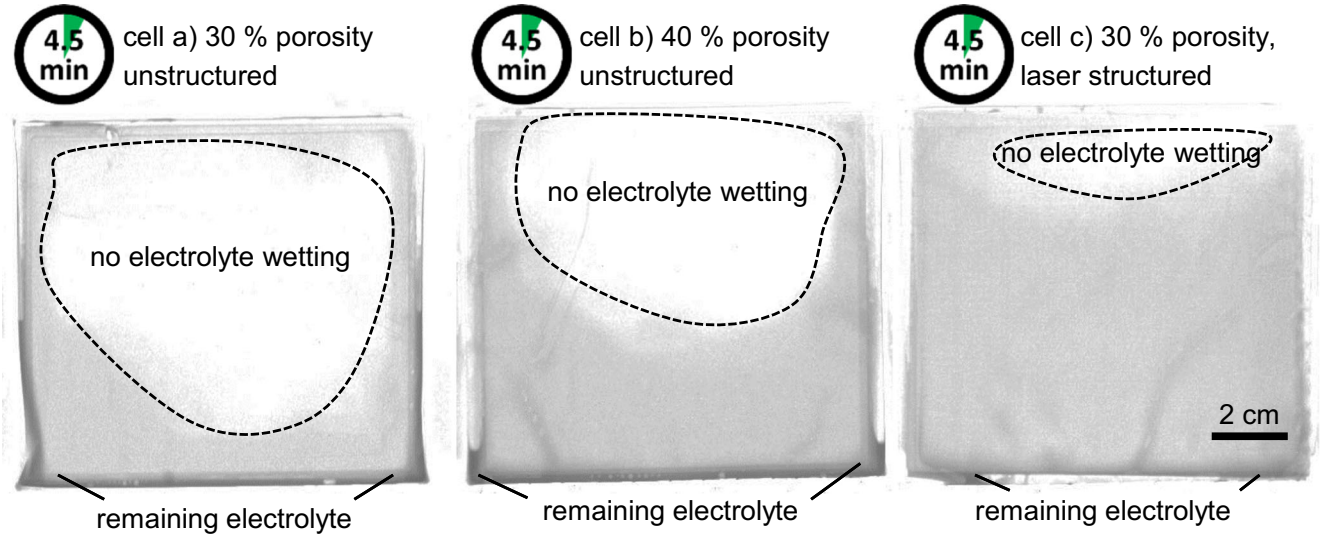

Fig. 6 Processed neutron radiography images; all images were recorded 4.5 min after the electrolyte dosing process. Left: reference cell with unstructured electrodes of 30% porosity (**a**), middle: cell with unstructured electrodes of 40% porosity (**b**), right: cell with laser structured electrodes of 30% porosity (**c**)

The time of the image acquisition for the images displayed in Fig. 6 is marked with a black line parallel to the *y*-axis. Before electrolyte dosing, the wetting degree is zero and no dark sections can be identified in the radiography images. After the electrolyte is injected into the cell, the grayscale evaluation shows a wetting degree of approx. 20% for all cells. When evaluating the corresponding radiography images, it becomes apparent, that at this time, the liquid is not homogeneously distributed but rather in large drops on the bottom of the cell stack. In the sealing and subsequent venting process, the electrolyte distribution is homogenized significantly by squeezing the excess electrolyte towards the inner parts of the cell stack. From that point in time on, the relative wetted area of the cell stack starts to differ for the three cell types. Cell a) shows a rather sluggish wetting progress, not getting close to complete wetting within the 90 min of observation time. Linear extrapolation of the wetting slope suggests that complete wetting might not be reached even within 180 min. Cell b) demonstrates faster electrolyte intake, almost reaching complete wetting after 90 min. Cell c) in contrast reaches complete wetting after only 15 min. In Fig. 8, neutron radiography images recorded 15 min after

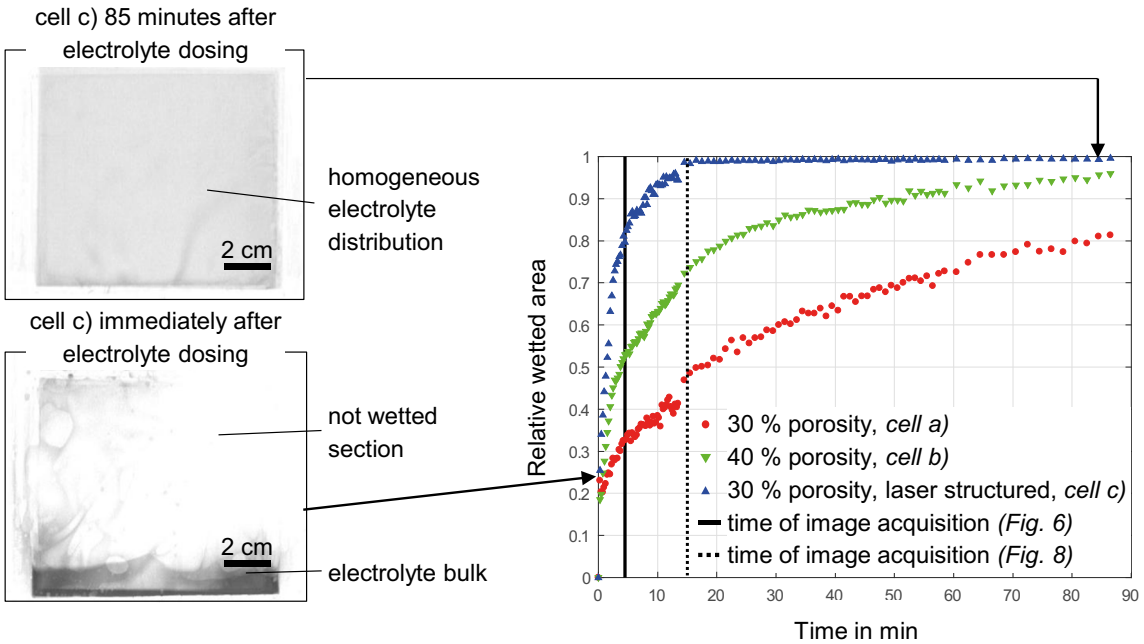

Fig. 7 Relative wetted area of the three cell types over time after electrolyte dosing

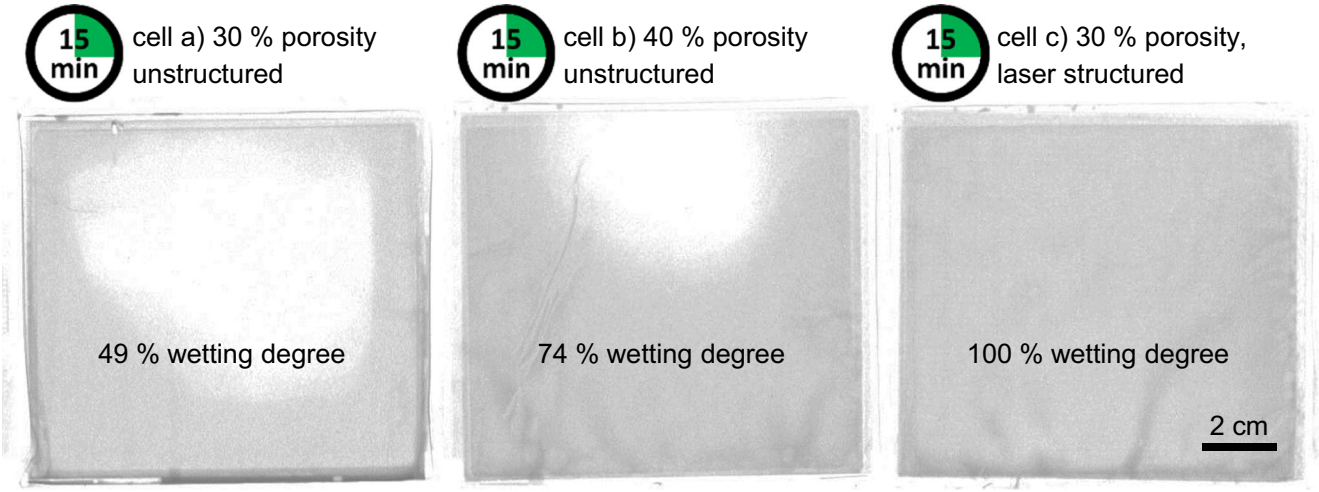

Fig. 8 Processed neutron radiography images; all images were recorded 15 min after the electrolyte dosing process. Cell c) has reached complete wetting, whereas cell a) and cell b) show incomplete wetting degrees of 49% and 74% respectively

electrolyte dosing are presented. At this point in time, the wetting degrees of cell a) and cell b) are at 49% and 74% respectively, whereas cell c) has already reached a wetting degree of 100%. In a production scenario, only cell c) would be ready for further processing, e.g., the start of the formation cycles, whereas cell a) and cell b) would have to be stored in a controlled environment, creating additional production costs. It has to be noted, that the observed wetting phenomena are taking place on a macro scale and neutron radiography—in this experimental setup—does not provide insight into the wetting phenomena on a micro scale, e.g., the wetting of single electrode and separator pores. These processes are likely to require more time, especially as all pores should be wetted prior to the subsequent formation cycles.

It can be concluded that porosity plays a significant role in the macroscopic wetting process, with higher porosities generally favoring a more rapid electrolyte intake. Laser structuring of the electrodes leads to an even faster macroscopic wetting process of battery cells. Considering the extrapolated 180 min of wetting time for cell a), the wetting process for cell c) was approx. 12 times faster. As a homogeneous macrodistribution of the electrolyte in the cell is the prerequisite for the further wetting on a micro scale, laser structuring of electrodes appears to have potential for the acceleration of the wetting process in general and thereby the reduction of production costs of lithium-ion batteries. Taking into account that neither the laser-induced electrode structures nor other process parameters (temperature, pressure, spatial orientation of the cell etc.) were optimized in any way, further potential for the acceleration of the wetting process seems likely.

3.3 Interaction with other cell characteristics

The presented measures for the acceleration of the wetting process (higher porosity and laser structuring) have to be carefully assessed, as the presented improvements in processing time will influence other important cell properties. For example, it has been shown that the porosity of the electrodes significantly influences their mechanical stability as well as their electrochemical performance. While the overall rate capability of LIBs containing electrodes with higher porosity is generally superior due to better ionic conductivity, the mechanical cohesion of the active material particles can be diminished [8]. This may lead to a loss of the electrical conductivity as well as delamination during cell production. Moreover, the volumetric energy density on a cell level is reduced with higher electrode porosities, as the electrodes occupy a larger volume with the same amount of active material. Depending on the range of application (high-power or high energy), these trade-offs between high and low porosity have to be considered.

The improvements in wetting time and costs due to laser structuring of the electrodes are achieved at the expense of an additional production process. This process is associated with investment costs for laser beam sources, optics, and additional machinery as well as processing costs, which are mainly due to the removal of active material. In order to minimize this effect, the active material removal has to be limited. As the active material loss is nearly proportional to the square of the pitch distance of the applied grid-structures, large pitch distances and small structure diameters are beneficial. By increasing the pitch distance, the speed of the laser structuring process can also be increased, as fewer structures have to be created per electrode area. Cost estimations in literature being based on an active material loss fraction of 4–5% show an increase of the total cell costs of 1.2–1.5% [17], which would have to be overcompensated by the cost reductions obtained in the electrolyte wetting process. This very low share of active material loss can be achieved by fine tuning the laser ablation parameters and using femtosecond laser pulses, reducing the

thermal impact of the deposited energy during ablation. Process investigations regarding a reduction of the structure dimensions are the subject of ongoing studies of the authors. Additionally, laser structuring of the electrodes has shown tremendous beneficial effects on the electrochemical cell performance. As stated in the introductory part of this paper, the C-rate capability can be drastically increased due to improved lithium diffusion kinetics, providing more usable energy at high discharge currents. These individual characteristics and conflicting priorities have to be carefully assessed and balanced for a specific production scenario by the LIB manufacturer with the aim to minimize the wetting time and the active material removal while maximizing the electrochemical performance enhancement. However, especially for large format LIBs with hundreds of electrode layers as commonly used in automotive applications, fast electrolyte dispersion will gain relevance. Thus, laser structuring can be considered as an additional lever for fine-tuning the production and use cases of LIBs. A detailed costs assessment for the laser structuring process as well as a thorough characterization of the interplay between the electrochemical performance of the cell and the wetting behavior are subjects of ongoing work of the authors.

4 Summary and outlook

In the presented work, the influences of different electrode porosities as well as laser structuring of the electrodes of LIBs on the electrolyte wetting process were investigated. Three large pouch cells were manufactured, one cell with conventional electrodes with 30% porosity, one with electrodes with a higher porosity of 40%, and one cell containing electrodes of 30% porosity which were additionally laser structured. For structuring, a grid pattern was chosen in order to create small channels in both directions of the electrode plane to enhance homogeneous electrolyte distribution after the electrolyte dosing procedure. The progress in electrolyte dispersion for the three cell types was visualized in situ using neutron radiography. Results show a significant influence of the electrode properties on the wetting behavior of the battery cells. Conventional electrodes exhibited a very slow electrolyte wetting, resulting in a required wetting time of several hours. Higher porosity electrodes showed slightly faster electrolyte wetting, presumably caused by the larger pore volume and thereby lower resistance in fluid dispersion. Laser structured electrodes presented a much faster wetting progress, even though the porosity of the bulk material of the electrode was 30%. The time for complete wetting was reduced to approx. 15 min, accelerating the wetting process at least by one order of magnitude. Interpretation of the acquired neutron images leads to the conclusion, that the liquid is soaked rapidly into the capillary grid structures and distributed effectively into the center of the cell stack. Thus, laser structuring of electrodes may play an important role in reducing the production costs of LIBs, since long and cost intensive storage procedures of the batteries after electrolyte filling can be avoided. Future work of the authors will focus on optimizing the structures with respect to minimized active material removal and simultaneous improvement of the electrochemical properties of the cells.

Funding information This study is funded by the German Federal Ministry of Education and Research (BMBF) under grant number 03XP0081 (ExZellTUM II).

References

1. Sakti A, Michalek JJ, Fuchs ERH, Whitacre JF (2015) A techno-economic analysis and optimization of Li-ion batteries for light-duty passenger vehicle electrification. J Power Sources 273:966–980
2. Wood DL, Li J, Daniel C (2015) Prospects for reducing the processing cost of lithium ion batteries. J Power Sources 275:234–242
3. Korthauer R (2013) Handbuch Lithium-Ionen-Batterien. Springer Berlin Heidelberg, Berlin, Heidelberg
4. Knoche T, Zinth V, Schulz M, Schnell J, Gilles R Reinhart G (2016) In situ visualization of the electrolyte solvent filling process by neutron radiography 15th International Meeting on Lithium Batteries (IMLB) 331, 267–276
5. Knoche T, Reinhart G (2015) Electrolyte filling of large-scale lithium-ion batteries. Main Influences and Challenges for Production Technology AMM 794:11–18
6. Günter FJ, Habedank JB, Schreiner D, Neuwirth T, Gilles R, Reinhart G (2018) Introduction to electrochemical impedance spectroscopy as a measurement method for the wetting degree of Lithium-ion cells. J Electrochem Soc 165:A3249–A3256
7. Zheng H, Li J, Song X, Liu G, Battaglia VS (2012) A comprehensive understanding of electrode thickness effects on the electrochemical performances of Li-ion battery cathodes. Electrochim Acta 71:258–265
8. Zheng H, Tan L, Liu G, Song X, Battaglia VS (2012) Calendering effects on the physical and electrochemical properties of Li [Ni1/3Mn1/3Co1/3]O2 cathode. J Power Sources 208:52–57
9. Sheng Y, Fell CR, Son YK, Metz BM, Jiang J, Church BC (2014) Effect of calendering on electrode wettability in lithium-ion batteries. Front Energy Res 2:83
10. Lee, S. G. & Jeon, D. H. 2014 Effect of electrode compression on the wettability of lithium-ion batteries 15th International Meeting on Lithium Batteries (IMLB) 265, 363–369
11. Weydanz, W. J., Reisenweber, H., Gottschalk, A., Schulz, M., Knoche, T., Reinhart, G., Masuch, M., Franke, J. & Gilles, R. 2018 Visualization of electrolyte filling process and influence of vacuum during filling for hard case prismatic lithium ion cells by neutron imaging to optimize the production process 15th International Meeting on Lithium Batteries (IMLB) 380, 126–134
12. Sears VF (2006) Neutron scattering lengths and cross sections. Neutron News 3:26–37
13. Mangang, M., Pröll, J., Tarde, C., Seifert, H. J. & Pfleging, W. 2014 Ultrafast laser microstructuring of LiFePO 4 cathode material. In *SPIE LASE* (ed. U. Klotzbach, K. Washio & C. B. Arnold), 89680M: SPIE
14. Habedank JB, Endres J, Schmitz P, Zaeh MF, Huber HP (2018) Femtosecond laser structuring of graphite anodes for improved

lithium-ion batteries: ablation characteristics and process design. Journal of Laser Applications 30:32205
15. Habedank JB, Kraft L, Rheinfeld A, Krezdorn C, Jossen A, Zaeh MF (2018) Increasing the discharge rate capability of lithium-ion cells with laser-structured graphite anodes: modeling and simulation. J Electrochem Soc 165:A1563–A1573
16. Bae, C.-J., Erdonmez, C. K., Halloran, J. W. & Chiang, Y.-M. 2013 Design of battery electrodes with dual-scale porosity to minimize tortuosity and maximize performance. Advanced materials (Deerfield Beach, Fla) 25, 1254–1258
17. Pfleging W (2018) A review of laser electrode processing for development and manufacturing of lithium-ion batteries. Nanophotonics 7:13
18. Pfleging, W., Kohler, R. & Pröll, J. 2014 Laser generated microstructures in tape cast electrodes for rapid electrolyte wetting: new technical approach for cost efficient battery manufacturing. In *SPIE LASE* (ed. U. Klotzbach, K. Washio & C. B. Arnold), 89680B: SPIE
19. Günther T, Billot N, Schuster J, Schnell J, Spingler FB, Gasteiger HA (2016) The manufacturing of electrodes: key process for the future success of lithium-ion batteries. AMR 1140:304–311
20. Marks T, Trussler S, Smith AJ, Xiong D, Dahn JR (2011) A guide to Li-ion coin-cell electrode making for academic researchers. J Electrochem Soc 158:A51
21. Schulz, M. & Schillinger, B. 2015 ANTARES. Cold neutron radiography and tomography facility JLSRF 1
22. Calzada, E., Gruenauer, F., Mühlbauer, M., Schillinger, B. & Schulz, M. 2009 New design for the ANTARES-II facility for neutron imaging at FRM II. Nuclear Instruments and Methods in Physics Research Section A: Accelerators, Spectrometers, Detectors and Associated Equipment 605, 50–53

Paving the way for industrial ultrafast laser structuring of lithium-ion battery electrodes by increasing the scanning accuracy

Jan Bernd Habedank, Daniel Schwab, Bernhard Kiesbauer, Michael F. Zaeh

Reproduced from:

Journal of Laser Applications 32 (2020) 2, pp. 22053/1–22053/6

Weblink: https://doi.org/10.2351/7.0000078

Journal of Laser Applications ARTICLE scitation.org/journal/jla

Paving the way for industrial ultrafast laser structuring of lithium-ion battery electrodes by increasing the scanning accuracy

Cite as: J. Laser Appl. 32, 022053 (2020); doi: 10.2351/7.0000078
Submitted: 1 April 2020 · Accepted: 1 April 2020 ·
Published Online: 6 May 2020

Jan Bernd Habedank,[1] Daniel Schwab,[2] Bernhard Kiesbauer,[2] and Michael F. Zaeh[1]

AFFILIATIONS

[1]Institute for Machine Tools and Industrial Management, Technical University of Munich, Boltzmannstr. 15, 85748 Garching, Germany
[2]ARGES GmbH, Werk 4, 92442 Wackersdorf, Germany

Note: This paper is part of the Special Collection: Proceedings of the International Congress of Applications of Lasers & Electro-Optics (ICALEO® 2019).

ABSTRACT

The performance of lithium-ion batteries is determined by the structural properties of the electrodes, e.g., the choice of an active material and porosity. An increase in performance is crucial for fulfilling the future requirements of various applications, such as electric vehicles and consumer electronics. Laser structuring with short and ultrashort pulses offers great potential, which has been demonstrated in many research studies. Based on already published preliminary work, which is primarily dedicated to the proof of electrochemical enhancements, requirements for the structuring process are examined. Starting from a realistic production scenario for lithium-ion electrode processing, calculations concerning the technical requirements for the laser scanner system are made. The results show high demands on usable control technology. For this reason, the development of a new type of control system is presented, which has significantly more temporal accuracy in signal transmission and thus provides the basis for fast and, at the same time, high-precision processing with pulsed laser systems.

Key words: laser structuring, lithium-ion batteries, electrodes, polygon scanner, scale-up, production technology

I. INTRODUCTION

Nowadays, a lot of consumer electronics and mobility solutions like electric vehicles are powered by lithium-ion batteries. The key factors for their success are high energy density, the long service life, and the high achievable cell voltage, among others. Lithium-ion batteries have been on the market for around 30 years, and during this time, the cells have been constantly improved in terms of energy density, service life, and safety. Nevertheless, there still remains scope for further development, and research activities concerning advanced materials and processes are conducted worldwide to meet the ever-rising requirements in cell performance. The central components of a lithium-ion battery are the two porous electrodes, the liquid electrolyte, and the porous separator. The latter electrically isolates the two electrodes from each other but is permeable to lithium ions. In a charged battery, the lithium ions are stored in the anode. As soon as electric current is consumed, the charged particles migrate through the electrolyte-wetted separator and intercalate into the cathode. When charging, this process is reversed. The electrode structure has a significant influence on the level of cell internal resistance in these charge and mass transport processes. If, for example, the porosity of the electrodes is not set correctly by adapted production processes, the ionic resistance of the lithium transport increases.[1] A promising approach that has received special attention in recent years is the introduction of three-dimensional structures into the porous electrode material using laser radiation.[2] The basic idea behind this approach is to shorten the long and tortuous lithium transport paths around the particles within the electrodes using additional ion transport channels. The schematic structure of a lithium-ion battery depicted in Fig. 1 shows a possible transport pathway for lithium in the laser-induced structure. As active materials, graphite is typically used for the anode and lithium metal oxides, such as lithium-nickel-manganese-cobalt-oxide, are employed for the cathode.

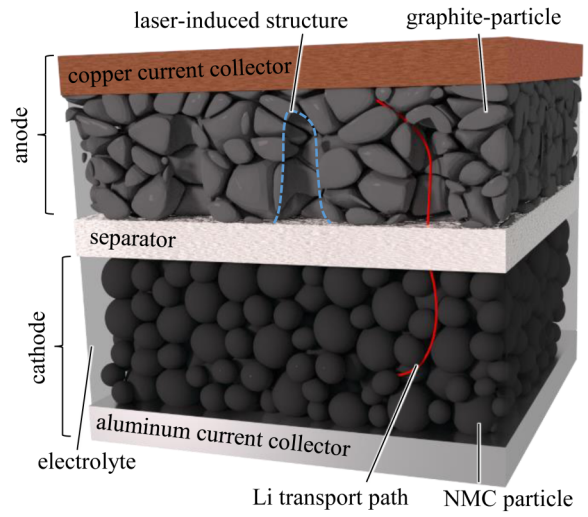

FIG. 1. Schematic illustration of a lithium-ion battery with a laser structured anode.

Both the structuring of the cathode[3] and the structuring of the anode[4] have been investigated in numerous research studies. For both electrodes, tremendous improvements in discharge capacity at high discharge currents could be measured, indicating a reduced cell internal resistance. Furthermore, electrochemical processes within the cells were modelled using simulation tools, which on the one hand increased the understanding of the influence of the geometric electrode design and on the other hand provided the basis for optimization approaches of the structures.[5] Furthermore, the production time of lithium-ion batteries during cell assembly was shortened by accelerating electrolyte wetting, as the created microcapillaries promoted rapid impregnation of electrodes with the electrolyte.[6,7]

The strong potential of the technology in terms of cell performance and subsequent production processes raises the question of why the structuring of the electrodes is not yet being used in industrial battery production. The process time appears to be a decisive factor here, since in industrial battery production large electrode areas have to be structured in a short time. Despite the constantly increasing power of the industrially available pulsed laser beam sources, great challenges remain in beam deflection and positioning, resulting from the structure requirements. The ablation process itself has been studied in the literature with different beam sources. Femtosecond laser systems have proven to be particularly suitable with regard to the achievable structural fineness, since there is almost no heat input into the surroundings of the process zone.[8,9] A thermal ablation outside the direct exposure zone of the laser beam, also caused by the evaporation of the binder holding the electrode together, can thus be avoided. The ablation by nanosecond pulses reduces processing times, but at the expense of the fineness of the structures produced.[10] Both processes have in common that the generation of structures is not possible by a single pulse, but (depending on the electrode material and the pulse parameters, for instance, the pulse energy) several pulses are necessary to achieve the required structural depth and aspect ratio. Thus, two machining strategies can be considered: the multiple pass, where a certain area is structured incompletely and then the same structures are hit again, and the "point-and-shoot" (PAS) strategy, where one structure is generated completely before the laser beam is deflected for the generation of the next structure. The PAS strategy has two fundamental disadvantages. On the one hand, shielding effects in the process zone may occur due to expulsion of ablation products and plasma, reducing the ablation efficiency.[4] On the other hand, significant amounts of time are required for the deflection of the laser beam, which further slows down the process. The multiple pass strategy, thus, seems to be the more promising alternative for industrial application, but very high demands on the accuracy and speed of the beam deflection systems have to be met, which is not state of the art yet.

II. OBJECTIVES AND APPROACH

Based on the potentials of laser structuring of electrodes described above, geometric requirements for the structures are derived from the literature. Here, the electrochemical details are discussed only briefly and reference is made to further sources. In the second step, the requirements for a beam deflection system are formulated that would be necessary for a use in industrial lithium-ion battery production. This results in enormous challenges for beam deflection technology. One of these challenges is the synchronization between the laser and the scanning device in one control unit, for which a solution concept is presented.

III. LITHIUM-ION BATTERY PRODUCTION AND STRUCTURE REQUIREMENTS

The lithium-ion battery production process chain is complex and characterized by a multitude of different production steps. In the conventional process chain, the calendaring process is used to adjust the electrode porosity systematically, and it represents the end of electrode fabrication. In the subsequent cell assembly steps, major electrode properties like porosity, thickness, and structure are not changed any further. Thus, the transition between electrode manufacturing and cell assembly is a suitable point in production to introduce the laser structuring process. The process chain is shown in Fig. 2, where the laser structuring process is highlighted. From an electrochemical point of view, a structure pattern consisting of hexagonally arranged holes is specifically useful, as this allows the material removal to be kept low, and, at the same time, a high electrochemical utilization of the electrode can be achieved.[11] A conceptual illustration of the approach for in-line electrode structuring is shown in Fig. 3.

Bore holes with a depth of at least 90% of the active material layer thickness and a diameter of $<30\,\mu$m on the side not facing the current collector are particularly promising. Furthermore, it seems reasonable to taper the structures in the direction of the current collector, since the ionic current density decreases in the direction of the current collector, and thus, finer structures are sufficient for ionic conduction. The area proportion of the structures on the side of the electrode not facing the current collector should not exceed 15%.[12] These geometrical requirements can be met by means of modern laser technology, but enormous challenges remain with regard to process time. For an exemplary structuring pattern as

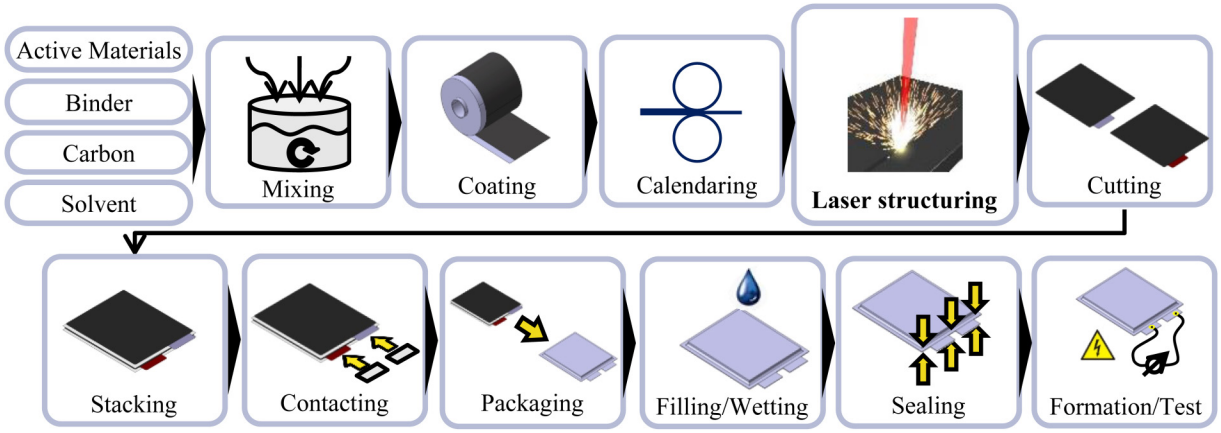

FIG. 2. Process chain for the production of lithium-ion pouch cells; the laser structuring process is highlighted at a possible point of integration into the production process.

shown in Fig. 3 and Table I (a hexagonally arranged hole structure with pulse distances $d_c = 200\,\mu$m and $d_l = 173\,\mu$m), this results in a structure density of ~2900 bore holes/cm^2. With a typical specific areal capacity of electrodes of 2 mAh/cm^2, $\sim 1.45 \times 10^6$ structures per ampere-hour of battery capacity are required, assuming that only the anode is structured. Table I summarizes the assumptions made here about the production process for lithium-ion electrodes and shows the calculated requirements for the laser scanner subsystem. It should be noted that the requirements described for battery production were estimated very conservatively and that significantly higher coating speeds and coating widths are common. Nevertheless, the extreme scanning speeds requested can only be achieved by polygon scanners. Certainly parallelization of several laser beam sources and scanners is also an option.

IV. CONCEPTS FOR ACCELERATING THE STRUCTURING PROCESS

For surface material removal or drilling applications, laser scanners are used to deflect the laser beam. Their accelerations and traversing speeds are limited by the mass and inertia of the drive and the deflecting mirror as well as by the rigidity of the controlled overall system. Specifically, in the PAS operation, this results in significant idle times for acceleration and deceleration in which the laser remains switched off. One possible solution to this problem is multiple passing with a constant scanner movement, in which the pulses have to hit the same spot repeatedly. In this case, the maximum laser power is the limiting effect on the process speed, since idle times caused by the mirror inertia are avoided. Advances in laser power of commercial pulsed beam sources, however, are currently mainly achieved by an increase in the maximum pulse repetition frequency f_p with almost constant pulse energy.[13,14] For comparable structuring results, this, in turn, is to be accounted for by drastically increasing the scanning speed, which can be achieved by highly dynamic optomechanical systems, such as polygon wheels.[15] However, the synchronous resolution of the control systems used must also be increased, which is often not addressed in the context of these developments. For this reason, the ARGNET interface for high-precision, phase-locked synchronization of several network participants in materials processing was

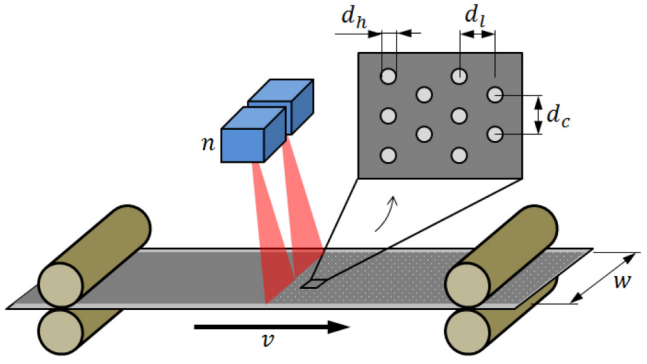

FIG. 3. Concept for in-line structuring of electrodes with n scan heads.

TABLE I. Assumed parameters for the structuring process and resulting requirements for the laser-scanner-subsystem.

Parameter	Value	Unit
Feed rate, v	20	m/min
Pulse distance, d_c	200	μm
Pulse distance, d_l	173	μm
Processing width, w	20	cm
Number of runs per structure[4]	6	—
Pulse energy (fs-pulses)[4]	40	μJ
Line rate	1926.8	s^{-1}
Scanning speed	2312.1	m/s
Laser power	462.4	W

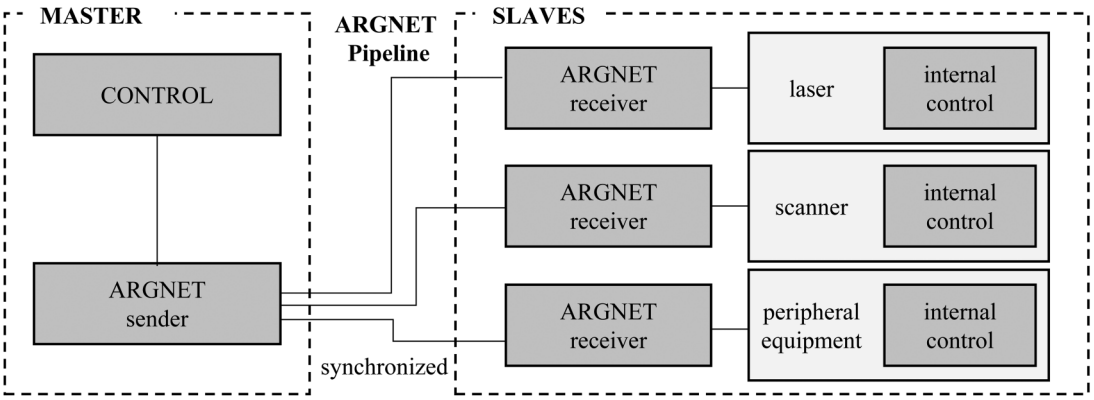

FIG. 4. Block diagram for the synchronization of network participants.

designed and implemented as part of the work presented here (Fig. 4).[16] In the considered example, we assume that with an infrared ultrashort pulse laser (USP laser) with pulse durations of 20 ps and a 2D scanner, hexagonally distributed holes with a borehole spacing of 200 μm are to be generated in multiple passes. The laser beam should move over the electrode at a constant traversing speed (not in the PAS operation) in order to combine high quality processing results with a minimum processing time. The deflection speed v_d required for this can be calculated using the specified structure distance a and the pulse repetition frequency f_p,

$$v_d = a \cdot f_p. \tag{1}$$

A short pulse laser with a pulse duration of less than 100 ns in the wavelength range from ~1030 to 1070 nm is used for referencing purposes. For comparability, the values for the average power of both laser systems are assumed to be identical at 5 W. With a focal length of 163 mm used for the F-theta lens, a focus diameter of ~30 μm is obtainable. The pulse repetition frequency of the USP laser is 1 MHz compared to 20 kHz of the short pulse laser (SP laser). In order to obtain a pulse distance of 200 μm, the traversing speed of the scanner has to be set to 4.0 m/s with the SP laser. The scanning speed for material processing with the USP laser has to be 200 m/s.

For the multiple pass operation, it is absolutely necessary to hit exactly the same target points repeatedly. The required spatial accuracy x of the system (jitter) results from the minimum temporal jitter t_{jit} of the controller according to

$$x = v \cdot t_{jit}. \tag{2}$$

This relationship applies exclusively under neglect of component-specific tolerances (e.g., laser stability, repetition accuracy of the scanner, etc.) in the laser and in the 2D scanner. Conventional controllers have a typical t_{jit} of about 10 ns, while the newly developed ARGNET controller has a t_{jit} of ~100 fs. From formulas (1) and (2), it results that the local resolution and accuracy deteriorate with an increase in the pulse repetition frequency and thus the deflection speed. This correlation is presented in Table II.

The accuracy for operating a USP laser at 1 MHz is unsuitable for the process, since the processing accuracy of 2 μm is already very poor. The operation of a conventional controller for synchronizing pulses with 20 MHz leads to even larger inaccuracies of ~40 μm, which makes precise processing impossible.

This work aims at the optimization of the conceptual design for synchronization of individual components involved in the process. The adaption of the controller serves to reduce the temporal jitter by appropriate hardware design in such a way that the local resolution is in the range below 0.1 μm despite the increasing deflection speed. The new ARGNET communication link was developed for this purpose (Fig. 4). A central master unit is still used to control the individual components, but communication takes place synchronously via a separate data interface, so that the slave network participants receive the necessary signals for a highly precise processing result with very low jitter.

At the same time, the network devices such as lasers, scanners, and other external peripherals (e.g., linear axes, cross tables, and measuring systems) can be set up locally separated, even though they are integrated in the communication pipeline.

V. SIGNAL RESPONSES OF THE CONTROL ARCHITECTURES

The electronic signal transmission of the conventional controller and the ARGNET controller were measured using an oscilloscope.

TABLE II. Spatial jitter for several pulse repetition frequencies at a fixed structure distance and fixed temporal jitter times.

Pulse rep. frequency f_p	Deflection speed for $a = 200\,\mu$m	Spatial jitter for $t_{jit} = 10$ ns	Spatial jitter for $_{jit} = 100$ fs
20 kHz	4 m/s	$4 \times 10^{-2}\,\mu$m	$4 \times 10^{-7}\,\mu$m
1 MHz	200 m/s	2 μm	$2 \times 10^{-5}\,\mu$m
20 MHz	4000 m/s	40 μm	$4 \times 10^{-4}\,\mu$m

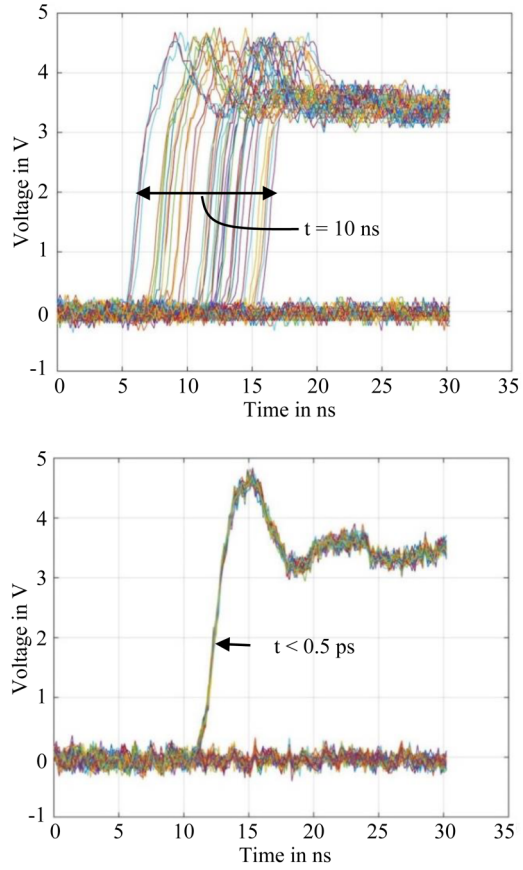

FIG. 5. Comparison of the electronic signal transmission of the conventional (top) and the ARGNET control (bottom).

A cyclic signal pulse was emitted by the master control, which was then made available to the slave network participants via the transmission path. The distributed synchronization signal was recorded several times and then compared. The improvement of the jitter by the ARGNET control compared to the conventional control is shown in Fig. 5. While in the case of the conventional controller (Fig. 5 top), there is a clear time offset between the measured signals which lies within the temporal jitter (10 ns); this time offset is not visible in the case of the ARGNET controller (Fig. 5 bottom). Here, the temporal jitter is less than 0.5 ps, which results in almost congruent curves for the time scale selected here. As a result, at high processing speeds, e.g., with polygon scanners, significantly lower local jitter will occur. This avoids machining errors and inaccuracies during high speed machining and thus provides the basis for fast electrode processing with polygon scanners.

VI. SUMMARY

The laser structuring of electrodes is a promising approach to improve the properties of lithium-ion batteries. In previous studies, various potentials have been identified, e.g., in increasing the discharge capacity at high current rates and in improving the ageing behavior and wettability with the electrolyte fluid. However, since very large electrode surfaces have to be structured rapidly in order to maintain economically reasonable process times, the current low process speed of laser structuring prevents an industrial application. In the presented work, therefore, requirements for the structures and the process were defined first. The required extreme demands on the beam deflection speed result in the need for a novel control system that reduces temporal inaccuracies. Thus, the transmission of control signals to the individual subsystems was optimized to achieve a higher temporal precision, so that at high beam deflection speeds a more accurate pulse overlap is possible. The improvement of signal transmission was demonstrated by measurement of electronic signal transmission with an oscilloscope. Subsequent work will include a validation of the system, which will encompass a detailed examination of the processing results.

ACKNOWLEDGMENTS

This work was made possible by funding from the Federal Ministry of Education and Research (BMBF) from the UKP Association of the German Photonics Research Programme (UKP) and by funding from the Federal Ministry of Economics and Energy (BMWi) in the SurfaLIB (No. 03ET6103F) Project.

REFERENCES

[1]H. Zheng, L. Tan, G. Liu, X. Song, and V. S. Battaglia, "Calendering effects on the physical and electrochemical properties of Li[Ni1/3Mn1/3Co1/3]O2 cathode," J. Power Sources **208**, 52–57 (2012).
[2]W. Pfleging, "A review of laser electrode processing for development and manufacturing of lithium-ion batteries," Nanophotonics **7**, 13 (2018).
[3]M. Mangang, J. Pröll, C. Tarde, H. J. Seifert, and W. Pfleging, "Ultrafast laser microstructuring of $LiFePO_4$ cathode material," in *SPIE LASE*, edited by U. Klotzbach, K. Washio, and C. B. Arnold (SPIE, San Francisco, CA, 2014), p. 89680M.
[4]J. B. Habedank, J. Endres, P. Schmitz, M. F. Zaeh, and H. P. Huber, "Femtosecond laser structuring of graphite anodes for improved lithium-ion batteries: Ablation characteristics and process design," J. Laser Appl. **30**, 32205 (2018).
[5]J. B. Habedank, L. Kraft, A. Rheinfeld, C. Krezdorn, A. Jossen, and M. F. Zaeh, "Increasing the discharge rate capability of lithium-ion cells with laser-structured graphite anodes: Modeling and simulation," J. Electrochem. Soc. **165**, A1563–A1573 (2018).
[6]J. B. Habedank, F. J. Günter, N. Billot, R. Gilles, T. Neuwirth, G. Reinhart, and M. F. Zaeh, "Rapid electrolyte wetting of lithium-ion batteries containing laser structured electrodes: *In situ* visualization by neutron radiography," Int. J. Adv. Manuf. Technol. **102**, 2769–2778 (2019).
[7]W. Pfleging, R. Kohler, and J. Pröll, "Laser generated microstructures in tape cast electrodes for rapid electrolyte wetting: New technical approach for cost efficient battery manufacturing," in *SPIE LASE*, edited by U. Klotzbach, K. Washio, and C. B. Arnold (SPIE, San Francisco, CA, 2014), p. 89680B.
[8]C. A. Hartmann, "Investigation on laser micro ablation of steel using short and ultrashort IR multipulses," J. Laser Micro/Nanoeng. **2**, 44–48 (2007).
[9]B. Neuenschwander, B. Jaeggi, and M. Schmid, "From fs to sub-ns: Dependence of the material removal rate on the pulse duration for metals," Phys. Procedia **41**, 794–801 (2013).
[10]M. Mangang, H. J. Seifert, and W. Pfleging, "Influence of laser pulse duration on the electrochemical performance of laser structured $LiFePO_4$ composite electrodes," J. Power Sources **304**, 24–32 (2016).

[11]J. B. Habedank, *Designing Structured Electrodes for Li-Ion Batteries* (Advanced Battery Power, Aachen, 2017).
[12]U. Sauter, "Battery e.g. lithium ion battery has porous layered electrode which is provided with several recesses at opposite side of electrode metal sheet," patent DE102012215921A1 (13 March 2014).
[13]G. Raciukaitis, "Use of high repetition rate and high power lasers in microfabrication: How to keep the efficiency high?," J. Laser Micro/Nanoeng. **4**, 186–191 (2009).
[14]K. Du, S. Brüning, and A. Gillner, "High-power picosecond laser with 400W average power for large scale applications," in *Laser-Based Micro- and Nanopackaging and Assembly VI*, edited by F. G. Bachmann, W. Pfleging, K. Washio, J. Amako, W. Hoving, and Y. Lu (SPIE, San Francisco, CA, 2012), p. 82440P.
[15]R. de. Loor, "Polygon scanner system for ultra short pulsed laser micromachining applications," Phys. Procedia **41**, 544–555 (2013).
[16]S. Nolte, "Ultrashort pulse lasers for precise processing: Overview on a current German research initiative," in *Frontiers in Ultrafast Optics: Biomedical, Scientific, and Industrial Applications XIV*, edited by A. Heisterkamp, P. R. Herman, M. Meunier, and S. Nolte (SPIE, San Francisco, CA, 2014), p. 89721D.

Meet the Authors

Jan Bernd Habedank is the head of the Joining and Cutting Technology department and a doctoral candidate at the Institute for Machine Tools and Industrial Management (*iwb*). He studied mechanical engineering at the Technical University of Munich and the Technical University of Darmstadt. His research is focused on improving the properties of lithium-ion batteries by means of laser-based processes.

Daniel Schwab is the project head for developing USPL-based high-speed scanning solutions at ARGES. He studied mechanical engineering with the focus on laser material processing at the OTH Amberg. His final examination was about laser processing of brittle materials and developing high speed focus shifting solutions.

Bernhard Kiesbauer is the head of research and development at ARGES. He studied automation technology at the OTH Amberg-Weiden. His work focuses on the development of control systems for laser scanning technologies.

Michael F. Zaeh is the head of the Institute for Machine Tools and Industrial Management (*iwb*) as well as a full professor for Machine Tools and Manufacturing Technologies at the Technical University of Munich. His work focuses on production engineering and, in particular, on machine tools, laser and joining technology, and additive manufacturing.